LITHIATED TERNARY COMPOUNDS FOR NEUTRON DETECTORS: MATERIAL PRODUCTION AND DEVICE CHARACTERIZATION OF LITHIUM ZINC PHOSPHIDE AND LITHIUM ZINC ARSENIDE

by

BENJAMIN W. MONTAG

B.S., Nebraska Wesleyan University, 2008

AN ABSTRACT OF A DISSERTATION

submitted in partial fulfillment of the requirements for the degree

DOCTOR OF PHILOSOPHY

Department of Mechanical and Nuclear Engineering
College of Engineering

KANSAS STATE UNIVERSITY
Manhattan, Kansas

2015

ABSTRACT

There is a need for compact, rugged neutron detectors for a variety of applications including national security and oil well logging. A solid form neutron detector would have a higher efficiency than present day gas filled ^{3}He and $^{10}BF_3$ detectors, which are standards currently used in the industry today. A sub-branch of the III-V semiconductors is the filled tetrahedral compounds, known as Nowotny-Juza compounds ($A^{I}B^{II}C^{V}$). These materials are desirable for their cubic crystal structure and semiconducting electrical properties. Originally studied for photonic applications, Nowotny-Juza compounds have not been fully developed and characterized. Nowotny-Juza compounds are being studied as neutron detection materials here, and the following work is a study of LiZnP and LiZnAs material development and device characterization.

Precursor binaries and ternary materials of LiZnAs and LiZnP were synthesized in-house in vacuum sealed quartz ampoules with a crucible lining. Synthesized powders were characterized by x-ray diffraction, where lattice constants of 5.751 ± .001 Å and 5.939 ± .002 Å for LiZnP and LiZnAs, respectively, were determined. A static vacuum sublimation in quartz was performed to help purify the synthesized ternary material. The resulting material from the sublimation process showed characteristics of a higher purity ternary compound. Bulk crystalline samples were grown from the purified material. Ingots up to 9.0 mm in diameter and 13.0 mm in length were harvested. Individual samples were characterized for crystallinity on a Bruker AXS Inc. D2 CRYSO, energy dispersive x-ray diffractometer, and a Bruker AXS D8 DISCOVER, high-resolution x-ray diffractometer with a 0.004^{o} beam divergence. High-resolution XRD measurements indicated reasonable out-of-plane and in-plane ordering of LiZnP and LiZnAs crystals. Devices were fabricated from the LiZnP and LiZnAs crystals. Resistivity of devices were determined within the range of $10^{6} - 10^{11}$ Ω cm. Charge carrier mobility and mean free drift time products were characterized for electrons at 8.0×10^{-4} cm^2 V^{-1} ± 4.8% and 9.1×10^{-4} cm^2 V^{-1} ± 4.4% for LiZnP and LiZnAs respectively. Sensitivity to 337 nm laser light (3.68 eV photons) was observed, where an absorption coefficient of 0.147 mm^{-1} was determined for LiZnAs devices. Thermal neutron sensitivity was evaluated with *unpurified* and *purified* LiZnP and LiZnAs devices. Sensitivity was observed, however material quality and crystalline quality significantly hindered device performance.

LITHIATED TERNARY COMPOUNDS FOR NEUTRON DETECTORS: MATERIAL PRODUCTION AND DEVICE CHARACTERIZATION OF LITHIUM ZINC PHOSPHIDE AND LITHIUM ZINC ARSENIDE

by

BENJAMIN W. MONTAG

B.S., Nebraska Wesleyan University, 2008

A DISSERTATION

submitted in partial fulfillment of the requirements for the degree

DOCTOR OF PHILOSOPHY

Department of Mechanical and Nuclear Engineering
College of Engineering

KANSAS STATE UNIVERSITY
Manhattan, Kansas

2015

Approved by:

Major Professor
Douglas S. McGregor

COPYRIGHT

ABSTRACT

There is a need for compact, rugged neutron detectors for a variety of applications including national security and oil well logging. A solid form neutron detector would have a higher efficiency than present day gas filled ^{3}He and $^{10}BF_3$ detectors, which are standards currently used in the industry today. A sub-branch of the III-V semiconductors is the filled tetrahedral compounds, known as Nowotny-Juza compounds ($A^{I}B^{II}C^{V}$). These materials are desirable for their cubic crystal structure and semiconducting electrical properties. Originally studied for photonic applications, Nowotny-Juza compounds have not been fully developed and characterized. Nowotny-Juza compounds are being studied as neutron detection materials here, and the following work is a study of LiZnP and LiZnAs material development and device characterization.

Precursor binaries and ternary materials of LiZnAs and LiZnP were synthesized in-house in vacuum sealed quartz ampoules with a crucible lining. Synthesized powders were characterized by x-ray diffraction, where lattice constants of 5.751 ± .001 Å and 5.939 ± .002 Å for LiZnP and LiZnAs, respectively, were determined. A static vacuum sublimation in quartz was performed to help purify the synthesized ternary material. The resulting material from the sublimation process showed characteristics of a higher purity ternary compound. Bulk crystalline samples were grown from the purified material. Ingots up to 9.0 mm in diameter and 13.0 mm in length were harvested. Individual samples were characterized for crystallinity on a Bruker AXS Inc. D2 CRYSO, energy dispersive x-ray diffractometer, and a Bruker AXS D8 DISCOVER, high-resolution x-ray diffractometer with a 0.004^{o} beam divergence. High-resolution XRD measurements indicated reasonable out-of-plane and in-plane ordering of LiZnP and LiZnAs crystals. Devices were fabricated from the LiZnP and LiZnAs crystals. Resistivity of devices were determined within the range of $10^{6} - 10^{11}$ Ω cm. Charge carrier mobility and mean free drift time products were characterized for electrons at 8.0×10^{-4} cm^2 V^{-1} ± 4.8% and 9.1×10^{-4} cm^2 V^{-1} ± 4.4% for LiZnP and LiZnAs respectively. Sensitivity to 337 nm laser light (3.68 eV photons) was observed, where an absorption coefficient of 0.147 mm^{-1} was determined for LiZnAs devices. Thermal neutron sensitivity was evaluated with *unpurified* and *purified* LiZnP and LiZnAs devices. Sensitivity was observed, however material quality and crystalline quality significantly hindered device performance.

TABLE OF CONTENTS

LIST OF FIGURES

LIST OF TABLES

ACKNOWLEDGEMENTS

The following work was performed at the Semiconductor Materials and Radiological Technologies (S.M.A.R.T.) Laboratory, Kansas State University, Manhattan KS 66506. The project was supported in part by the Advanced Materials program DOE – NNSA, grant # DE-FG52-08NA28766.

The author would like to first express gratitude to Prof. Douglas McGregor for taking a chance on a last-minute applicant to work in your laboratory. Thank you for the knowledge, skills, and life lessons, which I will carry with me for a lifetime. The author would also like to thank all of the members, past and present, of the S.M.A.R.T. Laboratory for their assistance and contributions to this work (*listed in no particular order*): Dr. Philip B. Ugorowski, Nathaniel S. Edwards, Michael A. Reichenberger, Luke Henson, Dr. Kyle A. Nelson, Ryan Fronk, Dr. Steven Bellinger, Cody Rietcheck, Kevin Arpin, Chris Linnick, Troy Unruh, Michael Meier, Dustin Werth, Tyler Krehbiel, Sam Browning, Adam Brooks, Harry McDonald, Sam Shelley, Juergen Greve, Edgar Alvarado, Dr. Elsa Ariesanti, Sam James, Brian McCurry, Brian Cooper, Dr. Alireza Kargar, Dr. Mark Harrison and Dr. Walter McNeil.

The author also extends gratitude to Dr. Madhana Sunder of Bruker *AXS*. Thank you for all of your help day and night, whether it was measurement question, data interpretation, or publication corrections. Your contributions and assistance with this work was a blessing.

Thank you to the Kansas State University TRIGA Mark II reactor staff and Dr. Jeffery Geuther for their time and patience during countless hours of neutron sensitivity testing.

Thank you to Tim Sobering, Russel Taylor, David Huddleston and the Electronics Design Laboratory team for their help with the $A^{I}B^{II}C^{V}$ device electronics (trans-impedance amplifier). Tim, thank you for your patience with all of my electrical engineering questions.

Thank you to John Desper, and the Kansas State University Chemistry Department for the use of their Bruker D8 Advance x-ray diffractometer.

Thank you to Dr. Brett DePaola and Dr. Kristan Corwin for the use of 250 μJ, 337 nm laser, Si photodiode, adjustable iris and protective equipment.

Thank you to Kevin Dennis and Dr William McCallum at Ames National Laboratory extending their knowledge of high temperature processing, and hosting a visit to their facility.

Finally, I would to thank my loving wife, daughter, parents, and family for their patience, support, and prayers throughout this journey. Lastly, I would like to thank my Lord and Savior, Jesus Christ for hearing my prayers every step of this journey.

DEDICATION

I would like to dedicate this work to my wife, Emma, daughter Agnes,
and my family; the Montag's, the Buchta's, and Radtke's.
Thank for the prayers, support and encouragement through this entire process.

Chapter 1 : Introduction

I didn't fail. I just found 2,000 ways not to make a lightbulb;

I only needed one way to make it work.

- ***Thomas Edison***

1.1 Solid-state radiation detection history

As early as the 1930's, neutron detection has been an integral component of nuclear studies. Chadwick proposed the existence of the neutron in *Nature* magazine where he described his work with what was known as *beryllium radiation* [1]. He noticed when the Beryllium nucleus was irradiated with α particles, the emission of the proposed neutron was observed. Gas-filled detectors, such as an ionization chamber, proportional counter, or Geiger-Müller counter were used to identify the radiation presence. Paraffin wax, or other materials containing hydrogen were placed in front of the ionization vessel window, where neutrons interacting in the hydrogen containing material released in abundance of protons through elastic scattering events that subsequently interacted in the gas-filled detector, thereby, providing a measureable response [2]. As the science progressed, the first of the solid-state charged particle detectors were developed from AgCl, known as crystal counters in the 1940's [3]. Shortly after, the first solid-state neutron detectors were developed by Yamakawa in 1949, known as the slow neutron crystal counter [4]. The mixed lithium and silver bromide crystals were annealed, and then cooled to liquid nitrogen temperatures to operate as neutron counters. The first of the layered solid-state devices was introduced by Babcock in 1959 [5]. The device consisted of a *pn* surface junction diode of silicon or germanium with a thin neutron sensitive coating on the surface. The device was compact, as seen in Fig. 1.1. This initial thin-film solid-state neutron detector was relatively inexpensive to fabricate, yet had relatively low gamma-ray sensitivity.

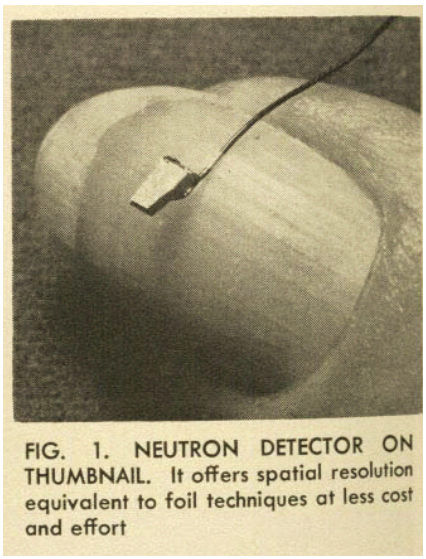

FIG. 1. NEUTRON DETECTOR ON THUMBNAIL. It offers spatial resolution equivalent to foil techniques at less cost and effort

Fig. 1.1. The first thin-film solid-state neutron detector [5].

As the age of nuclear energy progressed through the 1950's, the need for neutron counting became a necessity with the development of the first nuclear reactor by Argonne National laboratory at the University of Chicago [6]. Additionally, detection of special nuclear materials became pertinent as the development of the nuclear weapons progressed with the first test detonation of the United States the Trinity site on July 16, 1945. Since the introduction of nuclear weapons and the current heightened awareness of illicit materials entering the United States boarders, the need for neutron detectors has risen.

1.2 Motivation for Research

The filled tetrahedral compound class $A^{I}B^{II}C^{V}$ materials consist of the III-V-like compounds with Li interstitials, also referred to as Nowotny-Juza compounds. Nowotny-Juza materials are interesting for solid-state neutron detectors because the devices would be rugged, could potentially operate at elevated temperatures, have high thermal neutron detection efficiency, and adequate gamma-ray rejection. Materials containing, ^{6}Li, ^{10}B, ^{113}Cd, ^{157}Gd, and ^{199}Hg have been considered for solid-state neutron detectors [7-19]. The $^{10}B(n,\alpha)^{7}Li$ reaction is desirable for the ^{10}B microscopic thermal neutron absorption cross section of 3839 barns, but

boron-based compounds, such as BP, BN, and BAs, have shown limited success and thus far do not appear promising. These boron based materials typically fail due to crystal growth, purity, and materials preparation problems [15-19]. A high purity semiconductor is extremely important to reduce charge trapping, capacitance, and other charge transport related problems that greatly degrade the device performance. Additionally, thin-film coated boron devices suffer low neutron detection efficiency due to their geometry, where only one reaction product is absorbed in the semiconducting material. Consequently, the resultant signals may be small and difficult to distinguish from background and gamma-ray induced events [20]. Additionally, depending on the range of the reaction products in the boron material, film thickness is restricted, due to energy self-absorption, resulting in a maximum intrinsic detection efficiency of approximately 4.5% [20]. Solid-state detectors containing ^{113}Cd and ^{199}Hg devices also have limited detection efficiency due to the low absorption probability of the prompt gamma-rays that result from the reactions ^{113}Cd(n,γ)^{114}Cd and ^{199}Hg(n,γ)^{200}Hg [7-10]. The reaction ^{157}Gd(n,γ)^{158}Gd is desirable for the large ^{157}Gd thermal neutron capture cross section of 259,000 barns [21]. The reaction results in low-energy prompt gamma rays and conversion electrons below 220 keV, which are difficult to discern from background radiations [20]. Finally, ^{6}Li has not been explored to the same extent as other thermal neutron absorbers, and has an intrinsic thermal neutron absorption cross section of 940 barns. The reaction produces a total Q-value of 4.78 MeV, shown in the following reaction,

$$^{6}Li + {}^{1}_{0}n \rightarrow {}^{3}H(2.73MeV) + \alpha(2.05MeV)\,. \tag{1.1}$$

Nowotny-Juza compounds, namely LiZnP and LiZnAs, may provide on alternative to many neutron detection materials studied in the past. The high concentration of lithium in the cubic lattice of LiZnP and LiZnAs is very desirable for high-efficiency neutron detection devices. However, minimal literature is available regarding Nowotny-Juza materials, as will be further discussed in the following chapter. The following study was directed to overcoming the material challenges reported in the literature, contribute to the material characterization, characterize the electrical properties (charge carrier mobility-lifetime, resistivity), and finally, fabricate and test LiZnP and LiZnAs devices for neutron sensitivity.

1.3 Contribution to Nowotny-Juza compounds LiZnP and LiZnAs

A summary of the novel contributions to the development of LiZnP and LiZnAs materials and devices is listed:

- Contributed to the existing synthesis techniques for producing LiZnAs and LiZnP powders, and characterized the produced materials.
- Produced a way to purify LiZnP and LiZnAs, and characterized the process
- Developed a way to grow bulk ingots of LiZnP and LiZnAs. Grew the largest known ingots of LiZnP and LiZnAs using the high-temperature Bridgman technique.
- Determined idealized thermal neutron response spectra using MCNP6
- Determined the idealized charge collection efficiency profiles of LiZnP and LiZnAs based on experimental $\mu\tau$ products.
- Developed LiZnP and LiZnAs thermal neutron absorption curves as a function of thickness
- Built numerous devices from LiZnP and LiZnAs ingots.
- Characterized the hygroscopic nature of LiZnP
- Characterized conformal coatings that were not only UV transparent for 337 nm laser testing, but also coatings that would not flake, and preserve the hygroscopic material.
- Built and characterized numerous high temperature crystal growth systems to develop the ternary material
- Perhaps the first to witness 337 nm photon, and neutron induced currents in LiZnP and LiZnAs
- Contributed phase identification XRD scans to the International Crystal Diffraction Database (ICDD)
- Contributed to the material properties of LiZnP and LiZnAs: approximate melting temperatures, approximate density
- Contributed to the electrical properties of LiZnP and LiZnAs: bulk resistivity, $\mu^*\tau$ products

1.4 Organization of the Thesis

Lithium-based, solid-form neutron detectors have not been studied as aggressively as boron-based solid-form neutron detectors. Nowotny-Juza material studies have not been heavily reported in literature, likely due to the fact that Nowotny-Juza compounds are not trivial to produce, nor trivial to grow in bulk. Literature provided hints on the synthesis processes, however bulk crystallization has never been reported outside of following study. Since little work has been reported with this class of materials, LiZnP and LiZnAs were chosen from a collection of materials (LiZnN, LiMgP, LiMgAs, LiMgN, etc.) to focus efforts due to the most of the existing literature focused on LiZnP and LiZnAs, and needed to be developed further.

In Chapter 2, a brief discussion of the background of the neutron is given. Following, a review is presented of the literature that exists concerning LiZnP and LiZnAs material production, testing, and simulation work. Theoretical based studies of charge collection efficiencies (based on experimental work presented here), neutron absorption and idealized pulse height spectra are presented in Chapter 3. However, majority of the following study is an experimental study. Chapter 4 details the preliminary embodiments, the experiments that lead to the most successful synthesis, and bulk crystal growth routines, detailed in Chapter 5. Devices were fabricated and explored for electrical properties, and tested for radiation sensitivity as detailed in Chapter 6. Lastly, in Chapter 7, conclusions are discussed based on the results, and brief discussion of the future of LiZnP and LiZnAs material development.

Chapter 2 : Background

It is a question of much importance whether a compound of the positive and negative electrons (neutron, an electrically neutral massless molecule) really exists…

- Walther Nernst, 1904

The following chapter, the origin of the neutron, interactions involving the neutron, and detection of the neutron are discussed. Further, types of detectors are discussed, including functionality and limitations. Lastly, a review of LiZnP and LiZnAs materials in the literature is presented.

2.1 The Neutron

Scientists speculated almost 30 years before the neutron was discovered, that a neutral particle may exist [22]. Walther Nernst discussed in his book, *Theoretical Chemistry*, the existence of negative and positive electrons (the positive electron being a neutral particle), and at this point, had only a hypothetical existence [22]. Nernst states (resuming the quote above), "…we shall assume that neutrons are everywhere present like the luminiferous ether[1], and may regard the space filled by these molecules as weightless, nonconducting, but electrically polarizable, that is, as possessing the properties which optics assumes for the luminiferous ether." It was Ernest Rutherford, however, who proposed that the neutron had to exist [24, 25]. Years later, in 1932, Rutherford's student, James Chadwick published "The existence of the neutron", where he described that the neutron was a combination of an electron and a proton[2], that weighted between 1.005 and 1.008 amu [2]. Today, the neutron is known as a subatomic particle with a mass slightly higher than a proton, composed of two down quarks with charge

[1] Luminiferous ether is the postulated medium for the propagation of light from the late 19th century. This theory was disproved by the Michelson-Morley experiment [23], and has now been replaced by the theory of relativity and quantum theory.

[2] The combination of an electron and a proton is a very basic view of the neutron to modern physics of today.

-q/3 and one up quark with charge +2q/3, thus having a total charge of zero, neutral. The neutron decays into a proton (*p*), electron(*e*-), and antineutrino ($\bar{\nu}$), shown in Eq. (2.1) [26].

$$n \rightarrow p + e^{-} + \bar{\nu}, \tag{2.1}$$

The average mean lifetime, from birth until decay, of a free neutron is 885.7 ± 0.8 sec, therefore from birth, a relatively sufficient time for detection is provided [27]. Spontaneous neutrons are born with energies that range from a few meV to tens of MeV, where thermal neutrons are defined at an energy of 0.0259 eV. Neutrons are born from nuclear reactions, including nuclear fusion, nuclear fission, photo-neutrons, (n,2n) reaction, (α,n) reaction, and high-energy interactions (spallation sources, accelerators). Extensive listings of neutron sources can be found in the literature [28-30].

2.2 Neutron Detection with Solid-State Materials

As briefly summarized in Chapter 1, many materials have been explored for solid-state neutron detectors. Neutrons do not typically cause direct ionization[3], and therefore can be challenging to detect. For solid-state neutron detection, ionizing reaction products released from a neutron absorption are commonly the desired observables with a radiation detector. These detectors generally contain a neutron absorbing material, commonly ^{6}Li, ^{10}B, ^{113}Cd, ^{157}Gd, or ^{199}Hg, materials all with high capture cross sections for neutrons. They also all emit reaction products that can be *observed*. The isotope ^{10}B is 19.90% naturally abundant and has a microscopic thermal neutron absorption cross section of 3839 barns, which interacts with a neutron by,

$$n + {}^{10}B \rightarrow \alpha(1.47MeV) + {}^{7}Li(0.840MeV) + \gamma(0.480) \qquad 94\%, \tag{2.2}$$

[3] The (n,p) reaction is an example of direct ionization.

$$n + {}^{10}B \rightarrow \alpha(1.78MeV) + {}^{7}Li(1.02MeV) \qquad 6\%\,, \tag{2.3}$$

where each branch (94% and 6%) have a total Q-value of 2.79 MeV [31, 32]. Boron has been used in a variety of solid-state devices such as BAs, BN, B_4C, and is also commonly loaded with polyethylene for neutron shielding.

The isotope ^{113}Cd is 12.2% naturally abundant with a microscopic thermal neutron absorption cross section of 20,600 barns [21], which interacts with a neutron in the following,

$$n + {}^{113}Cd \rightarrow \gamma_1(558.6keV,\ 73\%\,\text{yield}) + \gamma_2(651.3keV,\ 13\%\,\text{yield}) + \gamma's\,. \tag{2.4}$$

Cd based materials have been explored for neutron detection capabilities, however the absorption of the prompt gamma rays is low, resulting in low-efficiency devices [10, 33]. Additionally, many neutron detector applications require neutron detectors to be gamma-ray blind, therefore, when the neutron signature is composed of gamma rays, it is difficult to discern background gamma-ray events from neutron events. Natural Cd, however, has a microscopic thermal neutron absorption cross section of 2520 barns [21] which appears to be ideal for neutron shielding, beam shutters, or beam choppers.

Gadolinium has also been explored for solid-state neutron detectors, commonly used as a dopant, or loaded into plastic scintillators [34]. ^{157}Gd has a microscopic thermal neutron absorption cross section of 259,000 barns, with a natural abundance[4] of 15.7%, which interacts with a neutron by ^{157}Gd(n,γ)^{158}Gd. The reaction also results in energetic conversion electrons between energies of 70 keV – 240 keV for approximately 60% neutron absorptions. Of the 60%, approximately 88.5% of the conversion electrons are less than 100 keV [35, 36]. The low absorption probability for the prompt gamma-ray emission from a thermal neutron capture hinders device efficiency. Additionally, absorptions of the low energy conversion electrons are difficult to discern from background radiations and electrical noise in detector system.

Mercury has been explored as a neutron detection medium with materials such as HgI_2 [7, 9]. HgI_2 is known for its high z-number (high stopping power for gamma rays), and semiconducting properties [37, 38]. Mercury contains the isotope ^{199}Hg that is 17% naturally

[4] ^{157}Gd is difficult to acquire, and as a result, natural Gd is generally used in device fabrication which has a microscopic thermal neutron absorption cross section of only 49,700 barns.

abundant, with a microscopic thermal neutron absorption cross section of 2150 barns, and interacts with a thermal neutron by,

$$n + {}^{199}Hg \rightarrow \gamma_1 (368.1 keV,\ 81\%\,\text{yield}) + \gamma_2 (1693.9 keV,\ 14\%\,\text{yield}) + \gamma's\ . \qquad (2.5)$$

where it is observed that prompt gamma rays are emitted from a thermal neutron capture [39]. Similar to Cd based devices, the absorption efficiency of the prompt gamma rays from absorption of a thermal neutron is low[5], therefore limiting the reaction product detection efficiency.

Lastly, lithium has been explored for neutron detector applications. ^{6}Li is 7.59% naturally abundant, and has a microscopic thermal neutron absorption cross section of 940 barns. The capture of a thermal neutron results in a total Q-value of 4.78 MeV where heavily ionizing particles, ^{3}H (2.73 MeV) and α (2.05 MeV), are released as shown in Eq. (1.1) [21]. These reactions products are short range, and highly energetic compared to reaction products from aforementioned neutron absorbers. These short-range reaction products can be completely absorbed in a detection medium, resulting in large signals easily distinguishable from background radiations. The microscopic thermal neutron absorption cross section of 940 barns for ^{6}Li is lower than other neutron absorbers, and is lower for natural lithium (7.59% ^{6}Li) at 70.5 barns [21]. However, enriched ^{6}Li is available in enrichment levels between 95-96% [40], and can increase the neutron sensitivity material in the detector as compared to natural lithium, thus increasing the neutron absorption in the device. The following sections describe solid-state detector operation, functionality and limitations of each technology.

2.2.1 Scintillators

A scintillation detector is a solid-state detector that emits light resulting from a radiation capture. The light is collected and converted into energetic electrons by means of a coupled

[5] Devices fabricated from ^{199}Hg, such as HgI_2, make much better solid-state neutron detectors than Cd based devices due to the lower energy, 368 keV prompt gamma ray, which has a much higher probability of being absorbed in the semiconductor than the high energy gamma rays from the ^{113}Cd(n,γ)^{114}Cd reaction.

photomultiplier tube (PMT) coupled to the scintillator, as shown in Fig. 2.1. For the case of neutron detection, the scintillation crystal, or plastic, is often doped, or loaded with a neutron reactive material [34]. In some cases, such as LiI crystals, the neutron reactive material is not a dopant, but instead a major constituent in the crystal lattice [41, 42]. When a neutron is absorbed in the scintillator material by a neutron absorber, the ionizing reaction products create electron-hole pairs caused by the promotion of electrons from the valence band into the conduction band. A free electron de-excites from the conduction band into an activator state between the valence band and the conduction band, thereby, producing a scintillation photon in the de-excitation process. Despite some losses, a scintillation photon may reflect off the reflector surrounding the scintillation solid, pass through the coupling material and PMT window, and interact with the photocathode. The scintillation photon is then converted into a photo-electron at the photocathode, and is drifted by electrical potential to the first dynode of the PMT. The photo-electron is absorbed in the dynode, and from the gained kinetic energy, is multiplied into more electrons that are subsequently directed to the next dynode. Electron multiplication occurs at each dynode until the mass of electrons is collected at the anode, and the signal is sent to processing electronics [30].

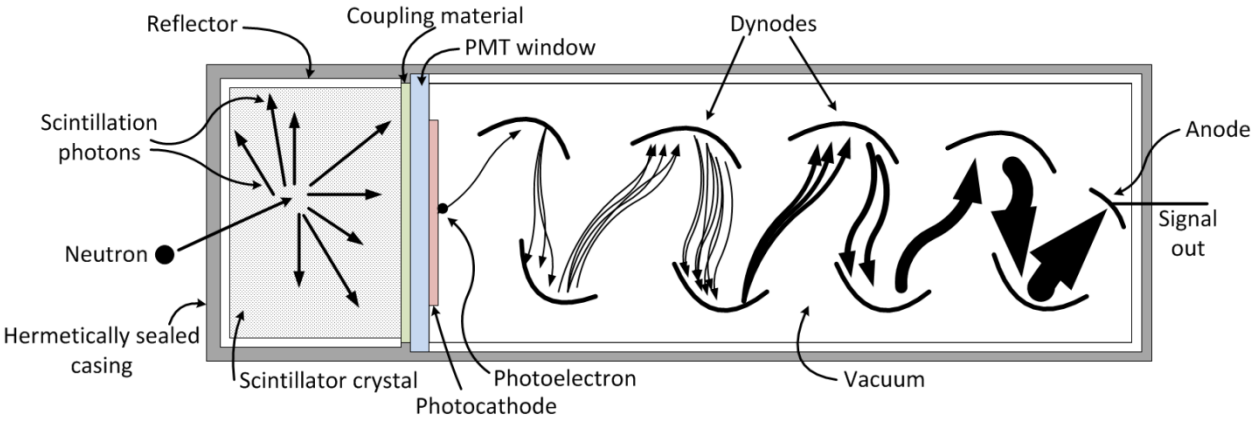

Fig. 2.1. The cross-sectional view of a scintillation neutron detector.

Scintillation neutron detectors, such as LiI, can have high thermal neutron absorption, however, inefficiency with any of aforementioned mechanisms can reduce the light collection efficiency, ultimately affecting the thermal neutron detection efficiency. Additionally, other scintillation neutron detectors are only doped with neutron sensitive materials (generally on the

ppm to 1% concentrations) which also reduce the neutron absorption in the material, and as a result, limit the thermal neutron detection efficiency. Many neutron detector applications may require the detection system to be rugged, and unfortunately, the PMT portion of the detection system is fragile, thus limiting the detector applications. To remedy the fragile PMT problem, high-efficiency photo-diodes (solid-state photomultipliers) have been developed that couple well with the scintillation photon emission from the scintillation material, making a lighter, compact, and more rugged scintillation detector system [43].

2.2.2 Semiconductors

A semiconductor is a solid material that has a conductivity between that of an insulator (no charge flow), and that of a conductor (charge flows easily). Semiconductor radiation detectors can have many advantages compared to other detectors, such as superior energy resolution, compact, rugged, and an effective area that can be varied to accommodate requirements of a specific application. For neutron detection however, high energy resolution is not as much of a concern because spectroscopy is not the primary focus, but instead high efficiency for neutron absorption and reaction product absorption. There are two primary semiconductor neutron detector designs, those being thin film coated devices, known as *semiconductor diode detectors*, and bulk semiconductor devices, known as *solid-state detectors* [31].

2.2.2.1 Thin film coated neutron detectors (semiconductor diode detectors)

The basic thin film coated device consists of a semiconductor with a contact layer, followed by a neutron sensitive material coating, as shown in Fig. 2.2. There are two common ways the device is designed. The first is by producing a *pn* junction diode, and then applying a contact on top of the device, followed by a layer of neutron reactive material. The second is by applying a metal contact to an intrinsic semiconductor, therefore producing a metal-semiconductor rectifying junction, known as a Schottky barrier, followed by a layer of neutron

reactive material. The Schottky barrier blocks excessive leakage current into the device, and as result, behaves similar to the *pn* junction, where a region of depletion region forms, a region where no free charges exist [44, 45]. Common semiconductors used in these processes are Si, Ge, and GaAs, and the layers are generally applied to the semiconductor by electron-beam evaporation or sputtering. The geometry of these devices inherently limits the achievable neutron detection efficiency to approximately 4.5%. From Fig. 2.1 it is observed that only one reaction product can be absorbed in the semiconductor medium. Reaction products are released 180^{o} apart as a result of a neutron capture therefore, in the best case scenario; one reaction product deposits all of its energy into the semiconducting medium. Additionally, there is a limit to the thickness of neutron reactive material. It would be ideal to apply a very thick neutron reactive material to increase the neutron absorption efficiency of the device, however, the thicker the layer, the more distance reaction products must travel in order to enter the semiconducting medium. For example, a 2.05 MeV alpha particle will travel on average 6.0 μm through a ^{6}LiF film upon being completely absorbed. Therefore, as the layer of neutron reactive material thickness increases, the probably of a reaction product reaching the semiconductor decreases. There is an optimal film thickness for neutron absorption and reaction product absorption, resulting at approximately a 4.5% maximum thermal neutron detection efficiency [20, 46, 47].

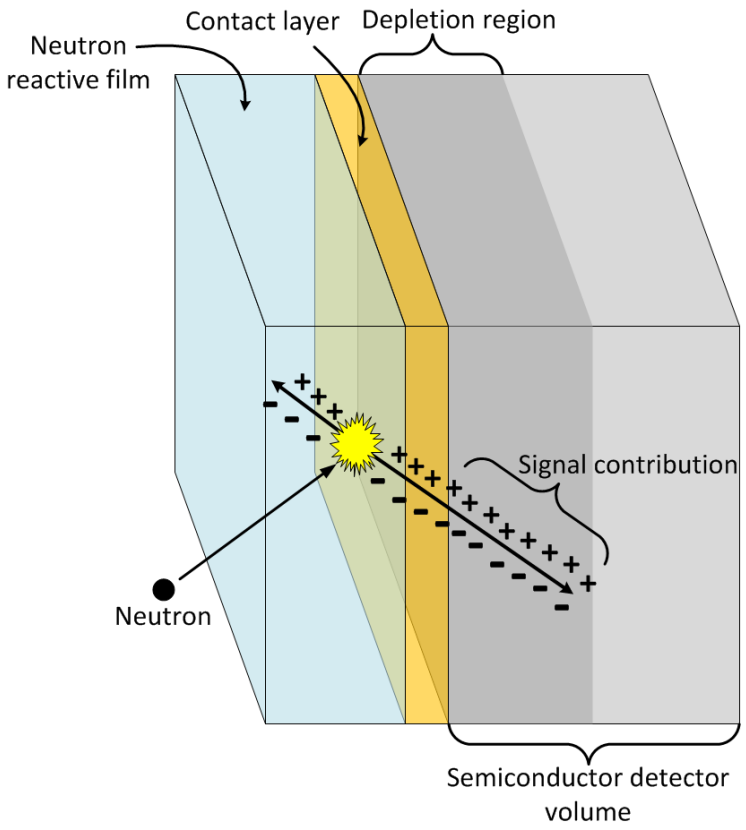

Fig. 2.2. An illustration of a traditional thin-film coated neutron detector.

2.2.2.2 The microstructured neutron detector (MSND)

The microstructured neutron detector (MSND) is a semiconductor diode detector design that reduces the drawbacks of the thin film style detector. Instead of the single thin film of neutron sensitive material, trenches are etched into the semiconductor and these trenches are backfilled with a neutron reactive material, as shown in Fig. 2.3. This design allows for measurement of both reaction products, which produces a large measureable signal, a signal easily distinguishable from background radiations and electronic noise. Neutron detection efficiency is increased drastically compared to thin-film devices due to more neutron material existent in the trenches, where reaction products can be absorbed in the fins, thus contributing to the signal. This technology takes advantage of relatively low-cost VLSI processing techniques for fabrication, and as a result are high-efficiency, compact, and requires a low power operation [48]. Devices have been reported to have a measured intrinsic thermal neutron detection

efficiency of over 42% with a recent stacked-style device [49] and over 35% for a recent single-sided devices [50].

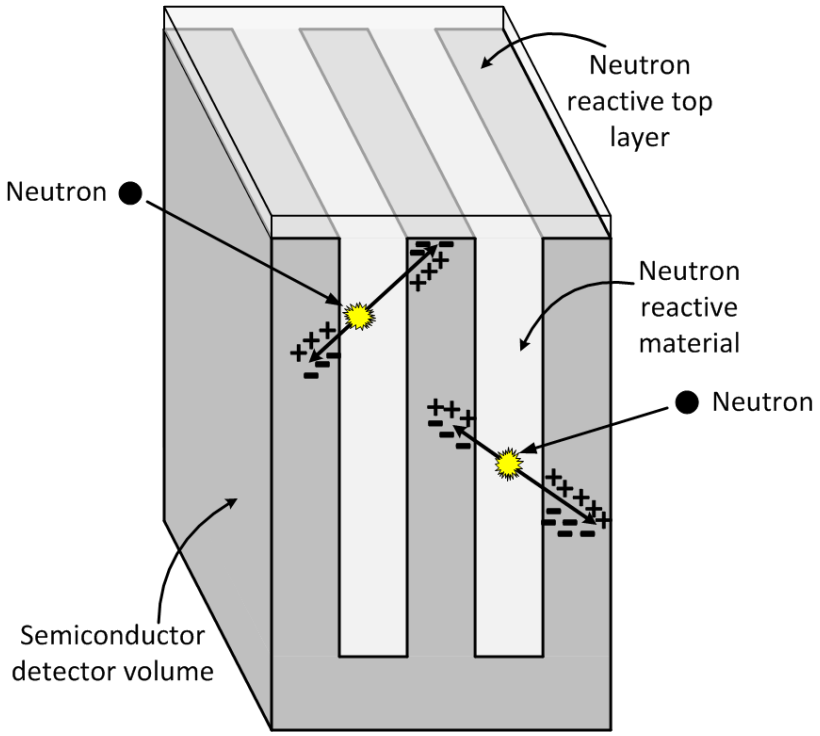

Fig. 2.3. An illustration of the microstructured semiconductor neutron detector (MSND).

2.2.2.3 The solid-state neutron detector

The solid-state neutron detector does not involve thin-film coatings, or any arrangement of conversion material coupled with a semiconductor. Instead, the neutron reactive material is incorporated into semiconductor medium, and is part of the semiconductor crystal lattice. The device consists of a bulk semiconductor (containing a neutron reactive material) with electrical contacts on opposing sides of the semiconductor as shown in Fig. 2.4. With this style of device, reaction products from a neutron capture are released in opposing directions and can be completely absorbed in the material. Electron-hole pairs are generated in the material as the reaction products travel through the material. With a positive bias applied at the anode, electrons drift toward the anode, and holes drift toward the cathode. The motion of electron-hole pairs

induces a charge, or current, that can be measured with a charge sensitive preamplifier and other accompanying signal processing components. Neutron captures extremely close to the surface of the material may result in only one reaction product, or a combination of one and a portion of the second reaction product being absorbed in the semiconductor[6]. However, for (n,α) reactions, most captures will result in both reaction products being completely absorbed in the semiconductor material due to the extremely short ranges of the reaction products. For example, from the $^{6}Li(n,t)^{4}He$ reaction in LiZnAs, the 2.05 MeV alpha particle will travel 12.6 µm upon being completely absorbed, and the 2.73 MeV triton will travel 64.6 µm upon being completely absorbed. As a result, the percent thermal neutron absorption will be approximately equal the percent thermal neutron detection efficiency because absorption of the resulting short-range reaction products is extremely high. In the following study, LiZnP and LiZnAs material was fabricated into devices using this detector design.

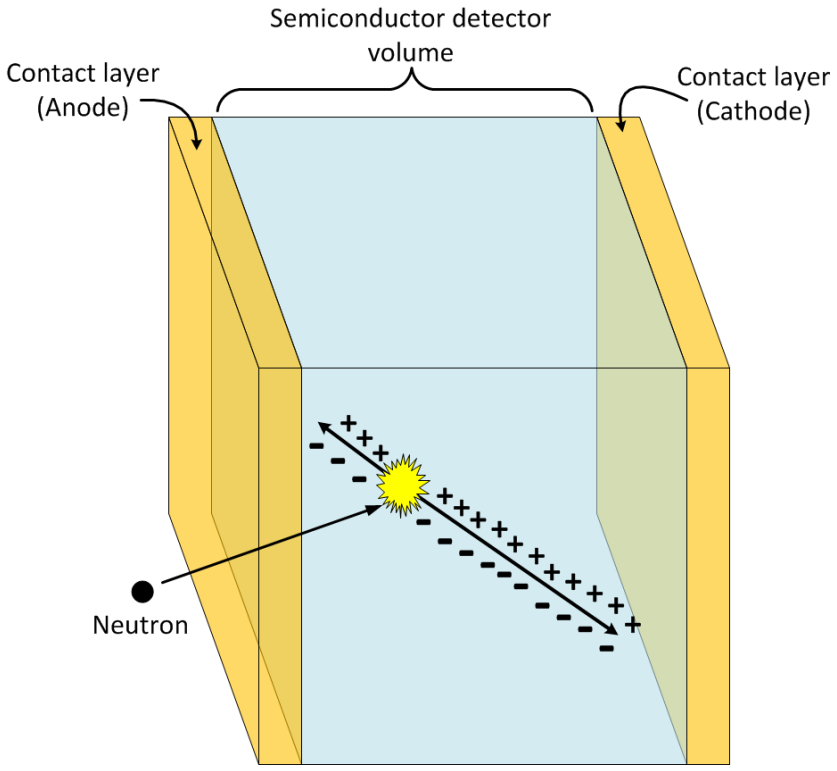

Fig. 2.4. An illustration of a bulk semiconductor device, known as a "solid-state detector".

[6] This phenomena is known as the wall effect, and can be reviewed in more detail elsewhere [31].

2.3 Nowotny-Juza compound prior art

Nowotny-Juza compounds were originally of interest for photonic devices, such as lasers and light emitting diodes, studied by Nowotny and Juza [51-53]. The work was driven to create direct-band gap materials for photonics applications. Light-emitting photonic applications generally require a direct band material due to a higher probability of photon emission than with an indirect band-gap material. In an indirect band-gap material an electron cannot excite from the valence band into the conduction band without a momentum change. Therefore, in the radiative recombination process, the process that photon emitting devices rely on is much slower, and less probable in an indirect band-gap material, hence the reason photonic devices are strictly considered with direct band-gap materials. In the following study however, LiZnP and LiZnAs are being considered as neutron detector devices, and band engineering is not as much of a concern. The following sections provide a brief history and analysis of LiZnP and LiZnAs from what was reported in the literature.

2.3.1 LiZnP and LiZnAs in review

The first reports of LiZnP and LiZnAs studies are from H. Nowotny and K. Bachmayer from 1949 and 1950 [51, 52]. The authors sealed elemental components Li, Zn and P, or As, in graphite lined ampoules, and reacted by direct fusion of the reactants in a furnace at 650 ^{o}C to form LiZnP, or 550 ^{o}C to form LiZnAs. They performed an x-ray diffraction study on the materials and were the first to present the material as a zinc-blende cubic lattice with a lattice constant of 5.76 Å for LiZnP, and 5.91 Å for LiZnAs. Nowotny and Bachmayer were also the first to provide the atom locations for the zinc-blende lattice, where it was suggested the group II atom is located at $(3/4, 3/4, 3/4)$, group V atom is located at (0 , 0, 0), and the lithium atom is located at $(1/4, 1/4, 1/4)$ [51]. Almost 20 years later R. Juza et. al. reports a lattice constant of 5.78 Å for LiZnP, and 5.92 Å for LiZnAs. LiZnP was synthesized by a process that began with the binary Li_3P. Zinc and excess P were added to the binary in an alumina crucible, and elevated to an unspecified temperature to produce the ternary product. LiZnAs was synthesized similarly beginning with Li_3As, and unspecified amounts of zinc and arsenic were added to the binary in

an alumina crucible, then elevated to an unspecified temperature to form LiZnAs. It is unclear whether a sealed crucible, glass containment, or an open crucible was used in the process. However, it was made clear that all processing was carried out under nitrogen or argon [53].

It was not until the mid-1980's and into the 1990's that LiZnP and LiZnAs were reported again. K. Kuriyama, R. Bacewicz and T.F. Ciszek were perhaps most active with LiZnP and LiZnAs research during this time. K. Kuriyama synthesized LiZnAs and LiZnP by direct reaction of equimolar portions of Li, Zn, and As, or P in a tantalum crucible sealed in a pyrex ampoule [54-56], or a graphite lined quartz ampoule [57, 58]. For LiZnAs reactions, the graphite, or tantalum, crucible was loaded with equimolar portions of Li, Zn and As with a 5 at. % excess Li and 3 at. % excess As to compensate for evaporative losses, then sealed in a pyrex or quartz ampoule at 10^{-4} torr. The ampoule was placed into a vertical resistance furnace and heated at a rate of 100 ^{o}C/hr, from 200 ^{o}C to 850 ^{o}C to promote crystallization. The temperature was maintained for about 70 hours, then cooled at a rate of 100 ^{o}C / hr [54]. Synthesis parameters vary depending on the report [57, 58]. Grown LiZnAs crystals were metallic gray and showed rapid oxidation and hygroscopy in air. Samples were examined for crystalline ordering with powder x-ray diffraction, and a cubic lattice constant of 5.940 ± 0.001 Å was reported. Atom locations in the lattice were also reported where group II atom is located at $\tau_1 = (0, 0, 0)a$ where a is the lattice constant, group V atom is located at $\tau_2 = (1/4\ ,1/4,\ 1/4)a$, and lithium atoms to fills the interstitial site at $\tau_3 = (1/2,\ 1/2,\ 1/2)a$, with a space group of F-43m. Thermal analysis of LiZnAs showed a broad endothermic peak at approximately 850 ^{o}C which was reported to indicate a melting point or decomposition of LiZnAs. No further explanation of material condition after the process was reported to further verify the 850 ^{o}C feature. LiZnAs samples were examined through electrical and optical measurements. The Van der Pauw technique was applied to LiZnAs where tungsten probes were used as ohmic electrodes. Resistivities of 10^{-1} – 10 Ω cm at room temperature were reported. Crystals exhibited a *p*-type conductivity, and a Hall mobility of ≤ 30 cm^2 V^{-1} was reported [54]. LiZnAs was also examined for bandgap properties using a scanning spectrophotometer. A direct bandgap of 1.51 eV at room temperature was reported [58].

For LiZnP reactions reported by K. Kuriyama, a tantalum crucible was loaded with equimolar portions of Li, Zn and As with a 4 at. % excess Li and 6 at. % excess As to compensate for evaporative losses, then sealed in a quartz ampoule at 10^{-4} torr. The ampoule was

placed into a vertical resistance furnace and heated at a rate of 100 ^{o}C/hr, from 200 ^{o}C to 680 ^{o}C to promote crystallization. The temperature was maintained for about 120 hours, then cooled at a rate of 100 ^{o}C / hr. Grown crystals were transparent red, and showed rapid oxidation and hygroscopy in air. Samples were examined for crystalline ordering with powder x-ray diffraction, and a cubic lattice constant of 5.765 ± 0.005 Å was reported, and atom locations in the lattice were reported the same as reported for LiZnAs [56]. Thermal analysis of LiZnP showed a broad endothermic peak at approximately 950 ^{o}C which was reported to indicate a melting point or decomposition of LiZnP. No further explanation of material condition after the process was reported to further verify the 950 ^{o}C feature. LiZnP samples were examined through electrical and optical measurements. Optical transmission spectra of LiZnP indicated a band-gap energy of 2.04 ± 0.01 eV [55]. The Van der Pauw technique was applied to a LiZnP sample where small indium contacts were applied to the sample, and coupled to the instrument with tungsten probes. A resistivity of 15 Ω cm at room temperature was reported. Crystals exhibited a *p*-type conductivity, and a Hall mobility of 25 cm^2 V^{-1} sec^{-1} was reported [56]. Thin films of LiZnP were prepared on quartz, and resistivity was measured of the LiZnP film at 10^2 Ω cm using the same Van Der Pauw technique. This higher resistivity was considered to be caused by the carrier scattering due to grain boundaries and defects in the LiZnP film [59].

R. Bacewicz and T.F. Ciszek published work on LiZnP and LiZnAs in the late 1980's [60, 61]. Two methods for synthesizing LiZnP and LiZnAs were reported. One method was similar to what was reported by K. Kuriyama, where the equimolar portions of the constituent elements were added to a graphite crucible with an excess of 2 - 4 at. % lithium and P or As to account for evaporative losses, then loaded into a carbon coated quartz ampoule. The vacuum pressure at which the ampoule was sealed was not reported. A two-step process was applied to the synthesis procedure. First, the reactants were raised in temperature to 430 – 550 ^{o}C. No specification was reported as the experimental temperature corresponding to a specific material. Also, no maintained temperature duration was reported. This particular report covered synthesis for LiZnP, LiZnAs, LiCdP, LiCdAs and LiZnSb. In step two, the reaction was followed by a long annealing stage, where the temperature was raised to 650 – 800 ^{o}C. Again, no specification of temperature to material syntheses, or time maintained at temperature was reported [61]. The resulting synthesized materials were evaluated for lattice constant, resistivity and band-gap energy. Lattice constants were reported at 5.755 Å and 5.939 Å for LiZnP and LiZnAs

respectively; however, no phase identification scans were reported. Band-gaps were estimated from the position of the absorption edge, where an energy gap of 2.1 eV and 1.35 eV were reported for LiZnP and LiZnAs respectively. Resistivity for LiZnP and LiZnAs was reported at $10^5 - 10^6$ Ω cm and 0.1 – 1 Ω cm respectively, however no procedure, or experimental process, was reported to arrive at these values. It was also reported that LiZnAs was found to melt congruently at about 1050 ^oC, with no description of the resulting crystals [61].

The second method for synthesizing $A^IB^{II}C^V$ materials reported by R. Bacewicz and T.F. Ciszek consisted of a horizontal technique to synthesize LiZnP [60], and a similar vertical technique for LiZnAs as reported previously [61]. LiZnAs was synthesized in a graphite crucible where an unreported arrangement of materials were raised in temperature to 550 ^oC and maintained at temperature for 48 hours. The graphite crucible was further raised in temperature to 650 ^oC and held for 140 hours. A black-grey solid of 1 – 2 mm crystals was harvested. The growth of bulk single crystals of LiZnAs was attempted, and it was reported that at least a temperature of 1050 ^oC was required to melt LiZnAs. X-ray and compositional analysis showed the presence of $ZnAs_2$ grains in the LiZnAs ingot, indicating incongruent melting of LiZnAs [60]. LiZnP however, was synthesized in a 45 cm long quartz tube in a two-zone furnace. A graphite crucible was loaded with the metals at one end of the ampoule, and red phosphorus was placed at the other end of the ampoule. The ampoule was evacuated and sealed at 10^{-6} torr. The phosphorus end of the ampoule was heated at 10 ^oC/hr to 420 ^oC and the metals were kept at 530 ^oC to allow reaction to commence for 48 hours. The metals end of the ampoule was then raised in temperature to 800 ^oC and maintained in temperature for 30-50 hours. Small dark red LiZnP crystals, about 1 – 3 mm^3 were harvested, that "hydrolyze" in air. The electrical resistance was determined using a four point probe method, where LiZnAs was determined to have a resistivity of approximately 10^{-1} Ω cm, and LiZnP was determined to have a resistivity between $10^5 - 10^6$ Ω cm. Optical transmission was performed on samples of 100 – 500 μm thickness, and photoconductivity was measured where band-gap energies were reported for LiZnP and LiZnAs at 2.1 eV and 1.25 eV respectively. X-ray diffraction phase identification scans were reported for LiZnP and LiZnAs with a determined lattice constant of 5.755 Å and 5.939 Å, respectively [60]. A. J. Nelson reported an evaluation of the electronic structure of LiZnP and LiZnAs with samples provided by Bacewicz and Ciszek using Ultraviolet Photoemission Spectroscopy (UPS).

Nelson reported valence band spectra for LiZnP and LiZnAs, and corresponding Zn 3d binding energies at 9.00 eV and 8.60 eV respectively [62].

Others reported computational studies of LiZnP and LiZnAs [63-66]. Su-Wei studied electronic structure and phase stability of LiZnAs. Wei determined the band diagrams for various phases of LiZnAs [66]. F. Kalarasse reported computational linear optical properties of LiZnAs and LiZnP. D. M. Wood reported band diagrams for LiZnP and LiZnAs, and reported band-gap energies of 1.72 eV and 0.74 eV[7] respectively, where primary goal was to prove that $A^{I}B^{II}C^{V}$ semiconductors were direct bandgap semiconductors. From his computations, Wood determined that Nowotny-Juza compounds of the LiZnP type are direct bandgap semiconductors. Wood concluded that the "directness of the bandgap can be enhanced by placing electron-repelling objects in the tetrahedral interstitial sites where the lowest conduction band has a higher electron density than other bands and hence is selectively shifted upwards". This rule therefore applies to LiZnAs and LiZnP where Li^{+} cations (atoms) fill the tetrahedral site at $(1/2, 1/2, 1/2)$ [63].

Recently, LiZnP and LiZnAs continue to be studied in solar cell applications and Li ion battery applications [67-69]. LiZnP was synthesized by a ball milling technique as reported by M.P. Bichat. Elemental components were placed in a stainless steel container with stainless steel balls. A Spex 8000 mixing mill was used to mix / grind the components. Reaction was complete after 8 – 12 hours of grinding to form LiZnP. X-ray diffraction was performed with the synthesized material, however no peak matching was performed, or comparison to previous literature. An experimental lattice constant was also not reported [68]. D. Kieven prepared a LiZnP target for sputtering purposes by loading a tantalum tube with equimolar portions of Li, Zn and P, then sealed the tantalum in a quartz containment. The reactants were "annealed" for 96 hours at 900 ^{o}C. The reaction product was then hot sintered into a "target" that was a dark reddish color. Optical analysis of the thin films of LiZnP resulted in a bandgap energy of 2.0 ± 0.1 eV.

Clearly the literature is limited for information regarding LiZnP and LiZnAs materials. Lots of synthesis parameters were left unclear in the literature, and no detailed information was available regarding bulk crystal growth of LiZnAs or LiZnP. The following study was directed primarily to study the material as possible neutron detection devices. However, there was also a

[7] These values are very different from prior experimental results reported by Kuriyama, and Bacewicz as discussed previously.

need to further develop the synthesis process, and develop and study bulk crystal growth processes for LiZnP and LiZnAs materials. The only other group to study $A^{I}B^{II}C^{V}$ materials as possible candidates for neutron detectors was K. Shah at Radiation Monitoring Devices, Inc. where a phase I Small Business Innovation Research (SBIR) was awarded [70]. Phase II was not funded and no findings from Phase I were reported in the literature.

Chapter 3 : THEORY

"We don't regard any scientific theory as the absolute truth."

- ***Kenneth R. Miller***

The following chapter entails the theoretical considerations for the described work. A foundation of crystal systems is discussed, and the language for crystal characterization is presented, known as Miller indices. A brief introduction to types of x-ray diffraction (XRD) measurements and the measurement importance is also presented. Models and simulations regarding XRD phase identifications, charge collection efficiency, and thermal neutron response pulse height spectra are presented here. Models and simulations were performed with programs such as PowderCell 2.4 [71] and MCNP6 [72] based on data presented in the literature, and from experimental data collected in the following study.

3.1 Brief crystal systems description

Crystallography is a large portion of the following work; therefore, it is necessary to understand what a crystal is, the various three-dimensional lattice arrangements, and the language of crystallography. A crystal is defined as a material composed of atomic or molecular structures with a specific arrangement, and then repeated in a specific order to make a lattice system. Shown in Fig. 3.1 is an ordered lattice and a basis, which consists of atoms, and when combined forms the crystal structure. For simplicity sake, the two dimensional depiction shows how the crystal is formed, though additionally, the three-dimensional model is shown in Fig. 3.2 [30, 73]

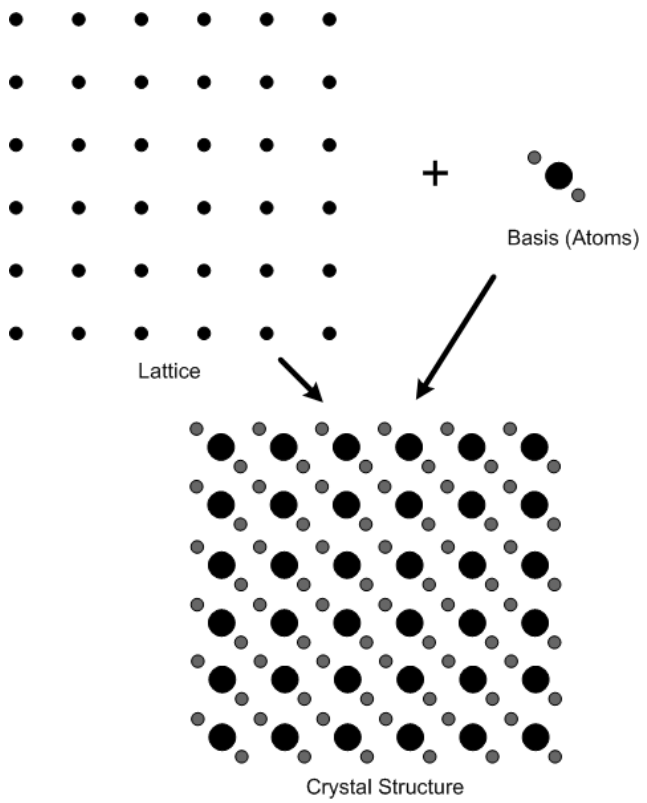

Fig. 3.1. The two-dimensional model of the crystal structure formation

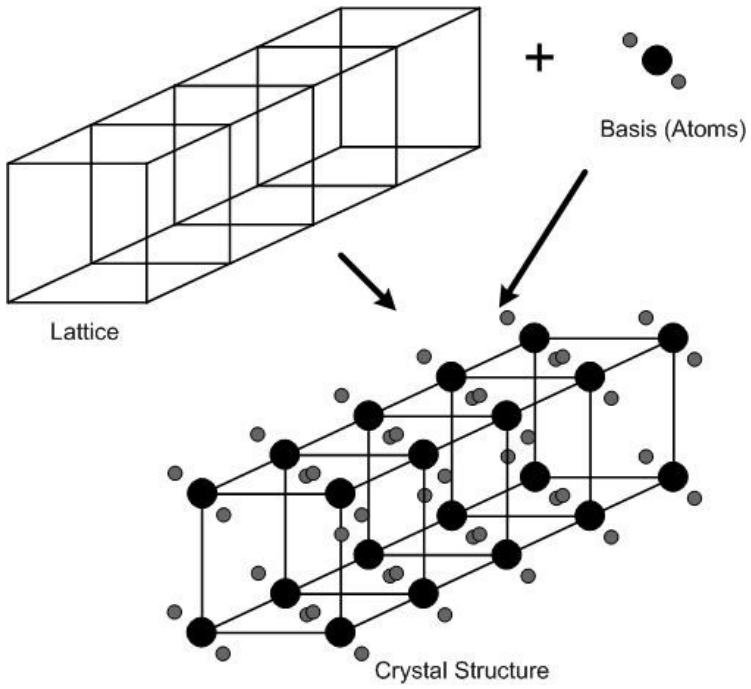

Fig. 3.2. The three-dimensional model of the crystal structure formation.

For the two dimensional case, there are only five possible lattice arrangements, and are referred to as the two dimensional Bravais lattices, named after French scientist, Auguste Bravais. However, for the three-dimensional case, Bravais proved in the 1840's that there are 14 ways of arranging the points in repetitive lattices. The 14 Bravais lattices are shown in Fig. 3.3.

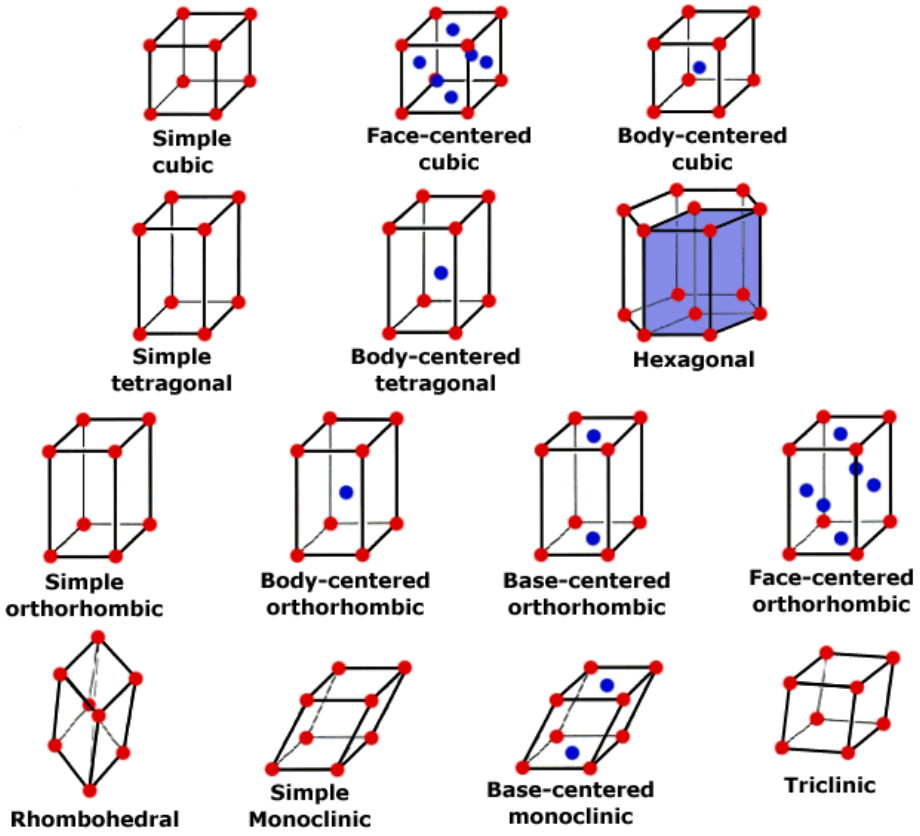

Fig. 3.3. The 14 Bravais lattices [74].

3.1.1 Miller Indices

Miller indices were introduced in 1839 by William Hallowes Miller, a mineralogist, who presented the method in his *Treatise on Crystallography* [75]. The method provides a common language, or a standard, for describing and identifying planes, directions, sets of directions, and sets of planes within a crystal lattice, in a simplistic way that is easily comprehensible. The method for identification for a single plane includes the steps,

1) Set up a coordinate system along the edges of the cell.
2) Find where the plane of interest intercepts the axes and record the integer values.
3) Take the reciprocal of the intercept values and reduce to the smallest set of whole numbers.
4) Enclose the number in brackets (*hkl*).

Identification of crystal directions can be found in the following steps,

1) Assign a vector in the desired direction
2) Compose a basis vector, r, by noting the projections along the coordinate axis
3) Reduce to the smallest set of whole numbers
4) Enclose in square brackets [*hkl*]

A set of equivalent planes and set of equivalent directions can be identified in curly brackets, {*hkl*}, and pointed brackets, <*hkl*>, respectively. An example of the (100) plane and [100] direction in a cubic lattice is shown in Fig. 3.4.a along with the (110) plane and (111) plane in b. and c., respectively [30, 45, 73].

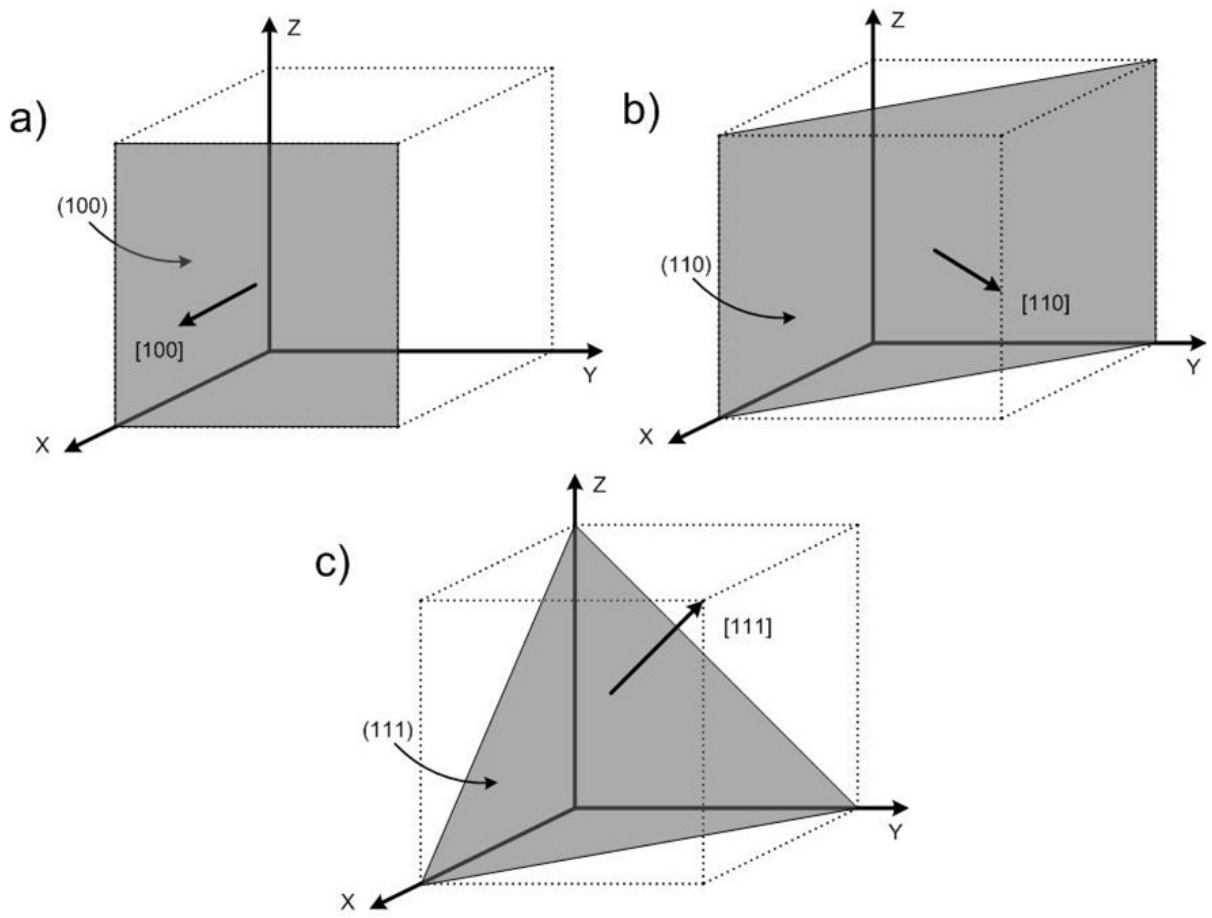

Fig. 3.4. Miller indices of basic planes and directions in a cubic unit cell.

3.1.2 X-ray measurements

X-ray diffraction measurements are useful for crystallinity characterization and material identification. In the following study, numerous x-ray diffraction (XRD) measurements were performed for material characterization, and crystallinity studies. X-ray diffraction measurements are based in Bragg's law,

$$2d\sin(\theta) = n\lambda\,, \tag{3.1}$$

where d is the d-spacing (distance between crystal planes), n is an integer, and λ is the wavelength of the incident x-rays. Every crystalline material has a unique diffraction pattern that

provides information regarding crystal structure, unit cell dimensions, and space group. The structure produces a condition where electromagnetic waves, such as x-rays, are diffracted from the crystal planes, as shown in Fig. 3.5. The common XRD cradle includes a number of axes that can be rotated at fine increments for desired measurements, as shown in Fig. 3.6.

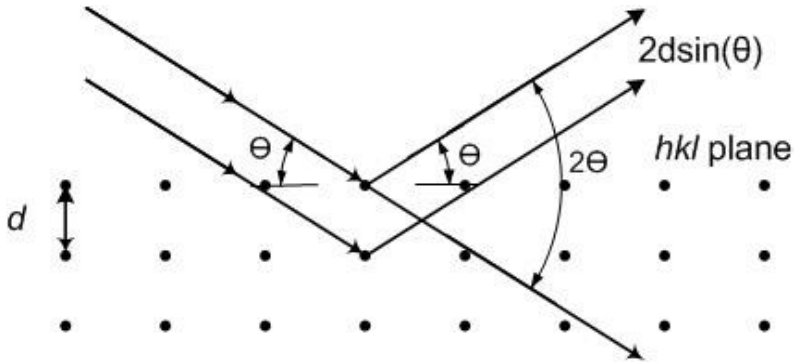

Fig. 3.5. The two-dimensional depiction of Bragg diffraction

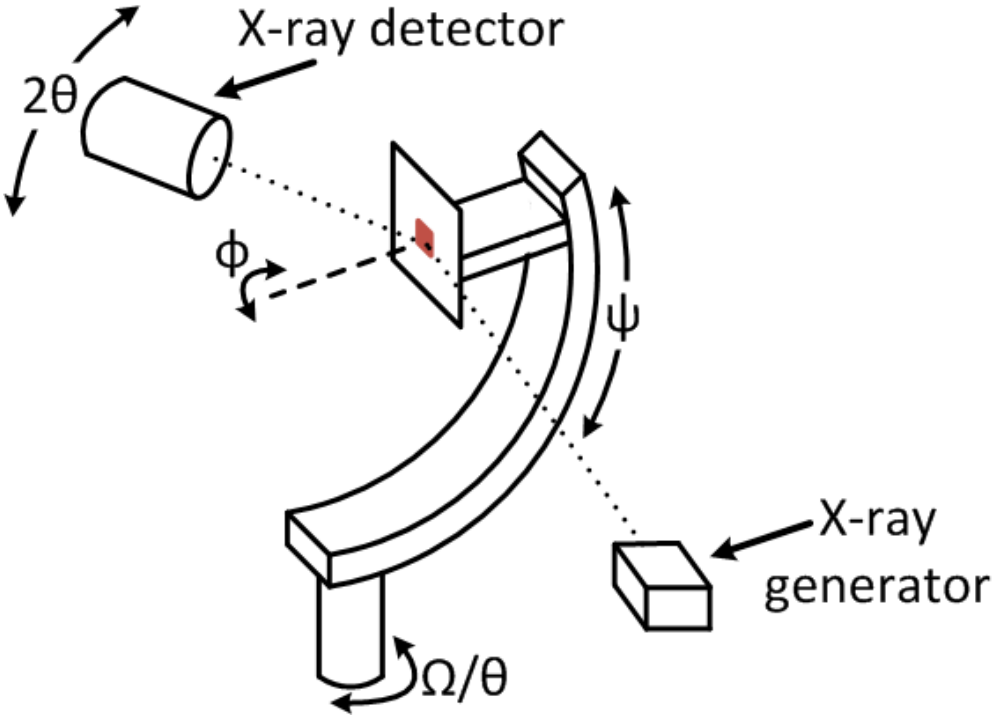

Fig. 3.6. The typical horizontal x-ray diffraction cradle. The sample is labeled in red and is shown mounted to the sample stage.

Phase identification is a common powder x-ray diffraction scan for material identification. Here, the sample is crushed into a fine powder so all crystalline orientations are present during the scan. The 2θ axis is set to scan the sample as the θ, or Ω, axis is rotated at half the rate of the 2θ axis, given the name: 2θ – Ω scan. The resulting pattern is in terms of intensity (counts or counts / sec) vs. 2θ angles, coupled 2θ – Ω. An example of a simulated pattern is shown in Fig. 3.8 for LiZnAs and LiZnP powder. These patterns can be matched to existing data in the International Centre for Diffraction Database (ICDD), and simulated with software such as PowderCell 2.4 [71].

A phi (ϕ) scan is typically a high-resolution XRD technique for bulk crystalline samples that explores the sample for single crystallinity, multiple domains, or twinning. The process involves the sample being rotated about the surface normal to examine all reflections about 360^{o}. A ϕ scan is a common measurement to examine in-plane ordering. Known as an off-axis measurement, psi (ψ) is angled at a position to explore an in-plane orientation. For example, if the material has a main plane orientation of (110) – the surface normal, an in-plane orientation of interest may be the (211) plane at 30^{o} ψ from the (110) plane. Reflections observed in the phi scan about the (211) are proof of in-plane ordering, and can be manipulated to find the projection direction of the (211) on the (110) using vector math as detailed in Appendix A.2. Once the projection direction is determined, the directions can be mapped on the sample, allowing for complete characterization of the crystalline directions in the sample.

The rocking curve, an Ω scan, is a measure of the crystalline quality of an orientation. The main orientation (surface normal) is measured, where the axes are positioned for the main orientation reflection, and the sample is "rocked", or rotated across Ω, providing a plot of intensity vs. Ω degrees. This plot consists generally of a single peak, and the full width at half maximum (FWHM) is the measure, or figure of merit, of crystalline quality. XRD instruments must be capable of a high-resolution for these measurements, generally less than the mosaic broadening measured in the sample. For example, electronic grade silicon is a very high-quality crystal and typically has a FWHM of 0.004^{o} to 0.007^{o}, meaning that incident beam divergence must be less than the measure of the FWHM. Typically in high-resolution systems, x-ray sources are cleaned of divergent x-ray energies by diffraction gratings that make the incident beam monoenergetic. For in-development materials such as mercuric iodide, cadmium zinc telluride,

or Nowotny-Juza compounds, the measured FHWM is typically between 0.01° to 0.9° as these materials are still being studied to improve crystallinity.

3.2 LiZnP and LiZnAs Crystal Structure

The filled tetrahedral compound class $A^{I}B^{II}C^{V}$ materials consist of the III-V-like compounds with Li interstitials, also referred to as Nowotny-Juza compounds. The primary allotrope of these materials is zincblende crystal structure of space group F-43m, that is arranged where the group II atom is located at $\tau_1 = (0, 0, 0)a$ where a is the lattice constant, and the group V atom is located at $\tau_2 = (1/4, 1/4, 1/4)a$. The spacious cubic structure allows for lithium atoms to fill its interstitial site at $\tau_3 = (1/2, 1/2, 1/2)a$, as shown in Fig. 3.7. The filling of these interstitial sites allows for a Li-loaded semiconducting material.

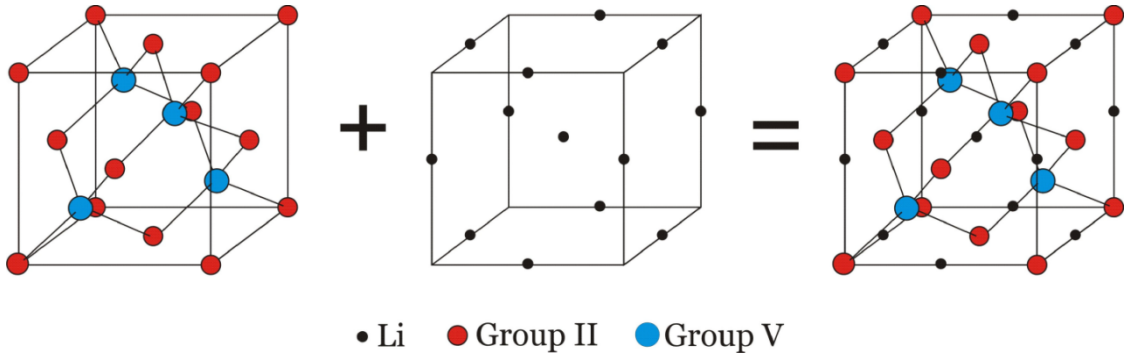

Fig. 3.7. Nowotny-Juza compound zincblende cubic crystal structure.

The theoretical phase identification comparison of LiZnP and LiZnAs was determined using a program for representation and manipulation of crystal structures, known as PowderCell 2.4 [71]. The lattice constant used in the calculation was used as determined by Bacewicz et.al [60]; LiZnAs: (F-43m) a = 5.939 Å, and for LiZnP (F-43m) a = 5.755 Å as shown in Fig. 3.8.

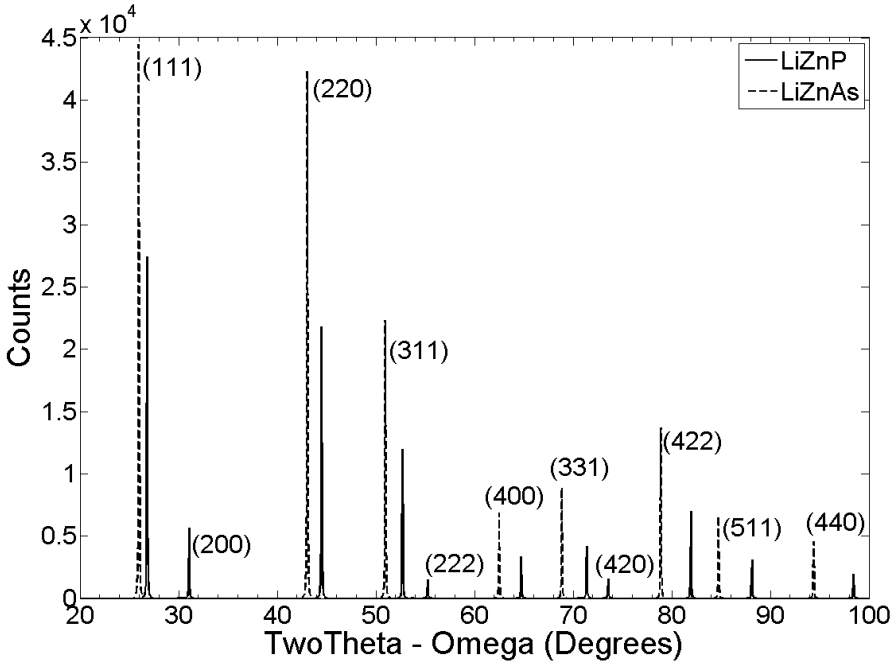

Fig. 3.8. The theoretical Cu x-ray phase identification of LiZnP (solid) and LiZnAs (dashed) powders calculated with PowderCell 2.4 [71]. Lattice constants and space groups were used in the calculation as presented by Bacewicz for LiZnAs: (F-43m) a = 5.939 Å, and for LiZnP (F-43m) a = 5.755 Å [60].

3.3 Conductivity in a Cubic semiconductor

Nowotny-Juza compounds are desirable for application as neutron detectors due to their cubic crystal structure. The cubic crystal structure has unique electrical properties, compared to other orientations inherit to materials examined as neutron detection materials, some of which are hexagonal, trigonal, etc. In a cubic system, since angles are isometric, the conductivity tensor, $\underline{\sigma}$, for a force applied (applied bias) in any direction are equal. For the case of silicon, with a force applied in the [100] direction results in total conductivity effective mass tensor (sum of [100], $[\bar{1}00]$, [010], $[0\bar{1}0]$, [001] and $[00\bar{1}]$),

$$\underline{\sigma} = (n_0 q^2 \tau^*) \begin{pmatrix} \frac{1}{3}\left(\frac{2}{m_t^*} + \frac{1}{m_l^*}\right) & 0 & 0 \\ 0 & \frac{1}{3}\left(\frac{2}{m_t^*} + \frac{1}{m_l^*}\right) & 0 \\ 0 & 0 & \frac{1}{3}\left(\frac{2}{m_t^*} + \frac{1}{m_l^*}\right) \end{pmatrix}, \tag{3.2}$$

where the conductivity effective mass tensor, for example, in the [100] direction is

$$\underline{\sigma}_{[100]} = (n^{[100]} q^2 \tau^*) \begin{pmatrix} \frac{1}{m_l^*} & 0 & 0 \\ 0 & \frac{1}{m_t^*} & 0 \\ 0 & 0 & \frac{1}{m_t^*} \end{pmatrix}, \tag{3.3}$$

where m_l^* is the longitudinal effective mass, m_t^* is the transverse effective mass, q is the elementary charge, n_0 is total number of available conduction electrons, $n^{[100]}$ is the number of conduction electrons available in the [100] direction, and τ^* is the free carrier mean drift time, or lifetime. The concept of effective mass implies that the motion of elections in a crystal can be described in a quasi-classical manner, where the periodic potential has changed the influence of an external force on an electron from what is expected [73]. The expression, Eq. (3.2), can be reduced to a simple expression for the conductivity effective mass, m_C^*,

$$\frac{1}{m_C^*} = \frac{1}{3}\left(\frac{2}{m_t^*} + \frac{1}{m_l^*}\right). \tag{3.4}$$

Suppose a force is applied in the [110] direction. The conductivity effective mass tensor in the [110] is,

$$\underline{\sigma}_{[110]} = (n^{[110]} q^2 \tau^*) \begin{pmatrix} \frac{1}{2}\left(\frac{1}{m_t^*} + \frac{1}{m_l^*}\right) & \frac{-1}{2}\left(\frac{1}{m_t^*} - \frac{1}{m_l^*}\right) & 0 \\ \frac{-1}{2}\left(\frac{1}{m_t^*} - \frac{1}{m_l^*}\right) & \frac{1}{2}\left(\frac{1}{m_t^*} + \frac{1}{m_l^*}\right) & 0 \\ 0 & 0 & \frac{1}{m_t^*} \end{pmatrix}. \tag{3.5}$$

The conductivity effective mass tensor in the [110] direction can be added to the conductivity effective mass tensors in the [011], [101], [$\bar{1}$10], [$\bar{1}$01], and [0$\bar{1}$1] directions to find the total conductivity tensor,

$$\underline{\sigma} = (n_0 q^2 \tau^*) \begin{pmatrix} \frac{1}{3}\left(\frac{2}{m_t^*} + \frac{1}{m_l^*}\right) & 0 & 0 \\ 0 & \frac{1}{3}\left(\frac{2}{m_t^*} + \frac{1}{m_l^*}\right) & 0 \\ 0 & 0 & \frac{1}{3}\left(\frac{2}{m_t^*} + \frac{1}{m_l^*}\right) \end{pmatrix}, \tag{3.6}$$

which can be reduced to a scalar in terms of the conductivity effective mass, m_C^*,

$$\frac{1}{m_C^*} = \frac{1}{3}\left(\frac{2}{m_t^*} + \frac{1}{m_l^*}\right). \tag{3.7}$$

Therefore, is observed the conductivity effective mass, m_C^*, is unchanged with a force in either the [100] or [110] of a cubic semiconductor. The importance of this result is that for a cubic semiconductor, the electrical properties are the same in every direction. It does not matter what orientation electrical contacts are applied on the material; the electrical properties will be the same. This is a direct result of the symmetry seen in a cubic lattice, and therefore is generally not applicable to non-cubic Bravais lattices. Other crystal structures are not geometrically equal in

all directions as they with the cubic lattice, and therefore electrical properties are not uniformly be the same.

3.4 Charge Collection Efficiency

Charge collection efficiency (CCE) is an important property of solid-state semiconductor radiation detectors as it defines the amount of charge induced on the readout electronics relative to the initial amount of charge generated at the site of radiation interaction. For high-resolution gamma-ray spectrometers, such as cadmium zinc telluride (CZT), it is necessary to explore the charge collection efficiency to help define the device performance of different device configurations, such as planar and Frisch-Collared device configurations. Frisch-collared devices alter the electric field, due to weighting potential distribution of the device that arises from a combination of the geometric weighting and electrode screening of the Frisch-collered device, thus enhancing the spectral resolution. Determination of the charge collection efficiency is, in part, based on the product of the charge carrier mobility, and the charge carrier mean free drift time denoted as the $\mu\tau$ product. The $\mu\tau$ product is regarded as a figure of merit for device performance, greater the $\mu\tau$ product quantity, the *better* the device performance. CZT has been characterized to have electron and hole mobility-lifetime products, $\mu_e\tau_e$ and $\mu_h\tau_{h,}$ of 4.5 x 10^{-2} cm^2 V^{-1} and 1.0 x 10^{-4} cm^2 V^{-1}, respectively. Frisch collar CZT devices have been reported with a sub-1% energy resolution for a 662 keV incident gamma ray, due to the high $\mu_e\tau_e$ product for electrons [76]. A decrease in the $\mu_e\tau_e$ product hinders the charge collection efficiency, and therefore degrades the energy resolution.

For neutron detection devices, high resolution of the spectral features is not as critical as in gamma-ray spectroscopy devices. Counts above a background noise level, or background radiations are desirable, and can be accomplished with a *lower* $\mu\tau$ product compared to energy spectroscopy devices. LiZnP and LiZnAs samples were characterized by the transient charge technique for charge carrier mobilities and mean free drift times as explained in detail in sections 6.4.2 and 6.4.3. Shown in Table 3.1 are the testing parameters and resulting μ and τ quantities.

Table 3.1. The device parameters and $\mu_e\tau_e$ results from the transient charge technique.

	Device length (cm)	Bias applied (V)	Mobility, μ_e, ($cm^2\ V^{-1}\ sec^{-1}$)	Mean free drift time, τ_e, (μs)
LiZnP	0.202	51	5.7	139
LiZnAs	0.210	48	4.8	190

Charge collection efficiency profiles were determined for LiZnP and LiZnAs devices using the $\mu_e\tau_e$ characterized. The charge collection efficiency at a given point within a radiation detection device can be defined as the normalized change in induced charge due to a radiation interaction event in the device at a certain point, x, written as,

$$CCE(x) = \frac{Q_{TOT}}{Q_0}, \tag{3.8}$$

the ratio between the total charge induced on the collecting electrode of the device, Q_{TOT}, and the initial charge generated from a radiation event in the device, Q_0. For a planar device, the Hecht equation can be used to describe the positionally-dependent *CCE* with the expression [44, 76],

$$CCE(x) = \frac{E(x)}{L}\left[\mu_e\tau_e\left(1-\exp\left[\frac{x-L}{E(x)\mu_e\tau_e}\right]\right)+\mu_h\tau_h\left(1-\exp\left[\frac{-x}{E(x)\mu_h\tau_h}\right]\right)\right], \tag{3.9}$$

where x is the interaction location in the detector measured from the cathode, L is the distance between the electrodes (device length), $E(x)$ is the magnitude of the electric field at position x, and $\mu_e\tau_e$, $\mu_h\tau_h$ are the mobility-lifetime product for electrons and holes, respectively. As introduced elsewhere [44] , Eq. (3.9) can be rewritten in terms of the charge extraction factor ρ,

$$\rho_{e,h} = \frac{v_{e,h}\tau_{e,h}}{L} = \frac{E\mu_{e,h}\tau_{e,h}}{L}, \tag{3.10}$$

where $v_{e,h}$ is the velocity of the electrons and holes, respectively, and E is the electric field through the device. Therefore, by substituting the charge extraction factor into Eq. (3.9), the *CCE(x)* reduces to,

$$CCE(x) = \rho_e \left(1 - \exp\left[\frac{x - L}{L\rho_e} \right] \right) + \rho_h \left(1 - \exp\left[\frac{-x}{L\rho_h} \right] \right) . \tag{3.11}$$

Eq. (3.11) was used to describe the *CCE(x)* profiles for LiZnP, LiZnAs and CZT devices. For comparison purposes, a planar CZT device *CCE(x)* profile was determined for a 10 mm device length, similar to the CZT device used for the test device for benchmarking the transient charge technique (Section 6.4) where the results compare to those stated in literature. The $\mu_e\tau_e$ and $\mu_h\tau_h$ values used were as reported elsewhere ($\mu_e\tau_e = 4.5 \times 10^{-2}\ cm^2\ V^{-1}$ and $\mu_h\tau_h = 1.0 \times 10^{-4}\ cm^2\ V^{-1}$) [76], and 400 volts was applied to the device. The length of the device was normalized from 0 (cathode location) to 1 (anode location), where the *CCE* was determined for position *x* as shown in Fig. 3.9. The charge collection efficiency profile for a CZT device at the aforementioned parameters is shown in Fig. 3.10. The slope of the CCE profile distribution near that cathode is approximately zero due to charge induction occurring from both electrons and holes. However, beyond approximately the first 5% of the device length from the cathode, hole trapping and recombination severely affect the outcome. Furthermore, the negative charge collection efficiency slope across the normalized device length shows that electrons contribute to most of the charge induced, while holes contribute only a small amount. As a result of the detrimental effects of hole trapping and recombination, the collected signal is *primarily* composed of electron induction. This can also be seen from the $\mu\tau$ product values, where the $\mu_e\tau_e$ is two orders of magnitude greater than $\mu_h\tau_h$.

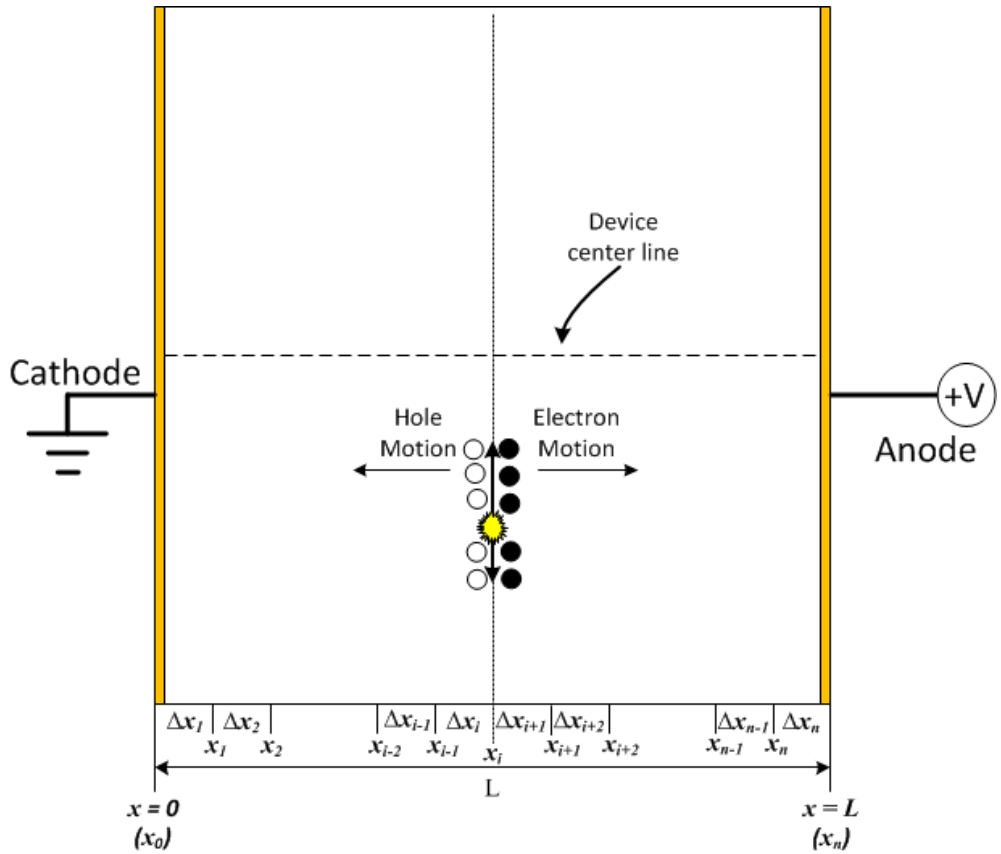

Fig. 3.9. A cross-section view of a LiZnP or LiZnAs device where a thermal neutron interacts (yellow dot) with ^{6}Li in the bulk of the material, thereby, creating a triton (2.73MeV) and an alpha particle (2.05MeV) released in opposite directions, the charged particle reaction product excites electron – hole pairs at position x_i.

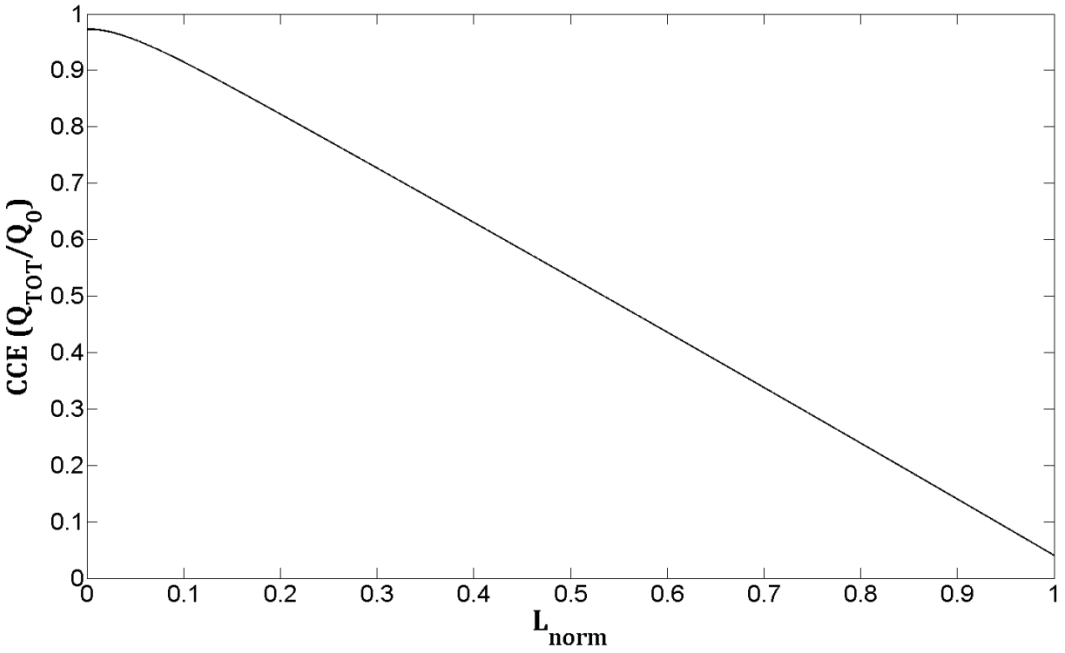

Fig. 3.10. The charge collection efficiency profile for a planar CZT device 1.0cm in length, 400 volts applied to the device, with a $\mu_e\tau_e$ *= 4.5 x* 10^{-2} cm^2 V^{-1} *and a* $\mu_h\tau_h$ *= 1.0 x* 10^{-4} cm^2 V^{-1}*. Position 0 represents the cathode end of the device and 1 represents the collecting electrode, the anode.*

Charge collection efficiency profiles were determined for LiZnP and LiZnAs as defined by Eq (3.11). Each charge collection profile was determined based on the parameters from the transient charge technique studies (Section 6.4). The *CCE(x)* profile for LiZnP was determined based on a device length of 0.202 cm, with 51 volts applied to the detector. The μ_e and τ_e values were used as determined by the Transient Charge Technique (μ_e *= 5.7* cm^2 V^{-1} s^{-1} *and* τ_e *= 139* μs). The $\mu_h\tau_h$ product was assumed to be 1.0 x 10^{-6} cm^2 V^{-1}, two orders of magnitude less than the $\mu_e\tau_e$ product (similar to the ratio of $\mu_e\tau_e$ / $\mu_h\tau_h$ for CZT) due to the unmeasurable hole transit time with the Transient Charge Technique as explained in Section 6.4. The *CCE(x)* profile based on an experimentally determined $\mu_e\tau_e$ product, and an assumed $\mu_h\tau_h$ product is shown in Fig. 3.11. A negative slope is observed, indicating a majority of the induced signal occurs from electrons.

The *CCE(x)* profile for LiZnAs was determined based on a device length of 0.210 cm, with 48 volts applied to the detector. The μ_e and τ_e were used as values were determined by the transient charge technique (μ_e *= 4.8* cm^2 V^{-1} s^{-1} *and* τ_e *= 190* μs). The $\mu_h\tau_h$ was assumed at 1.0 x

10^{-6} cm^2 V^{-1}, two orders of magnitude less than the $\mu_e\tau_e$ product (similar to the ratio of $\mu_e\tau_e$ / $\mu_h\tau_h$ for CZT), due to the same unmeasurable hole transit time with the Transient Charge Technique measurement as explained in Section 6.4. The *CCE(x)* profile is shown in Fig. 3.12. The slope of the *CCE(x)* profile distribution for both LiZnP and LiZnAs devices are negative, indicating detrimental hole trapping and recombination effects.

Comparison between the *CCE(x)* of planar CZT device and planar LiZnAs and LiZnP devices, it is observed there are some charge collection challenges with LiZnAs and LiZnP. The maximum charge collection in LiZnP and LiZnAs devices occurs near the cathode end of the device where approximately 62% of the initial charge deposited will be collected. The *CCE(x)* decreases for interactions near the anode. The charge collection can be improved by increasing the applied voltage to the device, therefore increasing the electric field, or by improving the $\mu_e\tau_e$ and $\mu_h\tau_h$ products of the material, or by decreasing the length of the device. Ultimately, this evaluation shows that neutron detection is possible from the charge collection point of view with LiZnP and LiZnAs devices. However, limitations on device operation parameters to optimize device performance, such as applied bias, are detailed in Section 6.4.

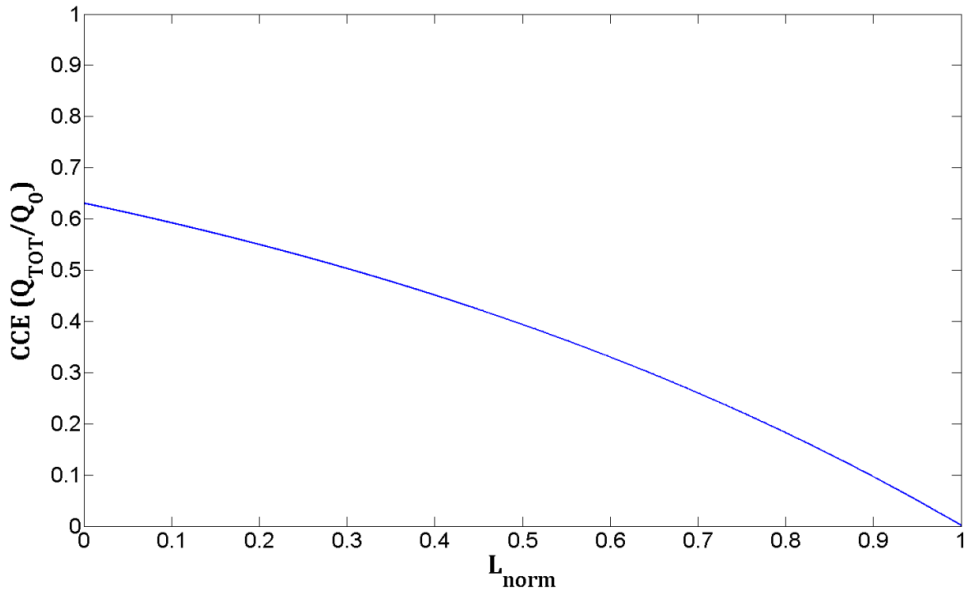

Fig. 3.11. The charge collection efficiency profile for a planar LiZnP device 0.202cm in length, 51 volts applied to the device, with μ_e = 5.7 cm^2 v^{-1} s^{-1} and τ_e = 139 μs as characterized by the transient charge technique. The $\mu_h\tau_h$ was estimated at 1.0 x 10^{-6} cm^2 V^{-1}, two orders of magnitude less than $\mu_e\tau_e$ = 8.0 x 10^{-4} cm^2 V^{-1}. Position 0 represents the cathode end of the device and 1 represents the collecting electrode, the anode.

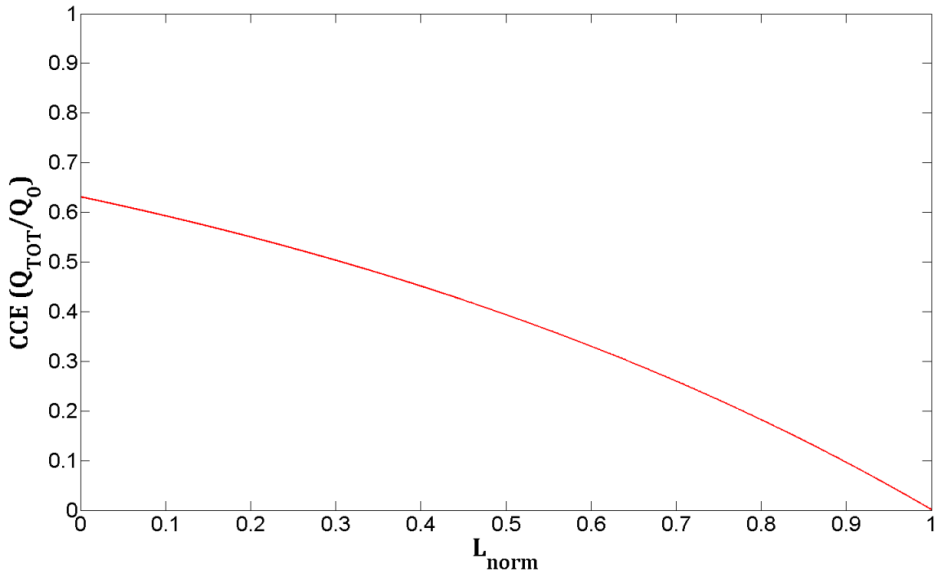

Fig. 3.12. The charge collection efficiency profile for a planar LiZnAs device 0.21cm in length, 48 volts applied to the device, with μ_e = 4.8 cm^2 V^{-1} s^{-1} and τ_e = 190μs as characterized by the transient charge technique. The $\mu_h\tau_h$ was estimated at 1.0 x 10^{-6} cm^2 V^{-1}, two orders of magnitude less than $\mu_e\tau_e$ = 9.1 x 10^{-4} cm^2 V^{-1}. Position 0 represents the cathode end of the device and 1 represents the collecting electrode, the anode.

3.5 Neutron Sensitivity

LiZnP and LiZnAs device design parameters for thermal neutron absorption, and thermal neutron response pulse height spectra. The macroscopic thermal neutron absorption cross sections were determined for LiZnAs and LiZnP devices. Using the cross section data determined, device thickness were determined for 95% thermal neutron absorption with devices fabricated from natural lithium (7.59 % ^{6}Li) and 96% enriched ^{6}Li. Idealized thermal neutron response pulse height spectra for each device design were also modeled.

3.5.1 Macroscopic thermal neutron cross sections for LiZnP and LiZnAs

The macroscopic thermal neutron cross sections for LiZnP and LiZnAs material were determined for devices containing natural lithium (7.59% ^{6}Li) and enriched ^{6}Li (96% ^{6}Li). Total thermal neutron cross sections ranged from 0.74 cm^{-1} to 11.00 cm^{-1}, where the calculation is outlined in Appendix B.

Table 3.2. The determined total (including σ_{Zn}, σ_P, σ_{As}) macroscopic thermal neutron absorption cross sections for LiZnAs and LiZnP material containing either natural lithium (7.59% ^{6}Li), or enriched ^{6}Li (96% 6Li).

	Macroscopic absorption cross section with natural Li (7.59%) (cm^{-1})	Macroscopic absorption cross section with enriched ^{6}Li (96% ^{6}Li) (cm^{-1})
LiZnP	0.88	11.00
LiZnAs	0.74	8.82

The intensity of a transmitted thermal neutron beam through a material decreases exponentially with material thickness as described by,

$$I(t) = I_o e^{-\Sigma t}, \tag{3.12}$$

where Σ is the macroscopic thermal neutron absorption cross section, t is the thickness of the absorbing material, I_o is the initial intensity, $I(t)$ is the intensity as a function of material thickness [32]. The neutron fraction absorbed, I_F, in the absorption thickness is defined by,

$$I_F = 1 - \frac{I(t)}{I_o} = 1 - e^{-\Sigma t}. \tag{3.13}$$

From the values listed in Table 3.2, the thermal neutron fraction absorbed (percent) was plotted as a function of material thickness for LiZnP and LiZnAs for materials containing natural lithium (7.59% ^{6}Li), as shown in Fig. 3.13, and 96% enriched ^{6}Li, as shown in Fig. 3.14. LiZnP appears

to be a better neutron absorbing material due to having a lower molecular weight and lower density. However, it is clear that using enriched ^{6}Li makes a much better neutron absorber, and in terms of neutron detection, a much more efficient device for a smaller, and more compact profile. In the following study only natural lithium was used to produce LiZnP and LiZnAs. The material purity of 95-96% enriched ^{6}Li was quoted from Y-12 National Security Complex, Oak Ridge, TN to have a lithium purity of 94-95% [40], therefore material purity would have been a major material problem. Semiconductor materials already suffer from material purity problems, where the starting desired purity minimum for semiconducting devices is 5N (99.999%). Finding commercial natural lithium at such a high purity is not possible at the moment. ESPI metals provides lithium ingots sealed in argon at a 99.9% purity, and was used in the following work. When enriched ^{6}Li material is available at a high purity, a highly neutron sensitive semiconducting material would be possible in an extremely small LiZnAs or LiZnP device. Shown in Table 3.3 are the thickness needed for 95% thermal neutron absorption with LiZnP and LiZnAs containing natural lithium, and enriched ^{6}Li, which is an indication of theoretical device efficiency for thermal neutrons.

Table 3.3. The material thickness (mm) needed for 95% absorption of thermal neutrons for LiZnP and LiZnAs containing either natural lithium, or 96% enriched ^{6}Li.

	LiZnP (natural)	LiZnP (96% ^{6}Li)	LiZnAs (natural)	LiZnAs (96% ^{6}Li)
95% absorption (mm)	34.04	2.72	40.48	3.40

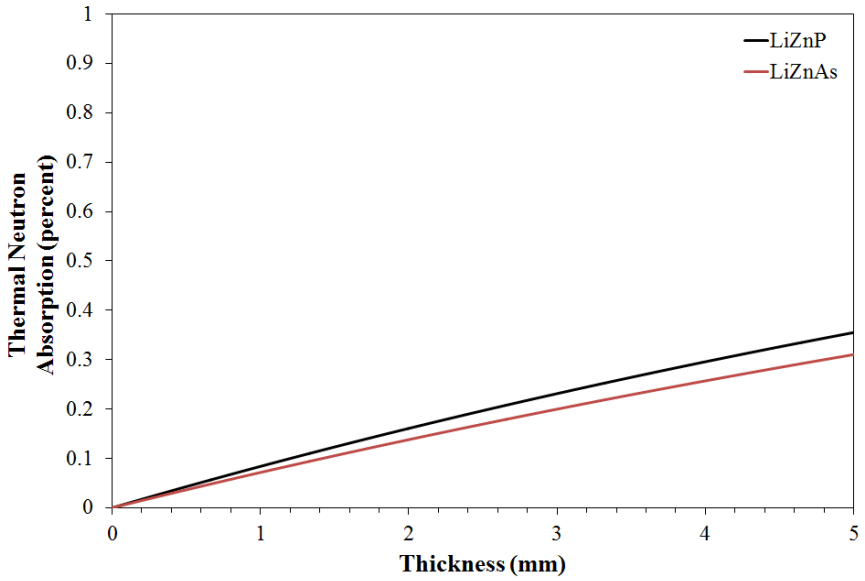

Fig. 3.13. The thermal neutron absorption percent as a function of thickness for LiZnP and LiZnAs containing natural lithium.

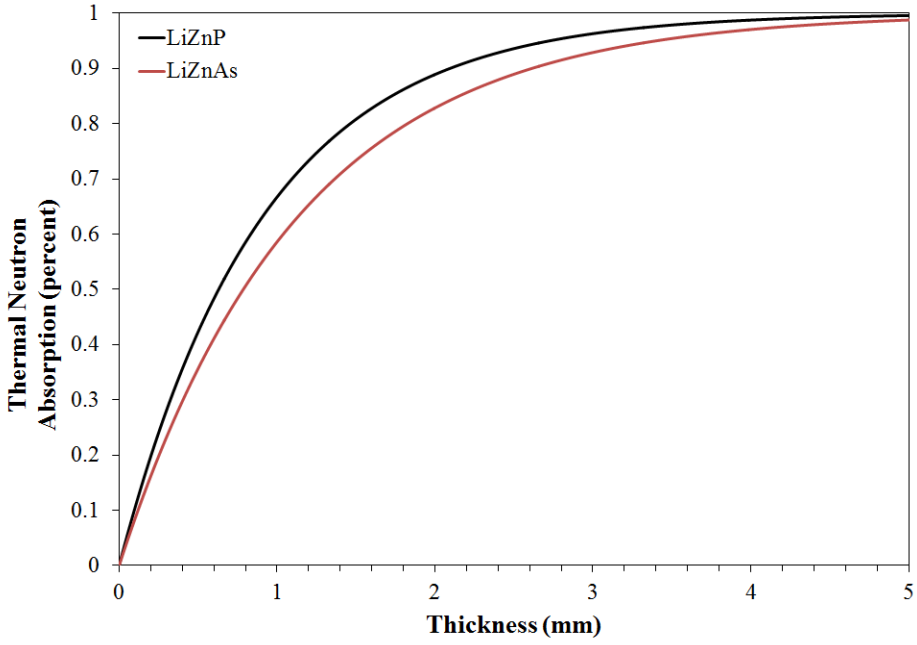

Fig. 3.14. The thermal neutron absorption percent as a function of thickness for LiZnP and LiZnAs containing 96% enriched ^{6}Li.

3.5.2 MCNP6 models with LiZnP and LiZnAs

LiZnP and LiZnAs devices were simulated with Monte Carlo N-Particle 6 (MCNP 6) for neutron sensitivity for devices containing natural lithium (7.5% ^{6}Li) and enriched ^{6}Li (96% ^{6}Li enrichment) [72]. These simulations were developed assuming perfect crystallinity of the LiZnP and LiZnAs devices, and perfect charge collection properties (i.e. no charge trapping) with no electric field effects. Therefore, these simulations provide a figure of merit as to what would be possible with ideal material properties.

LiZnP and LiZnAs were simulated based on the dimensions of tested devices (2.020 x 4.077 x 3.518 mm^3 – LiZnP, 2.100 x 4.155 x 4.060 mm^3 – LiZnAs), and the thermal neutron sensitivity test conditions at the KSU TRIGA Mark II nuclear reactor diffracted neutron beam port. Two simulations were performed, one with a LiZnP device composed of natural lithium (7.5% ^{6}Li), and the other composed of 96% enriched ^{6}Li, which were irradiated separately with a 0.5 inch diameter collimated beam of thermal neutrons. The simulated sample dimensions were 2.020 x 4.077 x 3.518 mm^3, and irradiated incident the 2.020 x 3.518 mm^2 sample face, similar to the experimental tests. The simulation was performed for 4.0 x 10^8 particle histories, and the resulting pulse height spectrum is shown in Fig. 3.15. The spectrum was plotted on semi-log scale to distinguish spectral features. However, when plotted on linear scale, the wall effect features are indistinguishable due to the large intensity of the full energy peak, confirming that a majority of the signal contribution is from full energy depositions of both ^{6}Li reaction products, resulting from the extremely short range of both reaction products in the LiZnP material. The thermal neutron capture efficiency (%) and absolute thermal neutron detection efficiency (%) were determined from the simulation as shown in Table 3.4.

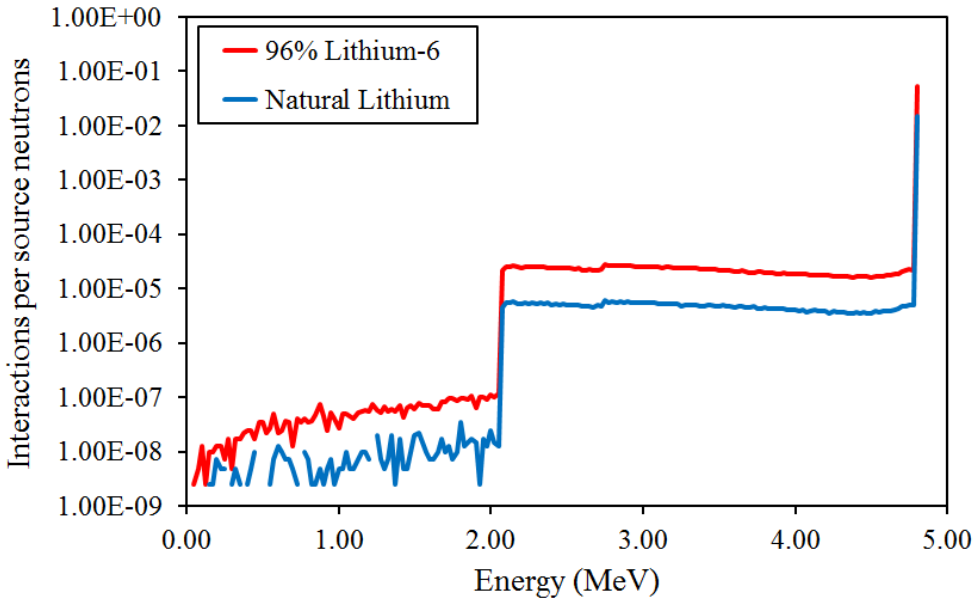

Fig. 3.15. The MCNP6 simulated resulting ^{6}Li reaction product spectra for two separate LiZnP neutron detectors. One detector had a composition containing natural lithium (7.5% ^{6}Li), and the other detector had a composition containing 96% enriched ^{6}Li.

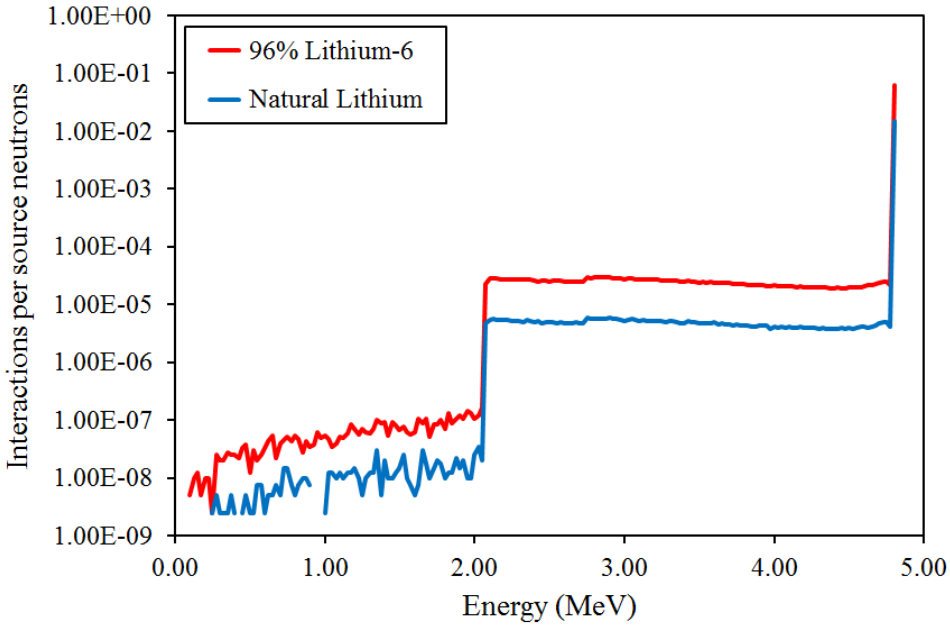

Fig. 3.16. The MCNP6 simulated resulting ^{6}Li reaction product spectra for two separate LiZnAs neutron detectors. One detector had a composition containing natural lithium (7.5% ^{6}Li), and the other detector had a composition containing 96% enriched ^{6}Li.

The same simulation was performed for a LiZnAs device using MCNP6. The device was modeled for the parameters of the experimentally tested device, with dimensions 2.100 x 4.155 x 4.060 mm^3. A collimated beam of thermal neutrons was incident on the 2.100 x 4.060 mm^2 sample face. Two samples were modeled separately, one with natural lithium and the other with 96% enriched ^6Li. The simulation was performed with 4.0 x 10^8 particle histories, and the resulting spectra appeared nearly identical to the simulated spectra obtained for LiZnP, as shown in Fig. 3.16. The resulting neutron capture efficiency (%) and neutron detection efficiency (%) determined from the simulation are shown in Table 3.4. The neutron capture efficiency is approximately equal to the absolute thermal neutron detection efficiency since reaction product absorption is extremely high in LiZnP and LiZnAs material.

Table 3.4. The thermal neutron capture and absolute thermal neutron detection efficiencies from MCNP6 simulations with LiZnP and LiZnAs.

Material	Enrichment	% Absolute Thermal Neutron Detection Efficiency	% Thermal Neutron Capture
LiZnP	96 % ^6Li	5.53%	5.53%
	Natural lithium	1.54%	1.54%
LiZnAs	96 % ^6Li	6.53%	6.53%
	Natural lithium	1.55%	1.55%

Chapter 4 : PRELIMINARY EMBODIMENTS

There is no adequate defense, except stupidity, against the impact of a new idea.

- Percy Williams Bridgman, U. S. physicist, Nobel Prize, 1946.

The following section describes the initial developments in the project, which include furnace design and construction, glove box design, initial synthesis methods, and crystal growth trials. These necessary steps lead to the final design and process of the production of Nowotny-Juza compounds for neutron detectors.

4.1 Furnace design and construction

4.1.1 Furnace Design

Reported melting temperatures of Nowotny-Juza materials are incomplete in the literature; however what was reported in the literature lead to the idea of designing a Stockbarger-type crystal growth furnace [77]. Little was initially known about these materials, the furnace was designed with the following features:

1) Capability of orienting the furnace in the vertical, horizontal or any angular position in-between.
2) Adjustable adiabatic zone between 1 and 4 inches for thermal profile adjustment between the *hot* and *cold* zones.
3) Adjustable 1 – 2 inch bore.
4) A *hot* zone capable of achieving 1450 ^{o}C at continuous operation, 1500 ^{o}C maximum.
5) Motion control that is capable of traveling rates as low as 0.001 mm/hr.
6) Six inch *hot* and *cold* zones.

The Mellon Furnace company was contracted to build the furnace with the aforementioned specifications and features. The blueprint of the design is shown in Fig. 4.1, and a cross-sectional drawing of the furnace design is shown in Fig. 4.2.

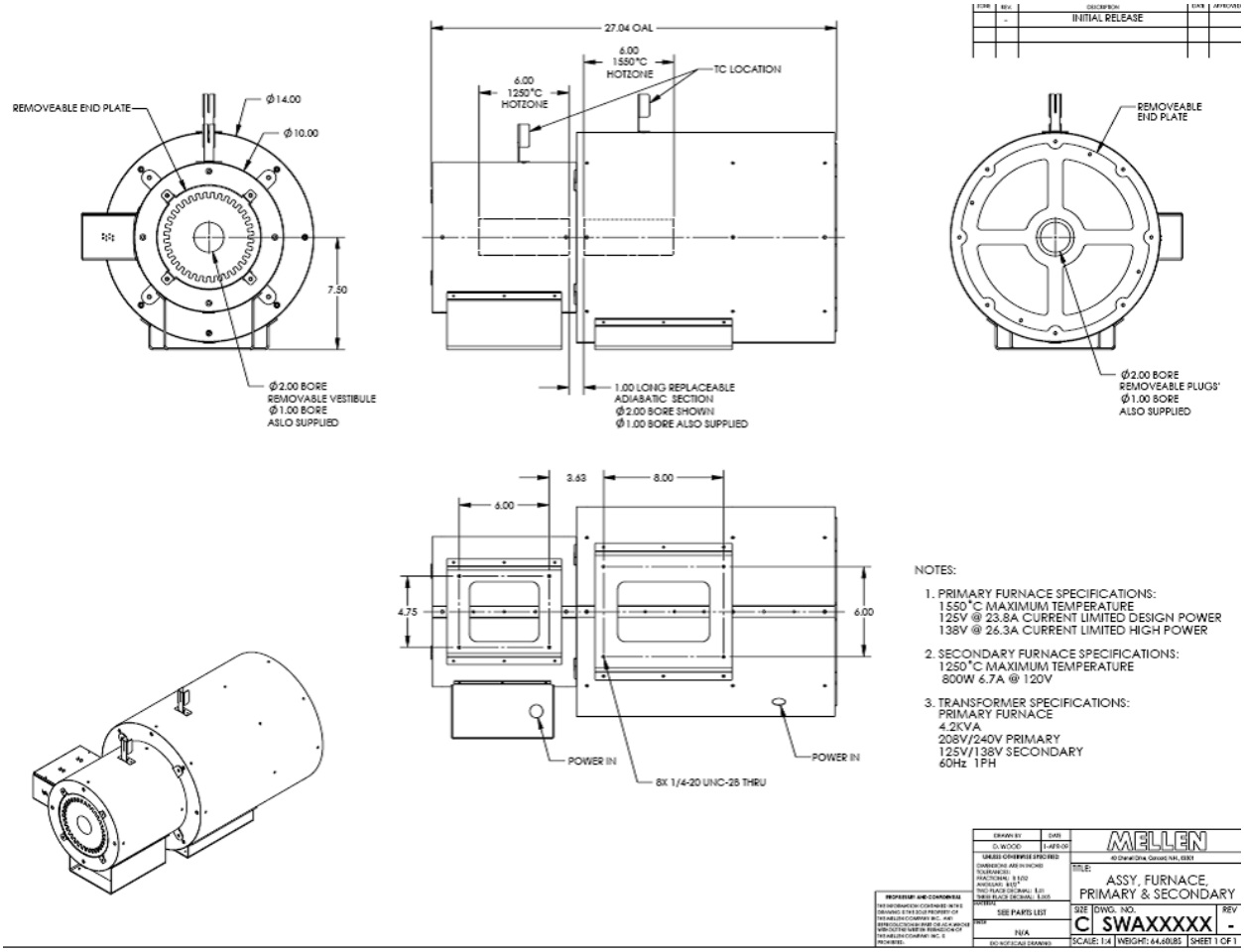

Fig. 4.1. The blueprint of the Stockbarger furnace design decided upon by the S.M.A.R.T. Laboratory and Mellen Furnace Company.

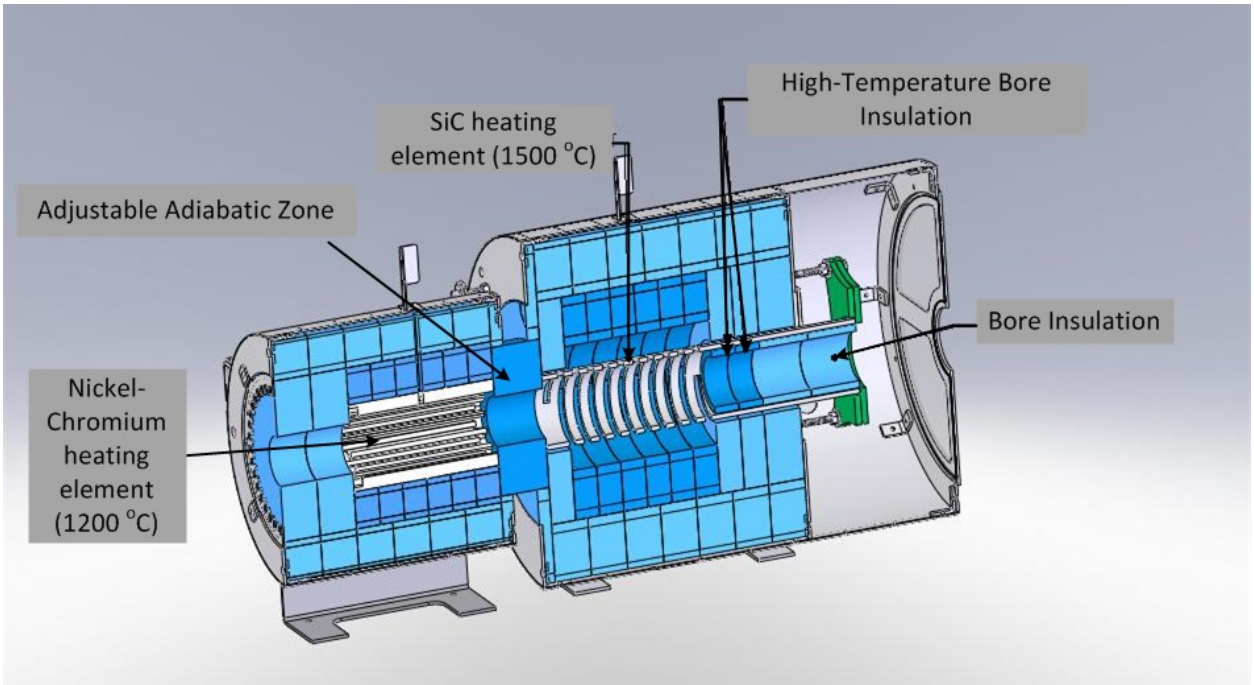

Fig. 4.2. The cross-section view of the Stockbarger furnace, which shows the internal structure of the two-zone furnace.

4.1.2 Furnace Frame Construction

A frame was designed to mount the furnace, electrical box, and other components necessary, as shown in Fig. 4.3. The frame was constructed from 1.5 inch square tubing with a 1/8 inch wall thickness. The frame was designed to be to rotate for various crystal growth orientations, including vertical, horizontal and angles in-between. In addition, the frame and reinforcement was designed to withstand the weight the tube furnace, counter weight and other necessary parts needed for operation. Drawings of the envisioned completed furnace in both the vertical and horizontal orientations are shown in Fig. 4.4.

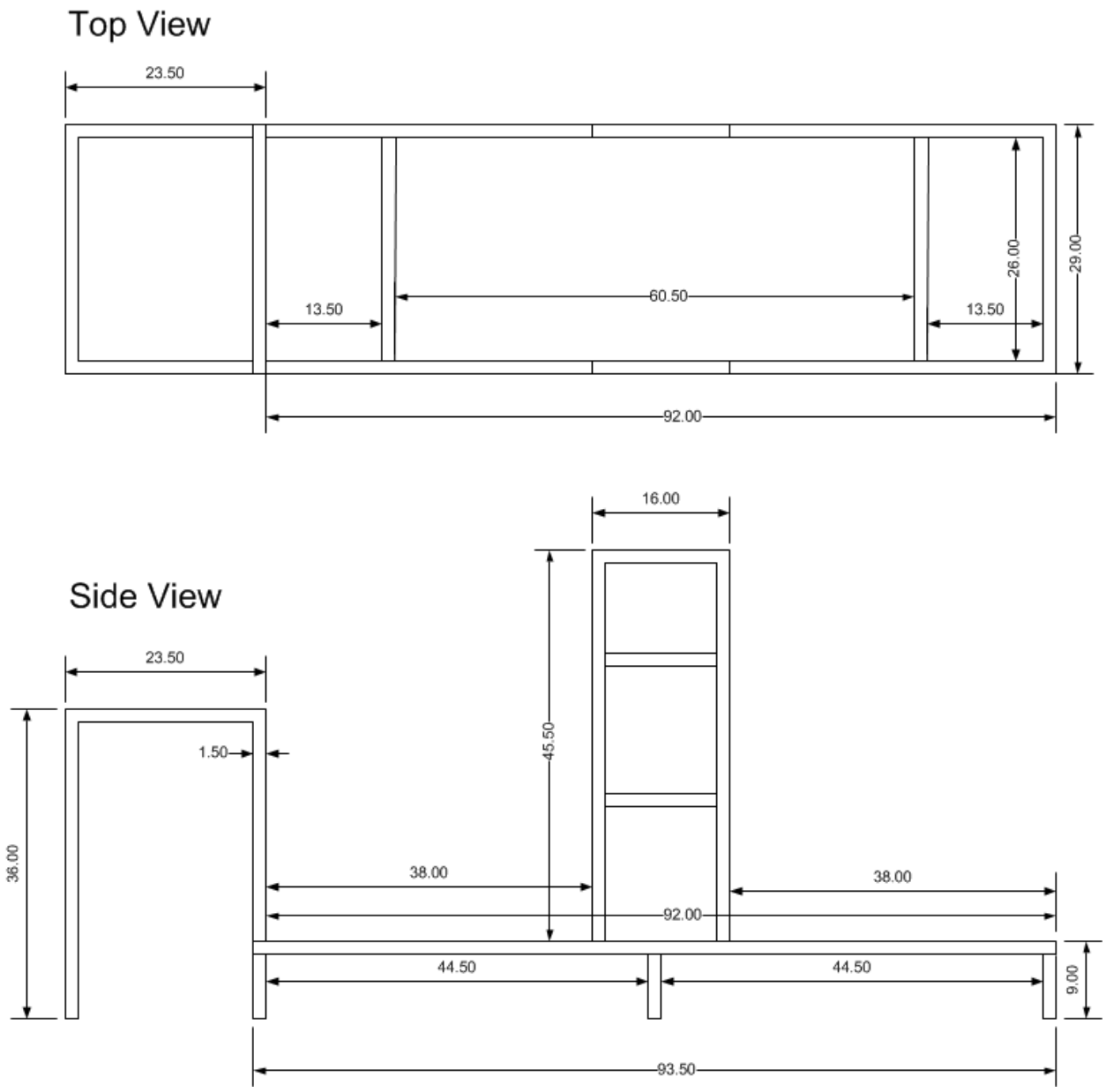

Fig. 4.3. Drawing of the top view and side view of the furnace frame.

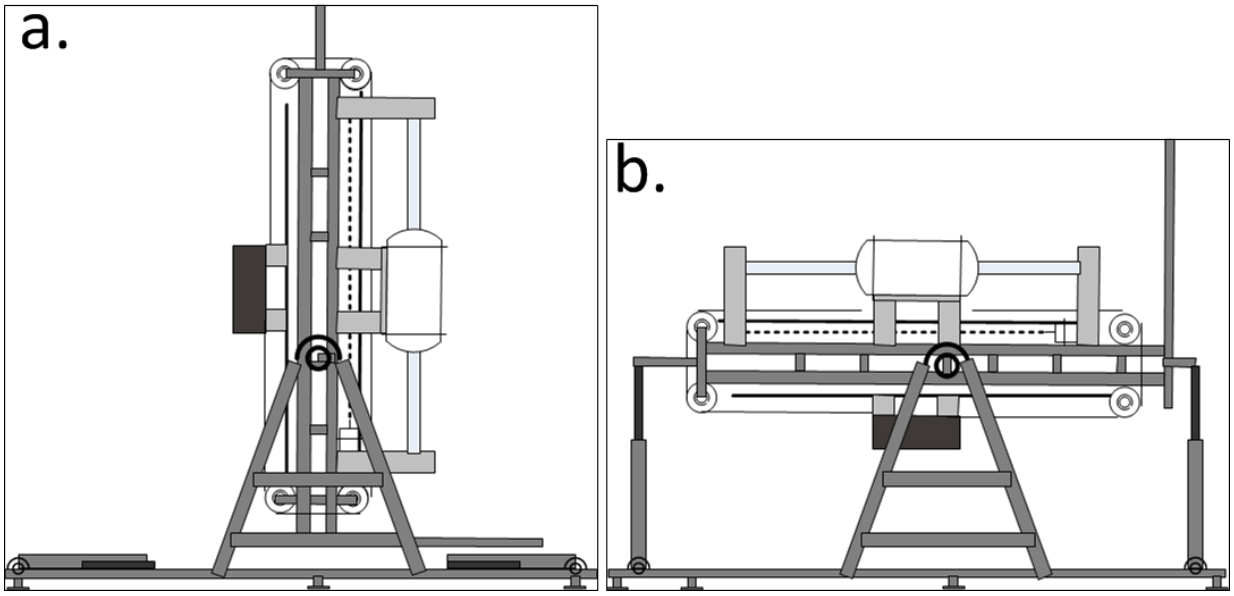

Fig. 4.4. Drawing of the custom furnace oriented in the vertical position (a.) and in the horizontal position (b.).

Once the frame was constructed, the frame was painted in two primer coats, and finished with two coats of paint to protect from surface rust as shown in Fig. 4.5; all additional components were coated with primer and additional paint layers. Precision linear rails were installed for easy movement of the furnace tubes and the counter weight, as shown in Fig. 4.6. The furnace table frame was equipped with a 1.0 inch stainless steel rod welded through the middle, where the table could be balanced in a particular orientation. The mounted furnace frame on pillow blocks is shown in Fig. 4.7.

Fig. 4.5. Furnace frame in the painting process.

Fig. 4.6. The furnace frame with the rotation table, and mounting plates installed.

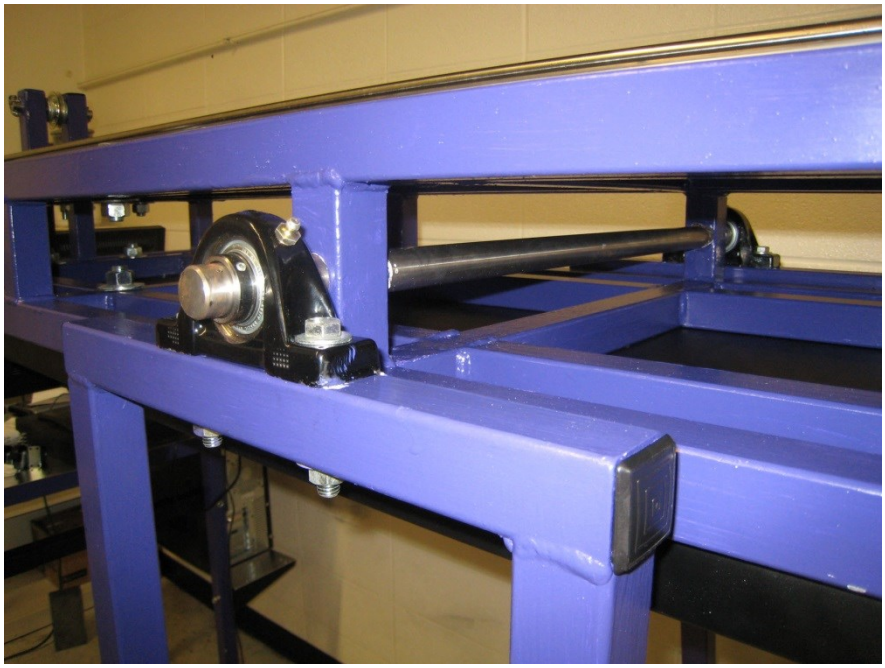

Fig. 4.7. A detailed look at the pillow block, and the rotation table design for vertical, horizontal, or tilted crystal growth.

The custom designed furnace tubes are shown in Fig. 4.8. These furnace tubes and the frame welding were the only major item outsourced for the furnace build. The electronics, program controls and the construction were all completed by S.M.A.R.T Laboratory personnel. The completed furnace is shown in Fig. 4.9 oriented in the vertical position. The counter weight shown in Fig. 4.9.a was designed for easy removal for using the furnace in the horizontal position.

Fig. 4.8. The furnace zone components for the two-zone furnace as provided by Mellen Furnace Company. The 1500 ^{o}C zone (hot zone) is on the left, and the 1200 ^{o}C zone (cold zone) is on the right.

Fig. 4.9. a. A view of the completed crystal growth furnace, where the removable counter weight is shown. b. A view of the completed crystal growth furnace, where the furnace zones are shown in the vertical position

Another important feature that was incorporated into the furnace design was the ability to move the furnace tubes manually without the threaded rod (motion control) connected. This feature allows for immediate movement of the furnace tubes, for ampoule loading and other maintenance, without having to wait for the motion control to move the furnace. Additionally, this feature also saves wear on the stepper motor, and helps stabilize the 64" long, ½ - 10 threaded rod in areas susceptible to sagging. This feature is shown in detail in Fig. 4.10 where the cart (controlled by the threaded rod) can be connected or disconnected to the furnace table by a long bolt that makes a solid connection between the two components.

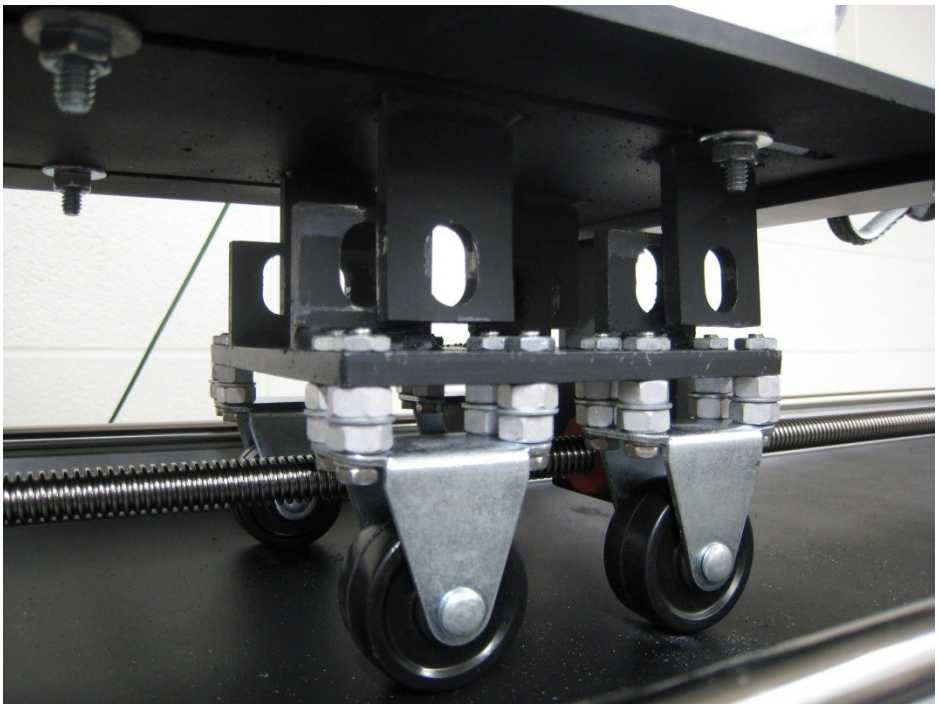

Fig. 4.10. A convenient feature that was included in the design was a motion cart that allows the user to disconnect the furnace table from the motion control for easy ampoule loading or other maintenance.

4.2 Electronics Design

The electronics to operate the furnace were designed and built at the KSU S.M.A.R.T. Laboratory. Shown in Fig. 4.11 is the circuit schematic. Traditional nickel chromium resistive heating elements can generally be switched on and off by a solid-state relay (SSR), however the higher-temperature silicon carbide heating elements require a current limiting and phase angle control relay system, known as a silicon-controlled rectifier (SCR). Additionally, over-temperature protection was included on each zone, by Eurotherm 2132i controllers. These controllers would signal a two-phase relay that opened the circuit to current flow in the case of an over-temperature occurrence. A step-up relay was required for both the SCR and SSR which supplied at least 15 mA for the SCR and SSR to open and close the circuit. The wiring diagram for the step-up relay is shown in Fig. 4.12.

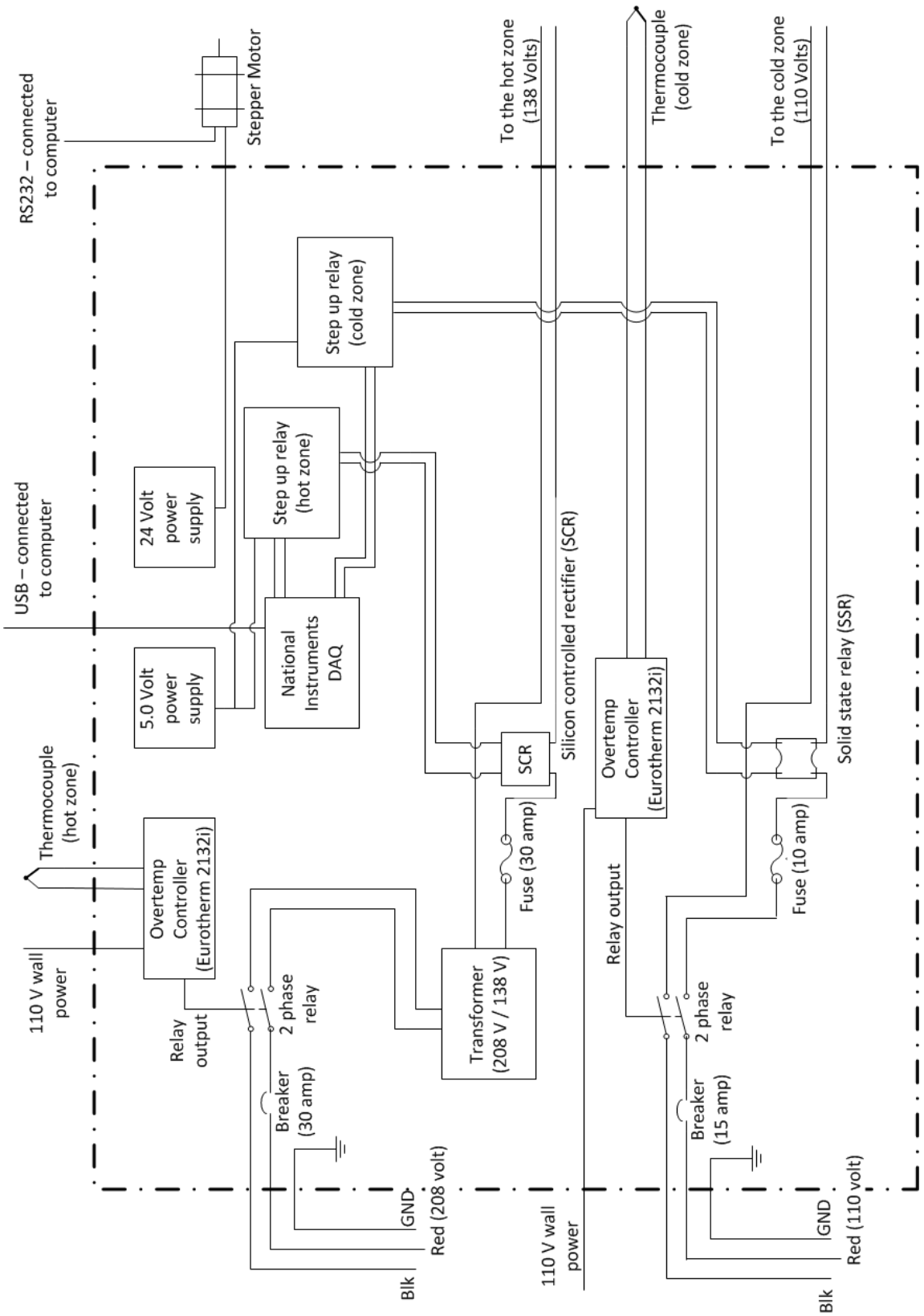

Fig. 4.11. The wiring diagram for the in-house designed electronics for furnace operation.

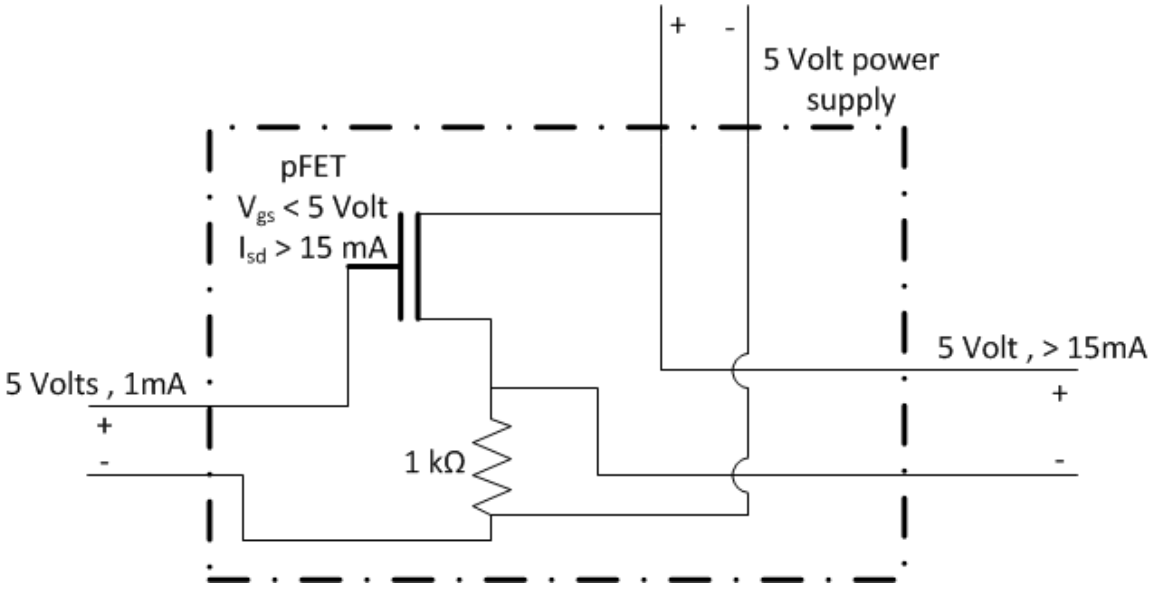

Fig. 4.12. The pre-relay circuit schematic that was necessary for the logic signal to trigger the silicon controlled rectifier (SCR) and solid state relay (SSR).

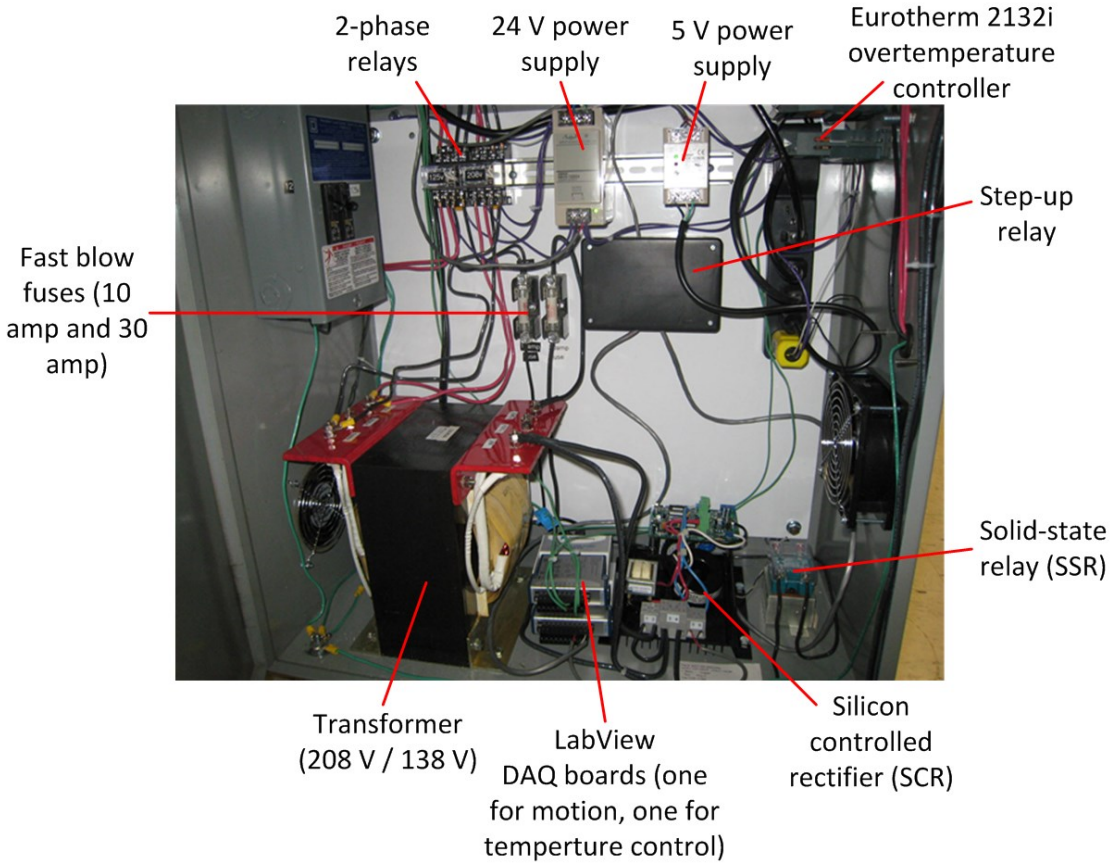

Fig. 4.13. A view of the inside of the electronic controls box, designed and built in the S.M.A.R.T. Laboratory.

4.3 LabView Furnace controls

LabView© design software was used to control the temperature and motion of the crystal growth furnace, where recipes can be designed and implemented for a desired crystal growth process. Fig. 4.14 shows the front panel of the program. The front panel contains manual motion and temperature control for immediate temperature and motion manipulation. A data log panel allows the user to save a spreadsheet with the data from a growth process, so the temperature profile and motion control can be viewed outside of real time, and can later be evaluated and reported. It also has a recipe control panel that allows for a new recipe to be created, shown in Fig. 4.15, and then initiated at a specified time. A near infinite amount of segments can be programed for a single recipe, which includes temperature, motion, and duration. Motion as slow as 0.001 mm/hr, or greater than 1000 cm/hr can be programed, as well as over-temperature control that will not let the user program an input higher than the threshold temperature for each zone (this is in addition to the relay over-temperature control of the electrical circuit previously described). The program runs on any LabView© Version 9 software or greater, and can easily be transferred to different versions of Microsoft Windows platforms.

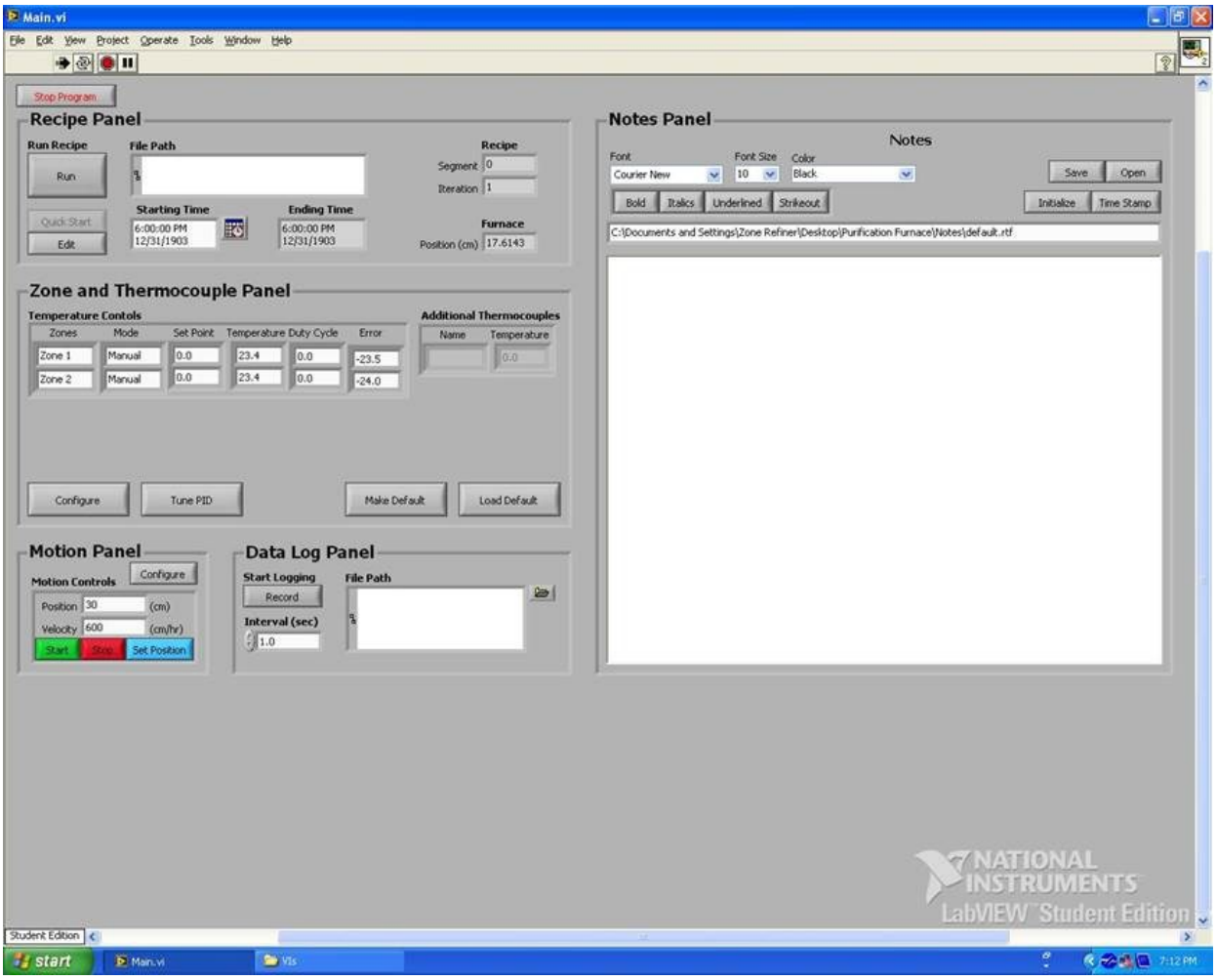

Fig. 4.14. A screen shot of the LabView© furnace controls front panel.

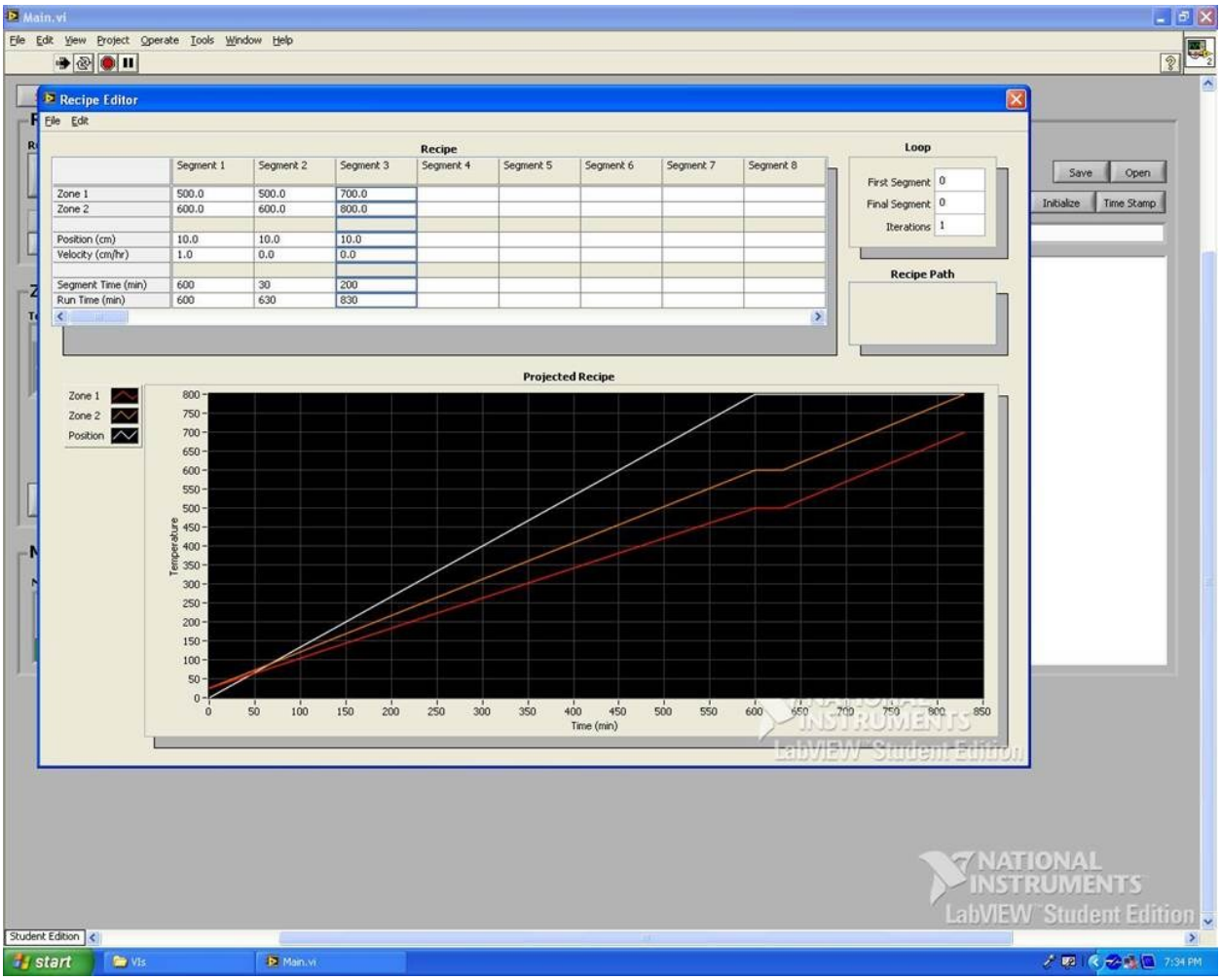

Fig. 4.15. A screen shot of the LabView© furnace controls recipe editor.

4.4 The first synthesis process - LiZnP

It was quickly determined that LiZnP, or any other aforementioned Nowotny-Juza compound, were not commercially available. As a result, it was necessary to perform the material synthesis in-house. The goal of the first synthesis process was to compound the ternary material, LiZnP in enough quantity to later be grown into a bulk single crystal for device

fabrication. The ampoule was designed[8] to house a graphite crucible inside which the synthesis reaction would occur, as shown in Fig. 4.16.

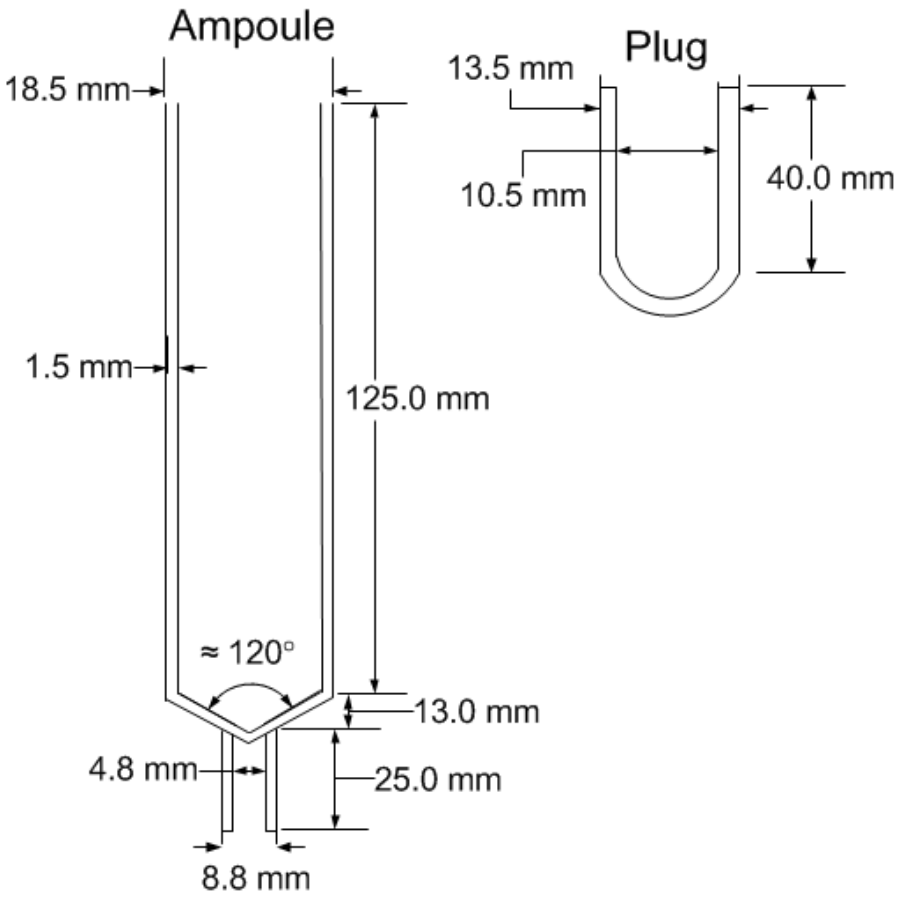

Fig. 4.16. A schematic of the ampoule and plug used in the first synthesis process.

The crucible was designed such that it could be used in both the vertical and horizontal positions, as shown in Fig. 4.17. The crucible was equipped with an angled bottom for the bulk crystal growth step, and was equipped with a cap that fit snuggly onto the top of the crucible, with a small opening on the side that allowed for the cap to be removed. The cap was intended to be used in the case of a horizontal crystal growth, however was never actually used in that fashion. These crucibles were used only in the vertical orientation.

[8] The ampoules were initially designed with an approximate 120^{o} angled bottom to promote crystallization for the subsequent bulk crystal growth process; however, these ampoules were applied to both processes (synthesis and bulk crystal growth).

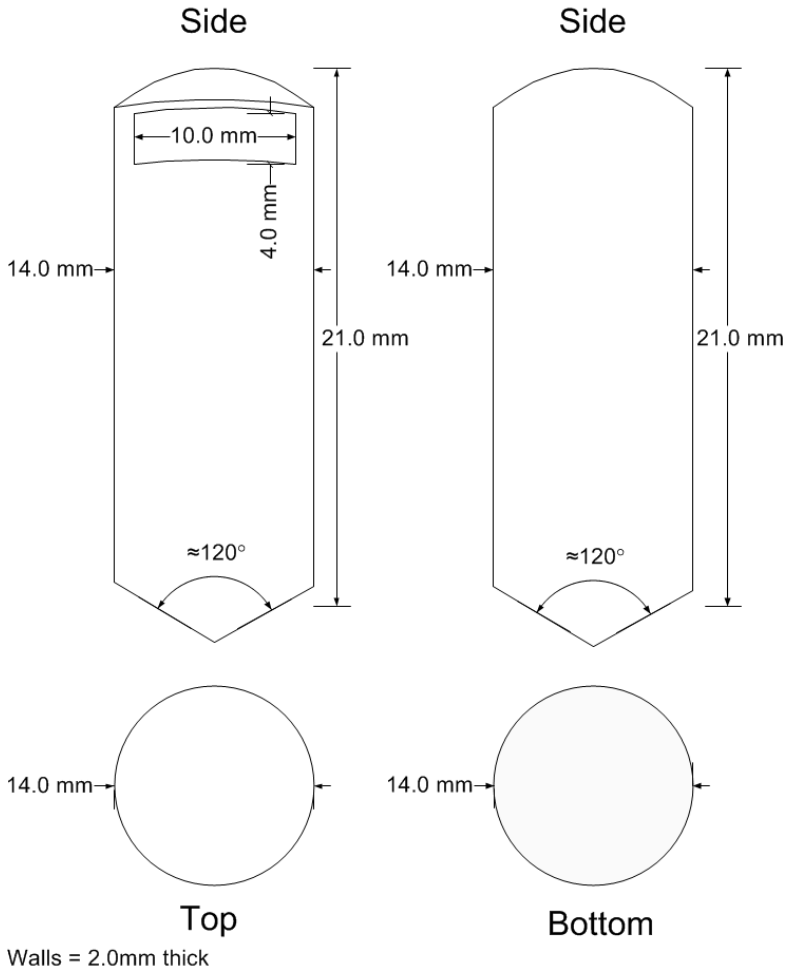

Fig. 4.17. A schematic of the crucible used in the first synthesis process

The custom ampoule was cleaned by the following process:

1. The quartz is rinsed with D.I. water at least five times
2. Prepare a 1:1:1 solution of: sulfuric acid, hydrogen peroxide, D.I. water. Fill the ampoule with this solution and etch for 15 min.
3. Rinse the ampoule with D.I water at least five times.
4. Prepare chromic acid by adding potassium dichromate to sulfuric acid. Add enough potassium chromate to the sulfuric acid until the fluid is a dark red. There is a precipitate, therefore decant the fluid into the ampoule, discard the precipitate, and etch for 2 hours.
5. Rinse the ampoule with D.I. water at least six times

6. Prepare a 1:20 solution of hydrofluoric acid:D.I. water. Fill the ampoule with the solution and etch for 4 hours.
7. Rinse the ampoule with D.I. water at least six times.
8. Rinse the ampoule with isopropanol at least three times.
9. Seal the ampoule in Parafilm© until use

Once the cleaning was complete, the ampoule was carbon coated, a process described elsewhere [78]. The ampoule was then loaded into nitrogen filled glove box[9]. Equamolar portions of elemental material, 99.99% zinc powder (Sigma-Aldrich) (0.2011 g), 99.99% phosphorus powder (Alpha-Aesar) (0.0925 g), and 99% lithium (granular) (Sigma-Aldrich) (0.0263 g) were added to the graphite crucible under nitrogen. This crucible was subsequently loaded into the carbon coated ampoule. The ampoule was connected to a vacuum valve attachment that kept the materials under nitrogen upon removal from the nitrogen glove box. The ampoule and fitting were loaded onto a vacuum sealing station similar to the one shown in Fig. 4.18. The ampoule was evacuated to 10^{-4} torr, with a roughing pump[10]. The ampoule was removed from the sealing station and placed into a tube furnace. The furnace temperature was ramped to 150 ^{o}C at 5.0 ^{o}C/min, and was held at 150 ^{o}C for 6 hours, then ramped to 680 ^{o}C at 1.0 ^{o}C/min. This recipe was based on the method reported by R. Bacewicz and T. F. Ciszek [60]. The goal was to raise the ampoule temperature to the approximate lithium melt temperature, and then begin the reaction process, as it is known that lithium becomes much more reactive once molten. Once the reaction was complete, the ampoule was removed from the furnace. There was a noticeable reaction between the quartz and vapors from the synthesis reactants, as shown in Fig. 4.19. Both lithium and phosphorus are very reactive at elevated temperatures, and can react with the quartz surface. The resulting material was extracted from the ampoule under an inert atmosphere, where the resulting material is shown Fig. 4.20. LiZnP should be a red color, and noticeable boundaries between colors and grains indicated that the resulting material was neither pure, nor ternary. This result lead to many further iterations into developing a method to produce Nowotny-Juza compounds in quantities large enough to grow into bulk crystals.

[9] At the time, only a nitrogen glove box was available. Later it was understood how crucial it is to store and prepare lithium under argon instead of nitrogen.
[10] A turbo pump was available on the "pump station," however it was not functioning properly for this particular experiment.

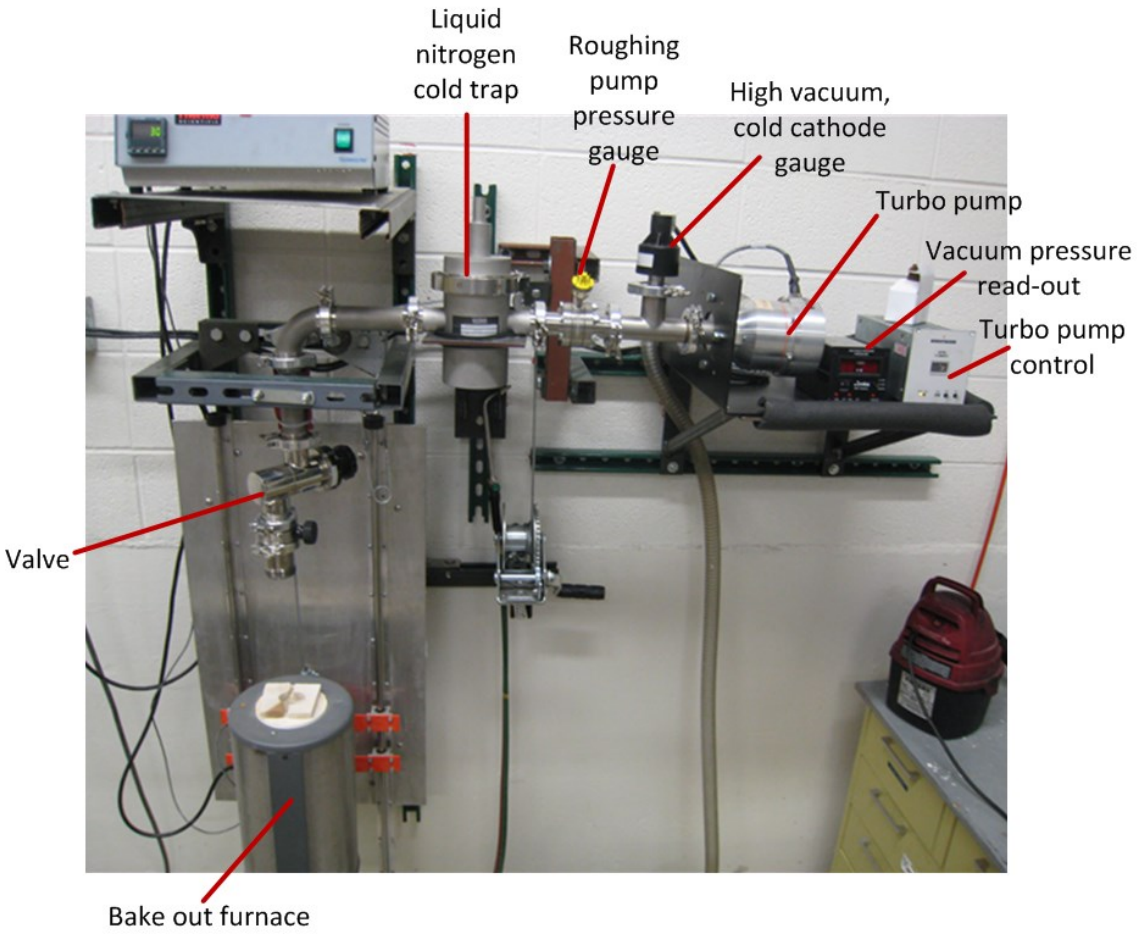

Fig. 4.18. The ampoule vacuum sealing station, referred to as the "pump station".

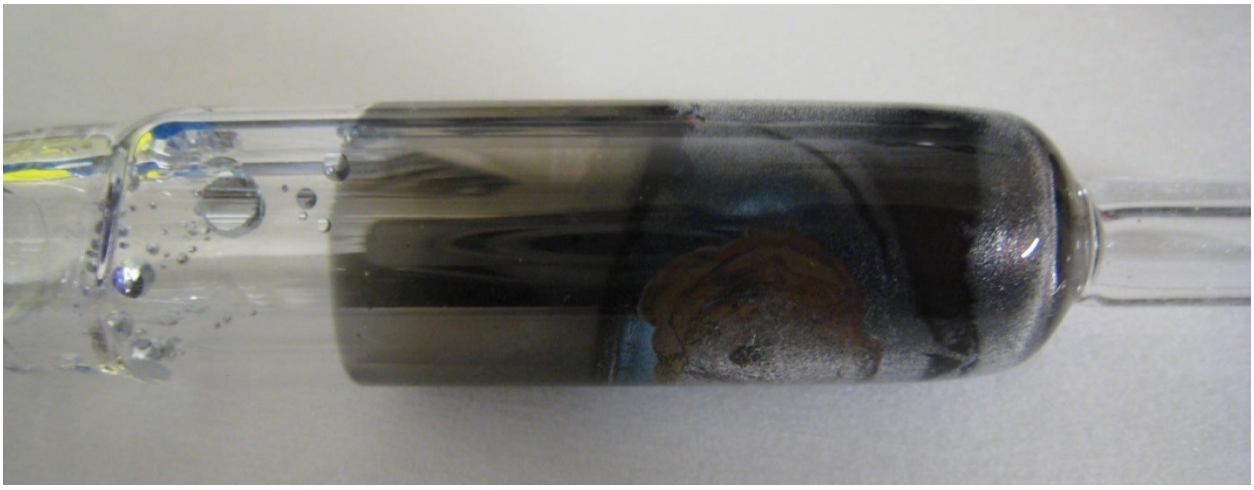

Fig. 4.19. The ampoule post the synthesis process. Notice the markings on the inner quartz wall. These markings are reactions between the quartz and lithium, and also phosphorus, vapors.

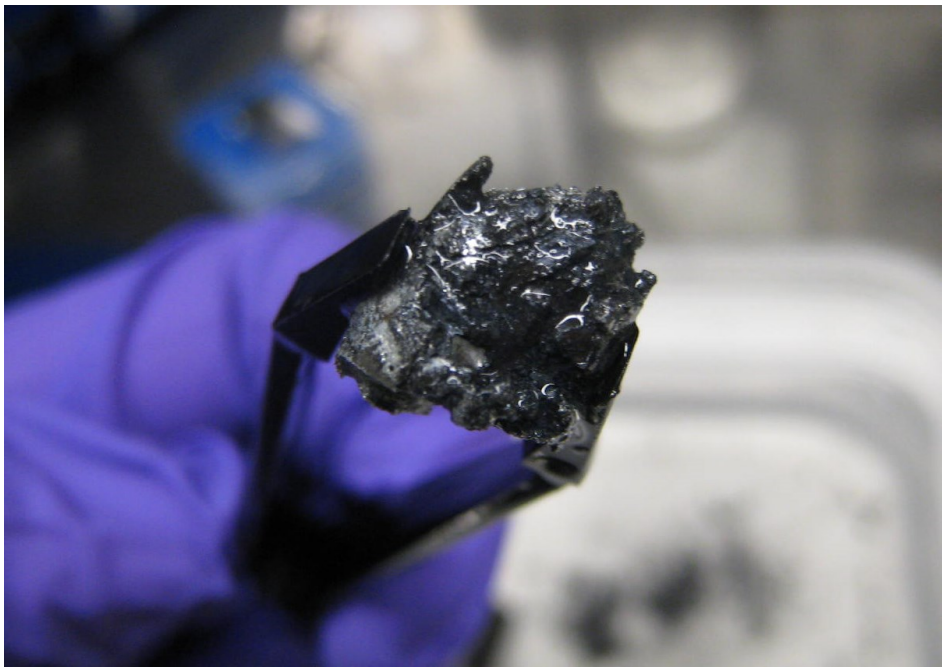

Fig. 4.20. The result from the first synthesis process.

4.5 Torch Heating Synthesis

The initial attempt to synthesize LiZnP ultimately failed. In order to understand and determine an appropriate synthesis method, the reaction in the ampoule needed to be studied. Rather than continue to load ampoules and changing small parameters for each experiment, it was decided to load the reactants into a small quartz ampoule and observe the reaction by heating with a H_2/O_2 torch.

The ampoule was loaded with equimolar amounts of lithium, phosphorus, and zinc (same purity as described previously) under an inert atmosphere (N_2), and then vacuum sealed (10^{-6} torr). The ampoule was attached to a quartz rod, and mounted to a ring stand. Shields and proper safety equipment were used during the reaction process. The torch flame was moved over the ampoule in an attempt to heat it evenly. Oxygen was also slowly added to the flame as more heat was needed. Once the reaction was observed to start, the flame was continually moved over the surface in an attempt to maintain heat for at least 10 minutes. The result of the experiment is shown in Fig. 4.21.

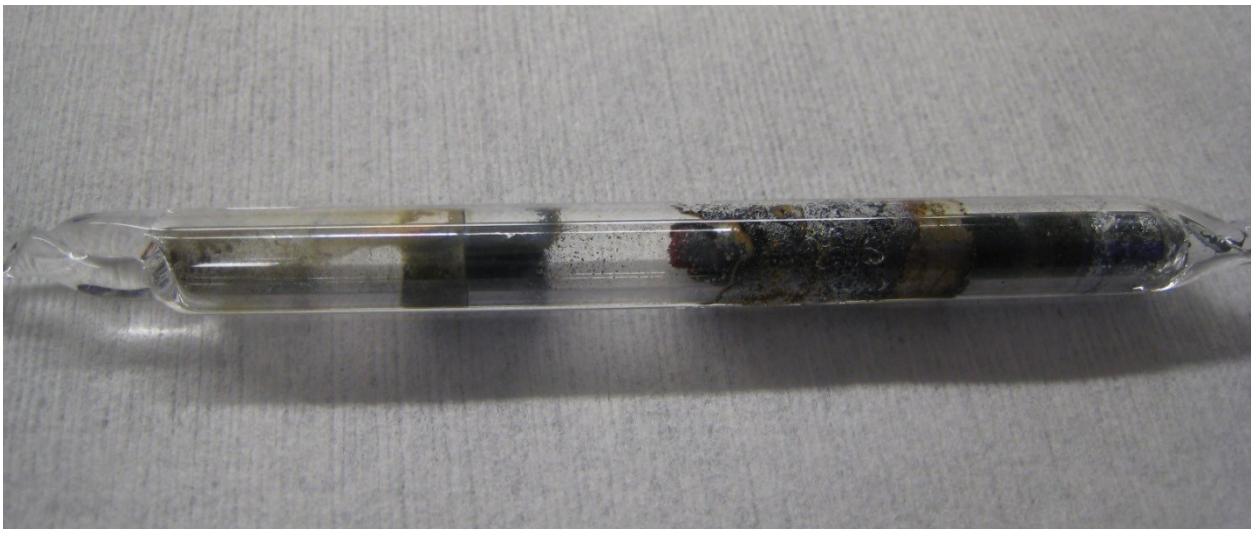

Fig. 4.21. The small ampoule (3 inches long, 3.80mm inner diameter, 6.35mm outter diameter) containing the reactants Li, Zn and P. Likely binary compounds, and the ternary compound LiZnP, are also included in the ampoule.

The ampoule wall appeared to experience a reaction with the reactants, most likely lithium. It is known that lithium reacts with quartz to make lithium silicates; however, only molten lithium in physical contact with quartz or silicates reacts violently, which can also destroy the containment, according to L.F. Epstein [79]. However, lithium vapor does not react with quartz or silicates in the same fashion, and does not compromise the containment vessel provided that molten lithium remains separated from the glass wall of the containment. Because the ampoule containment vessel was not compromised in this experiment, it is likely that lithium was rapidly consumed with the reactants zinc and phosphorus before reacting aggressively with the quartz wall.

A bright red material was observed at the top of the reacted material, as shown in Fig. 4.22. The red material was suspected to be the desired ternary product due to its color, and by the way it formed at the top of the ingot; indicating that vapor transport assisted in the reaction process. The ingot of reacted material likely consisted of binaries and unreacted material given the black and dull color throughout the majority of the ingot. The red and black materials from the ingot were not studied further, as it was determined that this method was not the direction with which to move forward. Instead, the following synthesis methods were to be investigated:

1. Vapor transport assistance in the reaction process.
2. Proper mixing of the constituent materials.

3. Temperature control to initiate the desired reaction.

These necessary changes were studied in the following experiments.

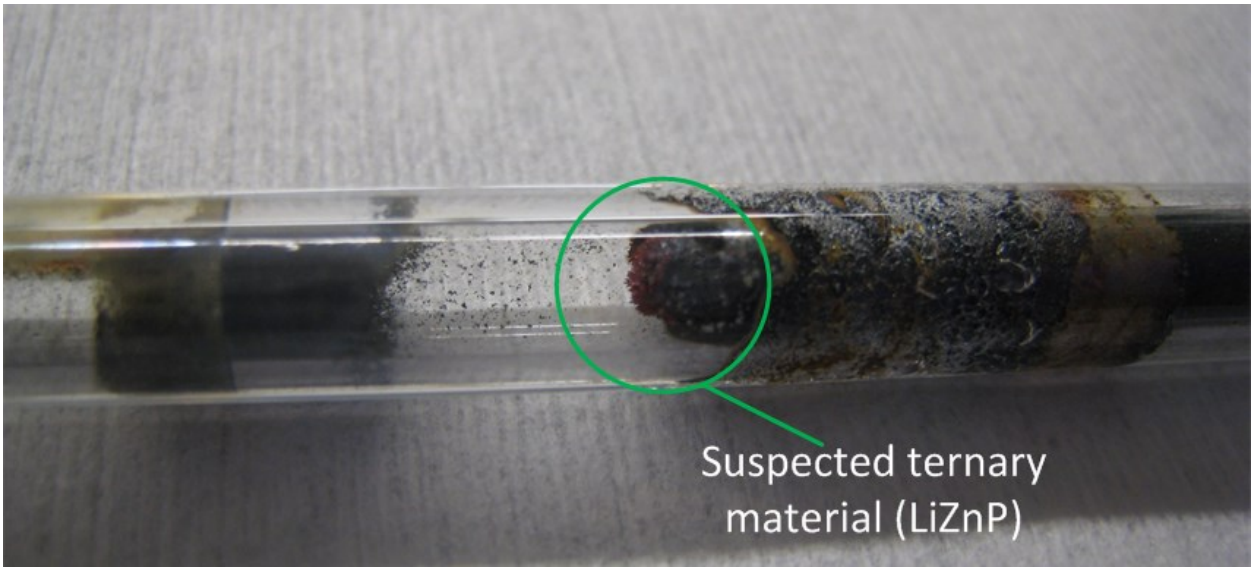

Fig. 4.22. A detailed view of the red material circled in green. This material was suspected to be ternary because of its color, and also because of the likelihood that vapor transport assisted with the reaction process.

4.6 Open Crucible Furnace in Argon Glove Box

To examine the mixing problem that was evident in the synthesis process, the idea was to use a crucible furnace to force mixing of the starting materials. However, this method required a high-temperature glove box where the reaction could be performed under a pure argon environment. It is known that lithium reacts with other common glove box gases, such as nitrogen, to make lithium nitrides [80]. Lithium nitride is also a known explosive, and can ignite spontaneously in the presence of moisture. A high temperature glove box with an internal heat removal system was designed and built in-house for reacting the LiZnAs and LiZnP.

4.6.1 High Temperature Glove Box Build

Glove box manufacturers were initially contacted to build a high-temperature glovebox for reacting LiZnP and LiZnAs. The following specifications were requested:

1. The box had to be able to withstand convective heat transfer from a crucible furnace maintained at 1200 ^{o}C continuously.
2. The temperature environment around the crucible furnace needed to be low enough that proper handling of materials in the glove box would be possible. It was likely that a gas conditioning system, or heat removal system, would be needed.
3. Adaptability for multiple feed-throughs was necessary.

Unfortunately, all commercial venders that were approached quoted prices that exceeded the project budget. It was determined to design a build the high-temperature glove box in-house.

The box was designed for a single user, with a single view port into the box, as shown in Fig. 4.23. The box was fabricated from 1/8 inch stainless steel sheet, and the window was built with 3/8" thick Pyrex® glass. The glove attachments were designed to the manufactures specifications, Renco Corporation. Renco Corp., the glove manufacturer, shared their glove port coupling design so that way their gloves would fit to specification. This design was built in-house from aluminum, as shown in Fig. 4.24. This coupling design is the same as that used by several glove box manufacturers, and employs a specific technique to couple gloves to the box without contamination leaks.

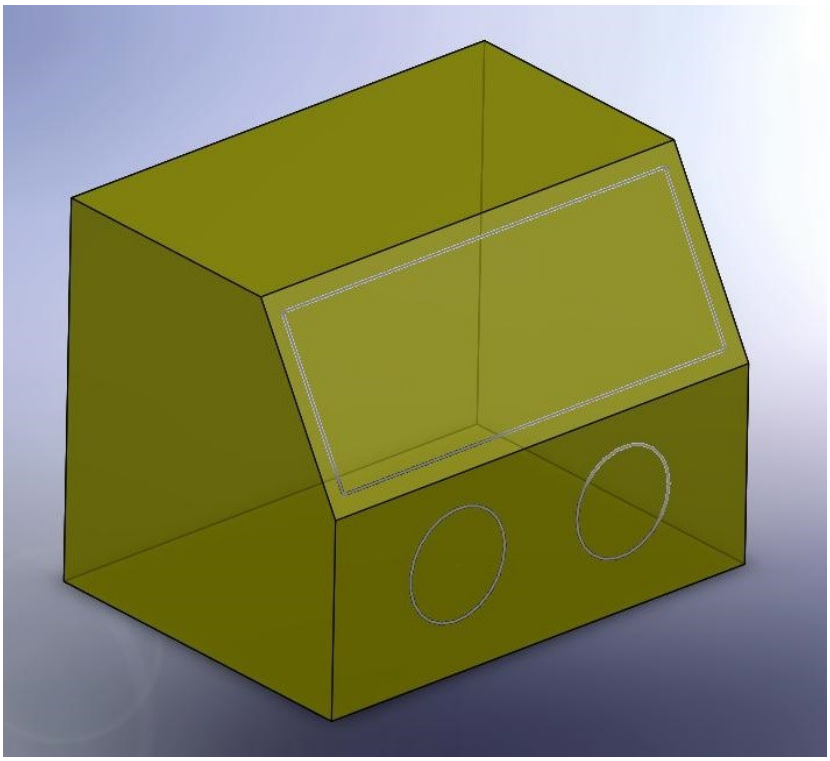

Fig. 4.23. A drawing of the proposed glove box design.

Fig. 4.24. The glove coupling produced at KSU from plans provided by Renco Corporation.

The welded box is shown in Fig. 4.25. Components were mounted to the box with high temperature sealants. The Pyrex® window was first sealed with a military specification joint sealant that maintains seal integrity up to 815 ^{o}C, followed by a high-temperature RTV sealant capable of withstanding temperatures up to 340 ^{o}C, shown in Fig. 4.26. The glove couplings and the glove box door coupling were bolted into place with the high temperature RTV between the glove box and the component for a leak free seal. The glove box door clamp was also mounted with a high-temperature RTV seal, and a high-temperature Viton o-ring was embedded on the door lid. Inside the box, an array of copper coils was mounted across the ceiling of the glove box as shown in Fig. 4.27. A radiative heat shield was placed over the coils to prevent radiant heat transfer to the copper coils during high-temperature processing inside the glove box.

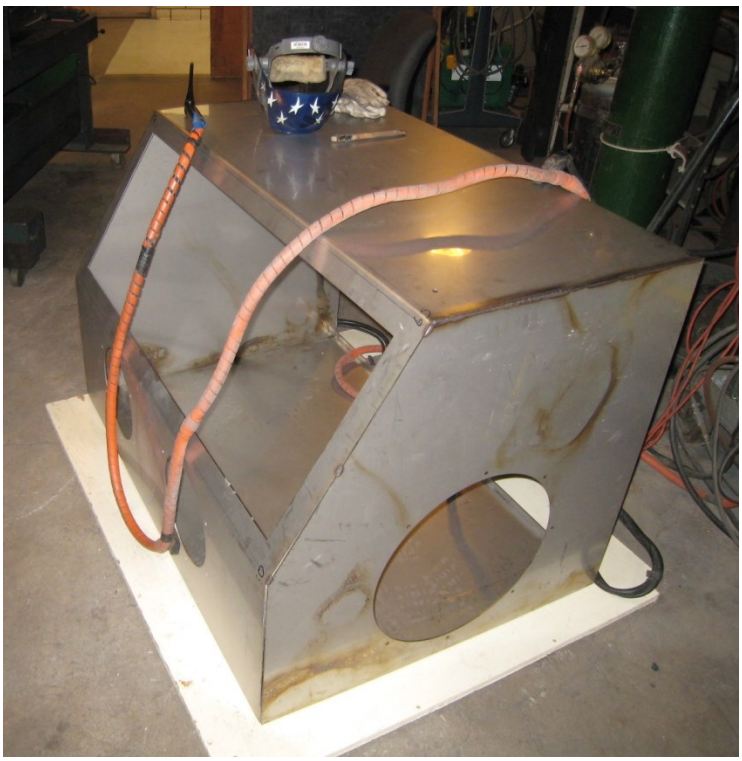

Fig. 4.25. The welded glove box

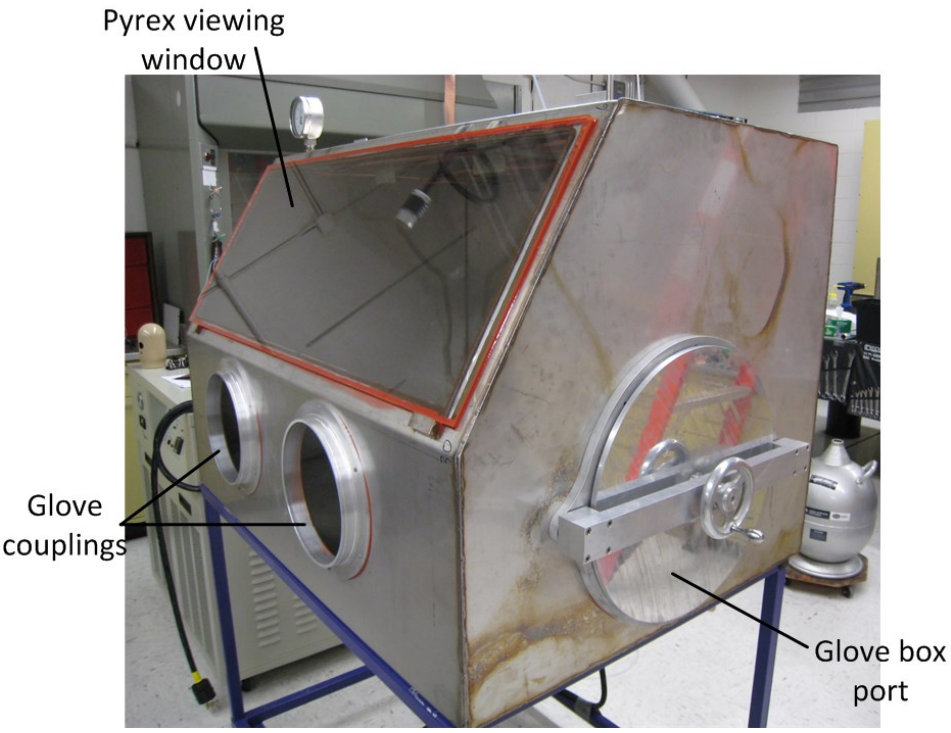

Fig. 4.26. The high-temperature glove box, showing the glove couplings, glove box port, and Pyrex® viewing window.

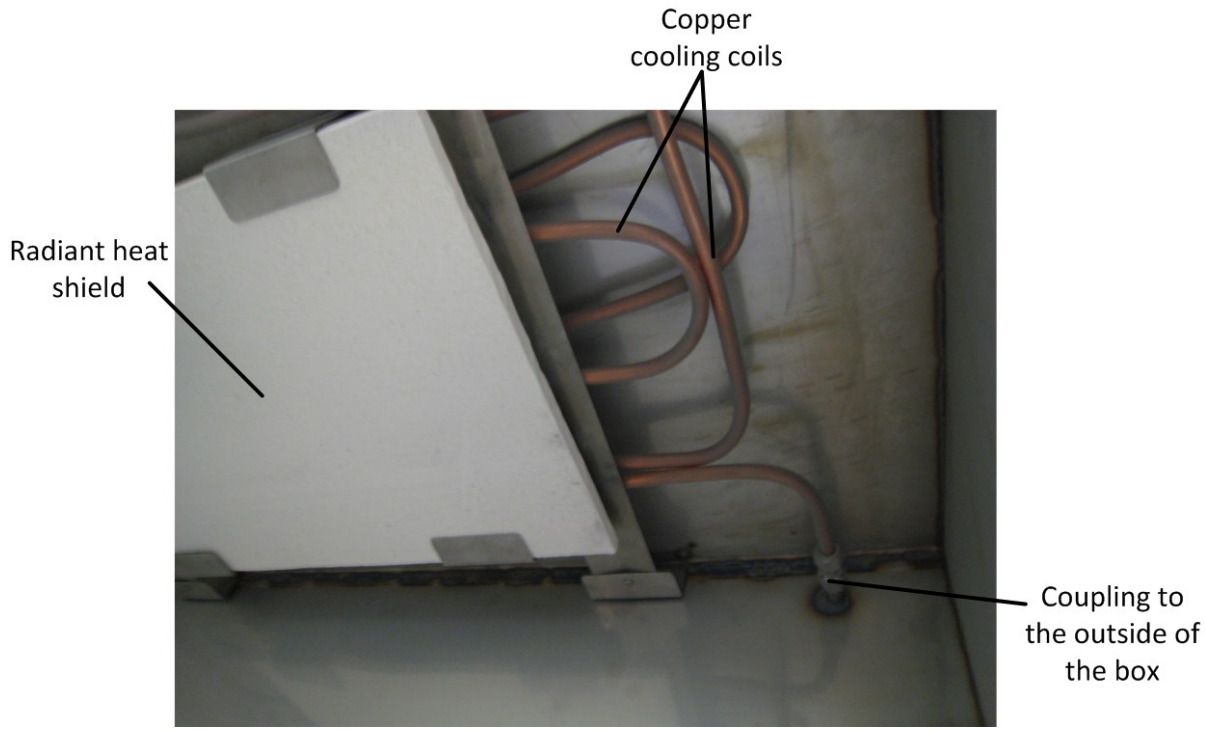

Fig. 4.27. The glove box ceiling with the copper cooling coils and radiant heat shield.

The completely assembled glove box is shown in Fig. 4.28. An industrial chiller was installed for the chilled water supply and connected to the glove box cooling coils. An electrical supply was also installed in the box. A safety breaker box was installed in the front of the frame for immediate electricity shut-off in case of an emergency. Adjustable florescent lights were installed to the roof of the box, allowing adjustable lighting to the interior of the box. Both nitrogen and argon valves were connected to the box; however, the argon was used strictly for lithium reactions.

The inside of the glove box was equipped with equipment shelves, a scale, and a crucible furnace, as shown in Fig. 4.29. The gloves coupled to the box were the highest temperature glove available (rated at 284 ^{o}F), a butyl type rubber. Additional "high heat" gloves were also purchased, rated to perform and insulate hands above 500 ^{o}C. The "high heat" gloves fit over the butyl gloves inside the glove box.

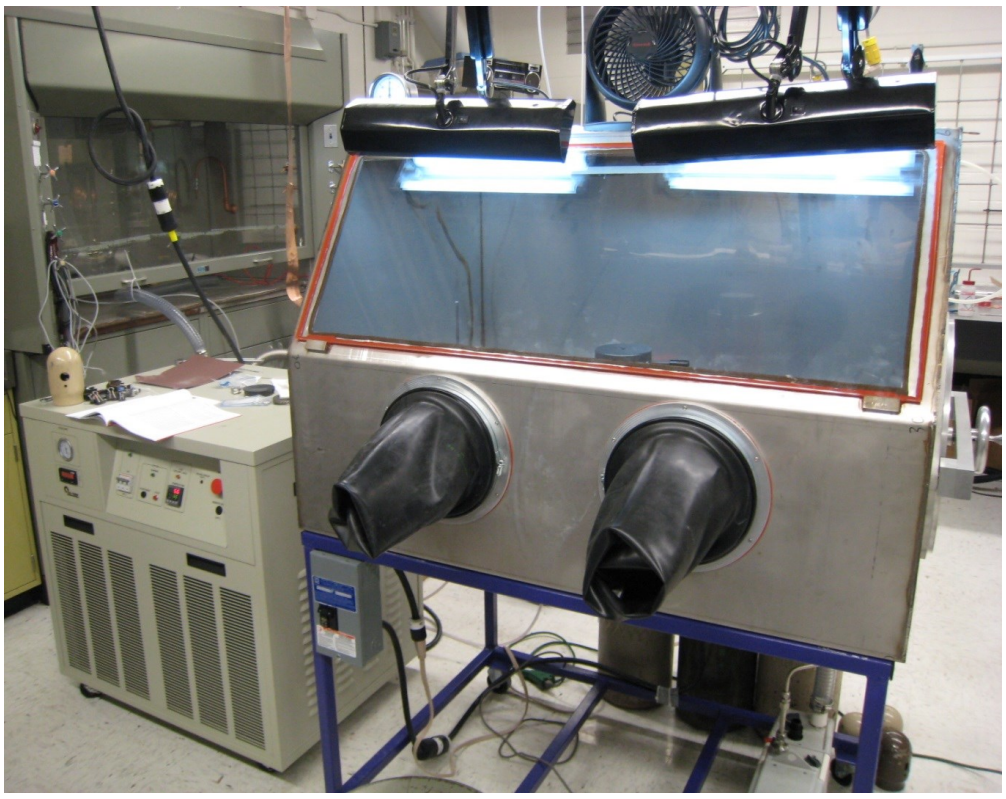

Fig. 4.28. The completed high-temperature glove box, equipped with an industrial chiller, cabinet lights, electrical breakers, and gas inputs / outputs.

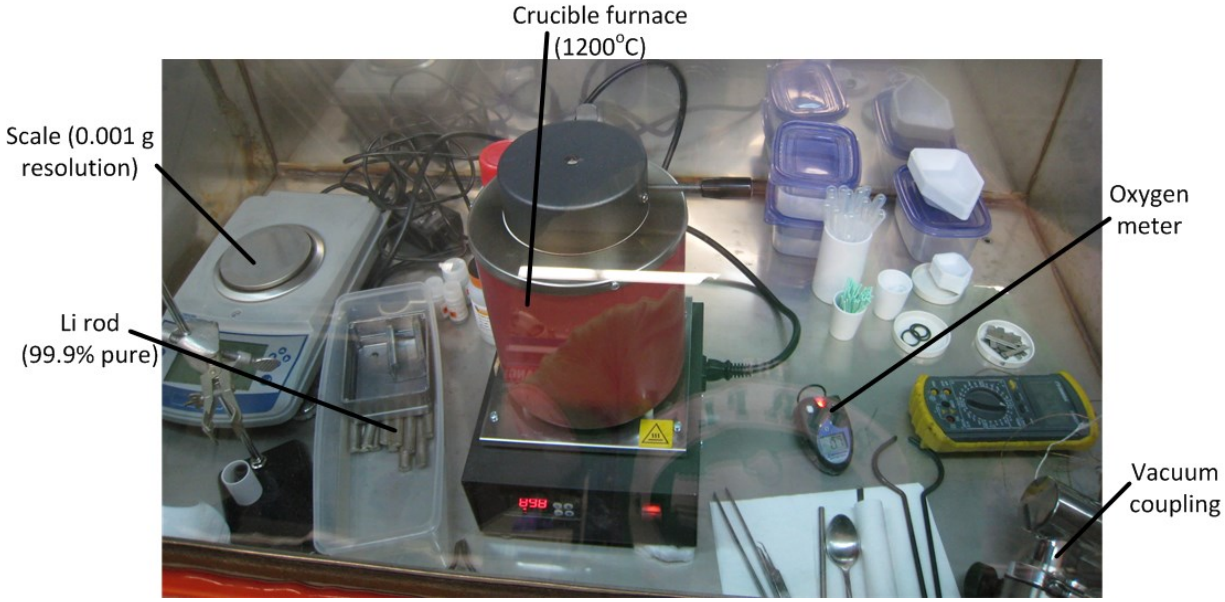

Fig. 4.29. Inside the high-temperature glove box, as seen through the viewing window.

4.6.2 Reactions in the glove box

Reactions in an open crucible furnace were carried out under argon in the custom built high-temperature glove box. The following procedures were performed to prepare LiZnP and LiZnAs.

4.6.2.1 Binary LiP and Li_3P

The goal was to form the binary alloys LiP and LiAs, and keep the 1:1 stoichiometric ratio as seen in the following equations;

$$Li + P \rightarrow LiP, \tag{4.1}$$

$$Li + As \rightarrow LiAs. \tag{4.2}$$

The reaction temperature, or alloying temperature, between both lithium and phosphorus, and lithium and arsenic, needed to be explored because phase diagrams are not readily available for these binary materials.

Everything that was needed for the experiment was loaded into the high-temperature argon glove box before the box was purged. A tantalum crucible was placed into the graphite crucible that came with the crucible furnace. The tantalum was propped in position by a series of high-temperature fiberboard rings and quartz wool. The box was purged with ultra-high purity (UHP) argon (99.999% pure) for at least 12 hours at an extremely low flow. The following day, the crucible furnace was pre-heated to 200 ^{o}C. Lithium pieces were cut from a 99.9% pure Li rod provided by ESPI Metals, and cleaned in anhydrous hexane to remove residual mineral oil. The pieces were loaded into the tantalum crucible, and the lithium began to melt (180.5 ^{o}C melting temperature [81]) as shown in Fig. 4.30. Once molten, freshly ground 99.999% phosphorus purchased from Alpha-Aesar was slowly added to the molten lithium. The temperature was increased until a reaction was observed, at 450 ^{o}C. The reaction was extremely exothermic as shown in the time sequence of Fig. 4.31. This exothermic reaction was difficult to control, and produced a lot of vapor in the process. This vapor was excess lithium surrounding the reaction area, causing a stoichiometry imbalance. This required for more lithium to be added to the reaction mixture until all the phosphorus was consumed. The addition of lithium, including an excess to compensate evaporative losses, was congruent to the stoichiometric ratio of the following reaction,

$$3\mathrm{Li} + \mathrm{P} \rightarrow \mathrm{Li_3P}\,. \tag{4.3}$$

Monolithium phosphide compound was not synthesized mainly because of the extensive amount Li vapor released during the reaction process disrupted the stoichiometry. As a result, it was lithium phosphide in its most stable state was made, trilithium phosphide, that resulted from the process. Therefore, the next step with the addition of zinc had to be performed with excess zinc to keep the desired 1:1:1 stoichiometric[11] ratios. Otherwise the reaction would result in,

[11] In this case, an excess of zinc and phosphorus would have to be added to the reaction mixture with the risk of Zn and P reacting prior to reacting with the binary, Li_3P.

$$Li_3P + Zn \not\rightarrow LiZnP. \quad (4.4)$$

Li_3As was made in an equivalent process. Reaction between the molten lithium and arsenic was also observed at 450 ^oC, however the reaction was not nearly as exothermic, and did not produce as much vapor. As a result, this method resulted in a process to make binary materials that are not commercially available, Li_3P and Li_3As. These binaries were used to further develop a method of synthesizing LiZnP.

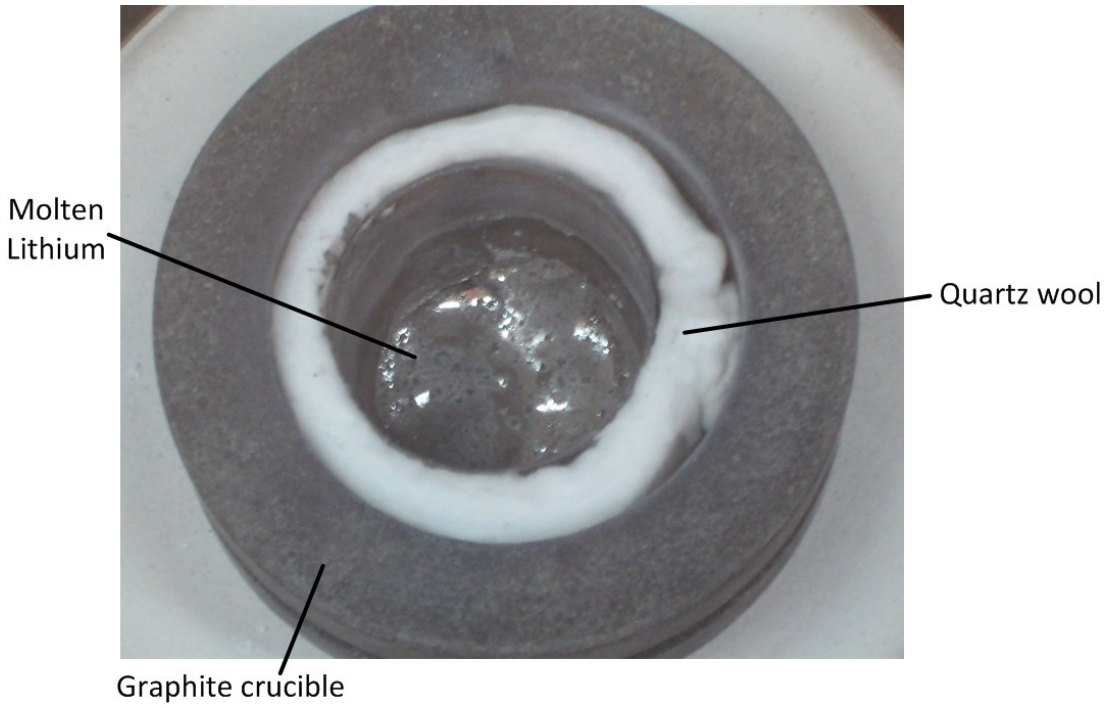

Fig. 4.30. A view of molten lithium in a tantalum crucible.

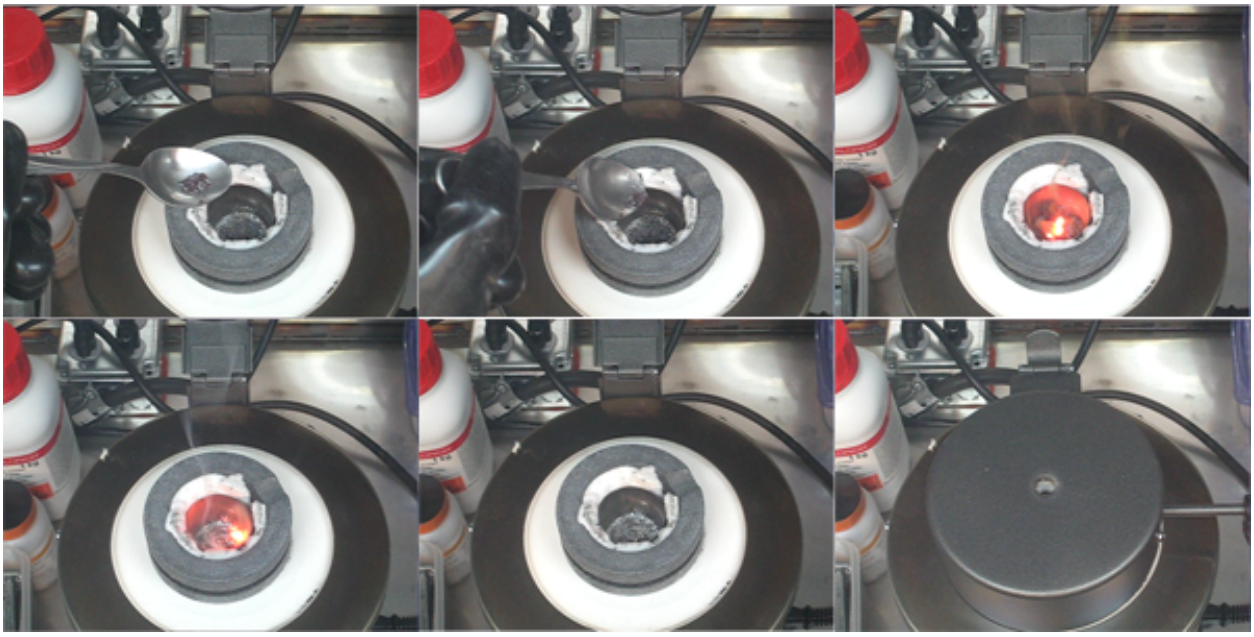

Fig. 4.31. Time sequence of the 3Li + P → Li_3P exothermic reaction between molten lithium and phosphorus.

4.6.2.2 Reacting Li_3P and Zn_3P_2

The binary materials, Li_3P and Li_3As, were synthesized in an open crucible furnace under an argon environment. Both materials where used in subsequent reactions to synthesize LiZnAs and LiZnP. The materials, zinc arsenide (Zn_3As_2) and zinc phosphide (Zn_2P_2) were both available commercially from Sigma Aldrich Corp. and Alfa Aesar. These materials are not nearly as dangerous to handle, or as difficult to synthesize, as were lithium arsenide and lithium phosphide. Zinc phosphide is an industrial chemical that is commonly found in rodenticides, such as rat poison [82].

The balanced reactions between the binary reactants are,

$$Li_3P + Zn_3P_2 \rightarrow 3LiZnP, \tag{4.5}$$

$$Li_3As + Zn_3As_2 \rightarrow 3LiZnAs. \tag{4.6}$$

Depending on the process, either Li_3P or Li_3As was increased in temperature to the upper limit of the furnace, 1150 ^oC (continuous operation), as shown in Fig. 4.32, and neither material melted within that temperature range. The material properties for these compounds are not well characterized and therefore the melting temperatures of these materials are unknown. It is difficult to assume the reaction temperature would be lower than the melting point, however zinc phosphide powder, or zinc arsenide powder, was added to its corresponding reaction mixture at an elevated temperature. The mixture of reactants was further increased in temperature to the upper limit of the furnace to observe if any reaction between the binary materials would occur, but no reaction was observed in either case.

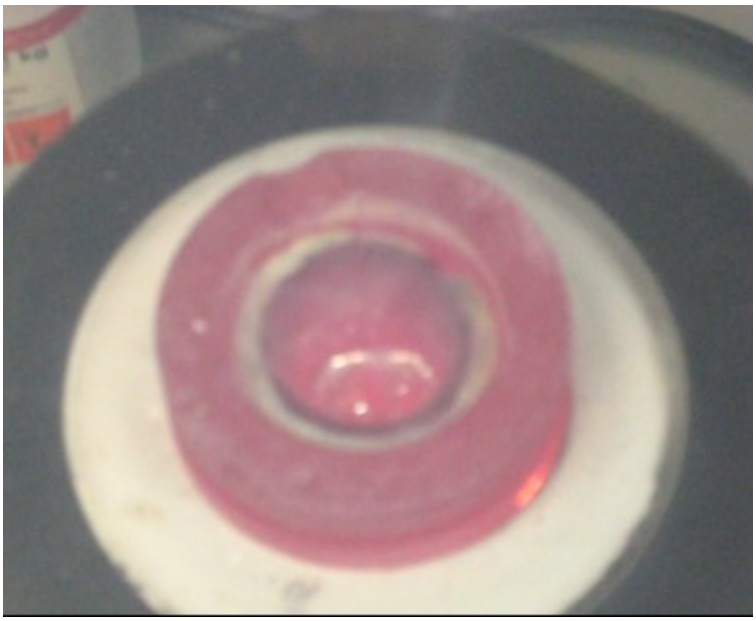

Fig. 4.32. The crucible furnace elevated in temperature at its point of continuous operation (1150 ^oC).

The melting temperature of zinc phosphide is reported at 1160 ^oC [83], and zinc arsenide is reported at 1015 ^oC [84] and 1019 ^oC [85]. Melting of these binaries was not observed at the upper limit of the crucible furnace; however, given the temperature profile across the crucible furnace, 1200 ^oC was not seen at the tantalum crucible. The furnace thermocouple was located at the bottom of the graphite lining crucible. A temperature of approximately 1050 ^oC was measured at the tantalum crucible with a thermocouple probe equipped with a type R thermocouple. Nevertheless, given what was observed with the binary formation of lithium

phosphide and lithium arsenide, the stoichiometric balance of the reaction would be more than difficult to control and manually mix at such an elevated temperature. Therefore, other paths were explored to find a repeatable and reliable process for producing the required ternary materials.

4.7 Additional Synthesis Methods

Additional methods were attempted to synthesize LiZnAs and LiZnP ternary materials. Often numerous iterations of experiments were performed, each with targeted parameters changed. The following experiments and iterations were performed with the same goal, to produce high yield and high purity ternary materials of LiZnP and LiZnAs.

4.7.1 Horizontal Flux

Reacting elements in a crucible furnace did not prove to be as stoichiometrically stable as needed, along with other problems. However, the glove box was still a useful tool for loading ampoules. To further explore the observation of ternary reaction through vapor transport as seen in the small ampoule experiment of section 4.5, a flux-type crystal growth [86] was explored. The flux method is a method of crystal growth where the components of a desired material are dissolved in a solvent. In the case of LiZnAs and LiZnP, the metals, lithium and zinc, would act as the solvent. The idea was to separate reaction components in a large evacuated horizontal ampoule. Vapor transport of the nonmetal, or metalloid, would react with the metals lithium and zinc. The metals, lithium and zinc would be placed at one end, and phosphorus, or arsenic, would be placed at the opposing end of the ampoule. An appropriate temperature gradient applied to the ampoule would allow the metalloid to transport to the metals side in the vapor state. At an appropriate reaction temperature, a reaction between the components may produce ternary material.

An ampoule 52.0 cm long, with an 38.0 mm outer diameter and 34.0 mm inner diameter (Fig. 4.33) was cleaned with the aforementioned quartz cleaning procedure. The ampoule was

loaded into the argon filled glove box, and was loaded with the metals on one side of ampoule housed in a boron nitride boat, and phosphorus, or arsenic, on the other, housed in a graphite boat. The ampoule was removed from the glove box while remaining under argon by a closed vacuum attachment, and loaded onto the vacuum sealing station. The ampoule was wrapped in a flexible heating coil and ramped up to 120 ^{o}C to insure all moisture was removed from the ampoule. The ampoule was reduced in pressure to 10^{-6} torr and sealed with an $H_2 - 0_2$ torch. The ampoule was placed into a three zone vertical furnace. The metals side of the ampoule was ramped to 530 ^{o}C at 3.0 ^{o}C/min so the alloy Li-Zn could form, and prepare for reaction. Temperature was maintained for 3 hours and the metalloid side was increased to 425 ^{o}C at 3.0 ^{o}C/min to begin vaporization of phosphorus. Temperatures were maintained for 24 hours, or until the metalloid was absent from the crucible.

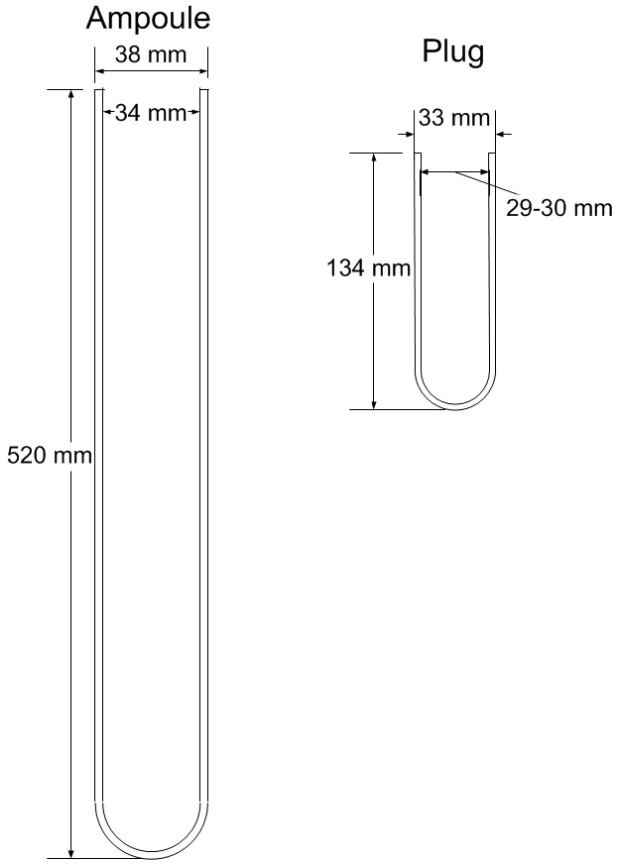

Fig. 4.33. The first horizontal ampoule design with a 2.0 mm wall thickness.

Many ampoules ruptured from this process. The exothermic reaction that occurs in the process produces a spike in pressure in the ampoule and would often cause a rupture. In addition,

the reactive nature of lithium and / or the reaction products produced in the ampoule appeared to react with the quartz containment. Thick wall ampoules (>3mm) would contain the reaction, along with a quartz sleeve over the metals / reaction side. However, in this particular experiment, the quartz sleeve still cracked and broke during the process. Fortunately, the reaction was still contained in the quartz ampoule, however, much of the reaction product (ternary material) was lost from vaporization where much of the vapor had reacted with the quartz, or condensed on the walls. Therefore reaction yields, if any, were extremely low. Other avenues of producing the material were explored, as more material was needed for bulk crystal growth of the ternary material.

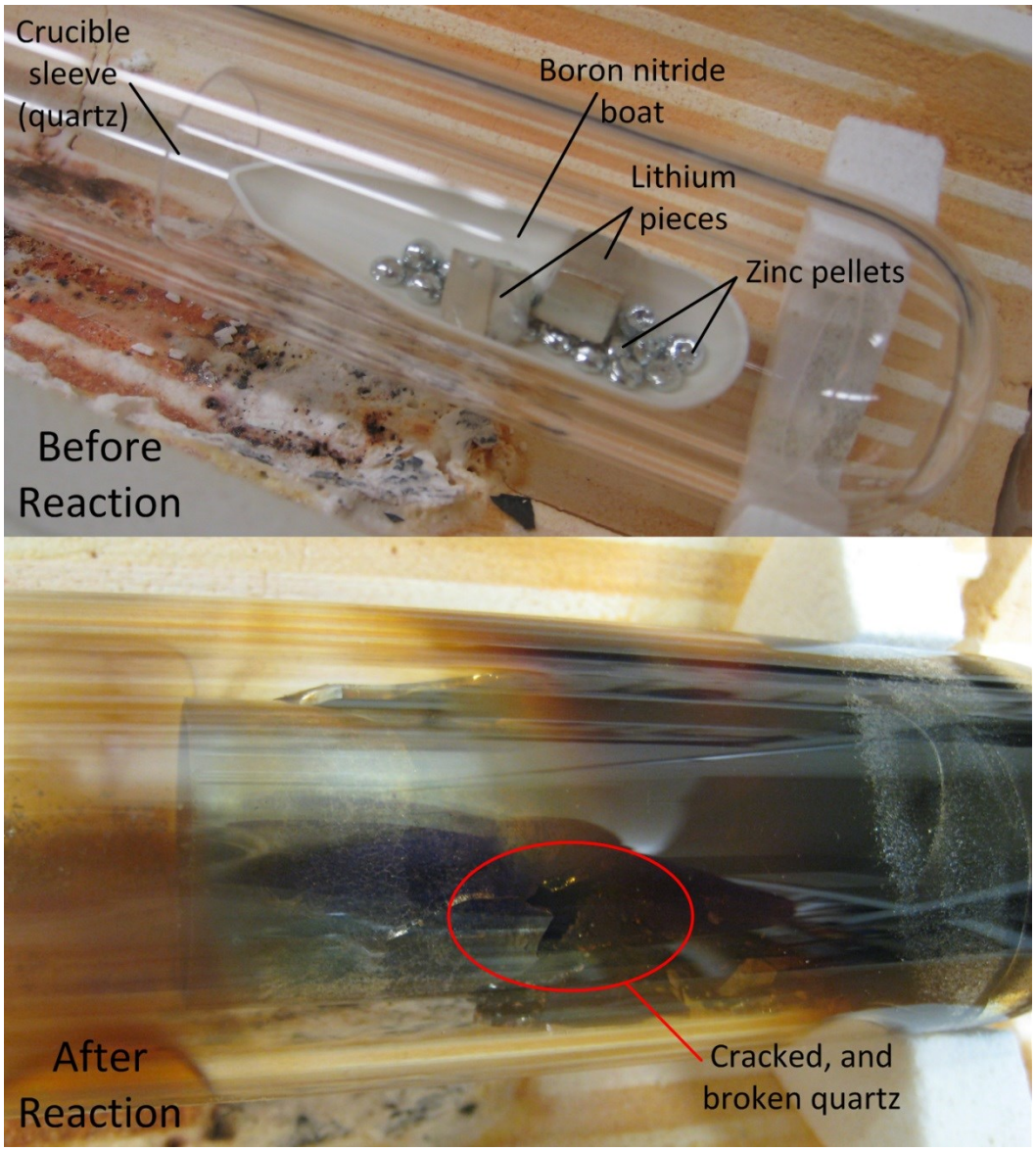

Fig. 4.34. The metals side of the horizontal ampoule before reaction (top) and after reaction (bottom).

4.7.2 Vertical Vapor Synthesis

Crystallization was observed on the top of material bulk from the small ampoule reaction described in section 4.5. This lead to the idea of trying to collect this material from the bulk contained in the crucible by a vertical vapor synthesis technique. Despite the low yields of this process, the material may have higher purity than the bulk material synthesized in the crucible,

where binaries and unreacted material may remain. Over many processes, enough material may have been accumulated to grow a single crystal of the material.

An ampoule was designed with the crucible at the bottom of the ampoule, and notches in the side, above the ampoule as shown in Fig. 4.35.a. These notches allowed for a cone-shaped material insert to sit comfortably above the reacted material, followed by a plug. This cone-shaped material was designed to act as a cold finger to allow material to sublime onto. Then, upon harvest, this cone could easily be removed from the ampoule, and the sublimate material removed.

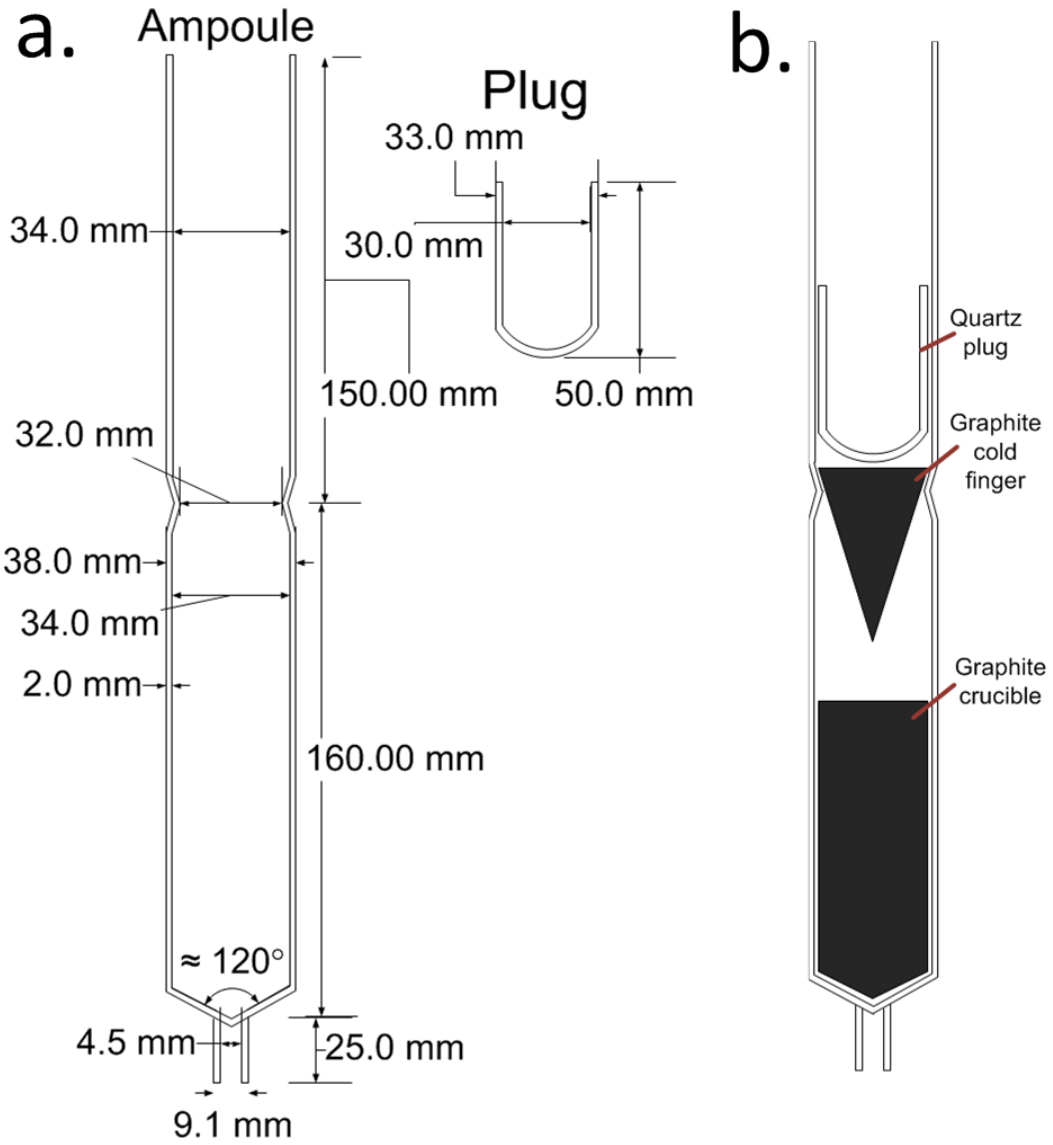

Fig. 4.35. a. The vertical vapor transport ampoule design. b. The vertical ampoule profile with a graphite cold finger.

Equimolar portions of reactants, lithium, zinc and phosphorus, were added to a graphite crucible while under an argon environment. Lithium was cleaned of residual mineral oil in an anhydrous hexane bath. Phosphorus was crushed into a fine powder, and dried over a hot plate to remove residual moisture. The graphite crucible was loaded into the custom quartz ampoule, and followed with a graphite cone (cold finger) pointed downward toward the top of the crucible as shown in Fig. 4.35.b. A plug was loaded on top of the graphite cold finger, and the loaded ampoule was removed from the glove box while remaining under argon by a valve coupled to the ampoule. The ampoule was loaded onto an ampoule sealing station where the ampoule was baked out of residual moisture, evacuated to 10^{-6} torr, and sealed with a H_2-O_2 torch. The ampoule was loaded into a vertical tube furnace where the coils could be manually adjusted to raise or lower the furnace across the ampoule. The furnace was adjusted so the graphite cold finger was outside of the coils, in ambient temperature as shown in Fig. 4.36.a. The furnace was ramped in temperature up to 550 ^{o}C at 1 ^{o}C/min, and the furnace was held at temperature for >24 hours. A dull black material was observed on the cold finger after the 24 hours. The temperature was increased to 700 ^{o}C so promote material transfer to the cold finger. More material formed on the graphite cold finger, however, the material color was remained dull, and it did not appear to have the luster as observed with the small ampoule synthesis processes, as explained in section 4.4. No material was harvested from this process.

This technique was revisited with a slightly different synthesis process. The ampoule was loaded with the same quantity of starting materials along with the same order of ampoule setup as shown in Fig. 4.35.b. However, for the following iteration, the entire ampoule was loaded into the furnace with the coils surrounding the entire quartz containment as shown in Fig. 4.36.b. The idea was to allow for the reaction to commence, and then move the furnace down so the cold finger would be exposed to ambient temperature. The furnace was ramped in temperature to 550 ^{o}C at 1 ^{o}C/min, and was held at temperature for approximately 24 hours. The furnace was moved down to expose the cold finger to ambient temperature, and very little material was observed on the cold finger at this point after the reaction. The furnace was ramped to 700 ^{o}C at 1 ^{o}C/min and the cold finger was observed over the following 5 days. More material was transferred to the cold finger over the five days, however the material looked as it did in the previous experiment. The material was a black, dull color with no indication that desired ternary material was

transferred to the cold finger. No further investigation was performed with the vertical vapor synthesis technique.

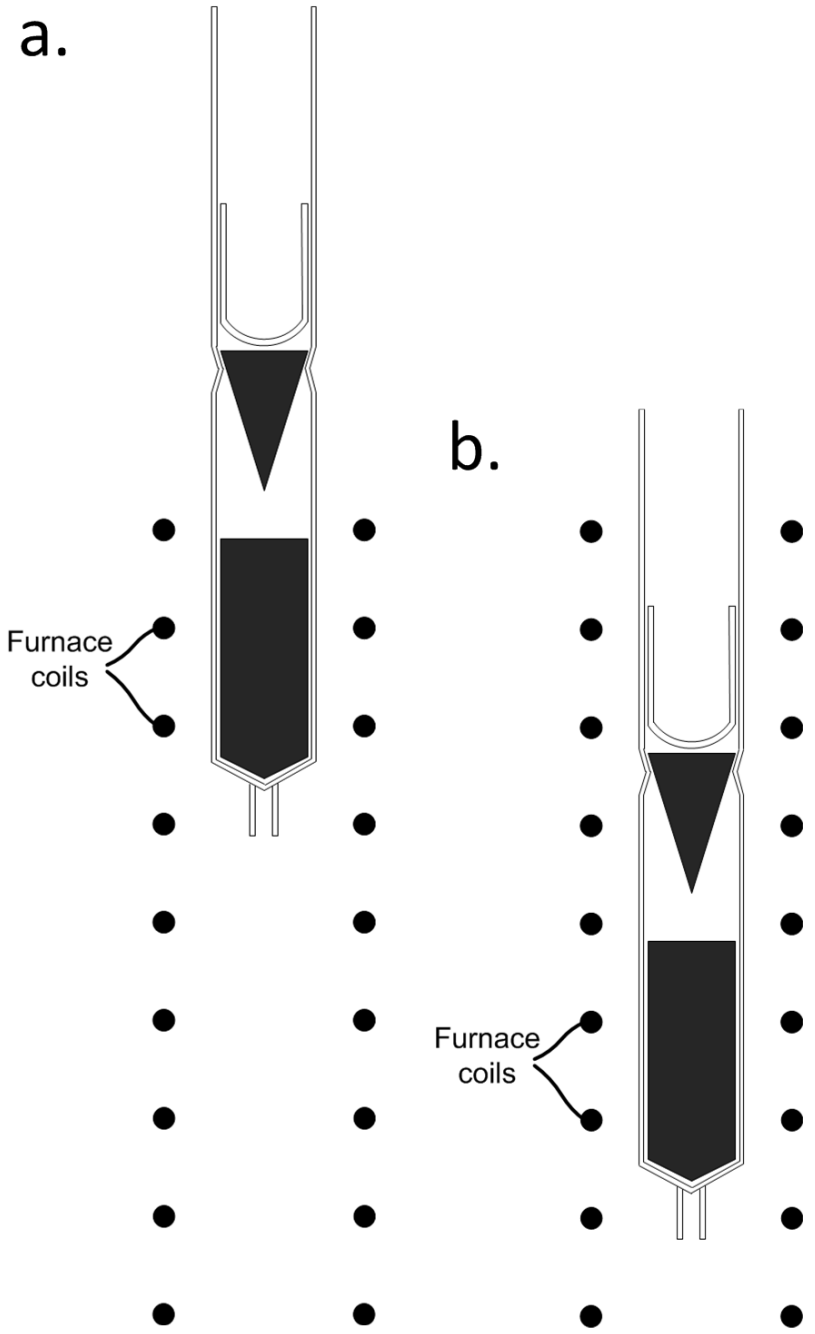

Fig. 4.36. a. Case 1 for the vertical vapor experiments, where the cold finger was outside of the furnace for the reaction process. b. Case 2 for the vertical vapor experiments, where the cold finger, and all the vacuum sealed area was contained in the furnace during reaction.

4.8 Revisit of the vacuum evacuated sealed ampoule method

Techniques were described in the literature for synthesizing ternary material, as explained in Chapter 2 [51-58, 60, 61] of which described processes containing the reactants in an evacuated, and sealed, crucible lined ampoule. An iteration of technique was attempted with marginal success (section 4.4), but was not completely characterized before moving to over methods, which also resulted with marginal success. Revisiting the evacuated and sealed ampoule technique fortunately resulted in the most success, and a final version of the process will be discussed in chapter 5.

4.8.1 Reactions with binaries; Li_3P and Zn_3P_2, Li_3As and Zn_3As_2

The binary reaction products produced from the open crucible method were used to synthesize LiZnP and LiZnAs in evacuated, sealed ampoules. Equimolar portions of Li_3P and Zn_3P_2 per the equation,

$$Li_3P + Zn_3P_2 \rightarrow LiZnP, \tag{4.7}$$

were loaded into a graphite crucible designed as shown in Fig. 4.37. The crucible was loaded into a quartz ampoule similar to the ampoule shown in Fig. 4.16 with a plug loaded dirrectly on top of the graphite crucible. All handling was performed under argon, and during removal from the argon atmosphere, the ampoule remained under vacuum by a coupled valve. The ampoule was loaded onto a vacuum sealing station, evacuated to 9×10^{-5} torr, and sealed with a H_2-O_2 torch.

The ampoule was loaded into the custom built furnace at discussed in section 4.1. The furnace was ramped in temperture to 500 ^oC, slightly above the temperature that was observed in reaction between lithium and phosphorus, and held for at least 24 hours. The furnace temperature was lowered to room temperature so the ampoule could be evaluated. No sign of a reaction was observed; the powder was still loose in the crucible, and no discoloring of the ampoule wall occurred. The ampoule was placed back into the furnace and ramped to 700 ^oC, held for at least

24 hours, and lowered back to room temperature. Again, the ampoule showed no sign of reaction between the reactants. This process was repeated to observe if a reaction temperture could be determined within the temperature limits of the quartz containment. Unfortunently, the quartz vessel ruptured between 1100 ^{o}C and 1200 ^{o}C. It is known that quartz softens beyond 1100 ^{o}C, and can be safe for containment under vacuum up to 1200 ^{o}C. Reaction may have occurred between the reactants, or the quartz may have been compromised. An example of quartz softening at tempertures beyond 1100 ^{o}C is shown in Fig. 4.38. More iterations of this process were performed for LiZnP and LiZnAs. All synthesis attempts resulted in no reaction, or ruptured ampoules. This lead to the conclusion that binary to binary reactions were not possible within the temperture contraints of quartz.

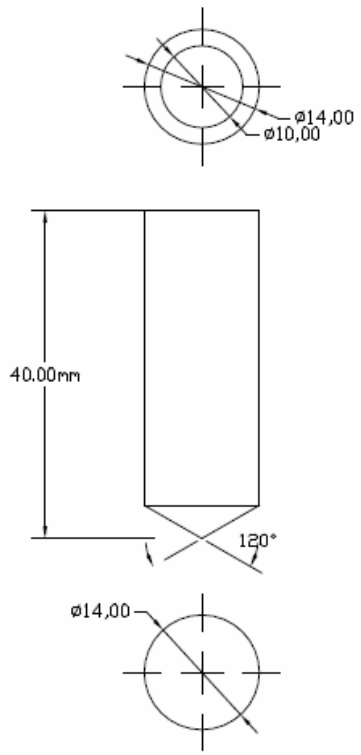

Fig. 4.37. The crucible design for a vertically oriented, evacuated and sealed ampoule synthesis

Fig. 4.38. An example of a vacuum sealed ampoule, containing a high vapor pressure material that was ramped in temperature to >1100 ^{o}C.

4.8.2 Reactions with elemental reactants

Reactions between binary reactants showed marginal results which ultimately directed the investigation to another reaction process that required vacuum sealed ampoules. Much of the literature, as described in Chapter 2, described processes that reacted elemental components to form the ternary component. A similar process was attempted as explained in section 4.4 and also produced marginal results. The process was revised, and LiZnAs was reacted instead of LiZnP, along with some modifications to the recipe. Modifications to the recipe, crucible material, handling gas, ampoule evacuation and reactant mixing were all necessary to produce a high-quality product, as will be detailed in Section 5.1.

Equimolar portions of the reactants, 99.99% zinc powder (Sigma-Aldrich), 99.99% arsenic powder (Alpha-Aesar), and 99.9% lithium rod (ESPI metals) were used in the synthesis process. All handling took place under argon (<1% oxygen as measured on a calibrated oxygen meter). Lithium was cleaned of all oxidized portions by removing all of the edges, so that only the shiny lithium surface was observed on all sides. Pieces approximately 2.0 cm^3 in size were cleaned in anhydrous hexane to remove any residual oil (lithium rod was stored in mineral oil within the argon environment). Phosphorus was crushed into a fine powder with a mortar and

pestle, and dried over a hot plate within the glove box. The following equimolar amounts of reactants were added to a graphite crucible: 0.157 g Li, 1.433 g As, and 1.110 g Zn. An excess of at least 4% lithium was added to the mixture to account for evaporative losses. The graphite crucible was loaded into a quartz ampoule with a plug. The ampoule was removed from the glove box with a temporary vacuum attachment attached to the ampoule to maintain the argon atmosphere in the ampoule. The ampoule was attached to the vacuum sealing station shown in Fig. 4.18, and was evacuated to approximately 10^{-6} torr, and baked of residual moisture at 150 ^{o}C for 5 hours. The ampoule was then vacuum sealed with an O_2-H_2 torch. The sealed ampoule was loaded into a vertical Thermolyne tube furnace equipped with a Eurotherm 2216e temperature controller. The furnace was ramped to 560 ^{o}C at 3.0 ^{o}C/min, and the furnace was held at temperature for 48 hours. The furnace was then ramped to 660 ^{o}C at 3.0 ^{o}C/min to anneal, and promote crystallization. The process was similar to a process outlined by Bacewicz and Ciszek [60] with additional material preparation steps, and modifications to the synthesis recipe. The resulting ampoule is shown in Fig. 4.39. Crystallization was clearly observed on the outside of the ampoule.

Fig. 4.39. The resulting LiZnAs reaction / synthesis process ampoule. Reaction with the quartz is seen by the dark coloration on the quartz wall, and crystallization on the outside of the ampoule was observed.

The ampoule was sliced open with a silicon carbide blade saw, and the ampoule was quickly evacuated in the antechamber of an argon glove box. Inside the argon glovebox, the

material was extracted from inside the crucible as shown in Fig. 4.40. Large black metallic, lustrous crystalline pieces up to about 2.5 mm in diameter were observed.

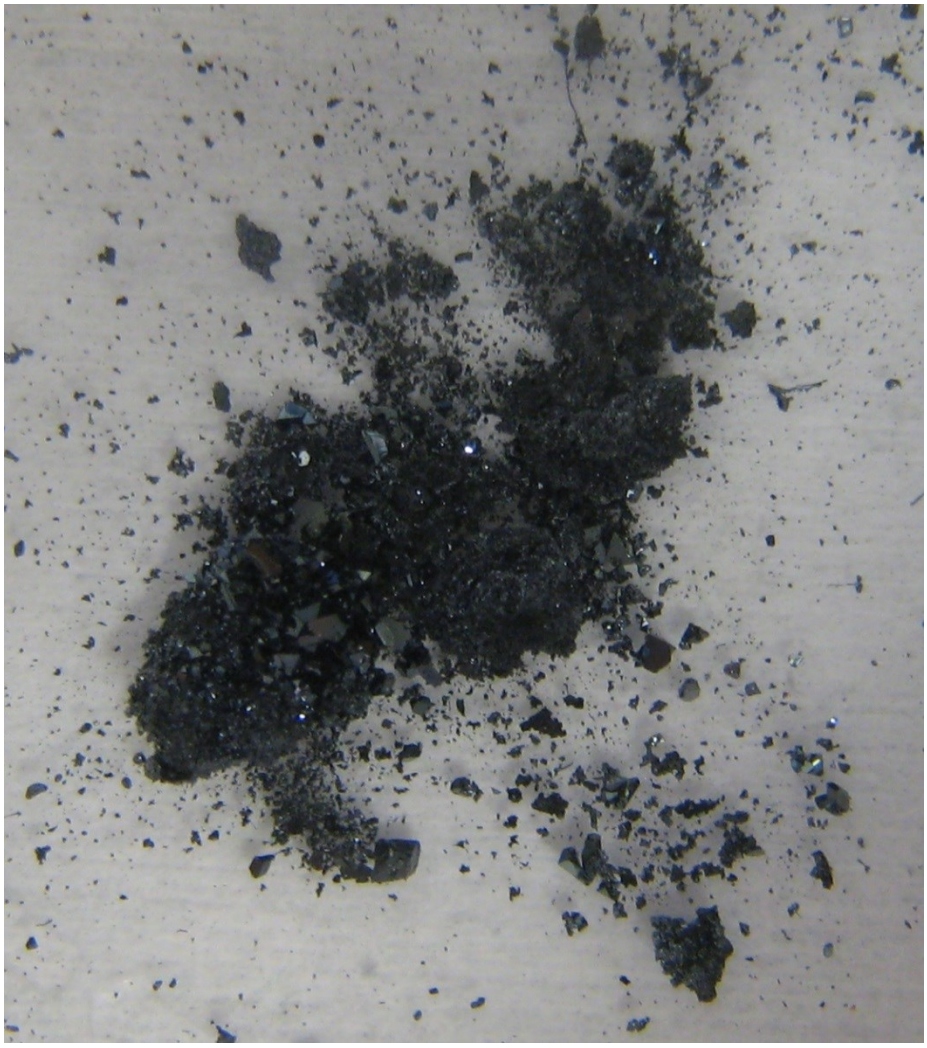

Fig. 4.40. The resulting LiZnAs material from inside the crucible.

This synthesis method was first apparent ternary synthesis success. From this point, the process was refined to what was used to produce an abundance of material that was further purified, and grown into bulk ingots for device processing.

Chapter 5 : TERNARY COMPOUND SYNTHESIS AND BULK CRYSTAL GROWTH

It has been a long time ago since I worked on that awful stuff. Cracking of quartz ampoules was quite frequent….

- ***Dr. Rajmund Bacewicz***

Nov. 12, 2010

The aforementioned preliminary embodiments lead to the following procedure that was relatively repeatable. The process also produced material that was identified as the desired ternary compound was and used to fabricate devices. The synthesis steps and parameters were optimized to achieve a high-yield that was reliable and repeatable. The bulk crystal growth was performed in high-temperature tantalum ampoules/vessels instead of quartz containments because the quartz would soften and rupture before the ternary material would melt. Described in the following Chapter are the LiZnAs and LiZnP synthesis processes, the purification processes, and the bulk crystallization processes to produce ingots that were large enough to fabricate into devices.

5.1 Ternary Synthesis and Characterization (LiZnP and LiZnAs)

After numerous attempts to synthesize LiZnP and LiZnAs, a process in crucible-lined, quartz ampoules resulted in a desirable ternary product, as described in section 4.8.2. That process evolved into the following procedure, a process with the highest yields and highest material quality observed throughout this work.

5.1.1 LiZnP and LiZnAs synthesis process

LiZnP and LiZnAs multicrystalline samples were synthesized from elemental material, 99.995% zinc powder (Sigma-Aldrich), 99.999% phosphorus chunk (Alpha-Aesar), 99.999% arsenic chunk (Alpha-Aesar), and 99.9% lithium rod (ESPI metals). The elemental materials were loaded into either pyrolitic boron nitride (pBN), tantalum, or graphite crucibles, all under an argon atmosphere. Phosphorus pieces were dried in an argon environment over a hot plate in a tantalum crucible, and then crushed into a fine powder with a clean mortar and pestle. Lithium pieces approximately 2 mm thick were cut from the rod, and the sides where oxidation had appeared were also removed. The remaining large pieces were sectioned into 1 – 3 mm^3 samples, and cleaned of residual oil in anhydrous hexane. Crucibles were cleaned of oil and other contaminants by ultra-sonic vibration in hexane, trichloroethylene, acetone, and isopropanol separately. Boron nitride porosity is minimal compared to what is observed with graphite materials, where the porosity is in the range of 9 – 12% depending on the material grade [87]. Lithium becomes very reactive once molten, and can react with graphite to make lithium carbides. Graphite has historically been used in the synthesis process [60], although a more repeatable process was found by using either a pyrolitic boron nitride crucible, or a sealed tantalum crucible under argon. Lithium (40% atom weight) and zinc (60% atom weight) were weighed and added to a crucible as understood from the Li-Zn phase diagram [88]. An equimolar portion of phosphorus or arsenic was added to the Li and Zn mixture. An excess of 3-5% lithium was included to account for evaporative loses during the reaction process. The crucible, along with a quartz plug, were loaded into a quartz ampoule and transferred to a vacuum station while remaining under argon by sealing the chamber with a vacuum valve attachment. The ampoule was evacuated to approximately 9.0 x 10^{-6} torr, staged by beginning with a roughing pump vacuum and followed by an Alcatel ATP 80 turbo pump evacuation. The vapor pressure of phosphorus limits the evacuation pressure that is achievable. It is known that after heating to only 90 ^{o}C, phosphorus vapor pressure rises to approximately 9.9 x 10^{-6} torr [89]. The ampoule was sealed using a hydrogen / oxygen torch.

The sealed ampoule was placed into a rotation-stage furnace system, where the ampoule was rotated at approximately 0.25 rotations per second at approximately a 45^{o} angle to promote mixing. The furnace was ramped upwards at 1 ^{o}C per minute to 200 ^{o}C while the ampoule was

rotated to form the alloy Li-Zn [88] and held for 24 hours. Afterwards, the rotation was stopped, and the furnace was ramped upwards at 0.5 ^{o}C per minute to 560 ^{o}C to promote ternary reaction[12]. The furnace was held for 48 hours, and then ramped upwards to 720 ^{o}C or 660 ^{o}C for LiZnP or LiZnAs, respectively in order to anneal and promote crystallization. The furnace temperature was held at the proper temperature for 48 hours. The furnace was then ramped downwards to room temperature at 1.0 ^{o}C per minute. The ampoule was removed from the furnace, and placed in an argon glove box where the material could be extracted and stored. Typical reactions yielded approximately 2.0 g of material. LiZnAs synthesis reactions were scaled up to yield approximately 6.0 g of LiZnAs in a 45.58 cm^3 internal volume crucible, as shown in Fig. 5.2, although LiZnP reactions had to remain in much smaller batches (2.0 g) due to problems with ampoule cracking that was observed with larger batches.

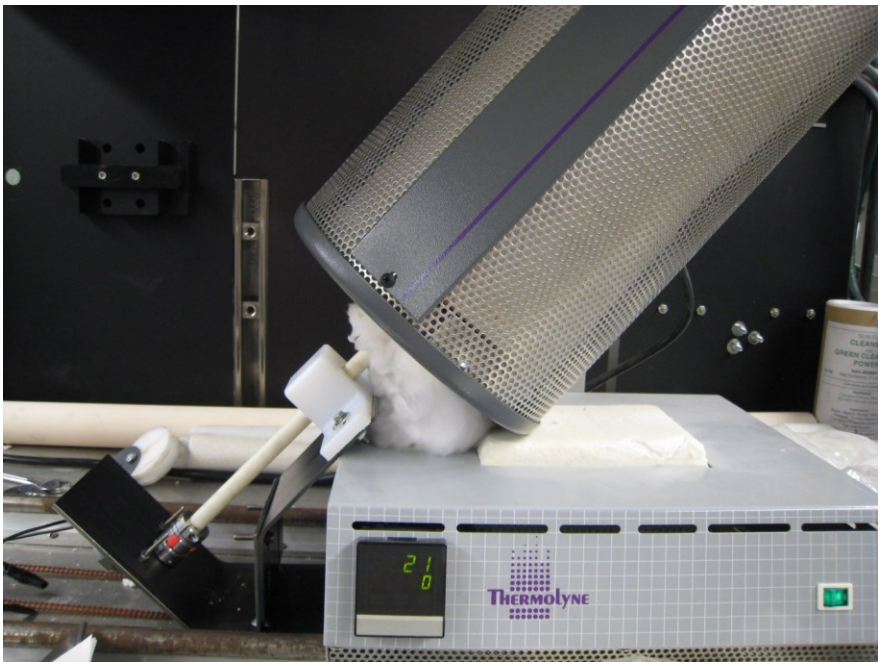

Fig. 5.1. The custom built tilt rotation stage, equipped with a Thermolyne tube furnace. The rotation stage was designed with a 110 VAC stepper motor with a constant rotation of 0.25 rotations / second. The stepper motor was coupled to an alumina tube. Ampoules were designed with a nipple that fit comfortably into the alumina tube, allowing it to be rotated and kept at a constant angle.

[12] The ampoule was no longer rotated after the initial Li-Zn formation stage. Continuous rotation during higher-temperature stages in the recipe would often result in ampoule cracking.

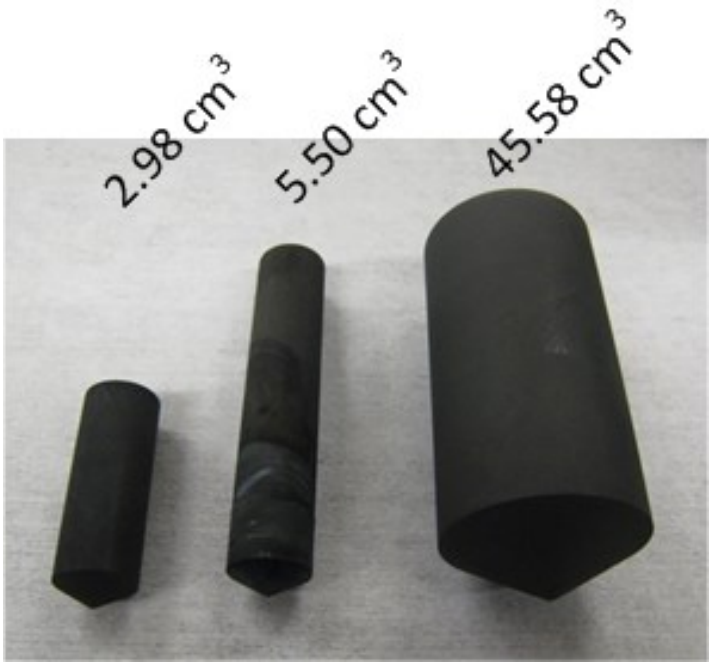

Fig. 5.2. The scale-up process crucibles for synthesizing ternary material (graphite shown here). The smallest crucible on the left was used primarily for initial trials. As the recipe was developed, the amount of material synthesized was scaled up. LiZnP was limited to the 5.50 cm^3 size due to overpressure issues in the ampoule. LiZnAs was scaled up to the 45.58 cm^3 crucible without significant problems.

5.1.2 LiZnP and LiZnAs synthesis characterization

Powder x-ray diffraction phase identification scans were collected for a LiZnAs sample and LiZnP sample. The $A^{I}B^{II}C^{V}$ material was crushed into a fine powder under argon, and loaded into a zero-background sample holder with a layer of Biaxially-oriented polyethylene terephthalate (BoPET), brand named Mylar®, over the top of the material, and sealed for protection from moisture in the air. Each scan was collected on a Bruker D8 ADVANCE diffractometer equipped with Cu radiation using a Bragg Brentano geometry, and was compared to experimental data cited in the International Center for Diffraction Data (ICDD) database [51, 60, 90]. Additionally, the phase identification patterns were calculated for both LiZnP and LiZnAs with PowderCell 2.4 [71] with experimental lattice constants and space groups determined by Bacewicz [60], as shown in Fig. 3.8 in Chapter 3. These results were compared with the experimental phase scans.

Small facets were cleaved from some of the large chunks that were produced in the synthesis process. These samples ranged in size up to approximately 1.5 mm in thickness and 7.5 mm in diameter. Shown in Fig. 5.3 is one LiZnAs sample sandwiched between sheets of Mylar®. Samples were polished under argon with silicon carbide polishing paper in stages up to a final polish with P4000 grit paper. The samples were characterized for evidence of crystalline ordering by using a Bruker D2 CRYSO Energy-Dispersive XRD system. Following that, the crystal orientation of the samples was determined using the same instrument. Once the family of planes and corresponding *d* spacing was determined, the crystalline perfection of the samples were examined by conducting rocking curves on a high resolution Bruker D8 DISCOVER DAVINCI Diffractometer, equipped with a four-bounce monochromator (beam divergence ~ 0.004^{o}).

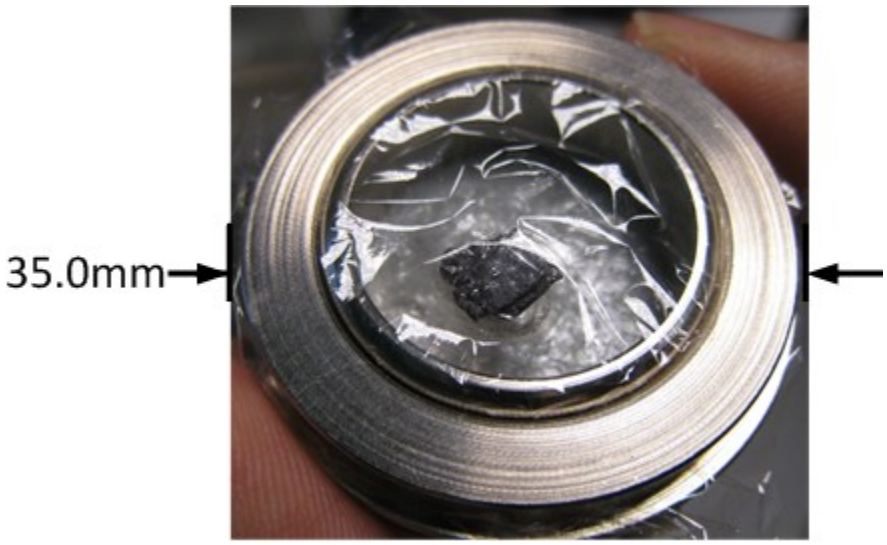

Fig. 5.3. A LiZnAs facet prepared for XRD measurements in a sample holder between two Mylar® films.

The exothermic reaction that results from synthesizing Nowotny-Juza compounds stresses the quartz containment, often resulting in cracking and a loss of material. By producing the alloy, Li-Zn, before final reaction, a much more stable reaction was achieved, resulting in a much higher harvesting yield, and where cracking or exploding ampoule issues were reduced. Shown in Fig. 5.4 are the ampoules after reactions for cases of cracking and non-cracking. Cracking usually forms at the bottom of the ampoule, and resulting in oxidized lithium and crucible material.

Fig. 5.4. Example of ampoule cracking (circled portion) (top), and example of a successful ternary material synthesis using a graphite crucible (bottom).

From a successful reaction, the resulting synthesized material can be seen in Fig. 5.5, which produced powder and chunks usually up to approximately 1.0 mm across, and in some cases, facets that were quite large, up to 7.5 mm in diameter. Three samples, one LiZnP and two LiZnAs, were sent to *Galbraith Laboratories Inc*. for inductively coupled plasma optical emission spectroscopy analysis (ICP-OES) to examine elemental concentration after synthesis to provide an indication of congruent reaction. The ICP-OES process was performed as described by the EPA, Method 6010b [91]. The ICP-OES results are shown in Table 1. The *analysis* column is the constituent element measured, where the resulting spectroscopy is presented as weight percent. Each weight percent was divided by the element molar mass to find the elemental molar mass concentration within the sample. Analysis of each constituent element is associated with a 10% relative standard error as stated by Galbraith Laboratories Inc.

Nowotny-Juza compounds were synthesized into powder and large pieces, and ICP-OES confirmed the materials can be synthesized into a 1-1-1 ratio. As seen in Table 5.1, the total weight percent of each sample equaled approximately 100% within the 10% standard error that is associated with each elemental measurement. The sample with the most deviation from a total of

100% was LiZnAs (1) with 78.23%. Additionally, the elemental molar concentration for the LiZnAs (1) sample also deviated most between constituent elements out of the three samples tested. These deviations raised concerns that some synthesis reactions may result in incongruent reaction, and contain more unreacted elemental material, or binary materials, which indicates that not each ternary reaction produces a consistent 1-1-1 stoichiometric ratio of constituent elements.

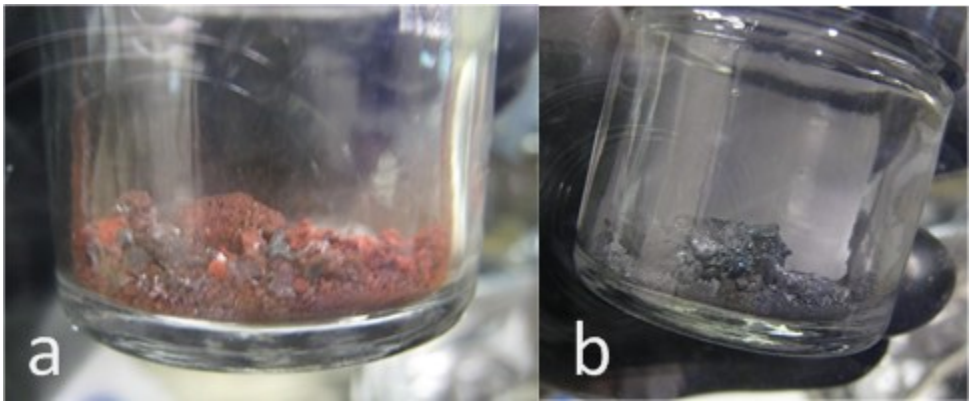

Fig. 5.5. Nowotny-Juza synthesized material. ***a****. LiZnP red metallic power and chunks.* ***b****. LiZnAs black metallic powder and chunks.*

Table 5.1. The ICP-OES results from Galbraith Laboratories Inc.

Sample: LinZnP		
Analysis	Result (%)	Molar Concentration (mol/vol)
P	31.3	0.010
Li	7.47	0.010
Zn	64.6	0.010
Total	103.37	
Sample: LiZnAs (1)		
Analysis	Result (%)	Molar Concentration (mol/Vol)
As	41.3	0.0055
Li	4.83	0.0070
Zn	32.1	0.0049
Total	78.23	
Sample: LiZnAs (2)		
Analysis	Result (%)	Molar Concentration (mol/Vol)
As	50.7	0.0068
Li	5.01	0.0072
Zn	41.5	0.0063
Total	97.21	

Numerous powder x-ray diffraction phase identification scans were collected for LiZnP and LiZnAs powders on a Bruker AXS D8 ADVANCE with Cu radiation, using the Bragg Brentano geometry. Examples of the collected patterns can be seen for LiZnAs and LiZnP in Fig. 5.6 and Fig. 5.7, respectively. Both patterns matched well with what was reported by Nowotny and Bacewicz cited in the International Center for Diffraction Data (ICDD) [51, 60]. Lattice constants were determined using TOPAS (Bruker AXS Inc). The Whole Powder Pattern decomposition approach was used. Refinement of the experimental phase identification data yielded lattice constants of 5.751 ± 0.001 Å and 5.939 ± 0.002 Å for LiZnP and LiZnAs, respectively.

Powder XRD phase identification scans also confirmed the formation of cubic $A^{I}B^{II}C^{V}$ materials for both LiZnAs and LiZnP, where the correlation between the measured and archival

peaks clearly show that both materials were formed. The reflections shown in Fig. 5.6 and Fig. 5.7 matched well with theoretical pattern calculated using PowderCell 2.4, as shown in Fig. 3.8, and also matched with the experimental patterns included in the ICDD powder diffraction database [51, 60]. Not all peaks can be identified in Fig. 5.6 and Fig. 5.7, which may indicate contamination in the synthesized powders. One indication of contamination in Fig. 5.6 is observed where peaks match with profiles from lithium oxide, shown in the vertical dashed lines. Other impurity peaks are consistent with profiles from lithium carbonate, lithium arsenide, lithium phosphide, and lithium hydroxide. This contamination likely occurred during the handling and measurement process, given the material is hygroscopic. In addition, the lithium rod that was used in the synthesis process provided by ESPI metals had a 99.9% purity. From the trace element analysis provided by the supplier, 99.9% lithium contains traces of elements including calcium (100pm), iron (10ppm), and copper (< 30 ppm) [92] which were observed in the EDXRD spectra shown in Fig. 5.8. Additionally, with the current synthesis method, it is suspected that unreacted elemental material, possible incomplete binary materials, or other undesired compounds from possible reaction with the crucible lining material, may be present in the reaction products; therefore purification of these synthesized materials must be performed for the material grade required for semiconductor devices.

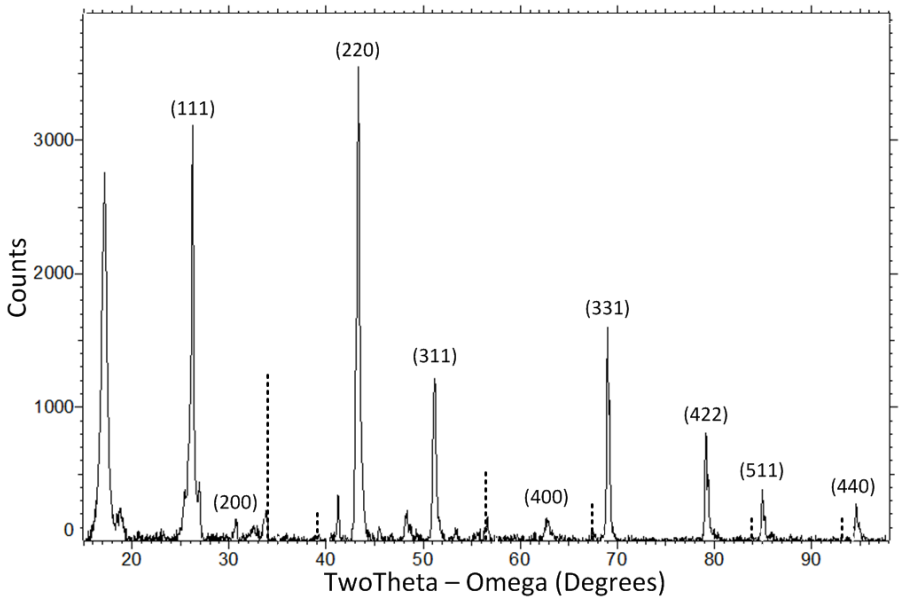

Fig. 5.6. LiZnAs phase identification scan collected on a Bruker AXS *D8 ADVANCE equipped with Cu characteristic x-ray radiation. The dashed vertical lines are experimental data of cubic LiO [90].*

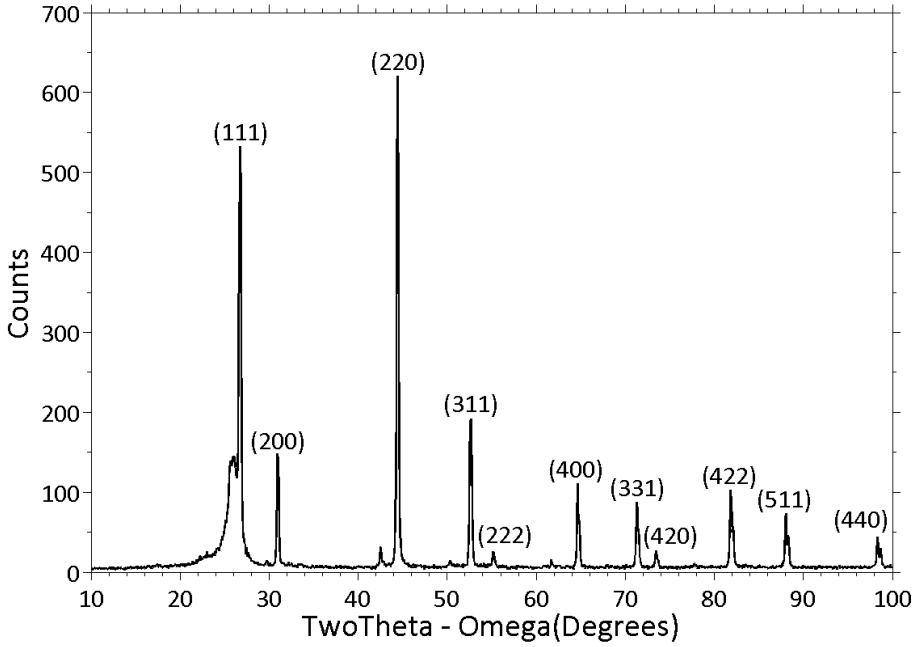

Fig. 5.7. LiZnP phase identification scan collected on a Bruker AXS *D8 ADVANCE equipped with Cu characteristic x-ray radiation.*

Cleaved facet sample crystals were analyzed for evidence of crystallinity using a Bruker AXS D2 CRYSO energy dispersive x-ray diffractometer (EDXRD). The instrument scans the sample at multiple ϕ angles, where a family of planes can be identified through a series of calculations [93]. For a particular LiZnAs sample, the {111} family of planes were identified as seen in Fig. 5.8, where each spectrum is a measurement at a different angle of phi across 360 degrees. A *d* spacing of 1.755 Å was determined from the location (energy) of these peaks, and the orientation and lattice constant of the sample. Characteristic x-rays are also collected by this method, thereby, providing an indication of impurities in the sample. Characteristic x-rays from calcium, copper and iron were also observed from the LiZnAs sample.

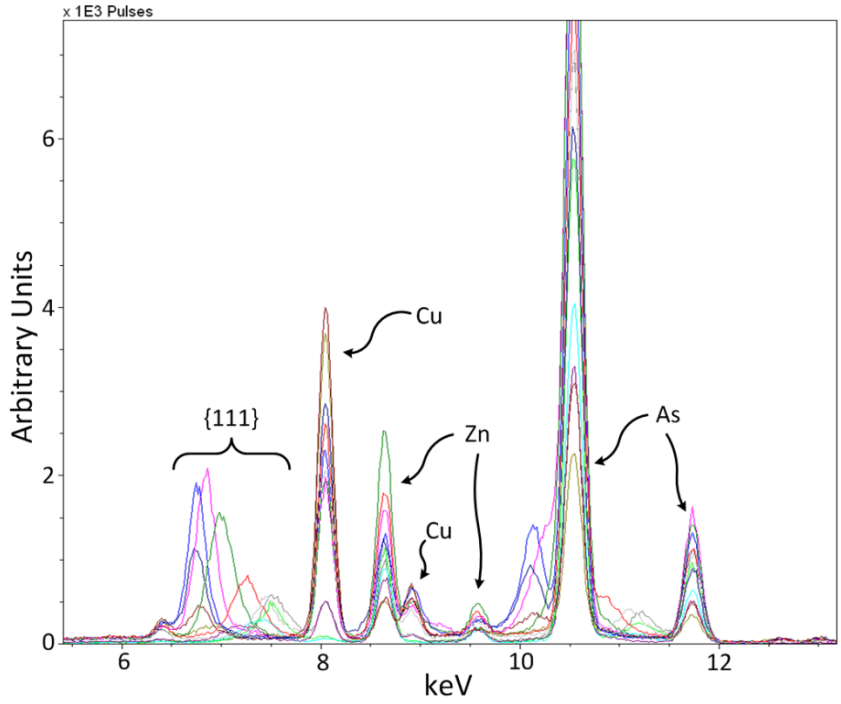

Fig. 5.8. Energy dispersive XRD scan of a single crystal sample of LiZnAs. Apparent iron, calcium and copper impurities were found in this specific sample as specified by the characteristic x-ray peaks. Other characteristic x-ray peaks for arsenic and zinc were located as labeled. Notice the Laue peaks of the {111} planes between 6.5 and 8.0 keV, which were used to verify the orientation of the sample.

The crystallinity of the {111} family of planes was examined by carrying out rocking curve measurements using a 4 bounce monochromator, with a line beam 12.0 mm tall by 9.5mm width (slit size). The full width of half maximum of the (111) atomic plane was determined to be

0.097^{o} as seen in Fig. 5.9. A rocking curve performed on a single crystal silicon standard (from Bruker AXS) yielded a FWHM of 0.004 degrees (14.4 arc seconds) for the Si (111) reflection, which indicates that the rocking curve FWHM broadening of the LiZnAs sample is primarily coming from the mosaicity of the sample. Finally, a phase identification scan was collected on the sample shown in Fig. 5.10. The (111) LiZnAs reflection is quite prominent at approximately 25.5^{o} 2θ and in addition there is indication of the (222) LiZnAs reflection at approximately 52^{o} 2θ. Samples were prepared under argon, and sealed using an x-ray transparent Mylar® film, in order to protect the samples from degradation during the measurement process.

Large single crystal facets grown in the synthesis process did exhibit in- plane crystalline ordering. A rocking curve collected on a LiZnAs sample of (111) planes is shown in Fig. 5.9. However, the rocking curve peak profile is not Gaussian and is indicative of other domains/facets in the sample. Evidence of other domains was also seen from the phase identification scan shown in Fig. 5.10. The most prominent peaks, at 25.5^{o} and 52^{o}, indicate the presence of the (111) and (222) LiZnAs reflections, as expected. However, extremely low intensity peaks are present at approximately 38.5^{o} and 44.7^{o}, which indicate the presence of other domains in the particular sample.

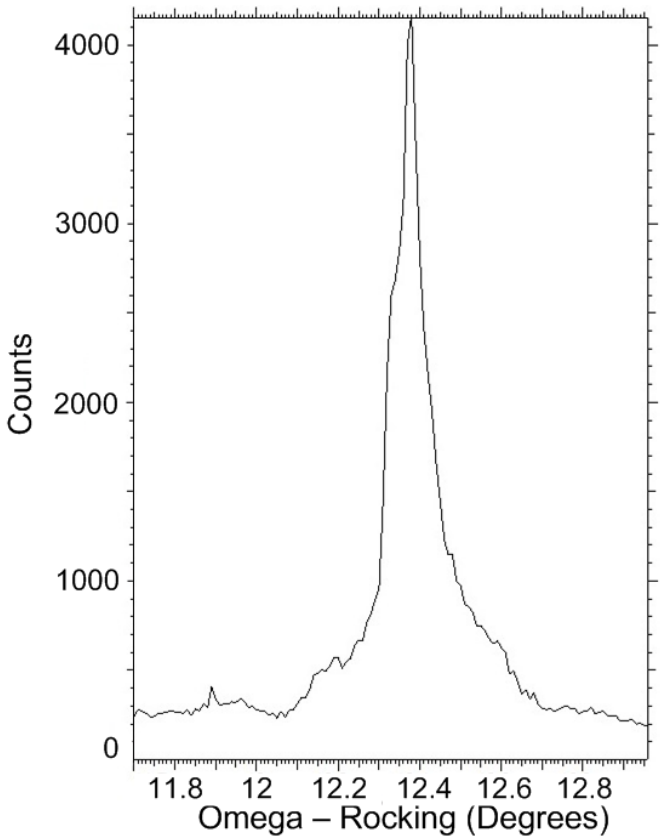

Fig. 5.9. High resolution rocking curve of the single crystal LiZnAs sample of the (111) orientation where a FWHM of 0.097^o (349.2 arc seconds) was determined with a beam divergence of 0.004^o.

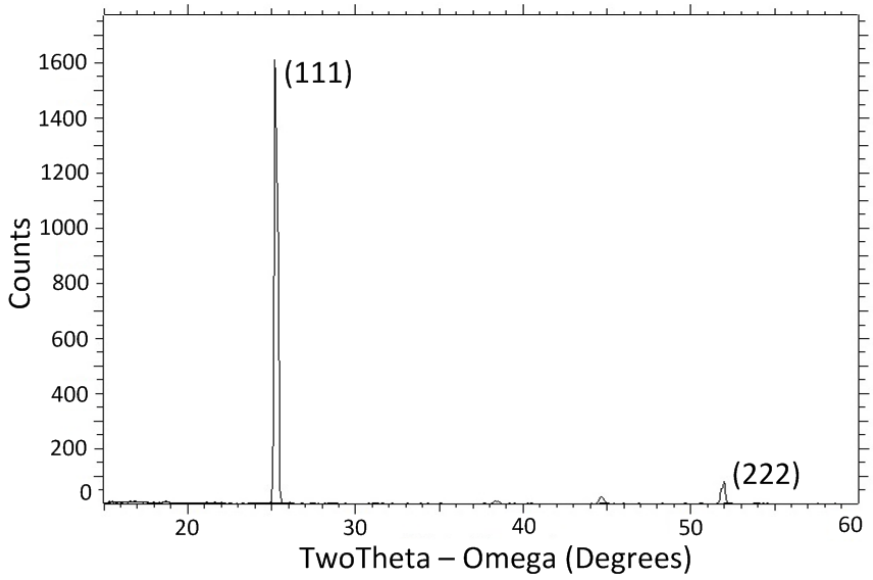

Fig. 5.10. Phase identification of the (111) orientation in the single crystal LiZnAs sample.

5.2 Purification Process and Characterization

It was observed that not all synthesis processes yielded high quality material, particularly observed while testing electrical properties of bulk devices as will be discussed in Chapter 6. A multi-step synthesis was performed to yield the highest purity product, although unreacted elemental and binary materials were likely included in the synthesized material. Nowotny-Juza compounds are hygroscopic, thereby, making handling quite difficult. Also, molten lithium reacts with quartz to make lithium silicates, which also narrows available purification techniques [79]. Typical non-solution based purification methods consist of: 1) dynamic vacuum sublimation, 2) static vacuum sublimation, 3) vacuum distillation, and 4) zone refining. Vacuum distillation is typically performed on elemental materials, or compounds, that do not sublime before becoming molten [94, 95]. LiZnP melts slightly above 1300 ^{o}C, and LiZnAs melts slightly above 1200 ^{o}C, where each sublimes before becoming molten, therefore a distillation method is not appropriate. Additionally, due to the high melting temperature, traditional zone refining is not a trivial process. A static vacuum sublimation was chosen over dynamic vacuum sublimation due to little concern of $A^{I}B^{II}C^{V}$ material exposure to the atmosphere in the handling process. Sublimation is a clean and effective way to purify elemental and compounded materials, as shown with many materials [96-98]. Synthesized ternary material was processed through a static vacuum sublimation that significantly helped reduced the material impurity level.

5.2.1 Static Sublimation Process for LiZnAs

LiZnAs was synthesized by the same method described in section 5.1.1. Afterwards, while inside a glove box backfilled with Ar, approximately 5.0 g of LiZnAs was added to a boron nitride crucible boat, and subsequently placed at one end of a clean thick-wall (>2.5mm) quartz ampoule, as shown in Fig. 5.11. A temporary vacuum seal was placed over the open end of the ampoule, and the ampoule was moved to an ampoule sealing station, where the ampoule open end was attached to a pumping station. The ampoule was then heated to remove any

residual moisture while under vacuum. When the ampoule vacuum reached approximately 9.8 x 10^{-6} torr, it was sealed using a H_2-O_2 torch.

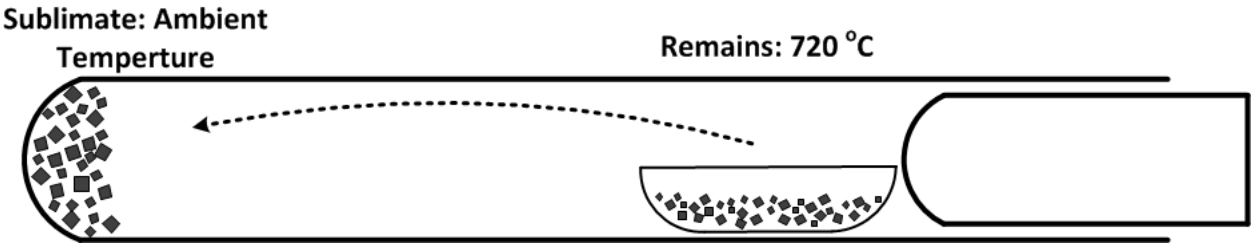

Fig. 5.11. Diagram of the static sublimation ampoule.

The sealed ampoule was placed into a three zone furnace, where the ampoule was mounted in the furnace so that the *cold* end of the ampoule extended to the edge of the furnace as shown in Fig. 5.12. All three zones were ramped to 550 °C at 3 °C/min and held at temperature for at least an hour. Two adjacent zones controlling the material temperature were ramped to 720 °C at 3 °C/min, and the third, cooler zone remained at 550 °C. Temperature was maintained for approximately 24 hours, or until no further material transport was observed.

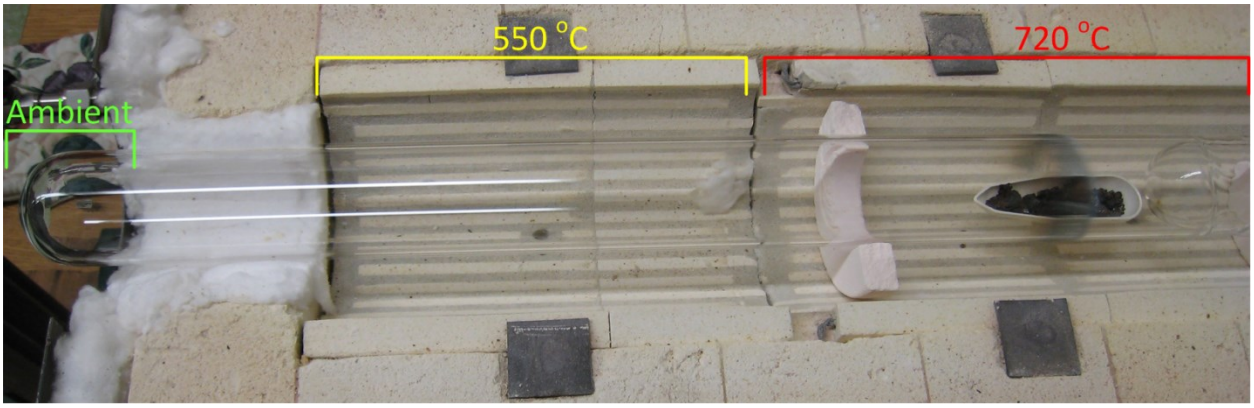

Fig. 5.12. Ampoule prepared for static sublimation process.

Once the process was complete, samples from each end of the ampoule were collected, one from the *sublimed material* and one from the *remains material* still in the boat, as shown in Fig. 5.13. These samples were analyzed by elemental analysis on a Varian 720-ES Inductively Coupled Plasma Optical Emission Spectroscopy (ICP-OES) instrument. This method uses

simultaneous optical systems, and axial or radial viewing of the plasma to measure characteristic emission spectra by optical spectroscopy. Note that this particular elemental analysis has been known to have up to 10% relative standard deviation about the measured elemental weight [99]. However, with careful preparation of the calibration standards, and samples, this relative error can be reduced.

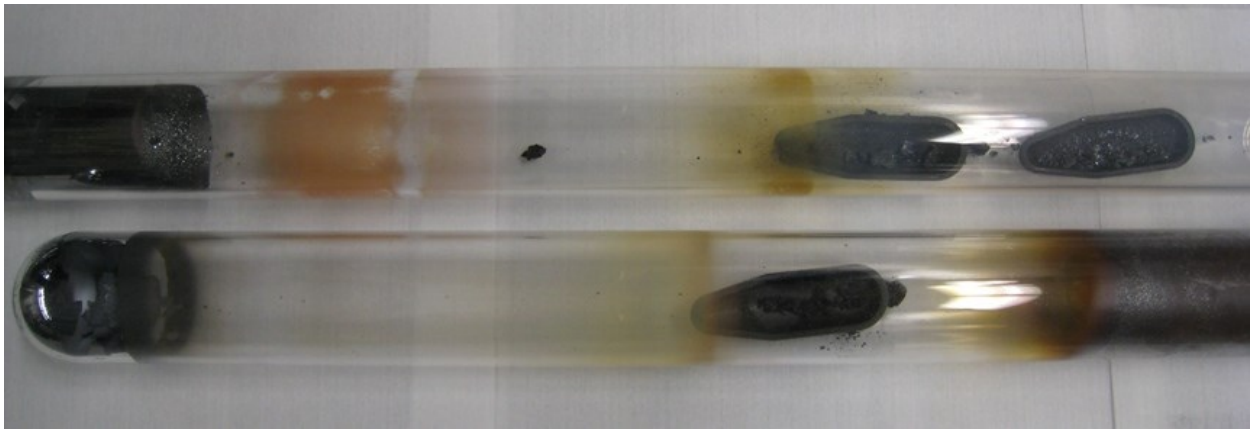

Fig. 5.13. Two ampoules of LiZnAs post static sublimation process (graphite crucibles were used in initial trials as shown here).

Phase identification x-ray diffraction scans were carried out using a Bragg Brentano Geometry on a Bruker D8 Advance Diffractometer, equipped with a Cu characteristic x-ray source, for each the *sublimed material*, and *remains material* samples harvested from the respective side of the purification ampoule. Samples were ground into a fine powder, placed into a sample holder, and sealed under argon by a layer of mylar to prevent air exposure. A phase identification scan was collected for each sample, and were compared with theoretical phase locations calculated with PowderCell 2.4 [71], and with data reported in the literature [51, 100].

5.2.2 LiZnAs ICP-OES Process

Standard solutions of varying concentrations (0, 1, 3, and 5 mg/L – Li; 0, 15, 30, 50, and 70 mg/L – Zn; 0, 15, 30, 50 and 70 mg/L – As) in water were prepared, and measured on a Varian 720-ES ICP-OES instrument to establish concentration curves. Percent deviation, or error, from the expected concentration of each standard solution was determined by the

instrument, the results of which are listed in Table 5.2. LiZnAs *remains material* and *sublimed material* were prepared for ICP-OES analysis. Each 100mg sample was loaded into a Pyrex sample container under argon, and sealed with Parafilm© to reduce air exposure when removed from the glove box. In a fume hood, the Parafilm© was removed, and 10 mL of freshly prepared aqua regia (1:4 volume HNO_3/HCl) was quickly added to each sample. The *remains* side of LiZnAs purification produced a noticeable reaction that produced a black vapor with the addition of aqua regia. The addition of aqua regia to the *deposition* side did not produce a noticeable reaction. The digestion was allowed to continue overnight.

Table 5.2. The standard solution percent errors, or deviations, from the expected concentrations. Negative values indicate the concentration deviation lies below the expected value.

Element	Concentration (mg/L)	% Error
Li	0	0
	1	5.116
	3	0.554
	5	-0.404
Zn	0	0
	15	7.151
	30	8.493
	50	3.184
	70	-3.513
As	0	0
	10	0.773
	20	1.222
	30	0.328
	40	-0.428

Most of the material was completely dissolved in each sample vial after a 24 hour period. To ensure dissolution of the remaining material, each vial was heated on a digestion block at 75 ^oC for 30 min, 100 ^oC for 30 min, 110 ^oC for 30 min, and 140 ^oC until the acid reduced to approximately 2.0 mL [101]. Each solution was then removed from the digestion block and each increased to a 50 mL by adding a 0.1% HNO_3 solution. Each 50 mL solution was then filtered through a Whatman© no. 42 filter paper. A 2.5 mL sample from each filtrate was diluted to 50 mL, each resulting in a solution possessing less than 100 mg/L of each element of interest.

Unfortunately, some sample solutions still exceeded detection limits of the ICP-OES instrument, thereby, requiring further dilution by 25% or 50% until a suitable dilution was obtained. At least two measurements were collected for each sample.

The analysis results are listed in Table 5.3. The percent result of each constituent element was determined based on the instrument analysis of the concentration of the particular element, and the total amount of material originally weighed for analysis. The elemental percent concentrations were then converted to molar concentration using each element's molar mass. The analysis percent error, and molar concentration standard error were determined based on the deviation from the average of the two measurements for each sample (Appendix C).

Table 5.3. The ICP-OES results of LiZnAs post static sublimation collected on a Varian 720-ES.

Sample: Remains (Purified)			**Sample: Sublimate (Elemental, binary)**		
Analysis	Result (Weight %)	Molar concentration (mol/L)	Analysis	Result (Weight %)	Molar concentration (mol/L)
As	38.9 ± 0.5	0.000535 ± 0.000003	As	55.6 ± 0.4	0.000720 ± 0.000003
Li	5.3 ± 0.7	0.000791 ± 0.000006	Li	n/a	n/a
Zn	44.9 ± 2.8	0.00071 ± 0.00002	Zn	52.2 ± 2.8	0.000774 ± 0.000002
Total	89.1 ± 4.0				

5.2.3 Static Sublimation Characterization for LiZnAs

Static vacuum sublimation of the in-house synthesized powders and chunks of LiZnAs appeared to produce a higher purity ternary material. The ICP-OES results are listed in Table 1 for a purified LiZnAs sample as collected on a Varian 720-ES ICP-OES. Li was not detected in the *sublimed material* sample; however, and the *remains material* was found to have the stoichiometric ratios expected for $A^{I}B^{II}C^{V}$ materials, as listed in Table 5.3. The total weight percent of the sample equaled 89.1 ± 4.0%. Although it is expected to observe an elemental total of 100%, the standard error associated with measured total is often larger when including the error associated with the concentration curves. Shown in Table 5.2 are standard errors up to

8.493% for the 30 mg/L Zn solution. The standard error from the slope of the concentration curve was included in quadrature for determination of the final standard error.

The elemental percent concentrations were converted to molar concentration from the molar mass of each element, where it is observed that each molar mass is approximately equal. Arsenic had a slightly lower molar concentration than Li and Zn. The concentration curve standard error for As was determined to be 1.222% for the 20 mg/L standard solution. This relatively high error may suggest the error associated with the As analysis may be slightly higher than the other measurements. Nevertheless, this result is further indication that impurities (binaries, unreacted elemental components) were transferred out of the in-house synthesized material during the sublimation process, leaving a much purer ternary material.

The theoretical phase identification for LiZnAs is shown in Fig. 5.14, as calculated using PowderCell 2.4 [71]. The x-ray diffraction phase identification of LiZnAs purification *sublimed material* is shown in Fig. 5.15, where an array of peaks is observed, many that match nicely with experimental data by Nowotny for LiZnAs [51]. However, the same *sublimed material* phase scan was compared to cubic Zn_3As_2 data collected by Banus [100], shown in Fig. 5.16, where many peaks also match the reported data. Further evidence that Zn_3As_2 was sublimed out of the raw synthesized material can be found by careful examination of the ICP-OES results. Zinc arsenide has a stoichiometric Zn to As ratio of 1.5, and the ratio of Zn to As, as listed in Table 2, is 0.92. These ratios are not consistent, but with an abundance of elemental arsenic mixed amongst the impurities, it is suspected that cubic Zn_3As_2 was formed and is present as an impurity.

The *remains material* phase identification, shown in Fig. 5.17, shows identifiable peaks, all of which match well with literature in terms of theoretical peak positions as shown in Fig. 5.14. A lattice constant was determined using TOPAS (Bruker AXS Inc.). The Whole Pattern decomposition approach was used [102]. Refinement of the *remains material* phase identification data yielded a lattice constant of 5.901 ± 0.002 Å, which is consistent with refinement data collected with the raw synthesized (unpurified) material as described in section 5.1.2.

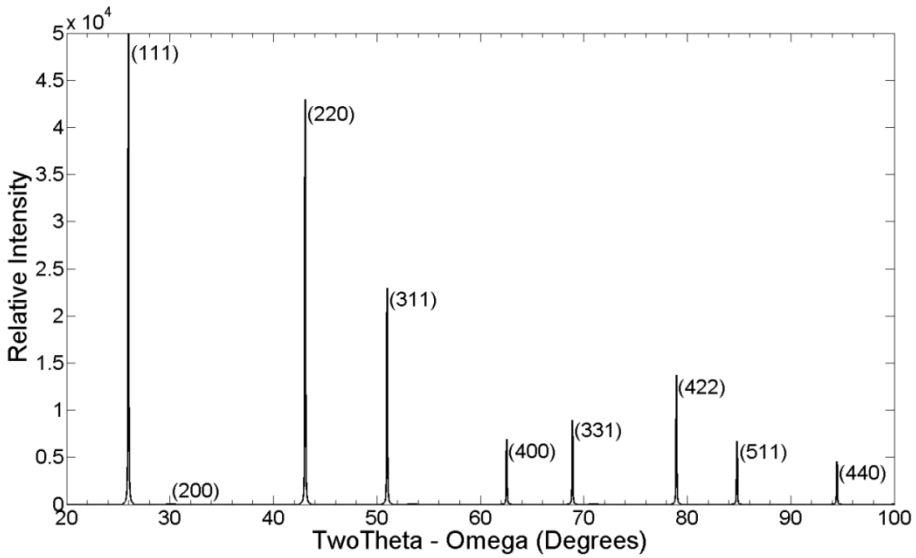

Fig. 5.14. The theoretical Cu x-ray phase identification of a Cubic LiZnAs $F\bar{4}3m$ powder with a lattice constant of 5.939 ± .002Å (section 5.1.2). Peak positions were calculated with PowderCell 2.4 [71].

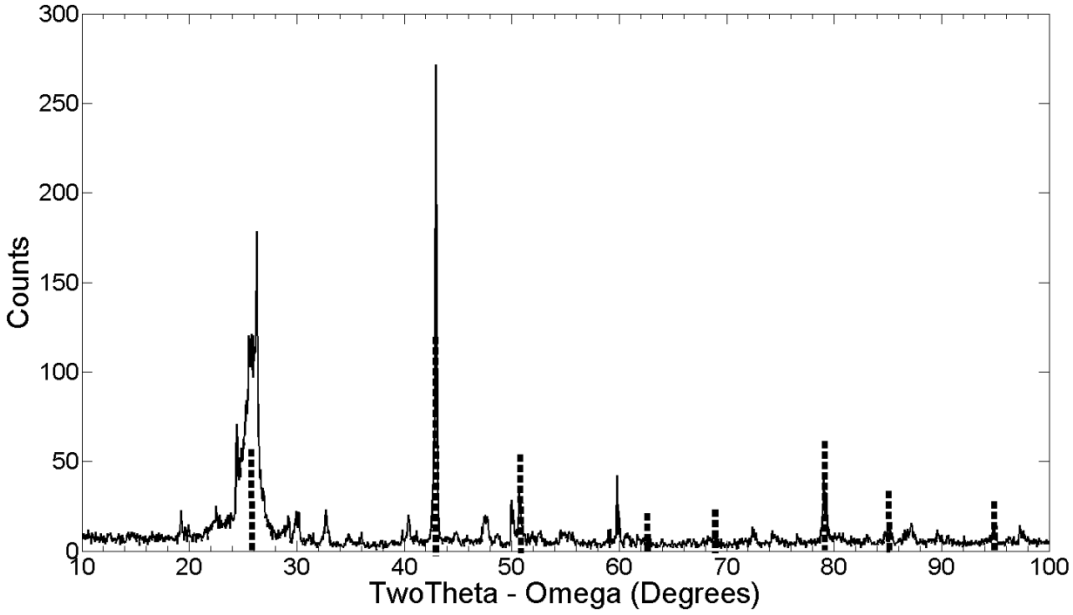

Fig. 5.15. LiZnAs sublimed material phase identification scan collected on a Bruker AXS D8 ADVANCE equipped with Cu characteristic x-ray radiation. The dashed black vertical lines are experimental peaks reported by Nowotny for LiZnAs [51].

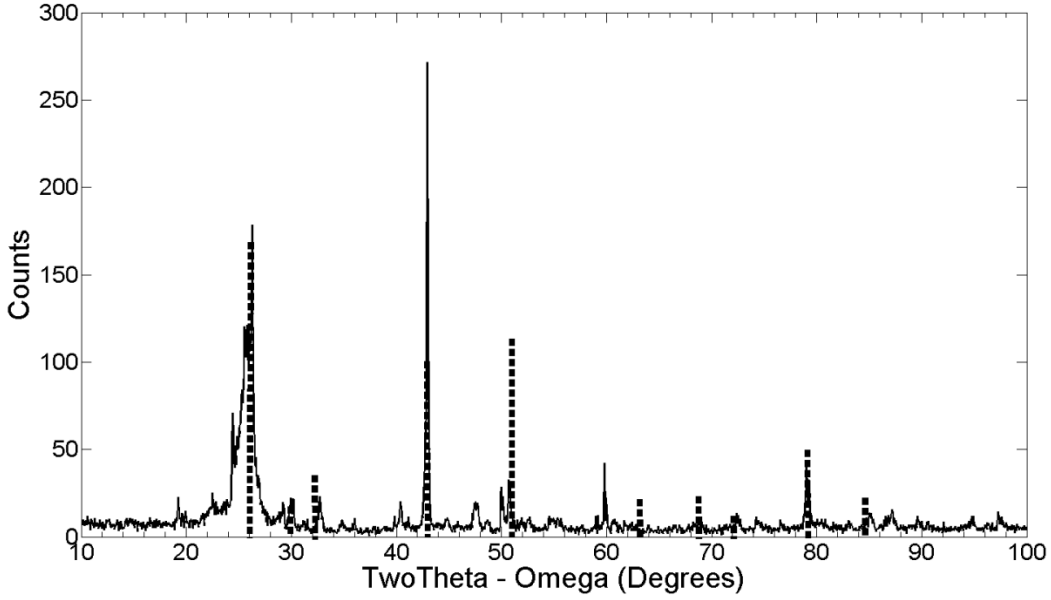

Fig. 5.16. LiZnAs sublimed material phase identification scan collected on a Bruker AXS D8 ADVANCE equipped with Cu characteristic x-ray radiation. The dashed black vertical lines are experimental phase peaks reported by Banus for cubic zinc arsenide (Zn_3As_2) [100].

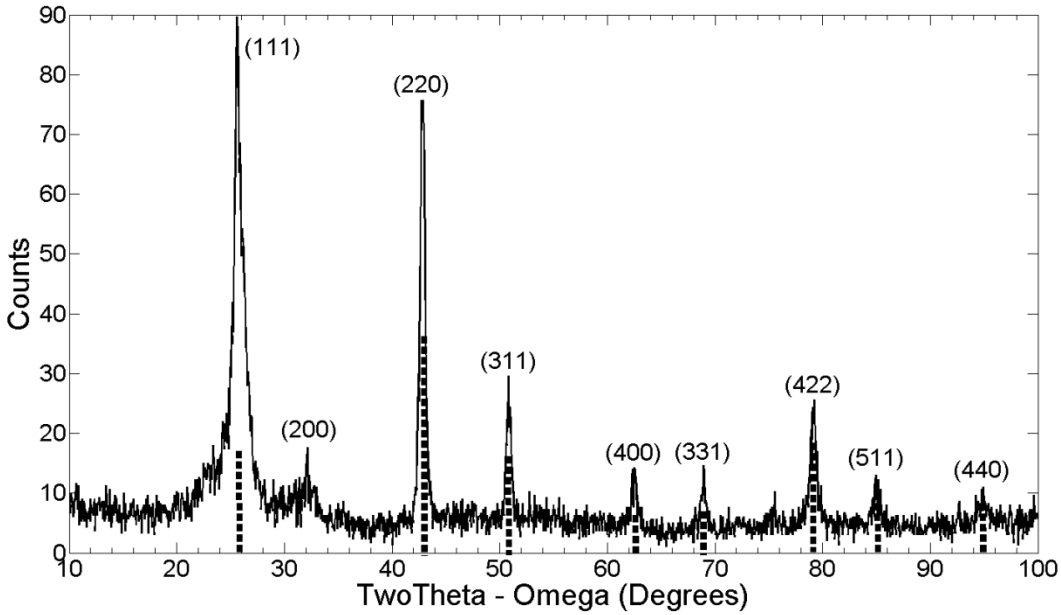

Fig. 5.17. LiZnAs remains material phase identification scan collected on a Bruker AXS D8 ADVANCE equipped with Cu characteristic x-ray radiation. The dashed black vertical lines are experimental peaks reported by Nowotny for LiZnAs [51].

5.2.4 Static Sublimation Process for LiZnP

LiZnP was synthesized, as described in section 5.1.1, in batches up to 2.0 grams. Approximately 5.0g of LiZnP was added to a boron nitride crucible boat, and loaded into one side of a clean, thick wall (>2.5mm) quartz ampoule as shown in Fig. 5.18. The ampoule was removed from the argon atmosphere while remaining under argon by a closed vacuum attachment. The ampoule was placed on a vacuum sealing station, where it was baked out to remove residual moisture, and evacuated to approximately 9.8 x 10^{-6} torr, subsequently sealed using a H_2-O_2 torch. The ampoule was placed into a three zone furnace, where two zones were ramped to 750 ^{o}C for LiZnP purification, and the third zone was ramped to 550 ^{o}C. The ampoule was also mounted in the furnace so that the *cold* end of the ampoule extended to the edge of the furnace as shown in Fig. 5.19.

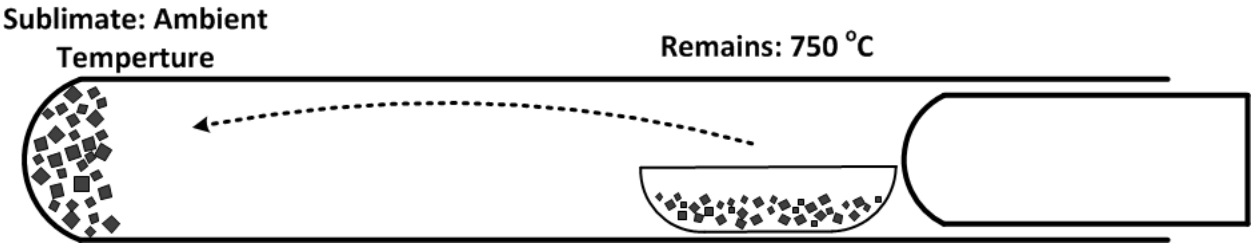

Fig. 5.18. Diagram of the LiZnP static sublimation ampoule.

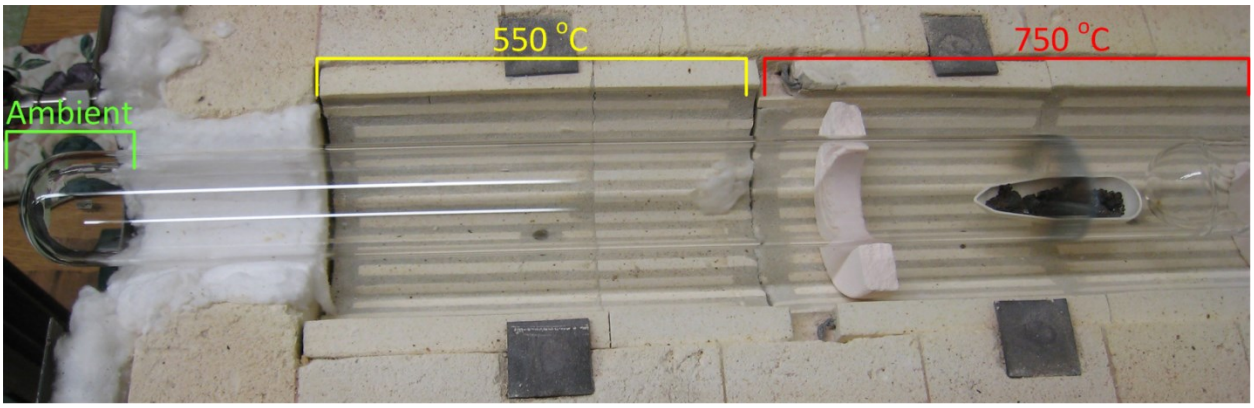

Fig. 5.19. Ampoule loaded with LiZnP material prepared for a static sublimation process.

Samples from each side of the ampoule were collected, one from the *sublimed* material, and one from the *remains* after purification, as regions for each in the ampoule are shown in Fig. 5.20. The samples were analyzed by elemental analysis on a Varian 720-ES Inductively Coupled Plasma Optical Emission Spectroscopy (ICP-OES) instrument that measures characteristic emission spectra by optical spectroscopy as described in section 5.2.1.

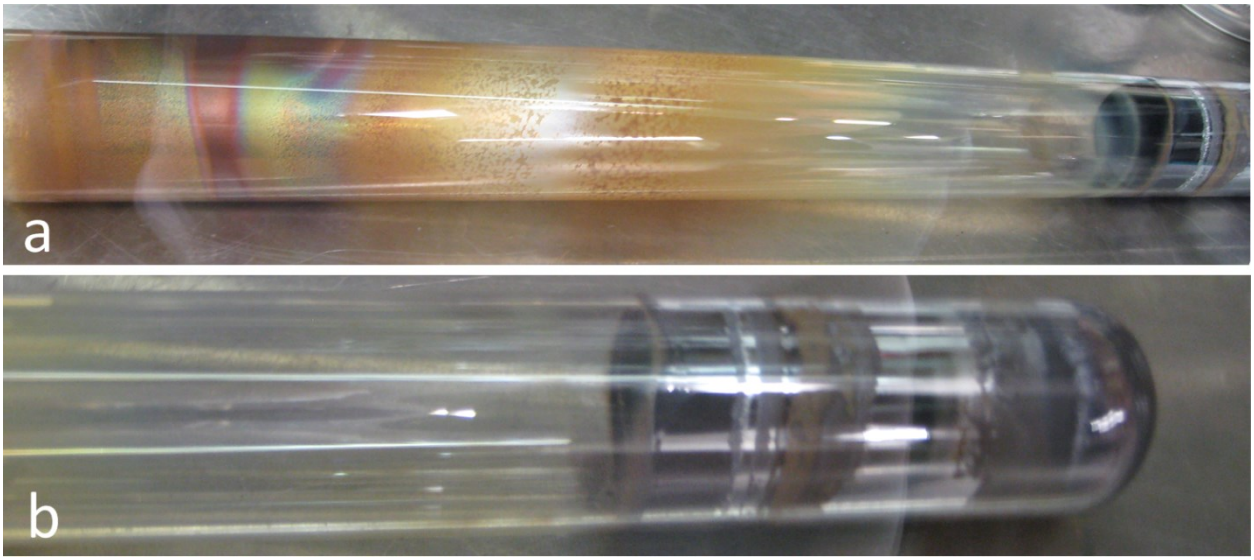

Fig. 5.20. Ampoule of LiZnP after static sublimation process. a) The remains end of the ampoule b) The sublimed portion of the ampoule.

Phase identification x-ray diffraction scans were collected on a Bruker D8 ADVANCE, equipped with Cu characteristic x-ray radiation, using the Bragg Brentano geometry. Samples from the *sublimed material* and *remains material* were harvested from the respective side of the purification ampoule, and ground into a fine powder using a clean mortar and pestle. Each powder was loaded into a zero-background sample holder with a layer of Mylar®, over the top of the material, and sealed for protection from moisture in air. A phase identification scan was collected for both samples. The results were compared with theoretical phase locations calculated with PowderCell 2.4, and data presented in the literature [60].

5.2.5 LiZnP ICP-OES Process

Standard solutions of varying concentrations (0, 1, 3, and 5 mg/L – Li; 0, 15, 30, 50, and 70 mg/L – Zn; 0, 10, 20, 30, and 40 mg/L – P) in water were prepared, and measured on a Varian 720-ES ICP-OES instrument to establish concentration curves. Percent deviation, or error, from the expected concentration of each standard solution was determined by the instrument, the results of which, can be found in Table 5.4. The LiZnP *remains material* and *sublimed material* were prepared for ICP-OES analysis. Each 100mg sample was loaded into a pyrex sample container under argon, and sealed with Parafilm© to reduce air exposure when removed from the glove box. In a fume hood, the Parafilm© was removed, and 10 mL of freshly prepared aqua regia (1:4 volumetric ratio HNO_3/HCl) was quickly added to each sample. The remains side of LiZnP purification produced a noticeable reaction that produced a black vapor with the addition of aqua regia. The addition of aqua regia to the deposition side did not produce a noticeable reaction. The digestion was allowed to continue overnight.

Table 5.4. The standard solution percent errors, or deviations, from the expected concentrations[13]. Negative values indicates the concentration deviation lies below the expected value.

Element	Concentration (mg/L)	% Error
Li	0	0
	1	5.116
	3	0.554
	5	-0.404
Zn	0	0
	15	7.151
	30	8.493
	50	3.184
	70	-3.513
P	0	0
	10	0.356
	20	0.813
	30	-0.404
	40	0.002

Most of the material had dissolved in each sample vial after a 24 hour period. To ensure complete digestion of the remaining material, each vial was heated on a digestion block at 75 ^{o}C for 30 min, 100 ^{o}C for 30 min, 110 ^{o}C for 30 min, and 140 ^{o}C until the acid was reduced to approximately 2.0 mL [101]. Each solution was removed from the digestion block and was increased to a 50 mL solution using 0.1% HNO_3. Each 50 mL solution was then filtered through a Whatman© no. 42 filter paper. A 2.5 mL sample from each filtrate was diluted a second time to 50 mL, to acquire a solution possessing less than 100 mg/L of each element of interest. Some sample solutions still exceeded detection limits of the ICP-OES instrument, so further dilution by 25% or 50% was required. Two measurements were collected for each sample.

The analysis results are listed in Table 5.5. The percent result of each constituent element was based on the instrument analysis of the concentration of the particular element, and the total amount of material originally weighted for analysis. The elemental percent concentrations were then converted to molar concentration using each element's molar mass. The analysis percent error, and molar concentration standard error were determined based on the

[13] Lithium and zinc concentration curve percent errors are the same as reported in Table 5.2 since all samples were evaluated at the same time, and one set of standards were made for the evaluation.

deviation from the average of the two measurements for each sample, and the systematic error associated with the concentration curves determined by the ICP-OES instrument.

Table 5.5. The ICP-OES results of LiZnP post static sublimation collected on a Varian 720-ES.

Sample: Remains (Purified)			**Sample: Sublimate (Elemental, binary)**		
Analysis	Result (Weight %)	Molar concentration (mol/L)	Analysis	Result (Weight %)	Molar concentration (mol/L)
P	33.0 ± 0.4	0.001011 ± 0.000004	P	23.0 ± 0.3	0.000780 ± 0.000003
Li	13.05 ± 0.09	0.001786 ± 0.000002	Li	< 0.1	negligible
Zn	54.3 ± 2.8	0.00079 ± 0.00002	Zn	85.6 ± 2.3	0.001375 ± 0.000004
Total	100.4 ± 3.3				

5.2.6 Static Sublimation Characterization for LiZnP

Static vacuum sublimation of the in-house synthesized powders and chunks of LiZnP appeared to produce a higher purity ternary material. Listed in Table 5.5 are the ICP-OES results for a LiZnP purification collected on a Varian 720-ES Inductively Coupled Plasma Optical Emission Spectrometer. Li was only slightly present in the *sublimed material* sample with a concentration of < 0.1%. The *remains material* appeared to have the stoichiometric ratios expected for $A^{I}B^{II}C^{V}$ materials with a Li concentration of 13.05 ± 0.09 %. Furthermore, the total weight percent of each *remains material* element equaled 100% within the propagated total 3.3% error from the three elemental measurements. Additionally, each elemental constituent molar concentration is approximately equal within the standard deviation. These results further indicate that impurities (binaries, unreacted elemental components) were transferred out of the in-house synthesized material during the sublimation process, leaving a much purer ternary material.

The theoretical phase identification for LiZnP is shown in Fig. 5.21, as calculated using PowderCell 2.4 [71]. The x-ray diffraction phase identification results of the *sublimed material* and *remains material* are shown in Fig. 5.22 and Fig. 5.23, respectively. The *sublimed material* did not indicate a significance of phase peaks, except for a single orientation, making the material difficult to identify from the phase identification pattern. However, the *remains material*

phase identification, shown in Fig. 5.23, showed an arrangement of peaks that match the literature [60], and also from the theoretical calculations (Fig. 5.21). A lattice constant was determined using TOPAS (Bruker AXS Inc.). The Whole Pattern decomposition approach was used [102]. Refinement of the *remains material* phase identification data yielded a lattice constant of 5.786 ± .002 Å which was consistent to what was reported from raw synthesized (unpurified) material, as reported in section 5.1.2.

The *remains material* phase identification, Fig. 5.23, clearly showed the (111), (220), (222) (331) (422) and (511) LiZnP orientations. In addition, preferred orientation along the (220) LiZnP is observed. However, the (200), (311), (400) and (420) orientations were not observed. The (200), (400) and (420) LiZnP orientations do have weak reflections, as shown in Fig. 5.21, and therefore, can be difficult to measure. Additional peaks were also observed near the (111) and (331) LiZnP orientations which could be due to secondary phases created as a result of oxidation during handling and measurement. The material was encapsulated under argon during the measurement, and degradation could have occurred over time due to leakage of air into the encapsulant. Additionally there is also the possibility of the presence of a secondary LiZnP phase with a slightly different lattice constant. Ultimately, the static sublimation process appeared to help clean the LiZnP material of unreacted metals, or other impurities, as clearly shown by comparison between Fig. 5.22 and Fig. 5.23.

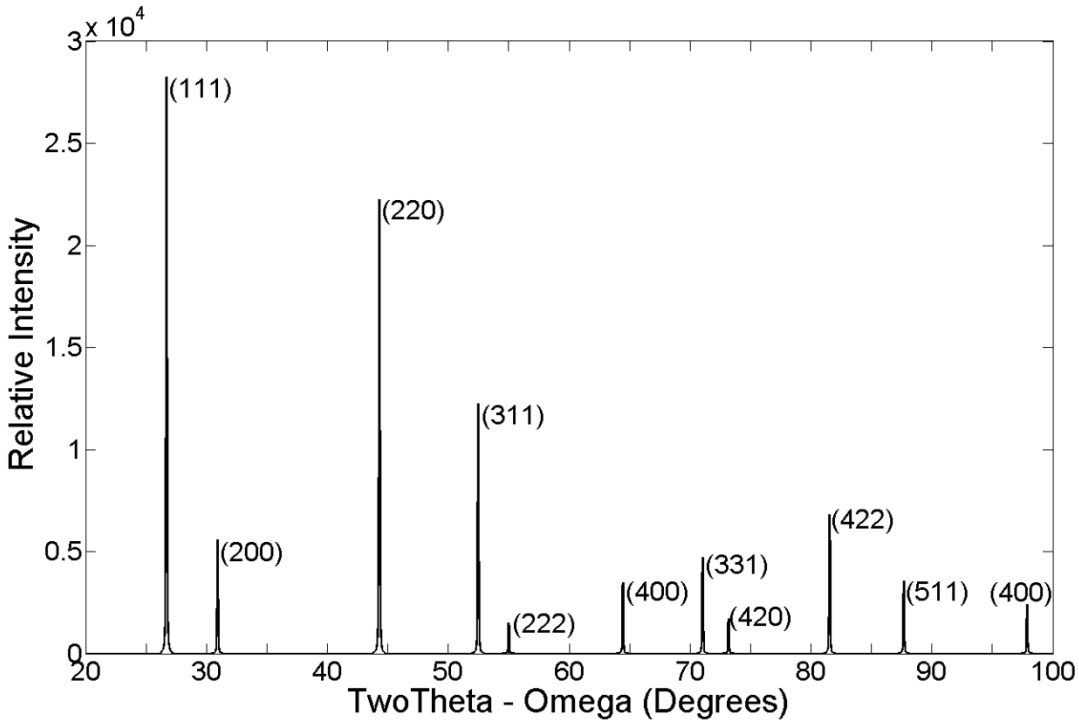

Fig. 5.21. The theoretical Cu x-ray phase identification of LiZnP. Calculated using PowderCell 2.4 [71]. A 5.751 ± .001 Å lattice constant and F-43m space group was used in the calculation as reported in section 5.1.2.

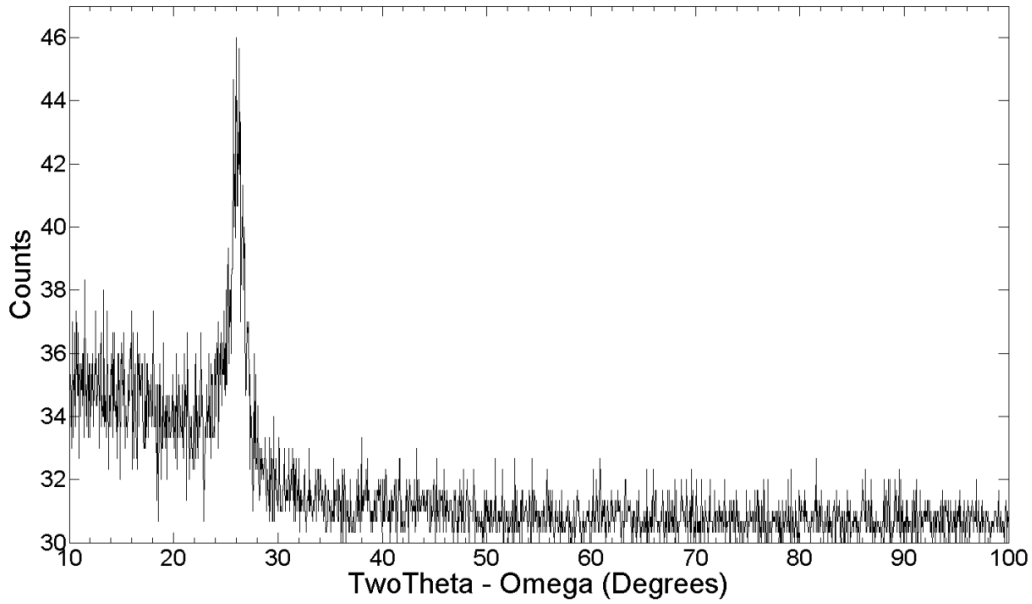

Fig. 5.22. LiZnP sublimed material phase identification scan collected on a Bruker AXS D8 ADVANCE equipped with Cu characteristic x-ray radiation, using the Bragg Brentano geometry.

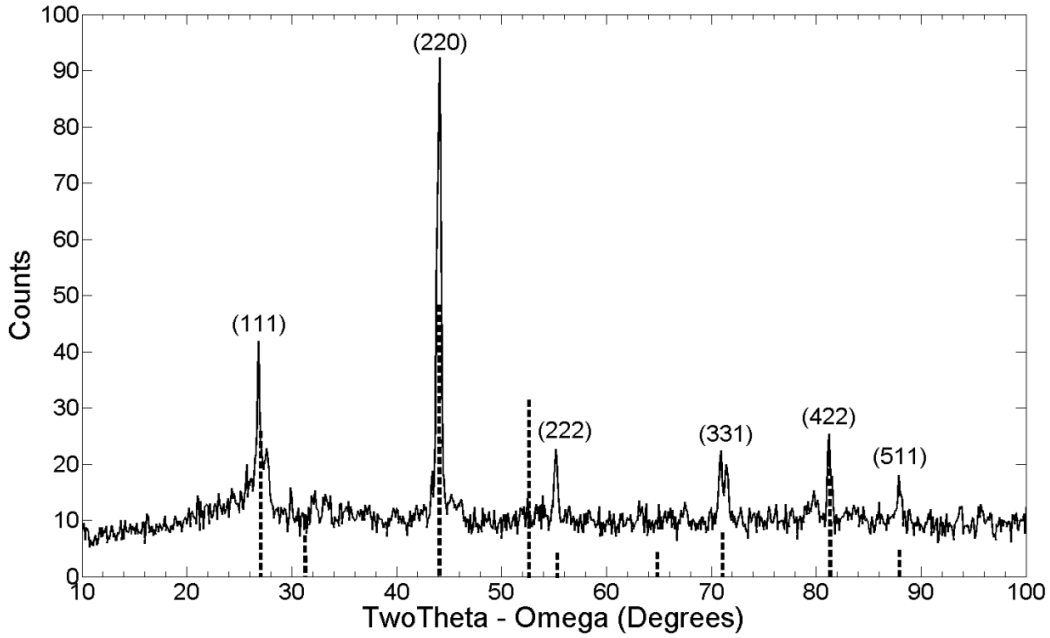

Fig. 5.23. LiZnP remains material phase identification scan collected on a Bruker AXS D8 ADVANCE equipped with Cu characteristic x-ray radiation, using the Bragg Brentano geometry. The black vertical dotted lines are experimental LiZnP reflections reported by Bacewicz [60].

5.3 Bulk Crystal Growth of LiZnAs and LiZnP

A complete routine for synthesizing LiZnP and LiZnAs was described in section 5.1; however, the samples were small and difficult to fabricate into devices. Bulk crystal growth of ingots large enough for post-processing, and device fabrication, is presented here. Bulk crystal growth of LiZnP and LiZnAs has not been reported in the literature therefore, melting temperatures have not been completely characterized. The only bulk samples of LiZnP and LiZnAs reported in the literature were small facets extracted from synthesis processes as described in section 2.3.1. No bulk growth techniques were reported. In the following study, bulk LiZnP and LiZnAs crystals were grown by a high-temperature Bridgman method. Crystals were grown from both unpurified and purified material. Crystals were characterized for crystallinity by energy-dispersive x-ray diffraction and high-resolution x-ray diffraction. These crystals were processed into devices for further electrical testing and radiation sensitivity.

5.3.1 Crystal Growth Process of LiZnP

LiZnP was synthesized, as described in section 5.1.1, in small batches up to 2.0 grams, and the synthesized material was purified by a static sublimation process as described in section 5.2.4. LiZnP material was subsequently grown into bulk crystals under the following high-temperature vertical Bridgman technique [103].

A 0.5 inch diameter tantalum tube (0.02 inch wall thickness) was cut into a 2.9375 inch long sample containment tube. Tantalum caps were punched with a 17 mm diameter from 0.02 inch thick tantalum sheet. The tantalum disks were formed using a custom-made die that would form a tantalum disk into a cap, as shown in Fig. 5.24. A pyrolytic graphite crucible was custom designed to fit in the tantalum tube (supplied by Mersen, Inc.). Each of the components were cleaned of oils and contaminants by ultrasonic vibration in a series of solvents namely, hexane, trichloroethylene, acetone, and isopropanol separately. The components were loaded into an argon glove box, with a minimal oxygen and moisture contamination of less than 0.1 %. The

bottom cap was welded on the tantalum tube by a Maxstar 150 STL arc welder. The welding torch/stick was fed through the glove box, and the argon environment allowed for the arc plasma to form, and therefore allowed for welding within the box. A view of the welded tantalum cap is shown in Fig. 5.25. LiZnP material (1.0 – 8.0 g) was loaded into the pyrolytic graphite crucible, which was loaded into the tantalum vessel. A tantalum cap was welded to the top of the vessel, thereby, making an air-tight containment of LiZnP material and atmospheric pressure argon as shown in Fig. 5.26.

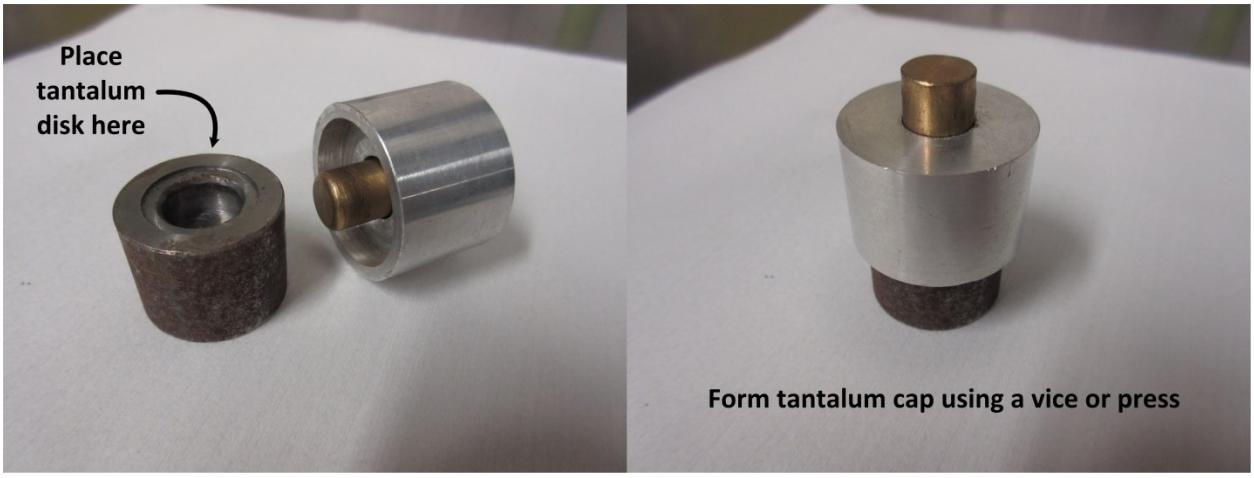

Fig. 5.24. The custom made die used for forming the tantalum caps. A 17 mm disk was punched from 0.02 inch tantalum sheet, and placed into the imbedded area of the die made from steel (left). The aluminum harness with the brass fitting was placed over the steel portion of the die (right), and pressure was applied to the brass fitting to form the tantalum cap using a vice, or hydraulic press.

Fig. 5.25. A view of the arc-welded tantalum cap that makes a pressure-tight seal.

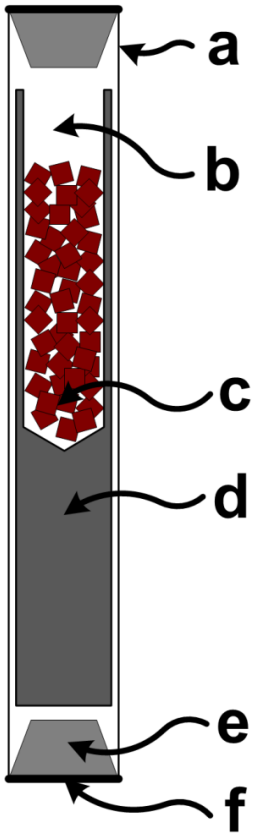

Fig. 5.26. Cross section of the loaded tantalum vessel. ***a*** *– tantalum tube,* ***b*** *– argon gas,* ***c*** *– LiZnP material,* ***d*** *– pyrolytic graphite crucible,* ***e*** *– tantalum cap,* ***f*** *– air-tight arc weld.*

A bulk crystal was grown in the tantalum vessel contained in a vacuum chamber, equipped with an Omega iR2C series fiber optic thermometer mounted on a two axis rotation stage for alignment purposes as shown in Fig. 5.27. The vacuum chamber was equipped with two feed-throughs connected to an R.D. Mathis LV 400 high-current, low-voltage power source, capable of achieving temperatures capable of melting tantalum (melting point – 3016 ^{o}C [104]) as shown in Fig. 5.28. The tantalum vessel was connected between two electrical connecting oxygen-free plates, referred to as a *copper harness*, depicted in Fig. 5.29. The copper harness connected to the electrical feed-throughs within a vacuum chamber and these feed-throughs connected to the high-current, low-voltage power source. Continuity was tested to confirm a stable connection outside of the vacuum chamber. The chamber was evacuated, and then purged with ultra-high purity argon at least six times. After the final purge, the chamber pressure was maintained between 300 – 400 mTorr argon pressure. The current was ramped typically from 0 amps to approximately 295 – 315 amps over the course of at least an hour, until the optical thermometer measured approximately 1345 ^{o}C at the tantalum surface. A sequence from approximately 850 ^{o}C to the final temperature, 1345 ^{o}C is shown in Fig. 5.30. The temperature was maintained at 1345 ^{o}C for at least an hour. The system was then ramped down to room temperature over a period of 40 hours. The vessel was extracted from the chamber, and opened with a pipe cutter under a pure argon environment. The ingot was harvested, and individual samples were cut from the ingot with a Laser Technology West Ltd. CS400 diamond wire saw while under a constant flow of mineral oil for protection from moisture in the air.

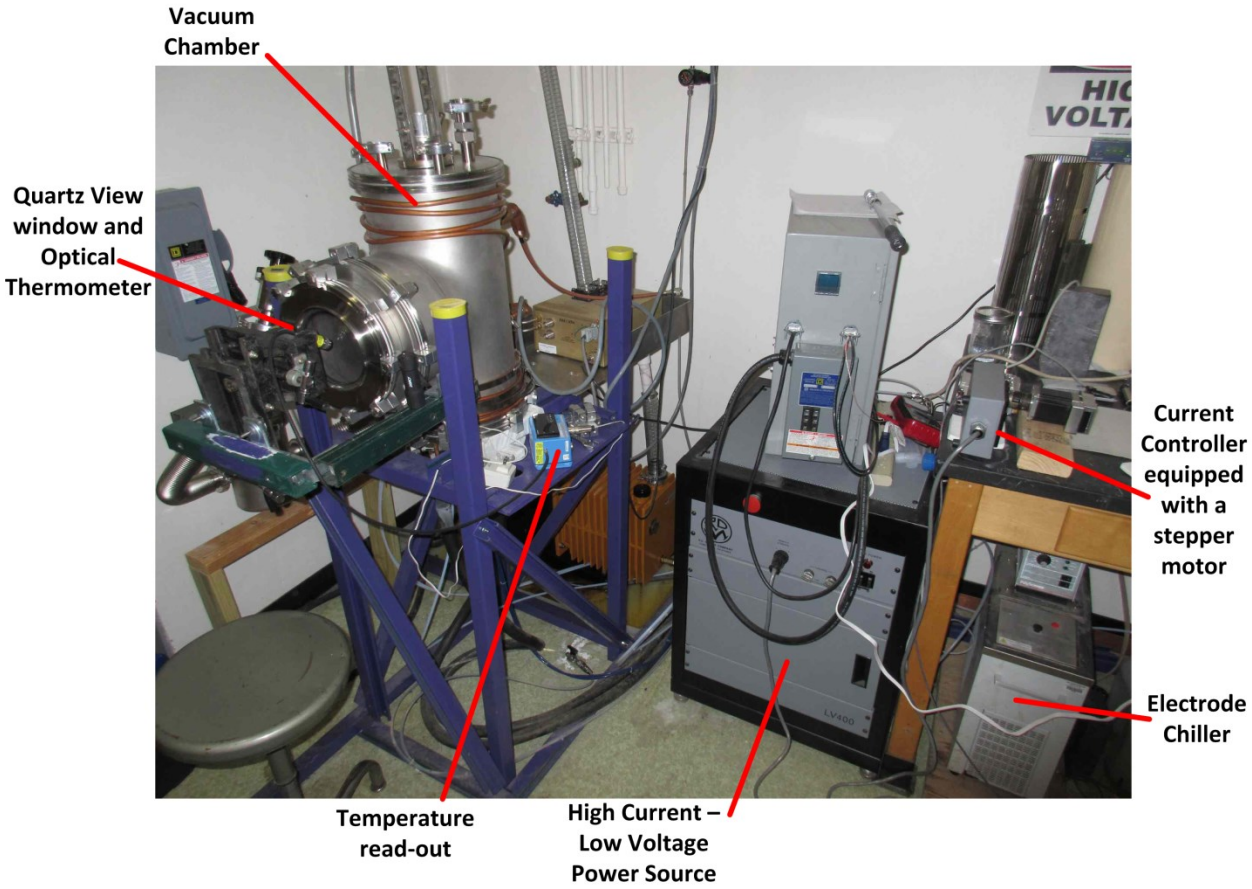

Fig. 5.27. A picture of the high-temperature crystal growth system for $A^{I}B^{II}C^{V}$ compounds. The instrument has the capability to reach temperatures up to the melting point of tantalum, 3017 ^{o}C [104].

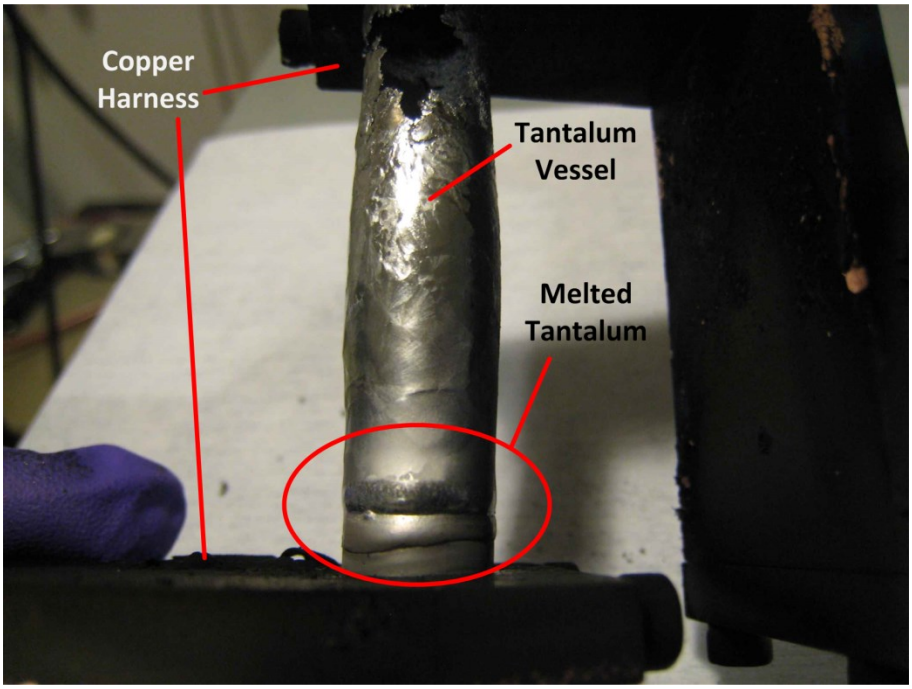

Fig. 5.28. A picture of a melted tantalum vessel after undergoing a test run in the custom high-temperature crystal growth furnace.

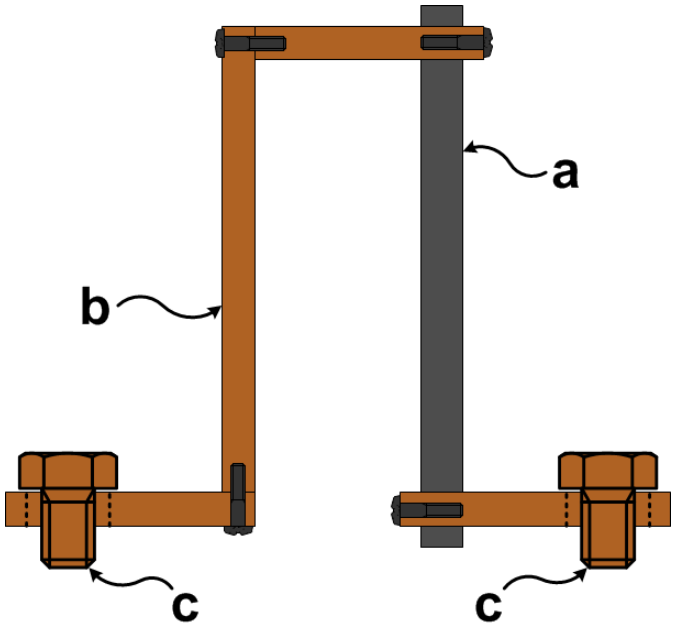

*Fig. 5.29. Schematic of the oxygen-free copper harness. **a** – tantalum ampoule, **b** – oxygen-free copper, **c** – electrodes that connect to the low voltage power source.*

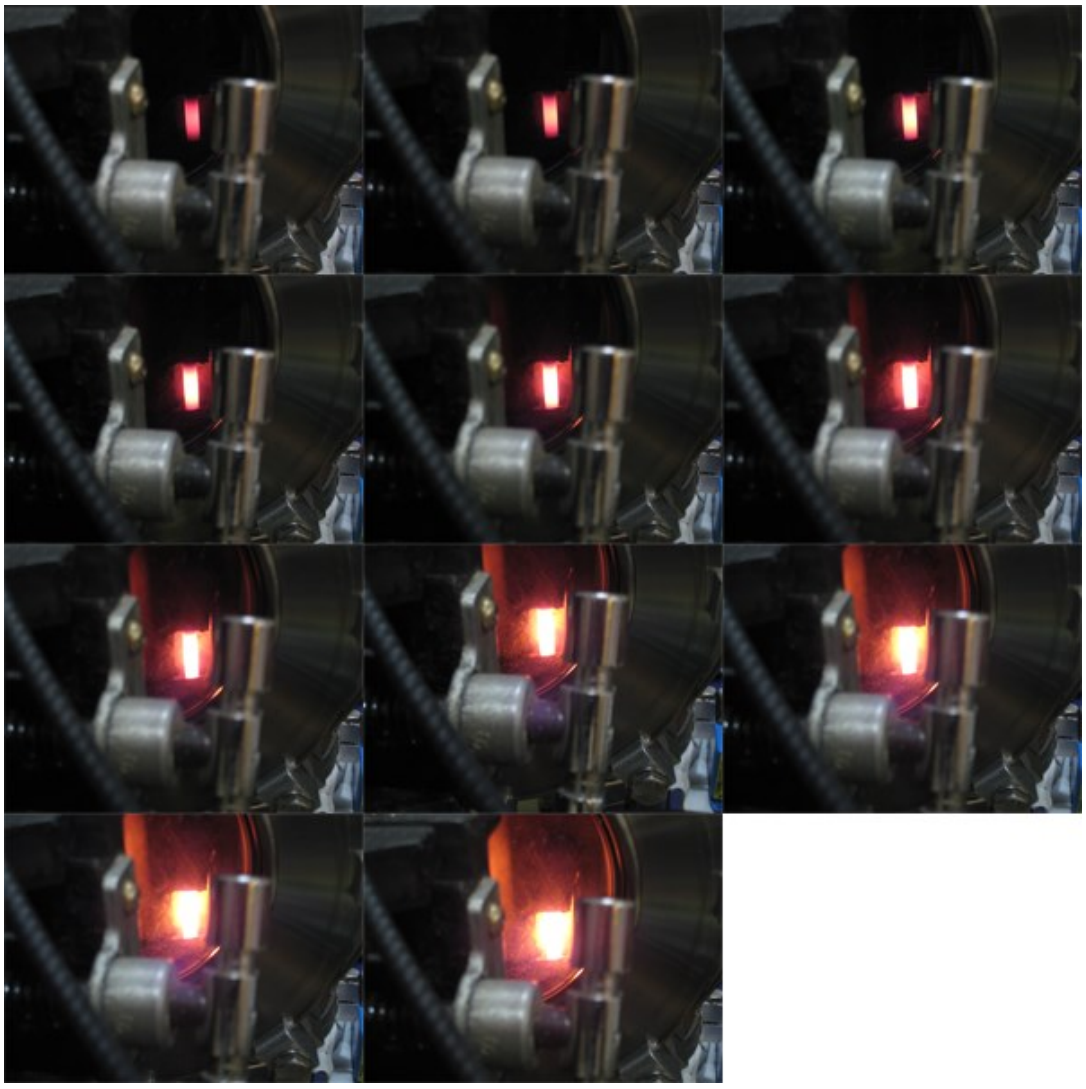

Fig. 5.30. A sequence of photographs of the inside of the chamber, showing the tantalum ampoule thermal sequence beginning at approximately 850 ^{o}C to the final temperature at approximately 1345 ^{o}C.

5.3.2 Bulk Crystalline LiZnP Ingots

The bulk crystal growth process produced ingots of various size, the largest being ≈13.0 x 9.0 x 6.0 mm^3, as shown in Fig. 5.31. Crystals from other growth trials are shown in Fig. 5.32, Fig. 5.33, and Fig. 5.34. The ingot grown from purified material was 9.6 mm in diameter and 4.0 mm in length. A slice of the purified ingot is shown in Fig. 5.35. The melting/decomposition temperature reported by K. Kuriyama was not confirmed, nor observed, in this study [55].

Numerous attempts to grow LiZnP by melt in crucible lined quartz ampoules always resulted in non-congruent melting up to temperatures of 1150 ^{o}C. Temperatures above 1150 ^{o}C in quartz resulted in the expansion of the soft quartz due to the high vapor pressure in the ampoule, and often resulted in ampoule rupture. Bulk crystal growth of LiZnP requires temperatures slightly above the threshold of conventional resistive coil furnaces that typically have a 1200 ^{o}C upper limit under continuous operation. Optical thermometer readings sampled through a quartz window of the crystal growth chamber typically indicated temperatures between 1335 – 1355 ^{o}C (depending on the focal depth of the optical thermometer), which allowed for the congruent melt of LiZnP.

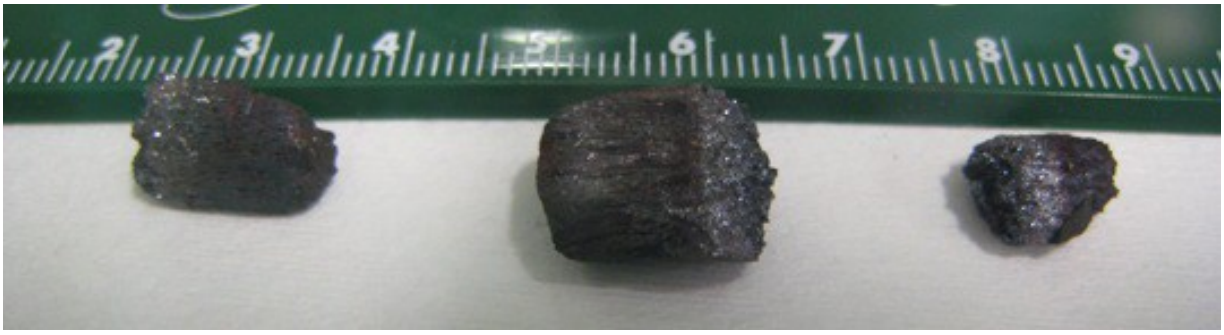

Fig. 5.31. LiZnP crystals grown by the high-temperature growth method (picture collected through the glove box window).

Fig. 5.32. LiZnP crystals grown by the high-temperature growth method (picture collected through the glove box window).

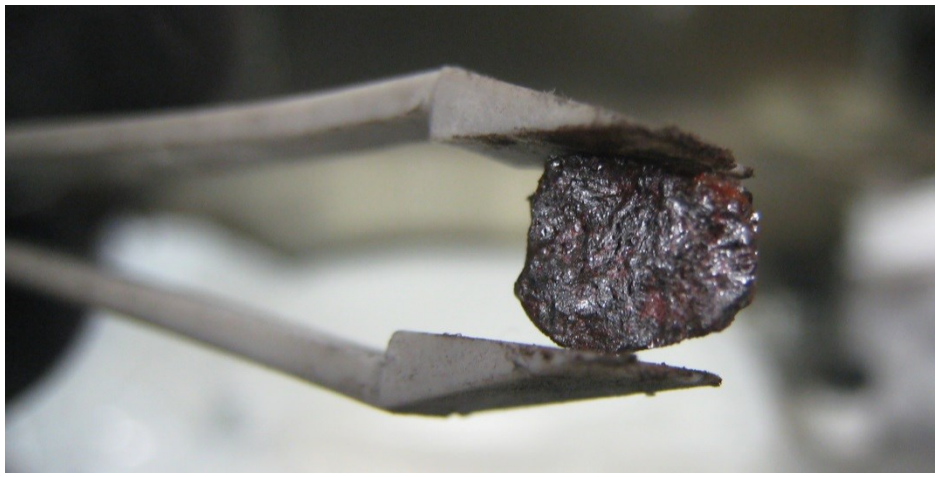

Fig. 5.33. LiZnP crystal grown by the high-temperature growth method (picture collected through the glove box window).

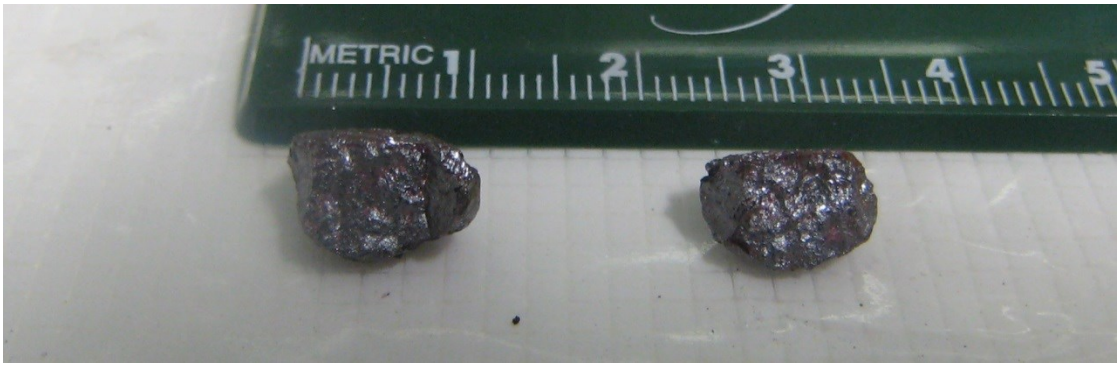

Fig. 5.34. LiZnP crystals grown by the high-temperature growth method (picture collected through the glove box window).

Fig. 5.35. Slice from the LiZnP purified ingot (picture collected through the glove box window).

5.3.3 Bulk LiZnP Crystallinity

A LiZnP sample was sliced to 4.077 x 3.518 x 2.020 mm as shown in Fig. 5.36, and XRD analysis was performed on one side of the 4.077 x 3.518 mm face. The sample was mounted into a polishing fixture by parafin wax. The sample face was polished with a series of silicon carbide polishing papers ranging from 15.3 – 2.5 micron grain size, ANSI grit: 600 (P1200), 800 (P2400), and 1200 (P4000) [105, 106]. The polished sample was mounted under argon between two Mylar® sheets in a custom sample holder designed to keep the sample air-tight (Fig. 5.37), and then evaluated on a Bruker AXS Inc. D2 CRYSO energy-dispersive x-ray diffractometer. The measurements were used to evaluate the crystal structure, orientation, lattice constant and *d* spacing. The sample was then mounted into an air-tight poly(methyl methacrylate) (PMMA) plastic sample holder with a beryllium dome with double-sided tape, as shown in Fig. 5.38. The sample was evaluated while under argon by a Bruker AXS Inc. high-resolution D8 DISCOVER x-ray diffractometer. The diffractometer was equipped with molybdenum optics with a four bounce monochromator (0.004^{o} beam divergence), and a line beam 12.0 mm tall by 9.5 mm width (slit size). The crystalline perfection of the sample was evaluated by out-of-plane and in-plane measurements.

Fig. 5.36. A 4.077 x 3.518 x 2.020 mm^3 bulk grown crystal of purified LiZnP.

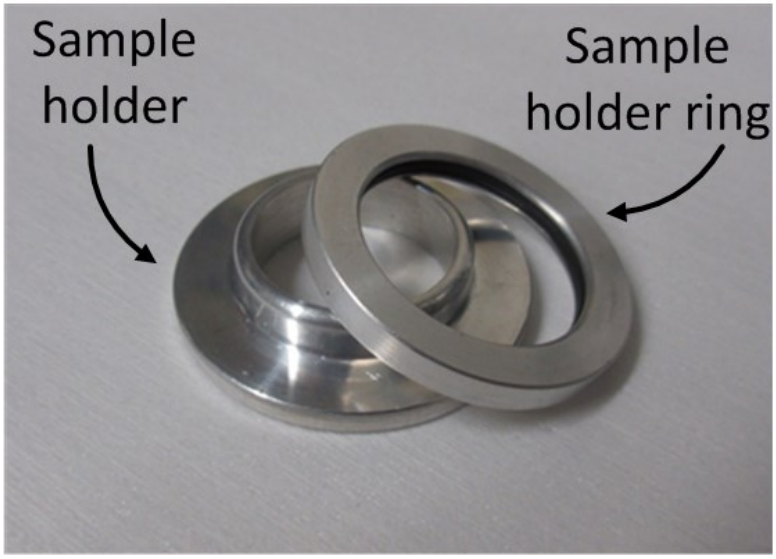

Fig. 5.37. A custom sample holder for XRD measurements. A sample can be prepared under argon, and sandwiched between two Mylar sheets. The mylar sheets are then pressed together by the sample holder ring (viton o-ring is imbedded in the sample holder ring) over the sample holder.

Fig. 5.38. Air-tight sample holder provided by Bruker AXS Inc. The PMMA plastic base with double-sided sticky tape (left) and the beryllium dome (right) that screws firmly to the o-ring seal on the base.

The polished LiZnP sample is shown in Fig. 5.36. The sample was sandwiched between sheets of Mylar® for protection against moisture and air. The 4.077 x 3.518 mm sample face was evaluated for crystal structure, lattice constant, *d* spacing, and orientation with a Bruker D2 CRYSO energy-dispersive x-ray diffractometer. The EDXRD method utilizes rhodium optics with a spectrum of x-rays that are oriented incident the sample surface. The sample is rotated about the sample surface (crystal surface normal), ϕ angles, and diffracted x-rays (now 'monoenergic') are collected in an energy dispersive silicon drift detector. The collection of energies correspond to crystallographic directions, and once a minimum of two crystal directions are determined, the orientation of the crystal with respect to the normal axes, and parallel to the surface, can be calculated [93]. A collection of Laue peaks were found with the LiZnP sample between 5.0 – 6.5 keV, as shown in Fig. 5.39. The mere observation of these peaks proved that the sample was crystalline. Additionally, these peak locations were used to determine the main orientation, crystal structure, lattice constant and *d* spacing, by comparing to theoretical locations. A *guess* of the crystal structure, orientation and lattice constant was programed into the Bruker AXS Inc. software, which then calculated the theoretical peak positions based on the

input parameters, and compared these locations to the experimental peak locations. The best fit to theoretical calculations was determined to be a cubic crystal structure with main orientation of (220), a lattice constant of 5.885 Å, and *d* spacing of 2.081 Å. The lattice constant was slightly higher than that of what was determined from the synthesized material (5.751 ± 0.001 Å).

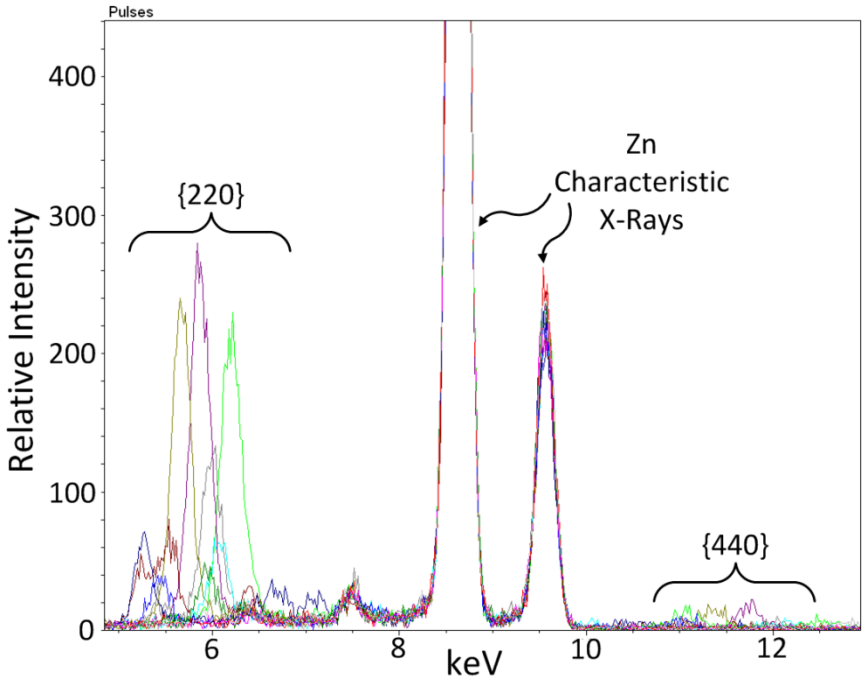

Fig. 5.39. The energy dispersive XRD spectrum. A crystal structure with a main orientation of (220) was determined. A lattice constant of 5.885 Å was determined based on the locations of the {220} Laue peaks.

The expected phase identification pattern was determined for LiZnP using PowderCell 2.4, shown in Fig. 5.40 [71]. The calculation was based on the lattice constant determined from the EDXRD lattice constant result, 5.885 Å, and molybdenum optics of a 0.71 Å wavelength. High-resolution out-of-plane measurements were first collected from the 4.077 x 3.518 mm LiZnP sample face, the same face analyzed by EDXRD. Diffraction was observed at $2\theta = 19.4620^{o}$ and $\Omega = 10.7294^{o}$. At this position, a ϕ scan was collected as shown in Fig. 5.41. From Fig. 5.41, multiple domains are evident in the sample. Ideally there would be four prominent peaks, 90^{o} apart corresponding to the (220) orientation. Intensity was maximized by parking the ϕ angle on the most intense peak location, 199.94^{o} ϕ, and a phase identification scan was

collected, as shown in Fig. 5.42. The (220) orientation is clearly prominent at 19.46^{o} 2θ which confirms with the EDXRD result. Additionally, the (440) orientation at 39.48^{o} 2θ was clearly seen and matches well with the theoretical position. The (440) orientation was also seen in the EDXRD scan where corresponding Laue peaks were observed between 10.75 – 12.5 keV as seen in Fig. 5.39. The 2θ axis was positioned on the (220) phase peak, and a rocking curve was collected as shown in Fig. 5.43. The full width at half maximum (FWHM) was measured to be 0.417^{o}. A rocking curve performed on a single crystal silicon standard (from Bruker AXS) yielded a FWHM of 0.004 degrees (14.4 arc seconds) for the Si (111) reflection, which indicates that the rocking curve FWHM broadening of the LiZnP sample is primarily from the mosaicity of the sample.

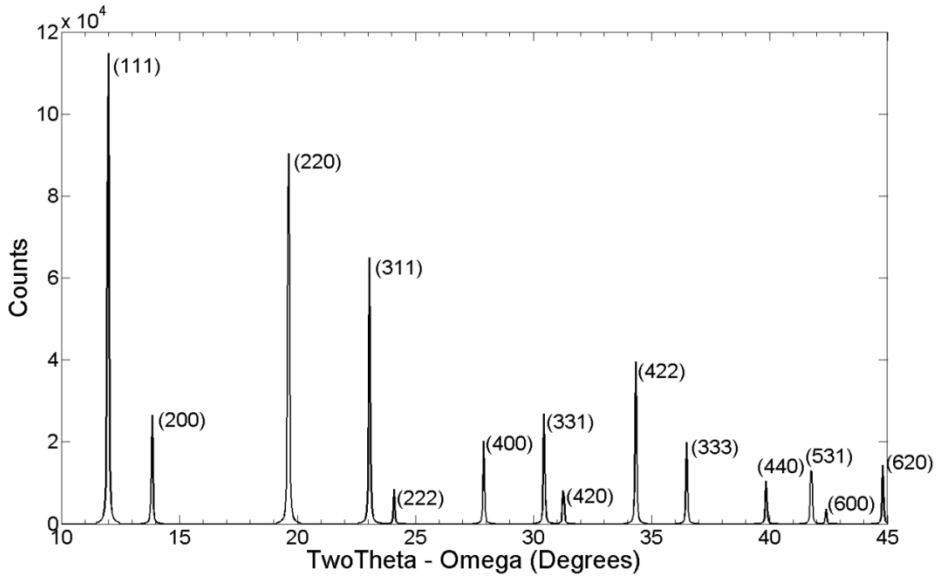

Fig. 5.40. The theoretical phase identification plot calculated with PowderCell 2.4 with a lattice constant of 5.885 Å and molybdenum optics.

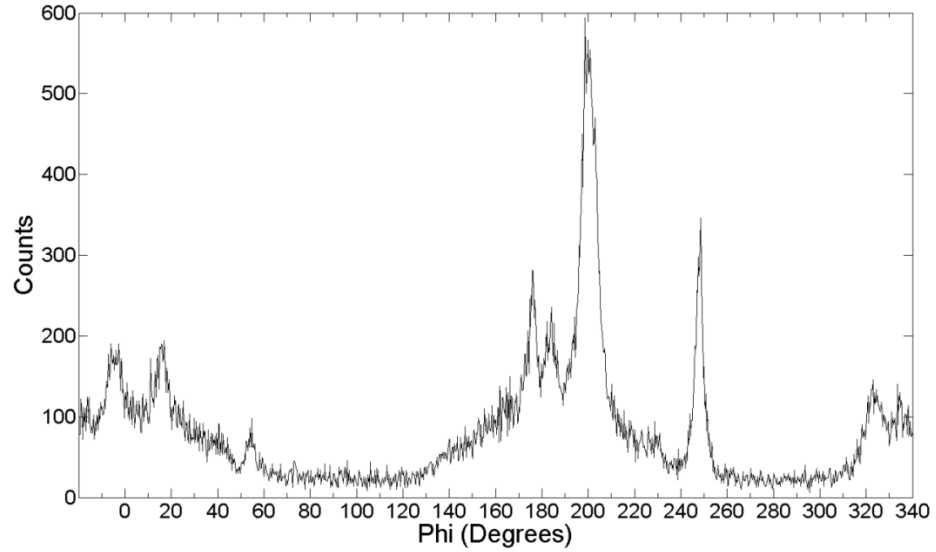

Fig. 5.41. A ϕ scan of the (220) main orientation. The array of peaks indicates multiple domains, or possible crystal twinning in the sample.

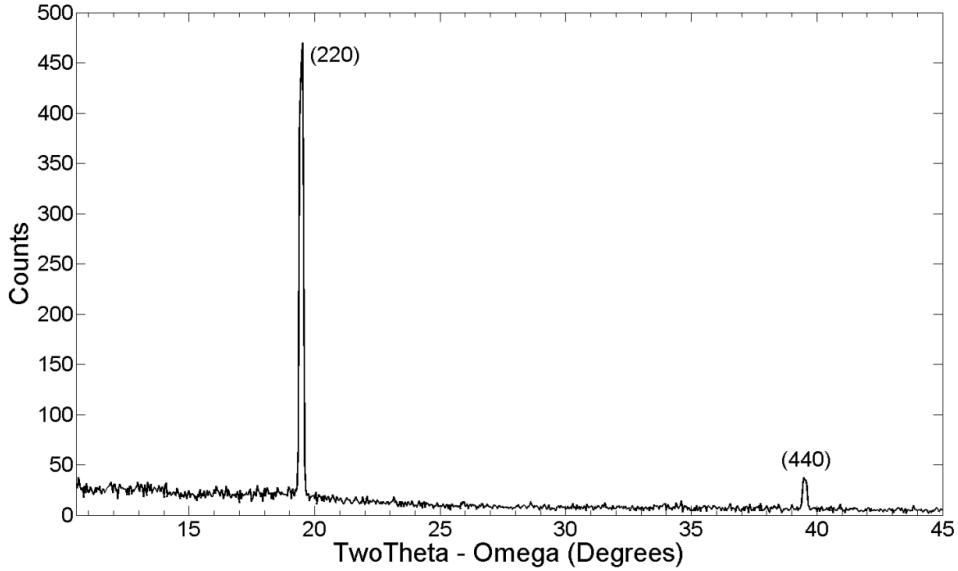

Fig. 5.42. Phase identification of main orientation. The (220) was most prominent and the (440) was also observed.

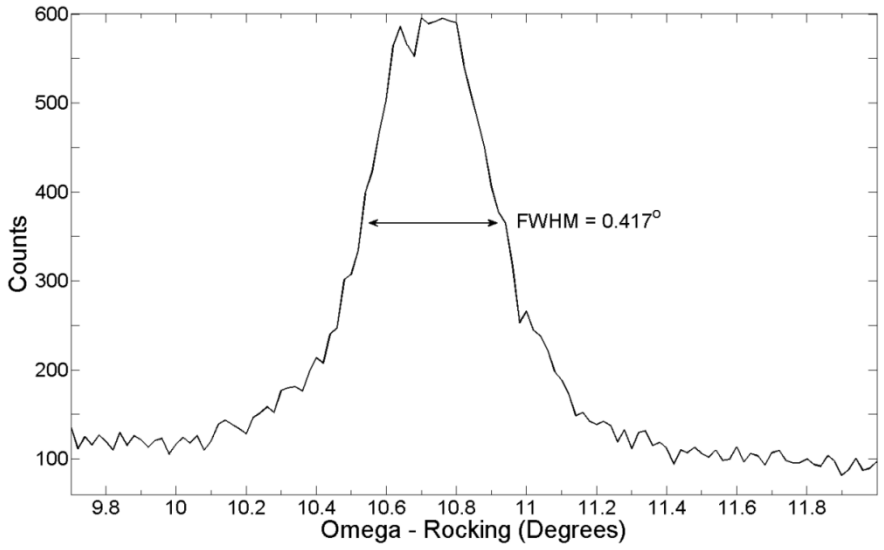

Fig. 5.43. An open detector rocking curve of the (220) orientation. A 0.417° FWHM was determined.

The ψ axis, the cradle (shown in Fig. 3.6 in Chapter 3), was moved down to explore the in-plane ordering of the sample. The angle between the (220) plane and other planes of interest are listed in Table 5.6. Diffraction was observed at 32.8560° ψ at complete optimization. A phase identification scan was collected which produced three prominent orientations, shown in Fig. 5.44. The peak located at 22.6° 2θ likely corresponds to the (311) phase, which is theoretically located at 23.05° 2θ. The other two phases likely belong to the (222) and (333) which are 35.26° from the (220). The peak located at 36.2° matches nicely to the theoretical position of the (333) phase at 36.5° 2θ. However, the peak located at 26.3° 2θ does not match well with the theoretical position of the (222) phase at 24.1° 2θ. This result indicates grain boundaries exist in the evaluated area of the sample, and multiple domains exist. The (400) orientation is theoretically located at 27.895° 2θ, which is a better match to the 26.3° peak, but is located 45° from the (220) orientation, where it would not likely be observed at 32.8560° ψ. Additionally, these domains may have a shift in lattice constants from what was seen in the (220) main orientation, thus adjusting the resultant *d* spacing.

Table 5.6. The angle between the (220) plane and the selected crystalline plane. See Appendix A.1 for calculation details.

(*hkl*) plane	Angle
(422)	30^o
(311)	31.48^o
(222)	35.26^o
(400)	45^o

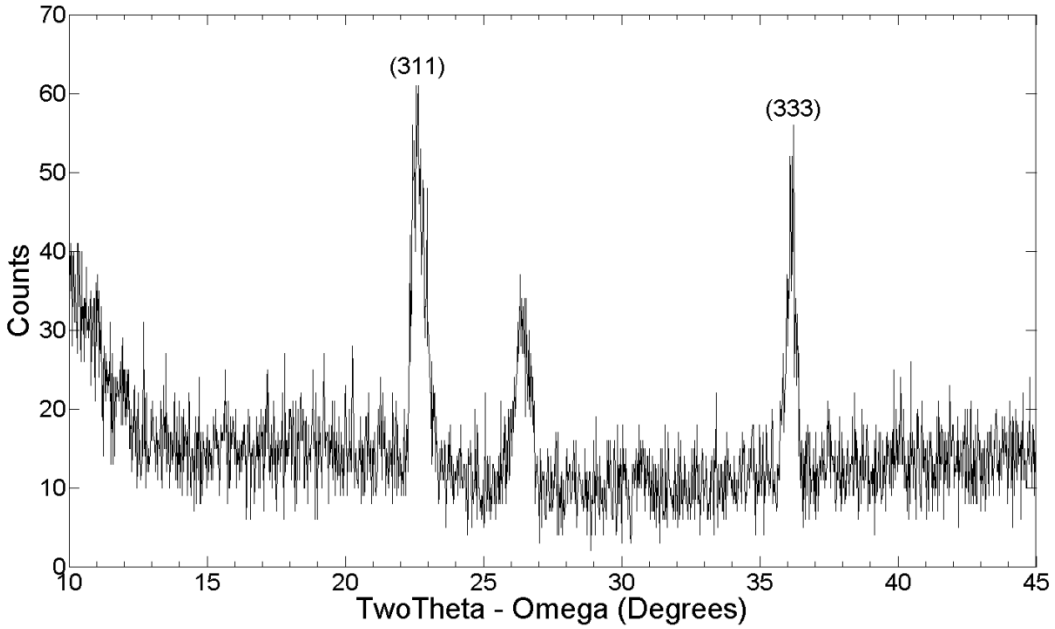

Fig. 5.44. In-plane phase identification measurement at 32.8560^o ϕ. The (311) and (333) orientations were identified. The peak in the middle may correspond to the (222) or (400) orientations, which is an indication of multiple domains in the sample.

At the same angle of ψ, the 2θ axis was parked at the (311) phase, 22.6^o, and a rocking curve was collected, shown in Fig. 5.45. The FWHM was determined to be 0.294^o. The same order of magnitude FWHM was found for the out-of-plane (220) and in-plane (311) measurements, indicating a reasonable crystallinity. Additionally, the (311) FWHM indicates an in-plane ordering exists; however, multiple domains were evident.

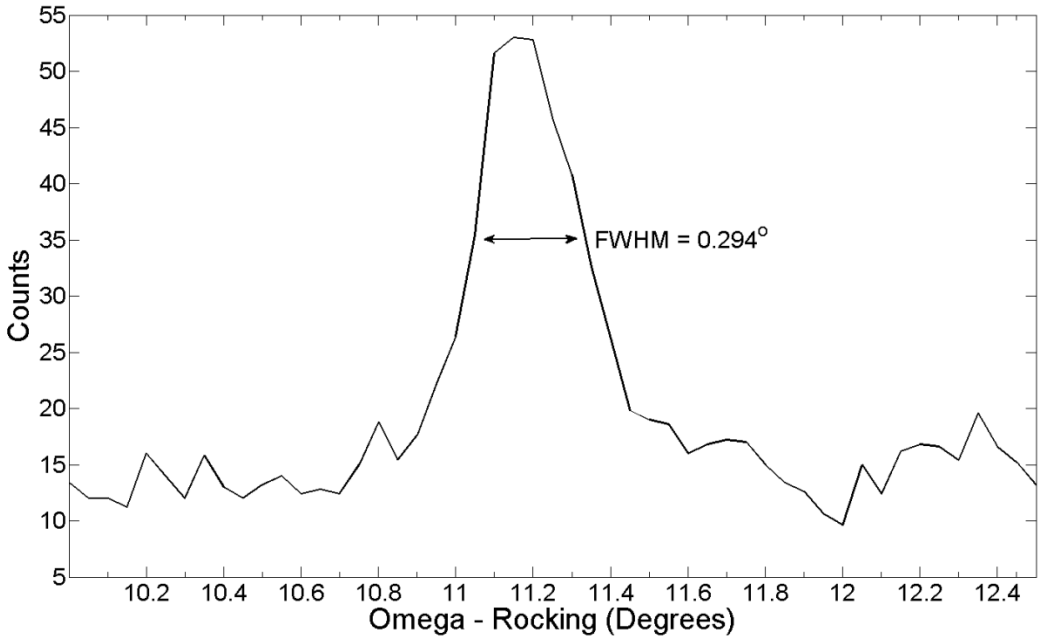

Fig. 5.45. An in-plane rocking curve of the (311) orientation. A 0.294° FWHM was determined.

5.3.4 Crystal Growth Process of LiZnAs

LiZnAs was synthesized, as described in section 5.1.1, in small batches up to 6.0 grams. The synthesized material was purified by a static sublimation process as described in section 5.2.1. LiZnAs material was subsequently grown into bulk crystals under the following high-temperature vertical Bridgman technique, similar to the process explained in section 5.3.1. A tantalum vessel was loaded and sealed, containing a pyrolytic graphite crucible, filled with approximately 1.0 – 8.0 grams of LiZnAs powder, depending on the desired ingot size. The tantalum vessel was loaded into the vacuum chamber, connected to a low-voltage, high current power source. The system was then evacuated and maintained at a vacuum between 300 – 400 mTorr argon pressure. The current was ramped from 0 amps to approximately 290 – 305 amps over the course of at least an hour, until the optical thermometer measured approximately 1240 °C at the tantalum surface. Temperature was maintained at 1240 °C for at least an hour. The system was then ramped down to room temperature over the following 40 hours. The vessel was extracted from the chamber, and opened with a pipe cutter under a pure argon environment. The

ingot was harvested, and individual samples were cut from the ingot using a Laser Technology West Ltd. CS400 diamond wire saw for further processing.

5.3.5 Bulk Crystalline LiZnAs Ingots

The bulk crystal growth process produced ingots of various sizes, the largest being ≈13.0 mm in length and 9.6 mm in diameter. The ingot grown from purified material was 9.6 mm in diameter and 4.2 mm in length. A sample cut from the purified ingot is shown in Fig. 5.46. The suggested melting, or decomposition, temperature reported by K. Kuriyama was not confirmed, nor observed in this study [57]. Numerous attempts to grow LiZnAs by melt technique using crucible lined quartz ampoules always resulted in non-congruent melting up to temperatures ≤ 1150 ^{o}C. Temperatures greater than 1150 ^{o}C resulted in the expansion of the soft quartz due to the high vapor pressure in the ampoule, and often resulted in ampoule rupture as described in Chapter 4. Bulk crystal growth of LiZnAs requires temperatures slightly above the threshold of conventional resistive coil furnaces that typically have a 1200 ^{o}C upper limit under continuous operation. Optical thermometer readings, sampled through a quartz window of the crystal growth chamber, typically indicated temperatures between 1230 – 1250 ^{o}C (depending on the focus of the optical thermometer), which allowed for the congruent melt of LiZnAs.

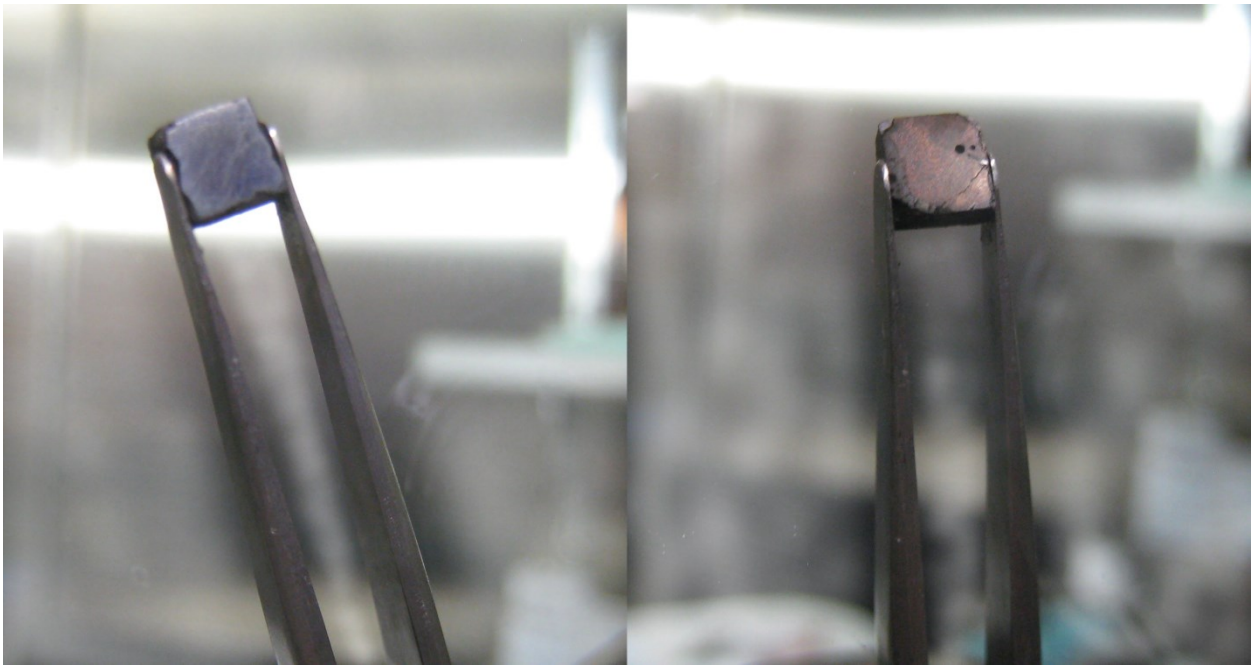

Fig. 5.46. Both sides of a LiZnAs sample, the sample used for x-ray diffraction analysis with dimensions of 2.100 x 4.060 x 4.155 mm^3.

5.3.6 Bulk LiZnAs Crystallinity

A LiZnAs sample was diced to 4.155 x 4.060 x 2.100 mm^3, and XRD analysis was performed on one side of the 4.060 x 4.155 mm^2 face. The sample was mounted into a polishing fixture by paraffin wax. The sample face was polished with a series of silicon carbide polishing papers ranging from 15.3 – 2.5 micron grain size, ANSI grit: 600 (P1200), 800 (P2400), and 1200 (P4000) [105, 106]. An example of a polished sample of purified LiZnAs is shown in Fig. 5.46. The polished sample was mounted under argon between two Mylar sheets using a custom sample holder designed to keep the sample air-tight as shown in Fig. 5.37. Following which, the sample was characterized on a D2 CRYSO energy-dispersive X-ray diffractometer (EDXRD), in order to determine the out-of-plane orientation, degree of miscut and *d* spacing. The sample was then mounted into an air-tight (PMMA) plastic sample holder with a plastic dome, shown in Fig. 5.38, using double sided tape and under argon. The sample was then characterized for out-of-plane orientation, mosaic spread and in plane ordering using a high-resolution D8 DISCOVER x-ray diffractometer.

The polished LiZnAs sample was sandwiched between Mylar sheets for protection against moisture and air. The 4.155 x 4.060 mm^2 sample face was evaluated for crystal structure and orientation with a Bruker D2 CRYSO energy-dispersive x-ray diffractometer (EDXRD). The EDXRD method utilizes a rhodium x-ray source that produces a polychromatic x-ray beam, a monocapillary optic to collimate the x-ray beam to a spot, and an energy dispersive silicon drift detector. Energy plots of the diffracted beam are collected as the sample is rotated about the crystal surface normal (phi). Peaks in the diffracted energy plots correspond to Laue reflections from the crystal. The out of plane *d* spacing, degree of miscut and main orientation can be determined from these plots [93]. In the case of the LiZnAs sample, Laue peaks are observed for energy values ranging from 2.6 – 3.7, 5.3 – 7.6, and 8.1 – 10.3 keV, as shown in Fig. 5.47. The mere observation of these peaks is evidence of crystalline ordering in the material under analysis. The collected spectrum was analyzed using the D2 CRYSO Measure analysis software and a main orientation of (110) was determined. In addition, an approximate *d* spacing and lattice constant of the LiZnAs crystal were determined at 1.9 Å and 5.5 Å respectively. The lattice constant observed in this case is different from that of the synthesized material, which had a lattice constant of 5.939 ± 0.002 Å (section 5.1).

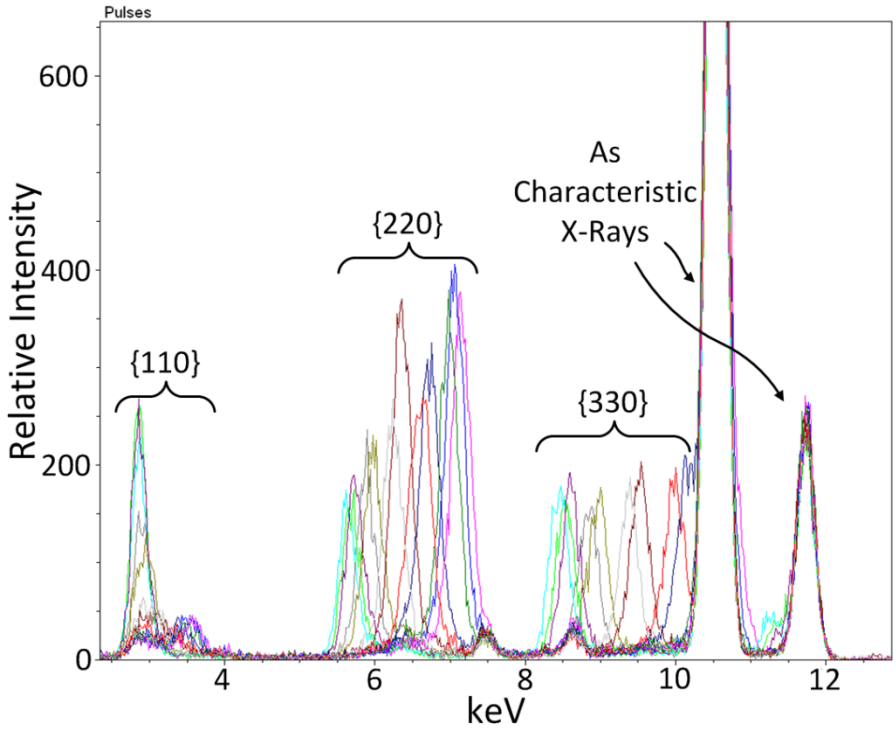

Fig. 5.47. The EDXRD spectrum for the LiZnAs sample. {110}, {220} and {330} Laue peaks and characteristic xray peaks from arsenic were observed. Each peak within a collection (i.e. {110}, {220} and {330}) corresponds to a single orientation within the family of crystalline planes.

Out-of-plane high-resolution XRD measurements were first collected from the 4.155 x 4.060 mm^2 LiZnAs sample face, the same face analyzed by EDXRD. A phase identification scan was collected as shown in Fig. 5.48. Four peaks were identified with each corresponding to the (110), (220), (330) and (440) LiZnAs with a P-43m space group. The indexing procedure was performed using the TOPAS (Bruker AXS Inc.) software to identify the space group [107]. The identified space group differs from what was seen from synthesized and purified powders as discussed sections 5.1 and 5.2, and what was reported by Bacewicz, et. al [60] where a F-43m space group was characterized for LiZnAs powders. Pictorial representation of each LiZnAs cubic unit cell for space groups F-43m and P-43m is shown in Fig. 5.49. Refinement of the phase identification pattern, Fig. 5.48, using TOPAS yielded a lattice constant of 5.5146 ± 0.0003 Å, which was consistent with what was determined from the EDXRD measurement. The Whole Powder Pattern decomposition approach was used in the refinement procedure [102]. Theoretical phase identification patterns of LiZnAs with a lattice constant of 5.5146 Å for the two different

space groups were determined using PowderCell 2.4, and are shown in Fig. 5.50 and Fig. 5.51 as identified with molybdenum optics of a 0.71 Å wavelength [71].

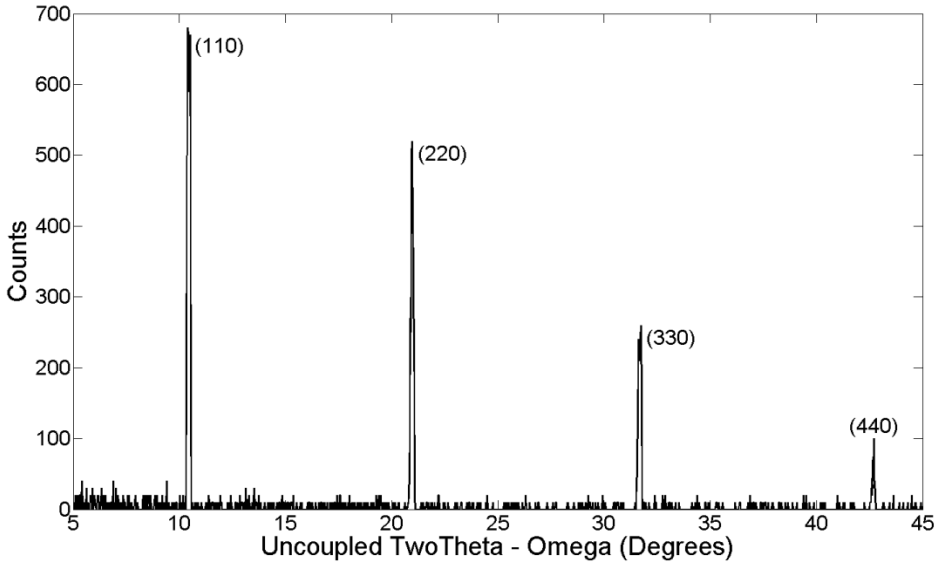

Fig. 5.48. A phase identification scan of the bulk LiZnAs sample main orientation with a 0.1471^{o} offset, ϕ at -2.20^{o}.

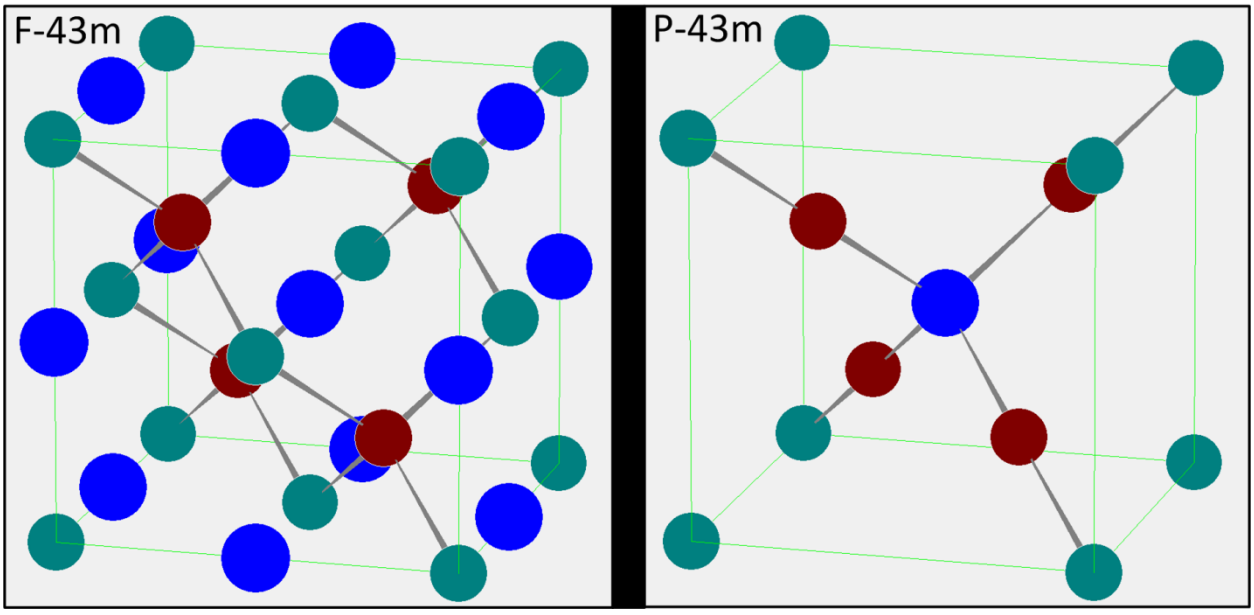

Fig. 5.49. The LiZnAs unit cells for space group F-43m (left) and P-43m (right). The red atoms are arsenic, blue are lithium, and green are zinc.

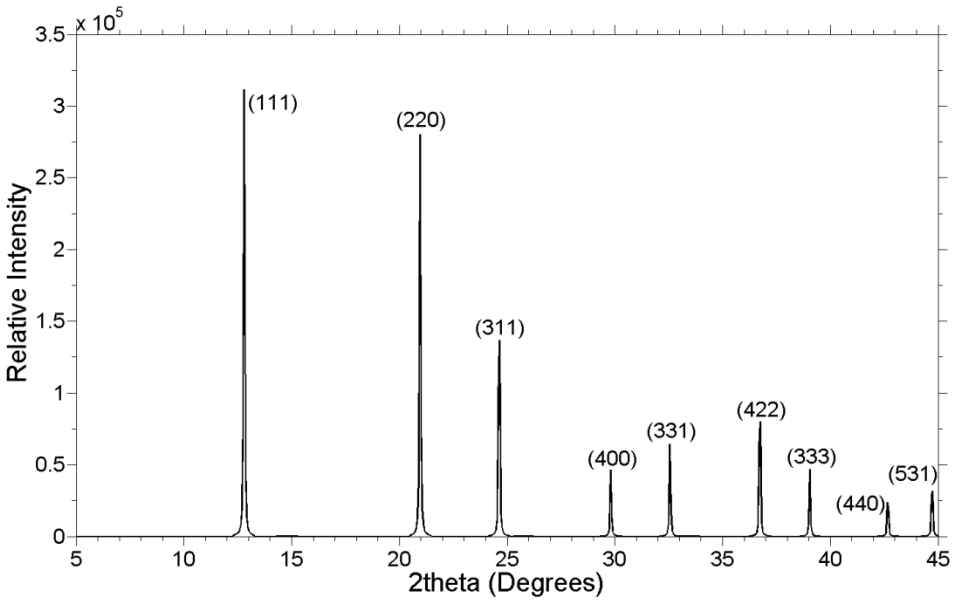

Fig. 5.50. Theoretical phase identification pattern of a polycrystalline LiZnAs with F-43m space group, using molybdenum $K_{\alpha 1}$ radiation. The calculation was performed using PowderCell 2.4 [71].

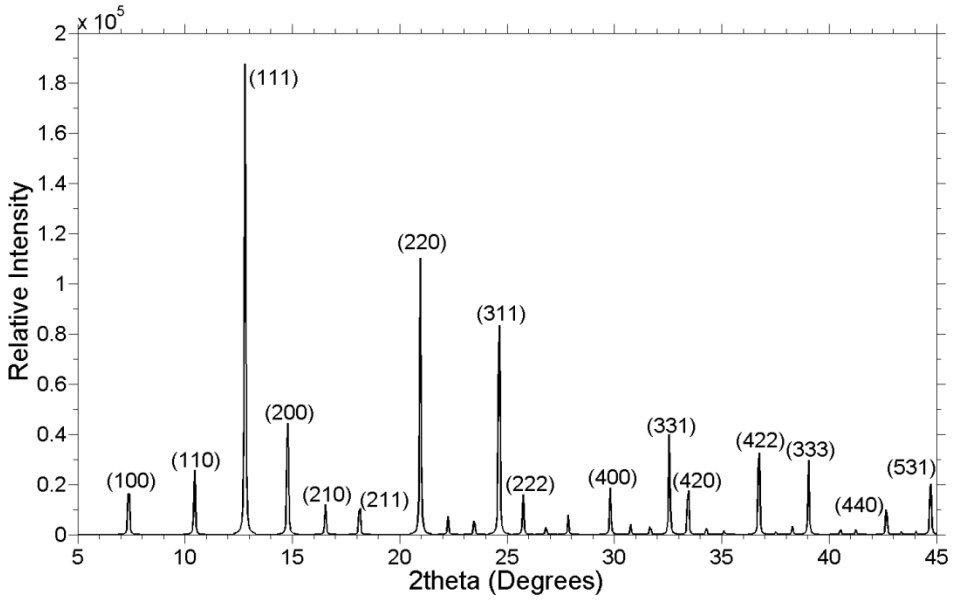

Fig. 5.51. Theoretical phase identification pattern of a polycrystalline LiZnAs with P-43m space group, using molybdenum $K_{\alpha 1}$ radiation. The calculation was performed using PowderCell 2.4 [71].

The crystalline perfection of the sample was examined by performing open detector rocking curves. The 2θ drive was positioned on the (220) reflection (20.931^{o}), and a rocking

curve was collected, as shown in Fig. 5.52. The full width at half maximum (FWHM) was determined to be 0.235°. In addition, it was observed that the peak profile is not Gaussian, which could indicate the presence of secondary or additional domains in the sample.

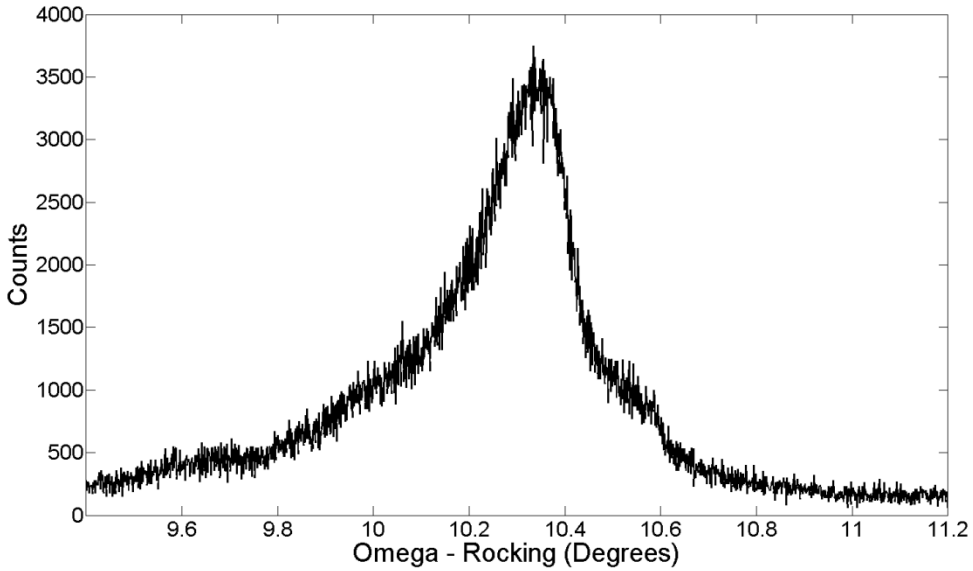

Fig. 5.52. Rocking curve of (220) LiZnAs. A full width at half maximum of 0.235° was determined.

The in-plane ordering of the sample was examined by carrying out off-axis phi scans on the (211) LiZnAs reflection. This was performed by tilting the sample in the ψ direction, in angles desirable for in-plane orientations as listed in Table 5.7. Five prominent reflections were observed at 32.6°, 153.0°, 213.2°, 332.8°, and 336.6°, as shown in Fig. 5.53. Using vector projection math (Appendix A.2), it is evident that the projection of the off-axis (211) LiZnAs on the (110) LiZnAs is along the [1$\bar{1}$2] LiZnAs direction. In other words, if the sample were to be a perfect single crystal, four reflections from the {211} LiZnAs family of planes should be observed in the phi scan. In addition, the angular relationship between the {211} LiZnAs planes in the phi scan should match the angular relationship exhibited between the <112> LiZnAs directions projected on the (110) LiZnAs surface, as shown in Fig. 5.54. However, five reflections were observed in the off-axis (211) LiZnAs phi scan, as shown in Fig. 5.53. This result is a clear indication that off-axis reflections are coming from multiple domains in the sample. Additionally, some of the (211) LiZnAs reflections are missing from the phi scan due to

a high degree of miscut in the polished sample. Complete interpretation of the phi scan results suggests that three major in-plane domains are present in the sample. The in-plane crystallographic relationships in the particular sample that were characterized for one of the domains with respect to the incident x-rays is shown in Fig. 5.55. An off-axis rocking curve of the (211) orientation was also collected, and resulted in a FWHM of 0.179^{o} as shown in Fig. 5.56. The rocking curve looks similar to the out-of-plane rocking curve shown in Fig. 5.52. , which is further indication of multiple domains in the sample.

Table 5.7. The angle between the (220) plane and the selected crystalline plane. See Appendix A.1 for calculation details.

(*hkl*) plane	**Angle**
(211)	30^{o}
(311)	31.48^{o}
(222)	35.26^{o}
(400)	45^{o}

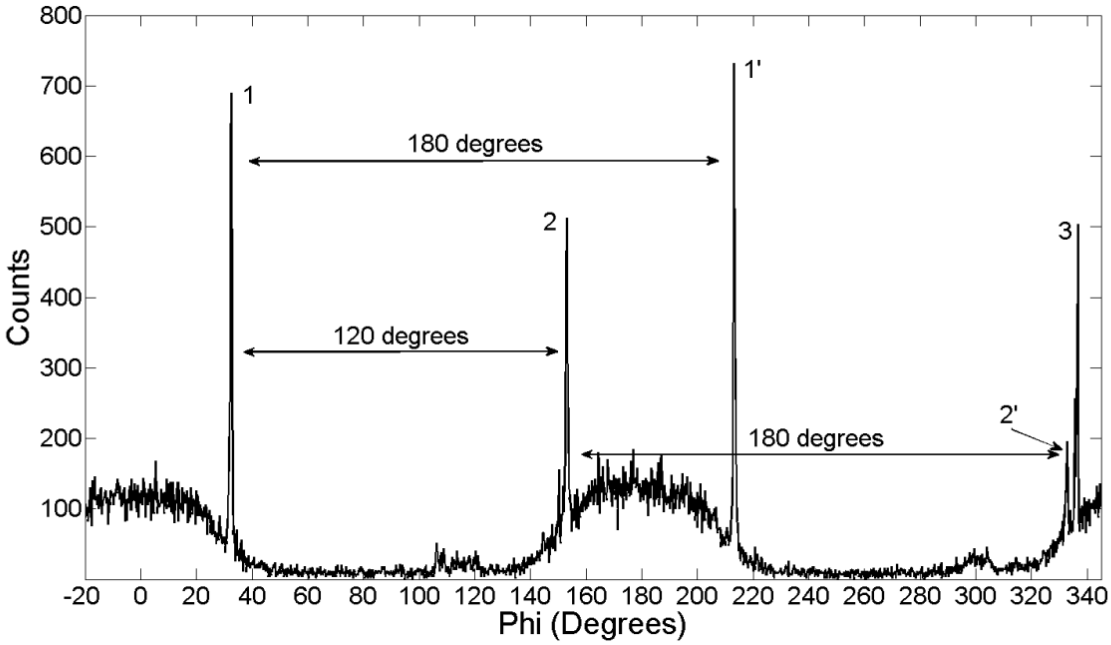

Fig. 5.53. An off-axis φ scan of the {211} planes collected at 30.6646° ψ, 19.1377° 2θ, 12.9185° Ω. Peaks 1 and 1′ belong to one domain, and peaks 2 and 2′ belong to a second domain, and 3 belongs to a third domain

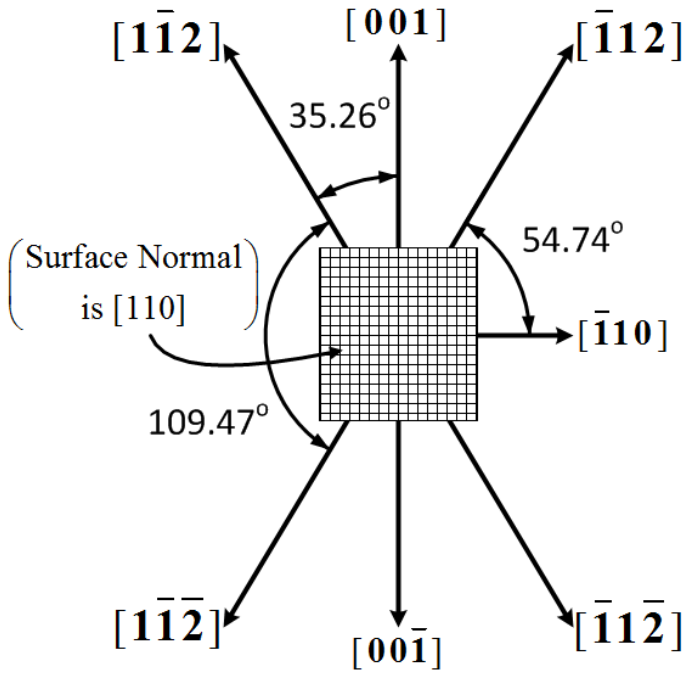

Fig. 5.54. A diagram of the angular relationship between the <112> LiZnAs directions on (110) LiZnAs.

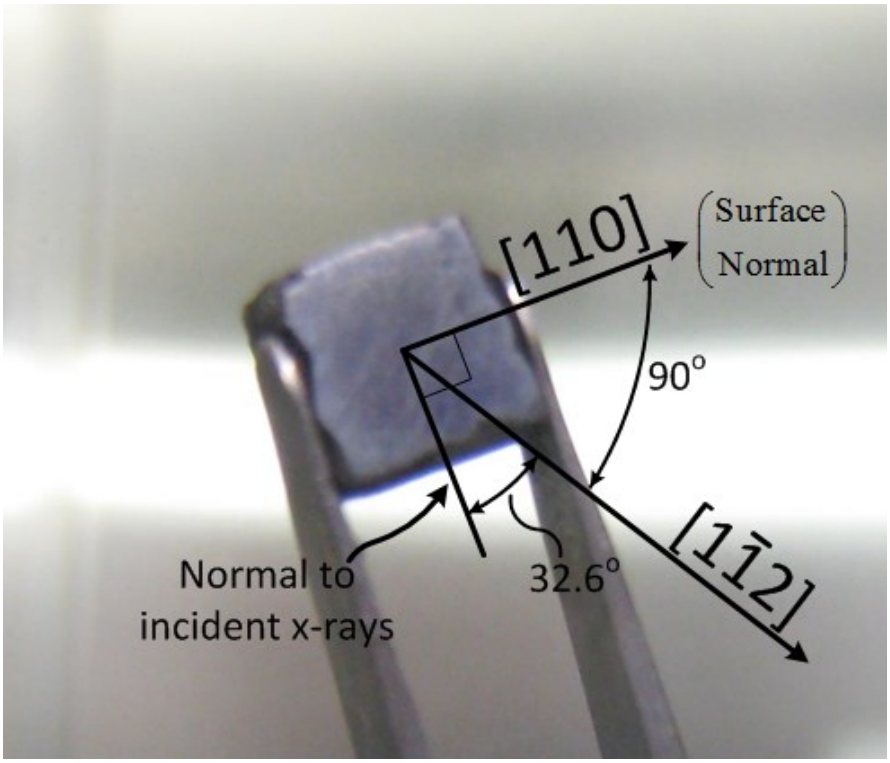

Fig. 5.55. The LiZnAs sample labeled with crystallographic relationships for the surface normal and the first [1$\bar{1}$2] *domain observed from the off-axis phi scan.*

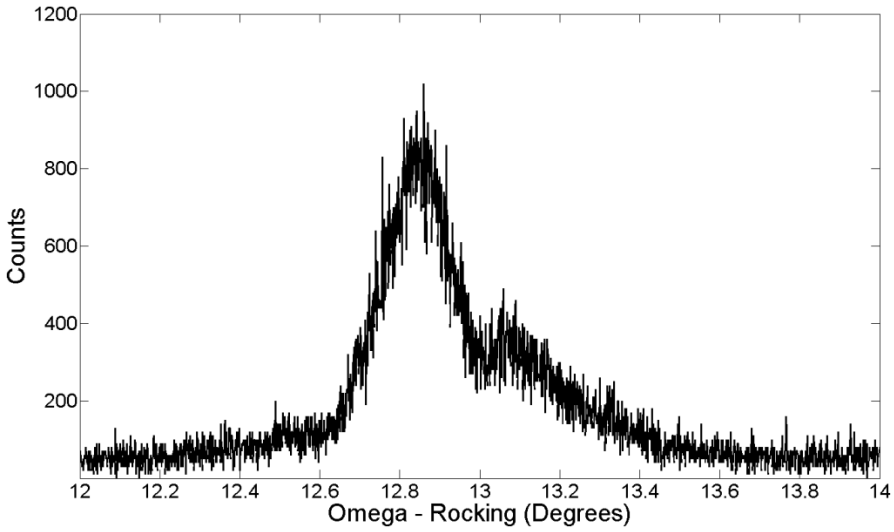

Fig. 5.56. An off axis rocking curve of the (211) orientation collected at 213.703° φ, 18.96° 2θ.

It is evident that the space group and lattice constant of the bulk LiZnAs crystal is different from the synthesized (5.939 ± 0.002 Å) and purified (5.901 ± 0.002 Å) LiZnAs

powders as described in sections 5.1.2 and 5.2.3. The high-temperature crystal growth method employed for growing bulk crystalline ingots of this material likely led to this change. The LiZnAs crystals grown in this study exhibited a P-43m space group instead of the more commonly observed F-43m space group. Therefore, these LiZnAs crystals do not have lithium atoms filling all the interstitial sites, unlike what is observed in the case of the F-43m space group (Fig. 5.49), and as a result the lithium content was reduced by ¾ (when considering all lithium atoms shared by surrounding unit cells). Lithium is highly volatile, and when these lithium atoms are located in interstitial sites where they may not be tightly bound in the lattice, excessive heat treatment can cause lithium depletion of lithium atoms [108]. The lattice parameter change can be explained by considering semiconductor doping, or adding an excess of a particular element for compensation purposes for desired electrical properties [73, 109]. When this practice is performed, the additives in the semiconductor can alter the lattice parameters, thereby, changing the lattice constant and *d*-spacing. In this study, the starting material was purified by a static sublimation process as described in section 5.2. However, an excess of an impurity yet remaining in material may be acting as a dopant, or a lack there of due to lithium loss in this case, which can form vacancies, and therefore altering the lattice constant. Here, the lattice constant reduction was likely caused by the reduction of lithium atoms in the unit cell. For the desired application of neutron detectors, it may be necessary for device performance, or neutron sensitivity, that the bulk crystallization process be modified, where an excess of lithium is added to purified powders, where the lithium over-pressure may keep the volatile lithium from escaping. Encapsulation using a high-temperature material such as boron oxide may also be required to keep the correct lithium balance for a lithium-rich F-43m LiZnAs unit cell. Nevertheless, the relatively high concentration of lithium that exists in the P-43m LiZnAs unit cell is still useful provided the material is still a semiconductor with a wide bandgap. The device processing techniques, electrical characterization (resistivity, mobility-lifetime, trapping time), and neutron sensitivity measurements using these newly synthesized materials are presented and discussed in Chapter 6.

Chapter 6 : DEVICE FABRICATION AND CHARACTERIZATION

The important thing is to never stop questioning

- ***Albert Einstein***

LiZnAs and LiZnP bulk crystals were processed into devices for electrical characterization and radiation sensitivity testing. Resistivity was calculated based on the I-V characteristics of the sample. The mobility-lifetime products were calculated based on data collected by the Transit Charge Technique [110, 111]. Laser induced signal of 337 nm was traced with LiZnAs samples using a trans-impedance amplifier, as measured with an oscilloscope. Thermal neutron sensitivity was studied using the thermal neutron diffracted beam port, and radial neutron beam port of the Kansas State University TRIGA Mark II nuclear reactor.

6.1 Device Processing

Numerous ingots of LiZnP and LiZnAs were cut and polished as described in Section 5.3.3 for x-ray diffraction measurements. These samples were further processed into devices for electrical testing, and radiation sensitivity. Samples were polished of any residual hygroscopic contamination that may have occurred during x-ray measurements with a mineral oil slurry over 4000 grit SiC paper. The surface of the sample was wiped clean with a hexane saturated cotton swab. Before being further processed into devices, LiZnP and LiZnAs were evaluated for density by determining a volume (based on the device dimensions) and weight. Three samples of purified LiZnP and LiZnAs were evaluated, were the results are shown in Table 6.1. The density for LiZnP and LiZnAs were determined at 2.07 ± 0.02 g cm^{-3} and 2.36 ± 0.03 g cm^{-3},

respectively. The standard deviation for each measured value was determined based on a Gaussian standard deviation from a mean (Appendix C).

Table 6.1. Results from an approximation of density for LiZnAs and LiZnP. Standard error was based on a Gaussian standard deviation from a mean (Appendix C).

	Samples	Dimensions (mm)	Weight (g)	Density (g/cm^3)
LiZnP	1	2.020 x 3.518 x 4.077	0.0600	2.07
	2	1.761 x 2.520 x 3.508	0.0328	2.11
	3	1.928 x 4.071 x 2.221	0.0356	2.04
			Average	**2.07 ± 0.02**
	Samples	Dimensions (mm)	Weight (g)	Density (g/cm^3)
LiZnAs	1	2.100 x 4.060 x 4.155	0.0825	2.33
	2	1.790 x 2.101 x 4.180	0.0363	2.31
	3	1.492 x 2.359 x 4.060	0.0348	2.44
			Average	**2.36 ± 0.03**

Samples were placed into a shadow mask designed to couple into the planetary of an electron-beam evaporator, as shown in Fig. 6.1 and Fig. 6.2. The mask in Fig. 6.1 was designed to hold large samples, between 3.0 mm x 3.0 mm and 5.0 mm x 5.0 mm. The mask in Fig. 6.2 was designed to hold smaller samples, between 1.0 mm x 1.0 mm and 3.0mm x 5.0mm. The loaded shadow mask was placed into an air-tight container for removal from the argon glove box. This containment prevented moisture exposure to the samples in the transition between the argon glove box and while being transported to the electron-beam evaporator for a contact evaporation. The air containment was opened, and the shadow mask was quickly loaded onto the planetary of the electron-beam evaporator, and the door was shut, followed by immediate evacuation of the chamber. Contacts were evaporated onto the polished surfaces of the ternary material; 500 Å of titanium followed by 8,000 - 10,000 Å of gold. Once complete, the electron beam chamber was back-filled with nitrogen, opened, and the shadow mask (containing the samples) was removed quickly, placed into the argon glove box anti-chamber and evacuated.

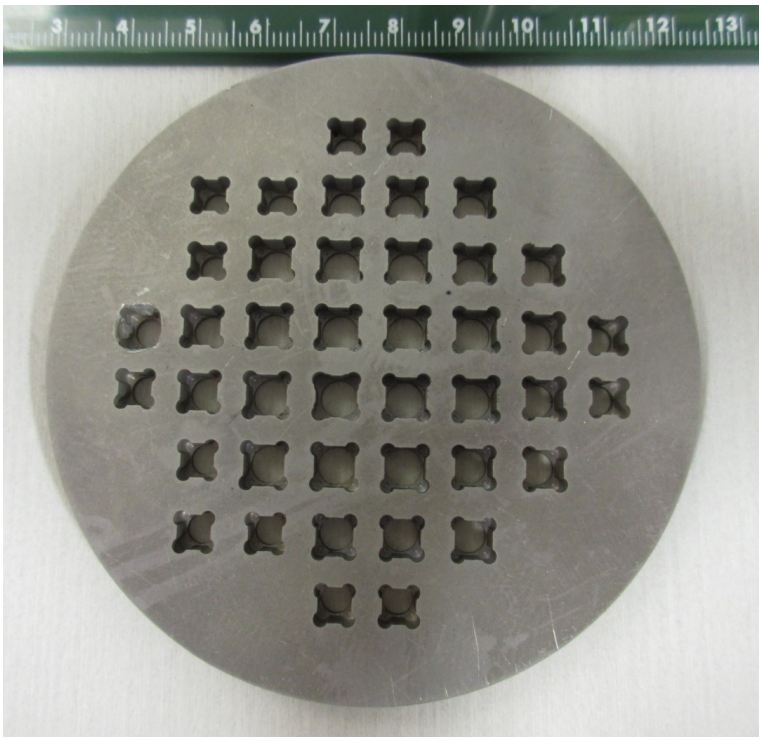

Fig. 6.1. A shadow mask designed for sample sizes between 5.0 x 5.0mm and 3.0 x 3.0mm.

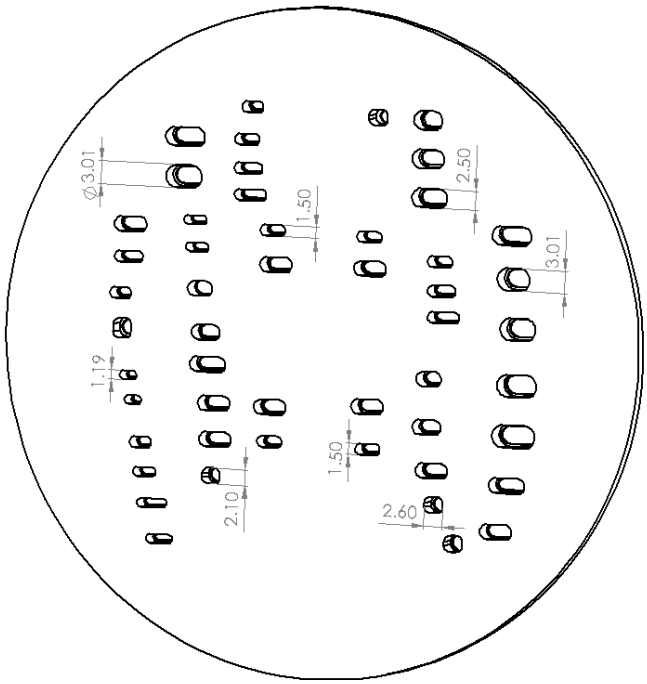

Fig. 6.2. A shadow mask designed to hold samples of all different sizes between 1.0 mm x 1.0 mm and 3.0mm x 5.0mm (units in mm).

6.2 Coating Materials

Nowotny-Juza compounds are hygroscopic and require methods to encapsulate the devices to prevent decomposition during testing, and other experimental analysis, when outside a moisture-free environment. Nowotny-Juza material that was not hermetically sealed or encapsulated over the time of exposure to humidity in air, would lose its rigidity and eventually decompose into a fine powder. Shown in Fig. 6.3 is a sample of LiZnP with silver epoxy contacts on two sides with a coat of HumiSeal® aerosol electrical conformal encapsulation. Later, the sample was polished of all coatings so the ternary material was exposed. After approximately 48 hours, a large portion of the sample was already decomposing into a powder, as shown in Fig. 6.4. A little portion of the silver epoxy contact was left on the sample surface, and appeared to help keep the material together. However, after a month of exposure in atmospheric conditions, the sample completely decomposed into a mix of gray and brown powders, as shown in Fig. 6.5. As exposure to air continued (> 2 months), eventually all of the powder converted to a gray color, as shown in Fig. 6.5. These comparisons are examples of how atmospheric conditions affect the Li-based ternary powders and bulk crystals. Generally only minutes of atmospheric exposure tarnishes the sample surface, yet can easily be polished away in an argon atmosphere; however, long exposures results in detrimental material degradation.

Fig. 6.3. A LiZnP sample with a silver epoxy contacts on two sides with HumiSeal® encapsulating the remaining sides

Fig. 6.4. The repolished LiZnP sample after approximately 48 hours of exposure to air.

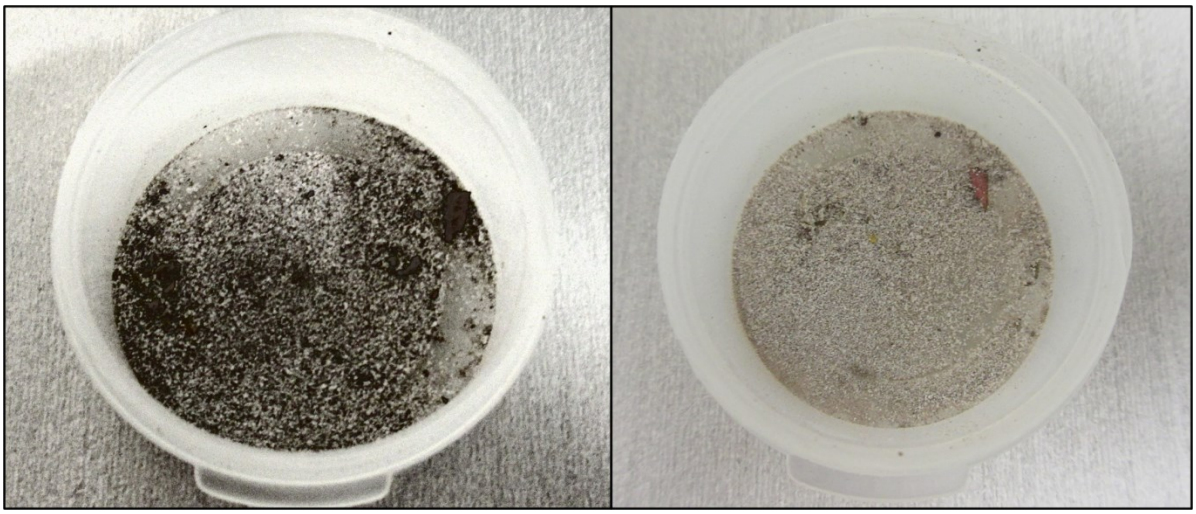

Fig. 6.5. The repolished LiZnP sample after 1 month (left) of exposure to air, and after >2months (right) of exposure to air.

6.2.1 HumiSeal® Coatings

HumiSeal® was explored as a potential hermetic coating because it has been used water resistant electrical coatings for over 50 years [112]. The most convenient type was HumiSeal®

1B73 spray. The bottle was loaded into the glove box, and was easily sprayed over a sample surface. The coating was allowed to dry, and followed by coating the other side. This method however did not pass extended lifetime testing. The coating would bubble, and not always congruently cover the sample, resulting in areas of exposed portions that would become contaminated by moisture.

Because HumiSeal® type 1B73 spray unfortunately did not perform well, a liquid version of HumiSeal®, type 1A20 was used. The single component liquid polyurethane coating was placed into a Ball® jar, and moved into an argon glove box. The liquid was painted onto the surface of a ternary sample, and allowed to cure. This material did not bubble as much as the aerosol spray, however, it would begin to flake, or detach from the material surface after an extended amount of handling and testing[14]. When flaking was observed, samples were reprocessed before further testing.

6.2.2 Other conformal coatings and UV transparency

Other coatings were studied as conformal coatings with a requirement that they needed to be transparent to ultra-violet light. A 337 nm nitrogen laser was used to induce charge in ternary samples, as detailed in Section 6.5. A coating was necessary to allow light to pass through, interact in the sample and then pass through the back of the sample through the conformal coating. Four coatings were studied, 3M Scotch-Weld DP-270 (clear), Devcon, Inc. 2 Ton® (clear), Epoxy Technology®, Inc. 301-2, and HumiSeal® 1A20. Each of the coatings were applied to a quartz disk (quartz is transparent to 337 nm photons). Each was tested to observe the amount of incident light that would pass through the coating, as shown in Fig. 6.6.

[14] It is likely that the surface was decomposing due to reaction with the HumiSeal 1A20 encapsulate, or an area of the sample was not completely encapsulated, causing surface decomposition.

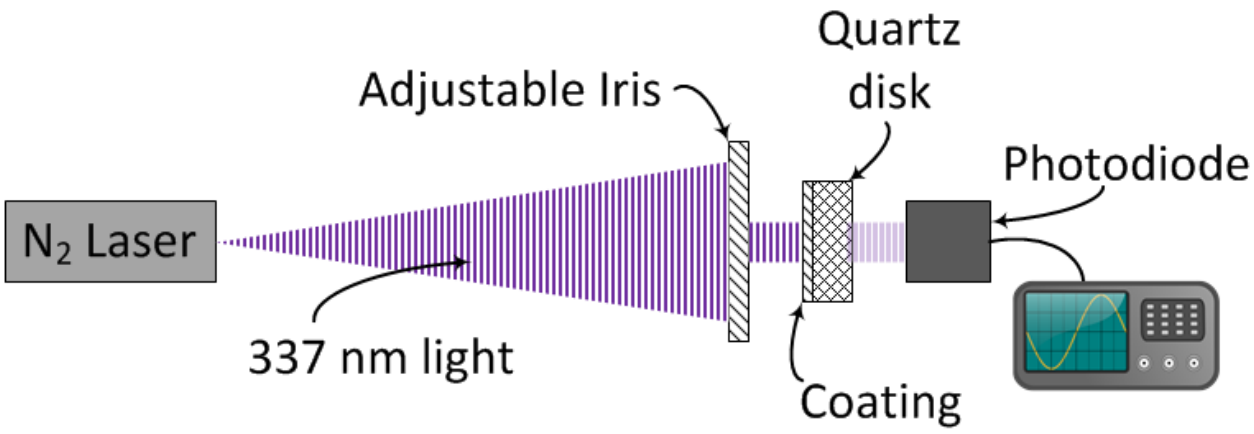

Fig. 6.6. The experimental arrangement for testing the 337 nm transparency of certain conformal coatings.

The incident light was first measured with no quartz disk in the beam (full intensity) for a baseline voltage output pulse observed on an oscilloscope as measured with a silicon photodiode (Fig. 6.6). Afterwards, a blank quartz disk was mounted between the adjustable aperture and photodiode, and then irradiated with the 337 nm laser. Full transmission of the 337 nm light was observed as shown in Fig. 6.8. The uncoated blank was replaced with a quartz disk[15] that had an encapsulation layer one of the four coatings applied to the surface. The resulting pulse height of transmitted light for each candidate encapsulate is shown in Fig. 6.9, Fig. 6.10, Fig. 6.11 and Fig. 6.12. The HumiSeal® 1A20 was found to absorb the highest amount of 337 nm light, as shown in Fig. 6.11; whereas the Epoxy Technology® 301-2 was determined to be the most transparent coating, as shown in Fig. 6.12. The Epoxy Technology®, Inc. 301-2 was selected as the best candidate for a ternary material conformal coating, and tested further testing confirmed the coating did not react with the ternary compound surface.

[15] Quartz disks were acquired from Quartz Scientific Inc., where each disk had the same thickness.

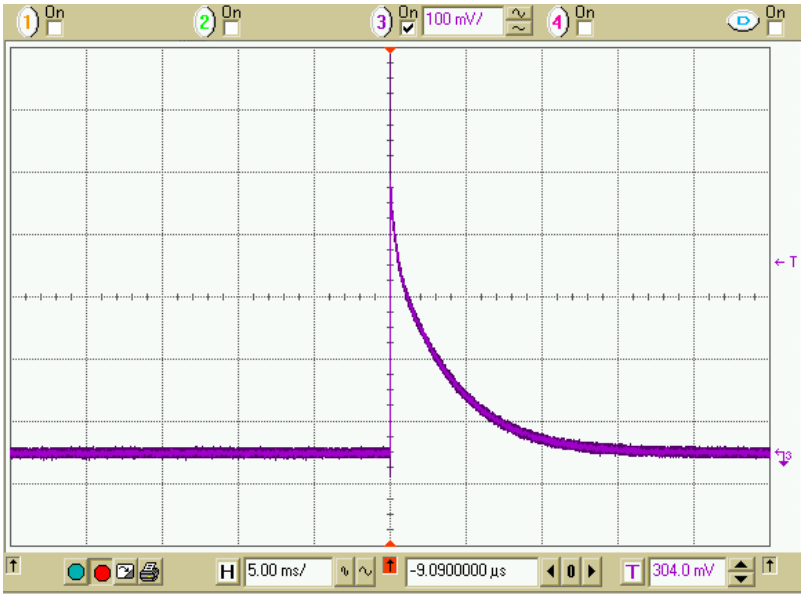

Fig. 6.7. The observed pulse height of a collimated 250µJ, 337 nm pulse measured with a silicon photodiode (scale: 5.0ms, 100mV per division).

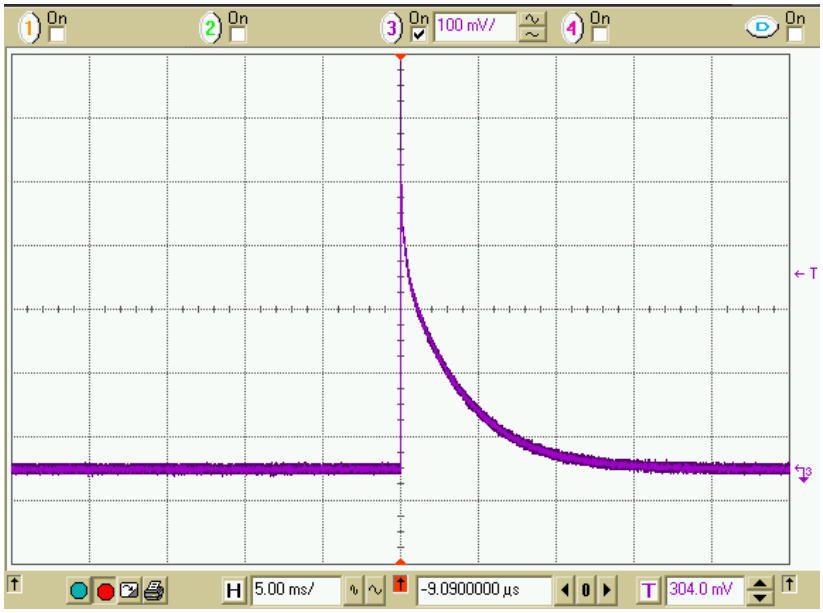

Fig. 6.8. The observed pulse height of a collimated 250µJ, 337 nm pulse after transmission through a quartz disk measured with a silicon photodiode (scale: 5.0ms, 100mV per division).

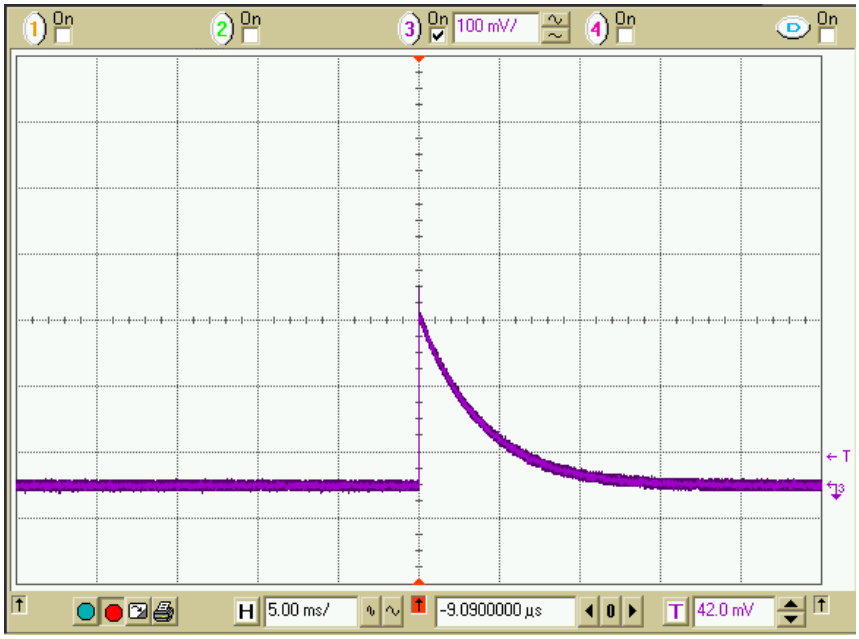

Fig. 6.9. The observed pulse height of a collimated 250µJ, 337 nm pulse after transmission through a coating of 3M Scotch-Weld DP-270 (clear) cured on a quartz disk, measured with a silicon photodiode (scale: 5.0ms, 100mV per division).

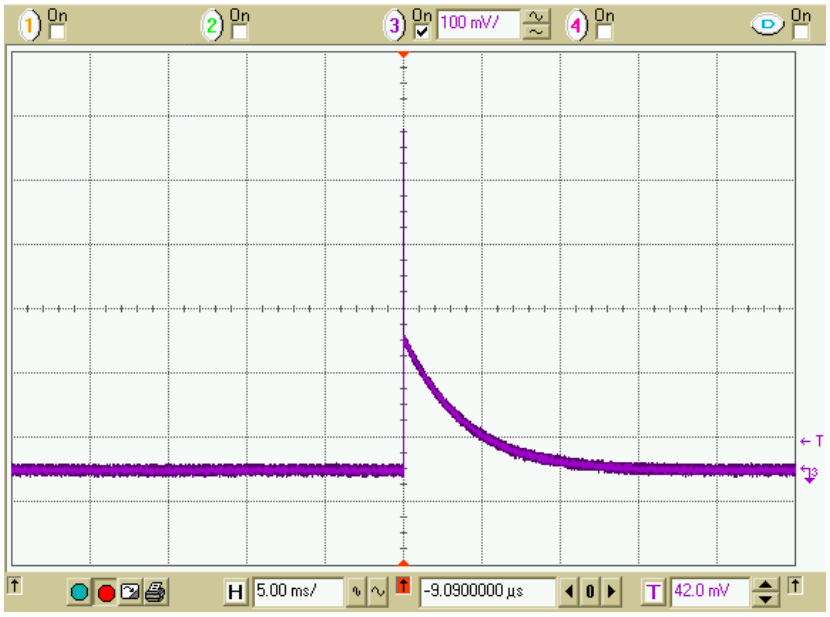

Fig. 6.10. The observed pulse height of a collimated 250µJ, 337 nm pulse after transmission through a coating of Devcon, Inc. 2 Ton® (clear) cured on a quartz disk, measured with a silicon photodiode (scale: 5.0ms, 100mV per division).

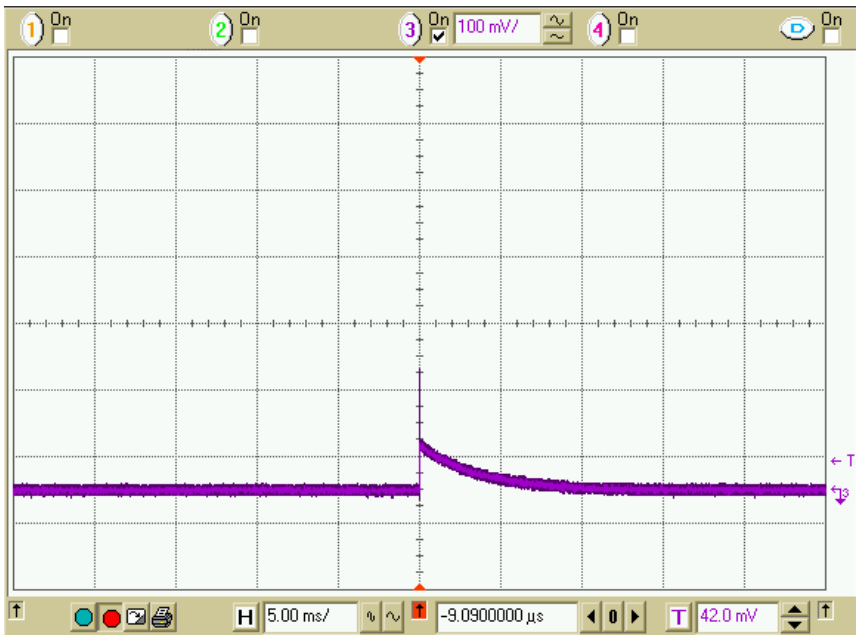

Fig. 6.11. The observed pulse height of a collimated 250µJ, 337 nm pulse after transmission through a coating of HumiSeal® 1A20 cured on a quartz disk, measured with a silicon photodiode (scale: 5.0ms, 100mV per division).

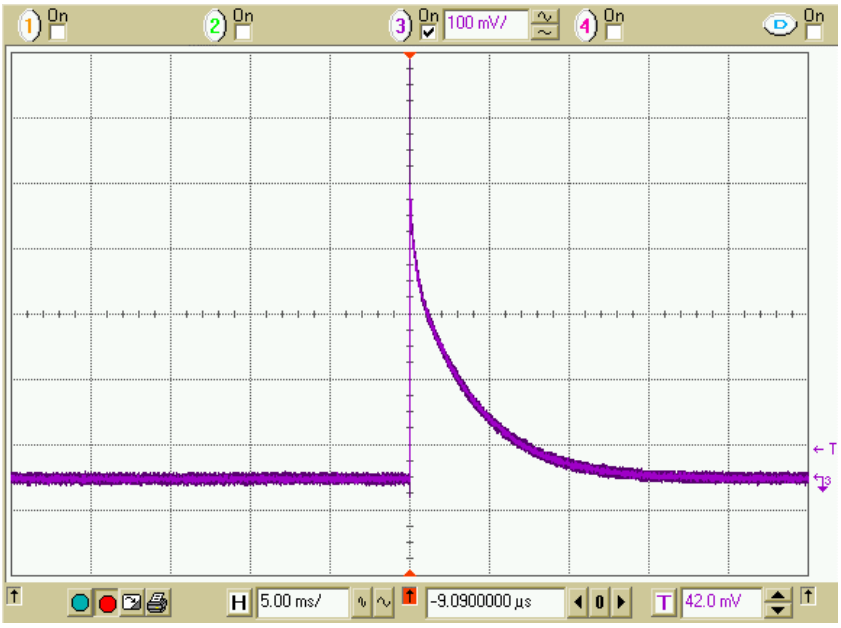

Fig. 6.12. The observed pulse height of a collimated 250µJ, 337 nm pulse after transmission through a coating of Epoxy-Technology Inc. 301-2 cured on a quartz disk, measured with a silicon photodiode (scale: 5.0ms, 100mV per division)

6.3 IV Curve Measurements

An I-V curve was collected on all processed samples prior to other measurements to confirm the conductivity/resistivity of the sample with a Keithley 237 High Voltage Source Measurement Unit coupled with a LabView interface. Resistivity was determined with the following expression,

$$\rho = R \cdot \frac{A}{\ell}, \tag{6.1}$$

where R is the resistance of the device, ℓ is the length of the device, and A is the cross sectional the contact area [113]. Resistance was determined from the I-V curve with Ohm's law, and was considered to be the average resistance through the bulk device.

6.3.1 Devices from synthesized material (*unpurified*)

Many devices fabricated from bulk grown ingots processed from the in-house synthesized material exhibited a typical ohmic resistance style I-V curve, as shown Fig. 6.13. However, a common problem with LiZnP and LiZnAs devices was that the conductivity was high, generally outside of 1-2 volt forward and reverse bias. The leakage current would reach compliance at 100 μV with only approximately 3 volts applied, for example, as shown in Fig. 6.14. The high conductivity was sometimes observed with newly processed devices, which made further electrical testing impossible.

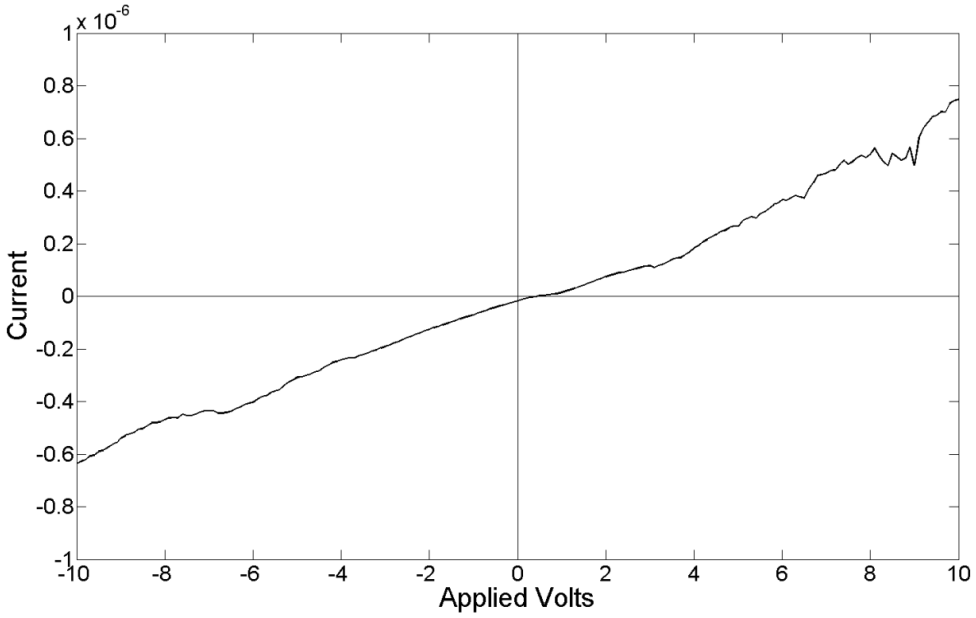

Fig. 6.13. An I-V curve of a LiZnP sample (0.98 x 4.34 x 3.95 mm^3) with silver epoxy contacts on both sides. Resistivity was determined at 2.75 x 10^7 Ω cm with the electric field applied through the 0.98 mm thick sample.

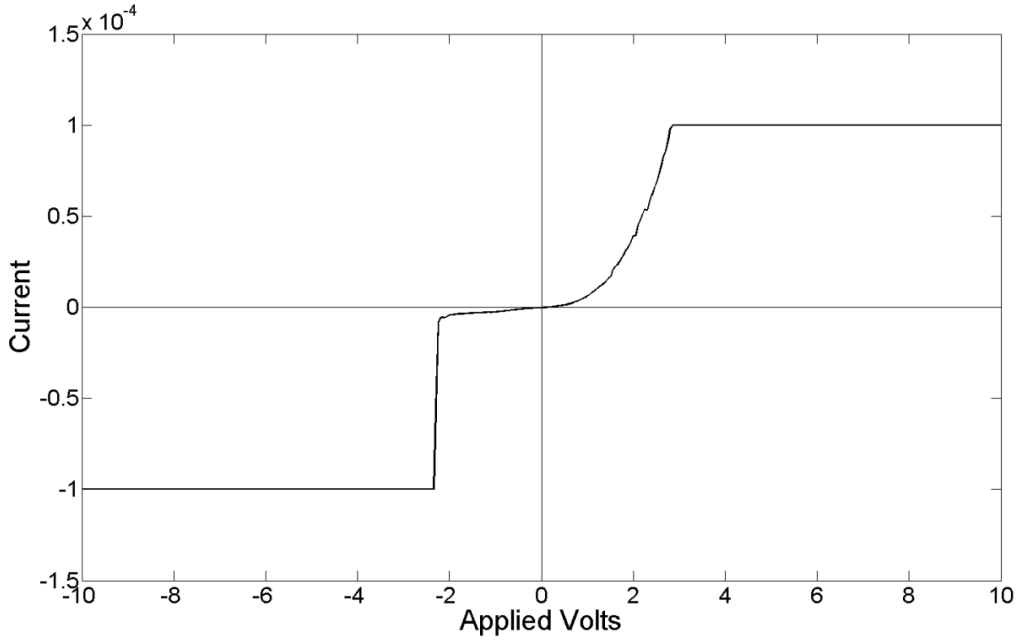

Fig. 6.14. An I-V curve of a LiZnP sample (2.01 x 3.48 x 4.91 mm) with silver epoxy contacts on both sides of the 2.01 mm thickness.

Some samples would first exhibit a resistor ohmic behavior at initial testing, and then after a long duration of time under an applied bias, the device would become electrically noisy, and I-V curve tests would show excessive leakage current at low applied voltages, similar to what is shown in Fig. 6.14. This observed change was permanent to the sample, not something that reverted back to its original state after the bias was removed. It was also observed that annealing silver epoxy contacts would make devices extremely noisy[16]. To reduce this problem, other contacts were explored, such electron beam evaporation of titanium and gold, as explained in section 6.1. A LiZnP sample of dimensions approximately 2.0 x 3.0 x 5.0 mm^3 was coated with a layer of silver epoxy for a cathode contact, then coated with a Ti/Au (600 Å / 10,000 Å) for an anode contact. The sample was coated with HumiSeal, type 1B73, to prevent moisture exposure. The sample was then biased at the Ti-Au contact, and current-voltage curves were collected, as shown in Fig. 6.15. The resulting curve showed a much more resistive characteristic, and appeared to have a "turn on" voltage near 9.8 volts forward bias, indicating space charge limitation. The resistivity was calculated to be 6.6 x 10^{10} Ω cm, allowing for further testing and characterization. The I-V curve indicates that a Schottky barrier may have been formed at the Ti-Au contact, and as a result, helped reduce the leakage current. Silver epoxy is commonly an ohmic contact material, and the current-voltage curve shown in Fig. 6.14 indicates high conductivity compared to the high resistivity commonly observed in detector-grade semiconductor materials, while still maintaining a high charge carrier mobility [114]. It has been seen in other semiconductor materials that degenerately doped, or high impurity levels, causes reduced resistivity and poor device performance [33]. It is likely that the sample impurity levels are high, thereby, causing the high conductivity observed. A purification method, by static sublimation was performed explained in section 5.2, and these samples were processed from bulk crystals grown from material purified with this method. The results indicate that the purity was improved and that a Schottky barrier was produced with Ti/Au contacts.

[16] The high noise that was observed was likely due to the silver contact diffusing into the material, thereby, lowering the material resistance.

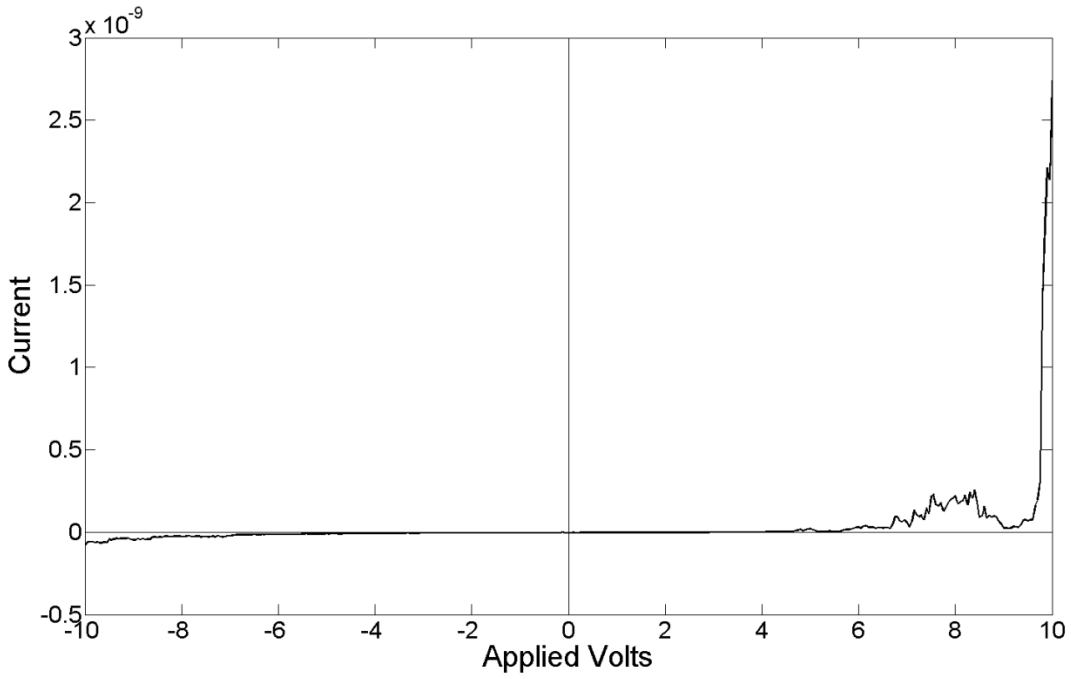

Fig. 6.15. An I-V curve of a LiZnP sample (approximately 2.0 x 3.0 x 5.0 mm) with a Ti/Au anode contact, and silver epoxy cathode contact.

6.3.2 Devices from purified ternary material

Bulk crystalline LiZnP and LiZnAs ingots were grown from purified material using the high-temperature Bridgman technique detailed in section 5.3. Devices were fabricated from the ingots with the process described in sections 5.3.3 and 6.1. Many devices were tested with various electrical contact configurations. The Ti/Au anode with a silver epoxy cathode contact yielded promising results, and also gave promising neutron sensitivity measurements, however problems with the silver epoxy continued. High-temperature curing was a challenge, as devices would become noisy after the high-temperature curing process. Room-temperature curing would sometimes work, but the cure would take weeks, and was observed to not always cure properly. Because Ti/Au showed promise, Ti/Au contacts (typically 500 Å Ti and 10,000 Å Au) were applied to each side of the purified ternary samples. Titanium is a known diffusion barrier for silicon devices [115], and also helps adhesion between the device material and the gold over layer.

Typical *purified* LiZnP devices exhibited I-V curves similar to that shown in Fig. 6.16. I-V curves were routinely collected prior to any other testing. Afterwards, devices were tested for neutron sensitivity, where up to 480 volts was applied through the preamp (≈ 48 volts at the device) before the device showed signs of high noise and signal degradation. It was commonly observed that noise would increase the longer the sample was biased, and/or the higher the voltage applied. Eventually the sample would become noisy at all applied voltages. An I-V curve was collected on the same sample evaluated in Fig. 6.16 after becoming noisy, which gave a result of high conductivity, as shown in Fig. 6.17. Samples were reprocessed with the routine described in sections 5.3.3 and 6.1, where contacts were applied in a different crystalline orientation. I-V curves were collected with reprocessed samples, and resulted in resistivities in the range of 10^6 - 10^7 Ω cm. However, it was observed that samples were even more susceptible to high voltage breakdown after reprocessing, and high noise was observed after further testing.

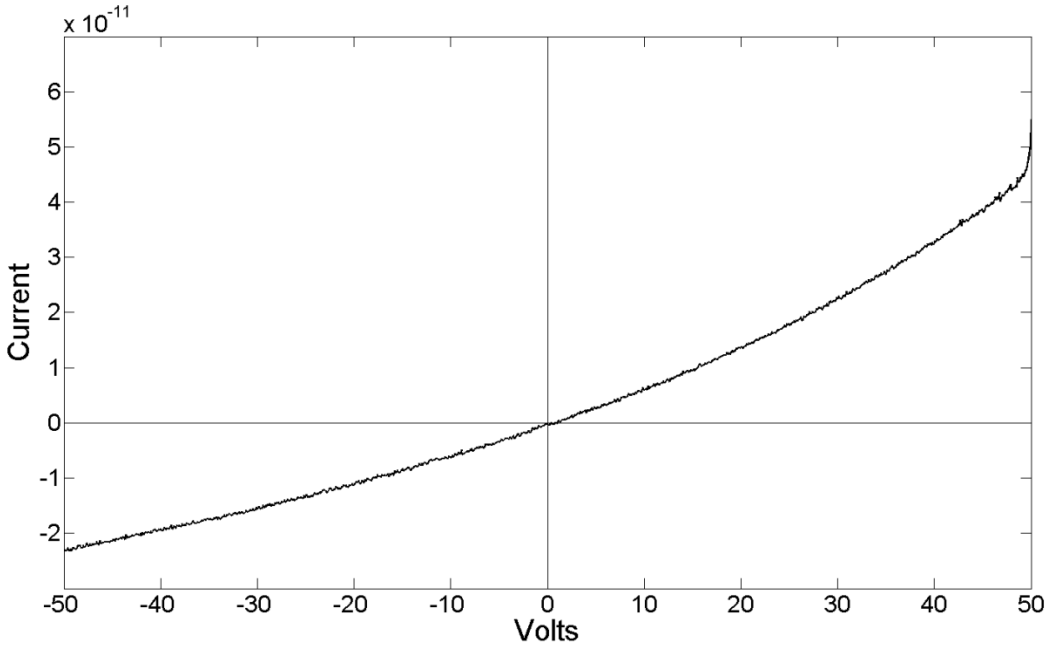

Fig. 6.16. I-V curve from a purified LiZnP device (2.020 x 3.518mm x 4.077 mm^3). The resistivity was determined to be 8.2 x 10^{11} Ω cm.

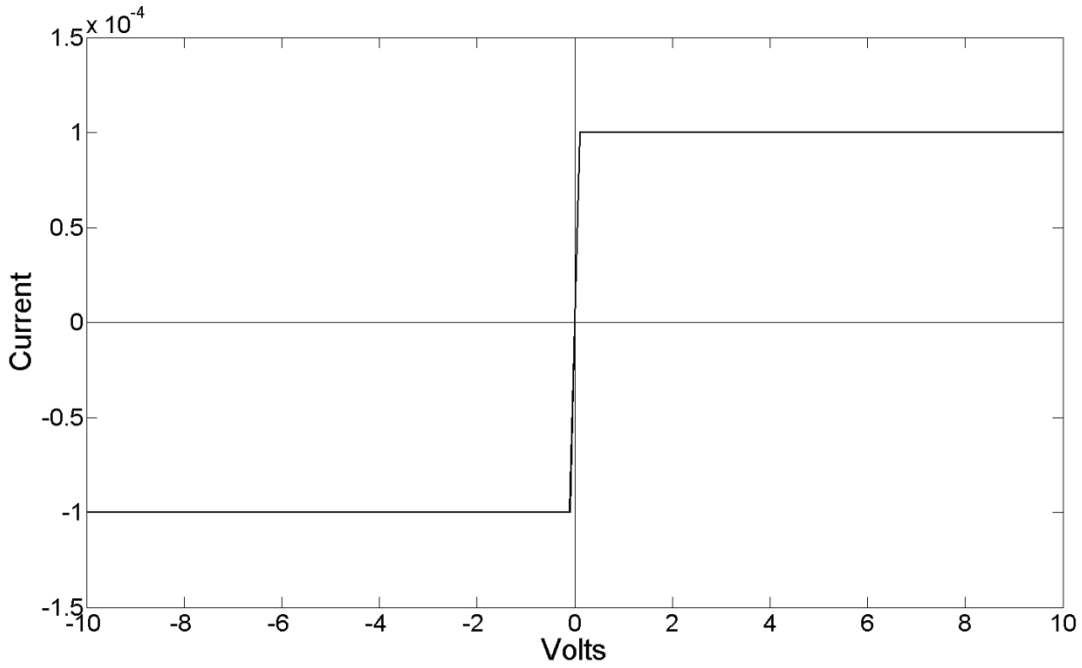

Fig. 6.17. An I-V curve of the same LiZnP sample as tested from Fig. 6.16 after being biased > 10 volts for a number of hours.

I-V characteristic curves from LiZnAs devices had similar properties as the LiZnP samples. A typical LiZnAs device I-V curve is shown in Fig. 6.18, which yielded a common ohmic I-V curve. Some devices, however, showed rectifying characteristics, as shown in Fig. 6.19 and Fig. 6.20. The rectifying behavior was similar to what was observed with the unpurified LiZnP sample shown in Fig. 6.15. The rectifying behavior assisted with noise reduction [116], which allowed for rectifying devices to be operated at lower voltages (< 10 volts). As a result, samples lasted much longer before becoming noisy, and could undergo further testing.

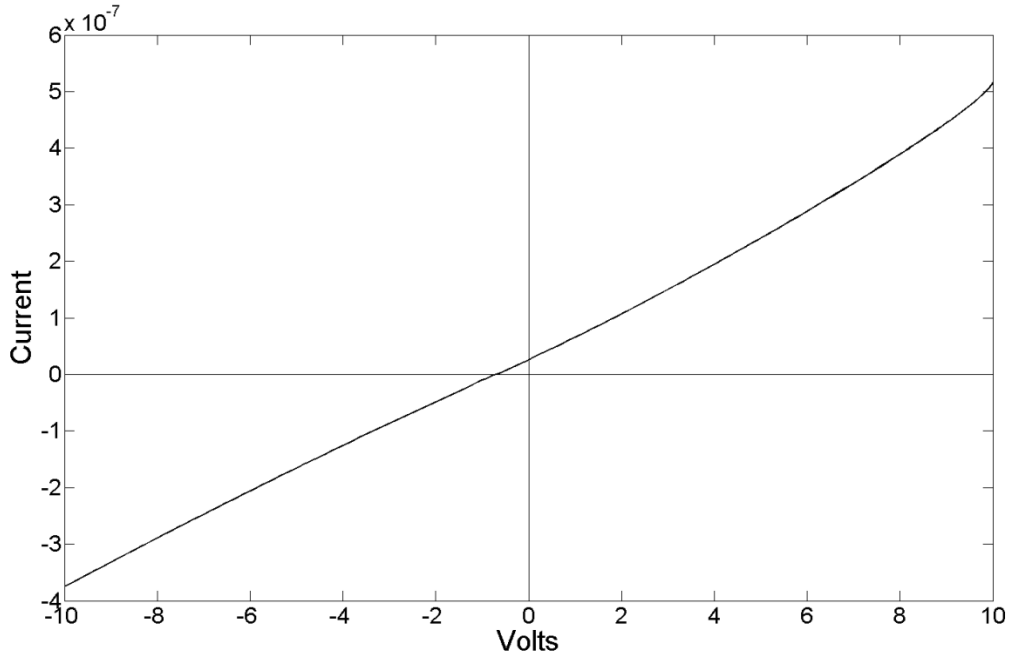

Fig. 6.18. An I-V curve from a purified LiZnAs device (2.100 x 4.060 x 4.155 mm^3). Resistivity was determined at 1.6 x 10^7 Ω cm.

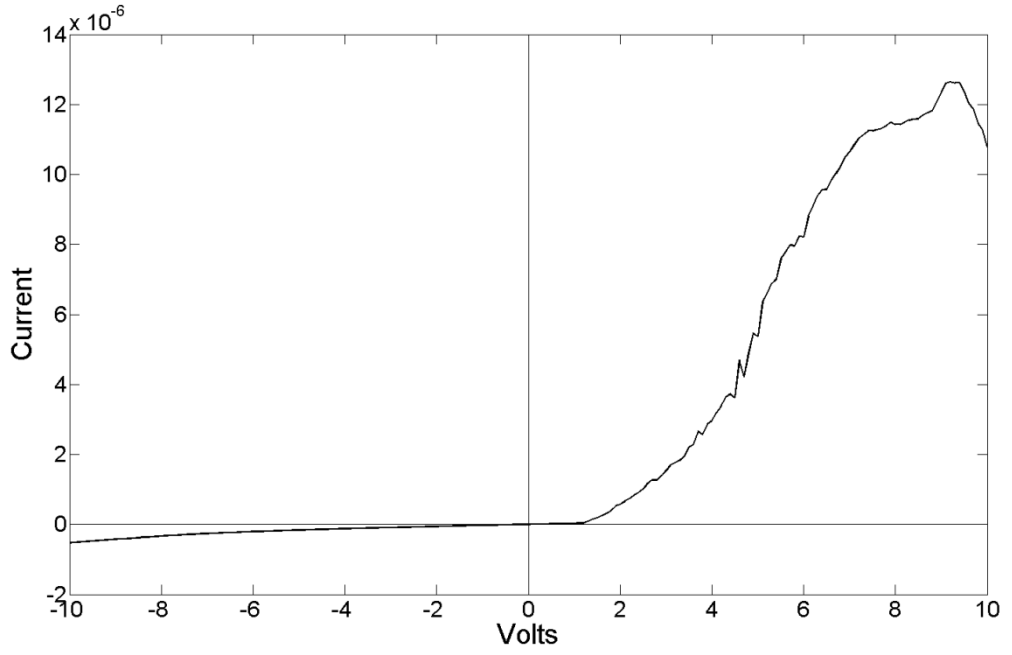

Fig. 6.19. An I-V from a purified LiZnAs device of dimensions 1.43 x 3.96 x 2.45 mm^3. This particular device exhibited a rectifying style I-V curve. Resistivity was determined to be 1.7 x 10^6 Ω cm at -10 volts.

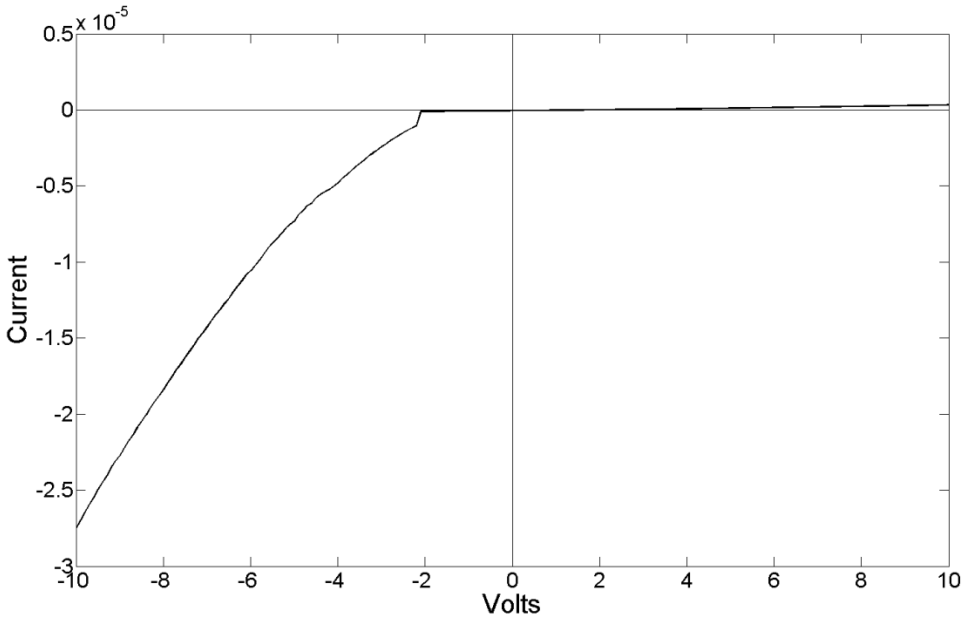

Fig. 6.20. An I-V curve measured from the same LiZnAs device from Fig. 6.19 with reversed leads. Resistivity was determined to be 2.5 x 10^6 Ω cm at 10 volts.

6.4 Transient Charge Technique

Devices were tested for electron mobility, μ_e, and mean free drift time, τ, by the transient charge technique (TCT) as described by Martini [110] and Roth [111]. The charge collection efficiency of a single carrier in a material when charge is introduced, η, as described in section 3.4, is defined as,

$$\eta = \frac{Q}{Q_o} = \frac{\mu\tau_T E}{L}\left[1 - \exp\left(-\frac{L}{\mu\tau_T E}\right)\right], \tag{6.2}$$

where μ is the mobility, τ_T is the trapping time, L is the length of the device (or crystal thickness), E is the electric field intensity, Q_o is the full charge created by the quantum of ionizing radiation, and Q is the charge collected. Intuitively, the larger the carrier mobilities and trapping times are, the more efficient is the charge collection. Therefore, $\mu\tau$ product is a common property used to

determine material quality. The TCT was chosen because μ and τ_T can be measured directly, and independently [110]. Other methods, such as the Van Der Pauw and Hall measurements, are common for lower resistivity materials, such as silicon. These techniques generally use a constant resonance frequency optimized for low resistivity materials. However when applied to high resistivity materials (> 1.0 x 10^7 Ω cm) the frequency mismatch leads to inductive reactance, or an opposition in current flow due to high inductance, which leads to inaccurate mobility measurements [117]. The TCT technique however, is a method based on tracing the current, or voltage, transit waveforms induced from ionizing radiation interactions in the material, and read-out from a charge-sensitive preamplifier. Various arrangements of this method have been used; from alpha particles [118], low-energy electron beams [119], or pulsed laser light [120]. For the following study, alpha particles from ^{241}Am (E_α = 5.48 MeV) were chosen for both their short range and relatively high energy. It is assumed however, that the Ti/Au contacts applied to the ternary material are non-injecting contacts, and detrapping was either negligible, or a major component of the signal where the detrapping time is longer than the trapping time and transit time.

The output waveform reflects the exponential decay of carriers due to trapping, and for the case of no detrapping where,

$$V(t) = \frac{V_o \tau_T}{T_R}\left[1 - \exp\left(\frac{-t}{\tau_T}\right)\right], \tag{6.3}$$

for $t < T_R$ where,

$$T_R = \frac{L}{\mu E}, \tag{6.4}$$

is the transit time, L is the length of the device, and t is time. At $t = T_R$, the rise time of the single, the voltage reaches a constant value of

$$V(t) = \frac{V_o \tau_T}{T_R}\left[1 - \exp\left(\frac{-T_R}{\tau_T}\right)\right], \tag{6.5}$$

and remains constant for $t > T_R$. Therefore, the transit time can be defined by the rise time of the induced signal, and allows for a determination of the mobility from Eq. (6.4).

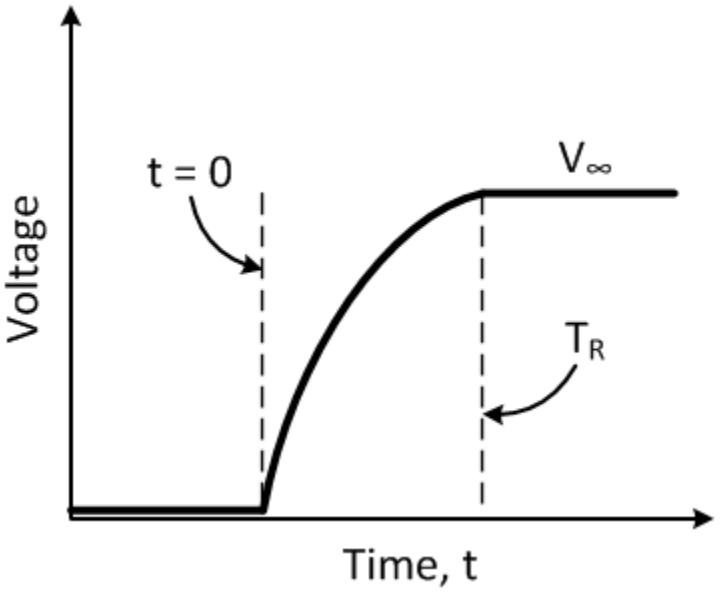

Fig. 6.21. A depiction of the voltage waveform where the signal begins at t = 0, and reaches its maximum point at V_∞ for $t = T_R$.

6.4.1 Alpha Particle Sensitivity

Purified samples of LiZnP and LiZnAs were tested for alpha particle sensitivity, and afterwards evaluated by the transient charge technique. The samples were grown as described in chapter 5, and were processed into devices as described in section 6.1 with Ti/Au (500 Å/ 10,000 Å) as a non-injecting contacts. The material was coated with HumiSeal® 1B73 to protect the materials from moisture in the air. A picture of a processed LiZnP sample is shown in Fig. 6.22. The sample was mounted into a project box with adjustable pressure contacts that connected firmly to each contact surface, as shown in Fig. 6.40. The project box with a mounted sample

was connected to a charge sensitive preamplifier (Ortec 142A), and the preamplifier signal was connected to a Canberra 2022 amplifier, and the output amplifier signal was connected to an Ortec TRUMP PCI multichannel analyzer as shown in Fig. 6.23. The high voltage power supply was a stable power supply manufactured by Matsusada Precision, Inc.

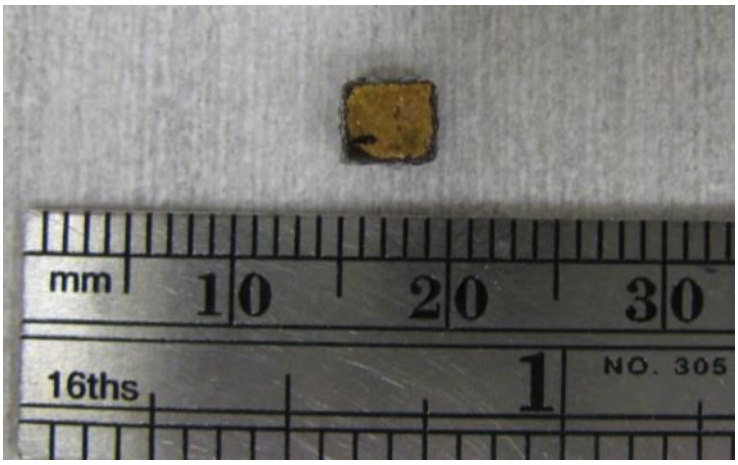

Fig. 6.22. A purified LiZnP sample (2.020 x 3.518mm x 4.077 mm^3) with Ti/Au (500 Å/ 10,000 Å) contacts and coated in HumiSeal® 1B73 conformal coating.

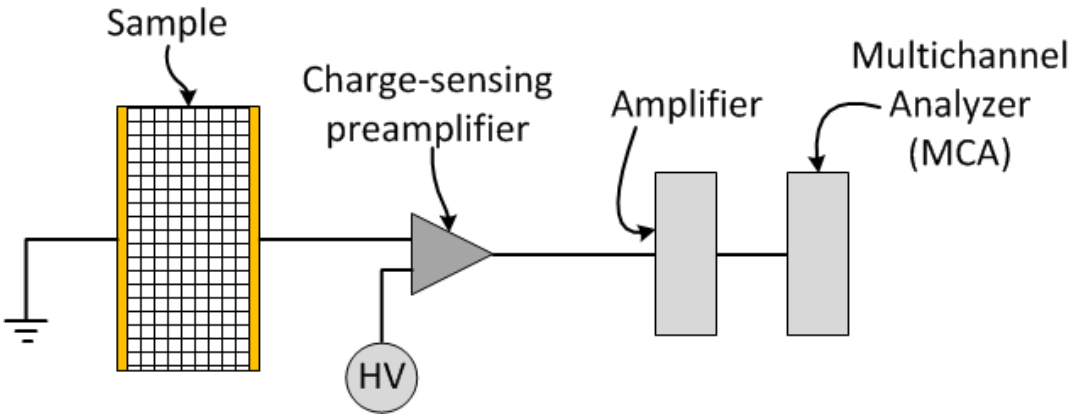

Fig. 6.23. The electronics read-out system for alpha particle sensitivity testing.

An ^{241}Am alpha particle source was placed between the ground and the cathode of a sample, as shown in Fig. 6.24. An Am-241 source acquired from a smoke detector was used because it fit over the sample contact. The package allowed connection between the Ti/Au

contact and the pressure contact, while eliminating chance of damaging the spectroscopic source during the testing process.

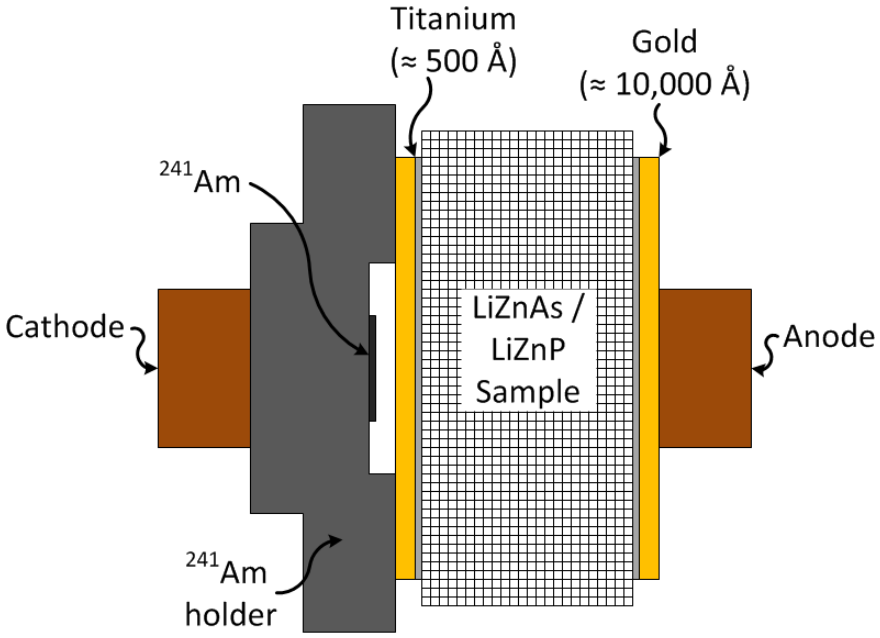

Fig. 6.24. The experimental setup for an electron dominated signal (cathode irradiation).

An ^{241}Am spectrum was collected initially with a CZT sample to insure that the measurement setup was operational. The CZT sample was provided by Redlin and was also a sample that had been used for high resolution spectroscopy studies with a Frisch collar [76]. The resulting spectrum with the ^{241}Am source placed at the cathode (electron dominated signal) with 650 volts applied at the preamplifier, and without the source with 650 volts applied at the preamplifier is shown in Fig. 6.25. Each spectrum was collected for 300 seconds.

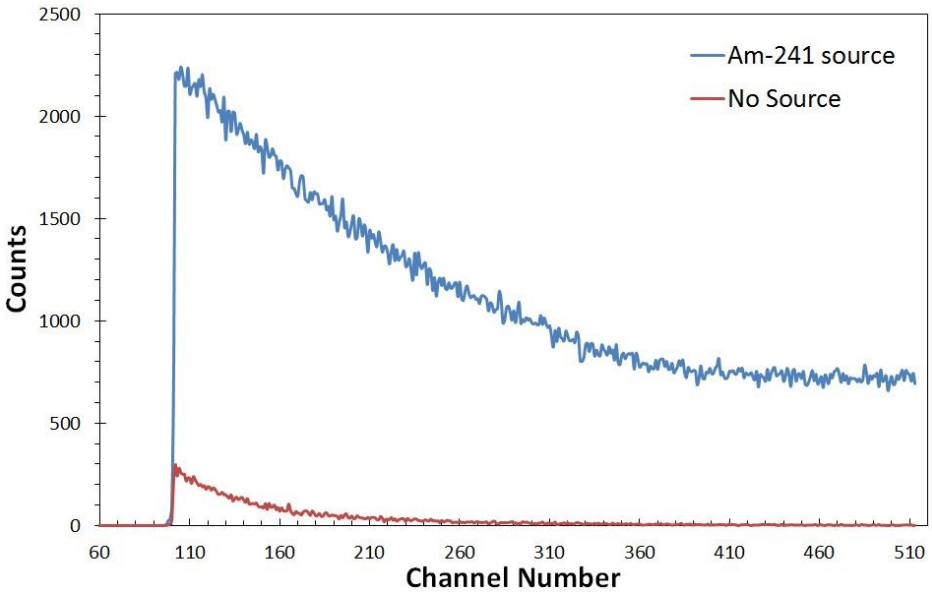

Fig. 6.25. The 5.48 MeV alpha particle spectrum from a CZT crystal with chemically deposited gold chloride contacts as irradiated from the cathode.

The CZT sample was replaced with a LiZnP sample, also with the ^{241}Am source at the cathode, as shown in Fig. 6.24. TRIM SRIM simulations indicated that a 5.48 MeV alpha particles are blocked by a contact composed of a 500 Å Ti layer followed by 94,300 Å Au layer, however, only 10,000 Å of Au was deposited, indicating that 5.48 MeV alpha particles should enter the LiZnP material, and not blocked by the contact layers [121]. The voltage applied was investigated, as it was evident that for the particular sample, there was an optimal voltage where the output signal was strongest. Shown in Fig. 6.26 is a ^{241}Am spectrum with an applied bias of 500 volts at the preamplifier. At higher applied voltages, the signal would often become either extremely noisy, or signals would be lost, as with the case with the LiZnP sample at 600 volts as shown in Fig. 6.27.

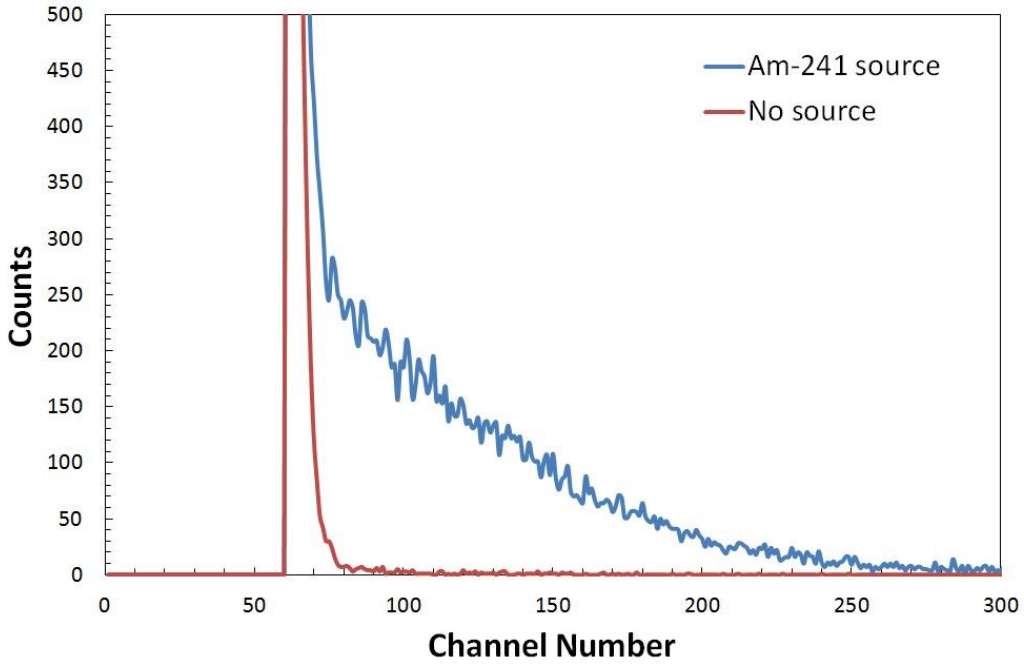

Fig. 6.26. The pulse height spectrum for a 600 second measurement of the response from 5.48 MeV alpha particles incident the cathode of a LiZnP sample at 500 volts at the preamplifier.

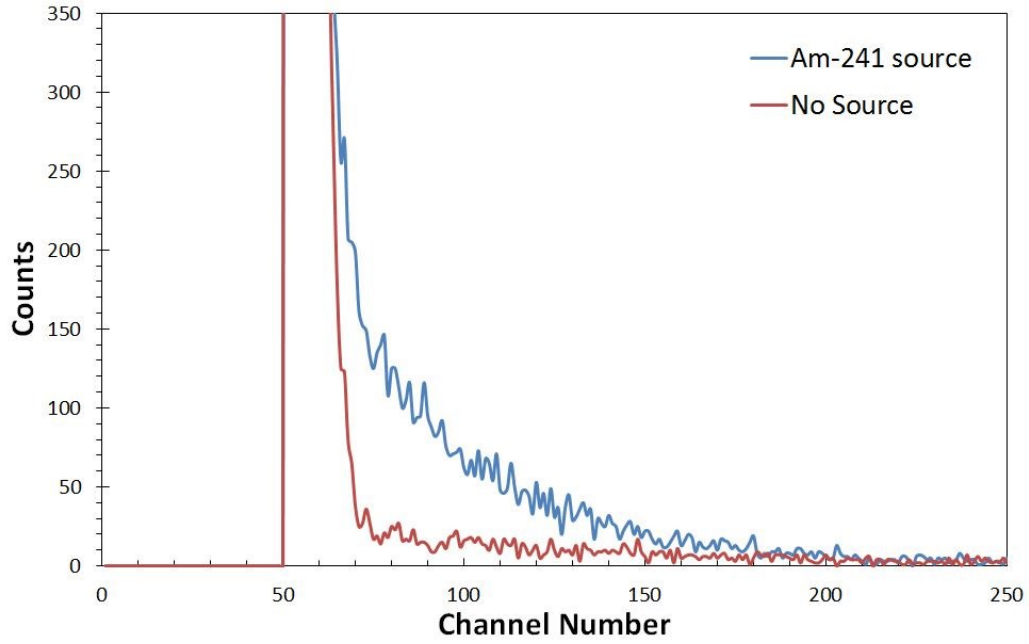

Fig. 6.27. The pulse height spectrum for a 600 second measurement of the response from 5.48 MeV alpha particles incident the cathode of a LiZnP sample at 600 volts at the preamplifier.

6.4.2 Transient charge technique with LiZnP

The same LiZnP sample used for the experiments described in section 6.4.1 was mounted into a project box with adjustable pressure contacts that connected firmly to each contact surface. The project box, with the mounted sample, was connected to a charge sensitive preamplifier (Ortec 142A), and output of the preamplifier signal was connected into the input of an Agilent Infiniium 54832D MSO oscilloscope as shown in Fig. 6.28. The same ^{241}Am source described in section 6.4.1 was mounted at the cathode of the LiZnP sample, as shown in Fig. 6.24.

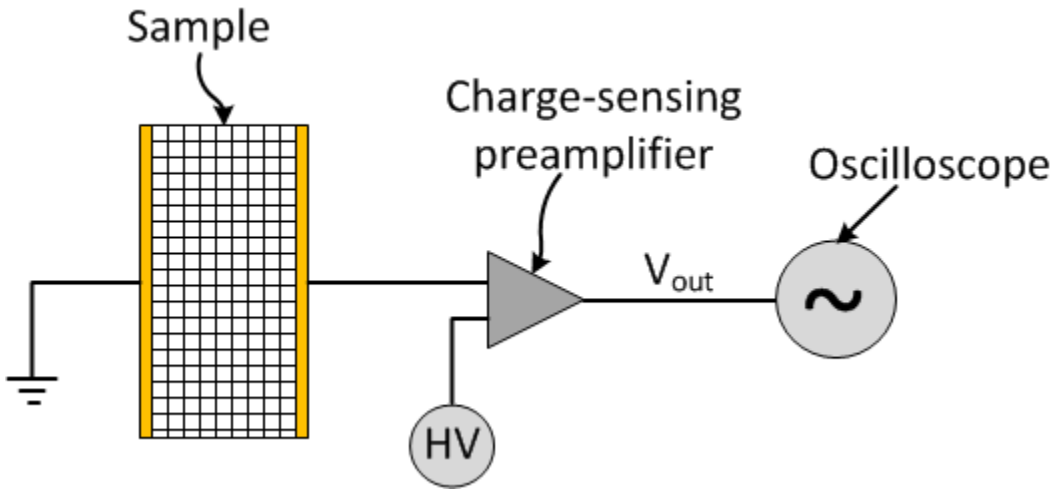

Fig. 6.28. The electronics read-out system for the transient charge technique.

The oscilloscope was set to determine the rise time of a resulting waveform as described by M. Martini [110]. The oscilloscope algorithm defined the rise time at 10% from initial rise to 90% of full energy. Fifty measurements were collected as shown in Table 6.2

Table 6.2. The results of the 50 rise-time measurements for LiZnP.

T_R (μs)				
80.8	115.1	82.3	147.0	143.6
150.5	180.8	127.4	118.2	113.8
143.3	133.5	156.6	169.2	93.4
101.9	106.6	162.6	110.8	171.6
118.0	134.1	144.7	199	155.7
83.6	170.3	151.2	126.6	121.8
136.9	88.6	135.5	188.7	198.7
89.7	181.6	150.0	168.8	80.7
185.4	125.3	132.4	164.8	148.2
137.4	192.2	184.6	99.0	193.3

The series of measurements were averaged to find an average electron transient time of 139.9 μs ± 3.4 %. The device was 0.202 cm in length, and 51 volts was measured at the detector. From Eq. (6.4), the electron mobility was determined to be 5.7 cm^2 V^{-1} s^{-1} ± 3.4 %. Standard error was determined based on a Gaussian distribution about the 50 measurements as explained in Appendix C. An example of one of the waveforms is shown in Fig. 6.29. Anode irradiation was performed on the sample, however, no response was observed, thus indicating that the hole trapping time was much shorter than the hole carrier transient time, therefore making it impossible to measure the hole trapping time. Unfortunately, higher applied bias generally introduced an abundance of noise.

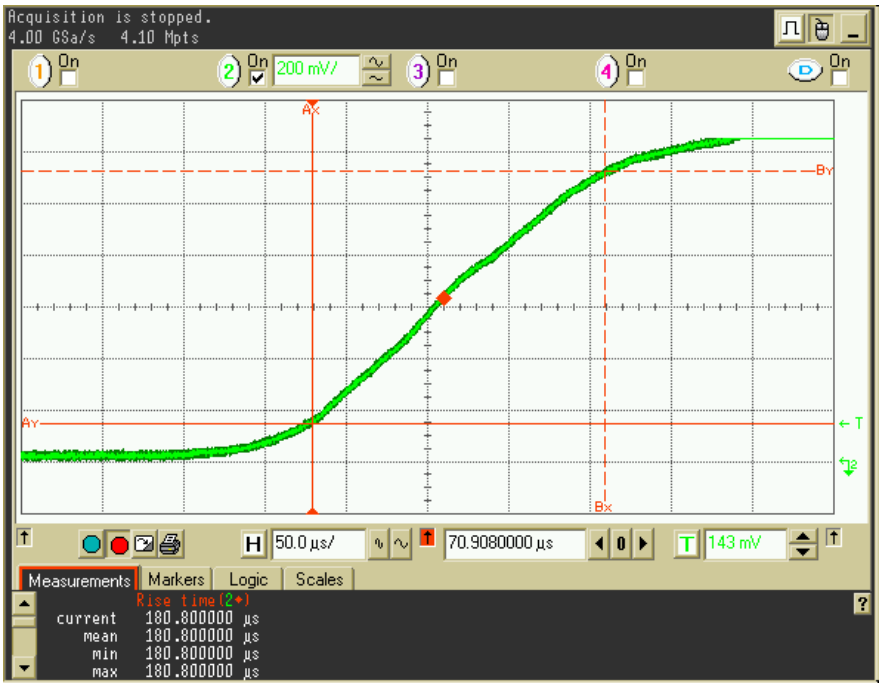

Fig. 6.29. A close-up examination of the resulting signal from 5.48 MeV alpha partial absorption from cathode irradiation in LiZnP.

Another method to measure the transit time was presented by M. Roth [111] which described the use of evaluating a single waveform, and finding the transit time from a single waveform. A plot of ln[V_∞ - $V(t)$] vs. time, t, was formed from the waveform, where V_∞ is the peak of the waveform where the slope approaches zero, as shown in Fig. 6.21. Points along the waveform were selected as shown in Fig. 6.30, where V_∞ was determined at 1210 mV. The unit-less quantity [V_∞ - $V(t)$] was determined for each data point, and was plotted for each corresponding time, t, as shown in Fig. 6.31. A best fit line was determined, where the inverse of the slope yields T_R.

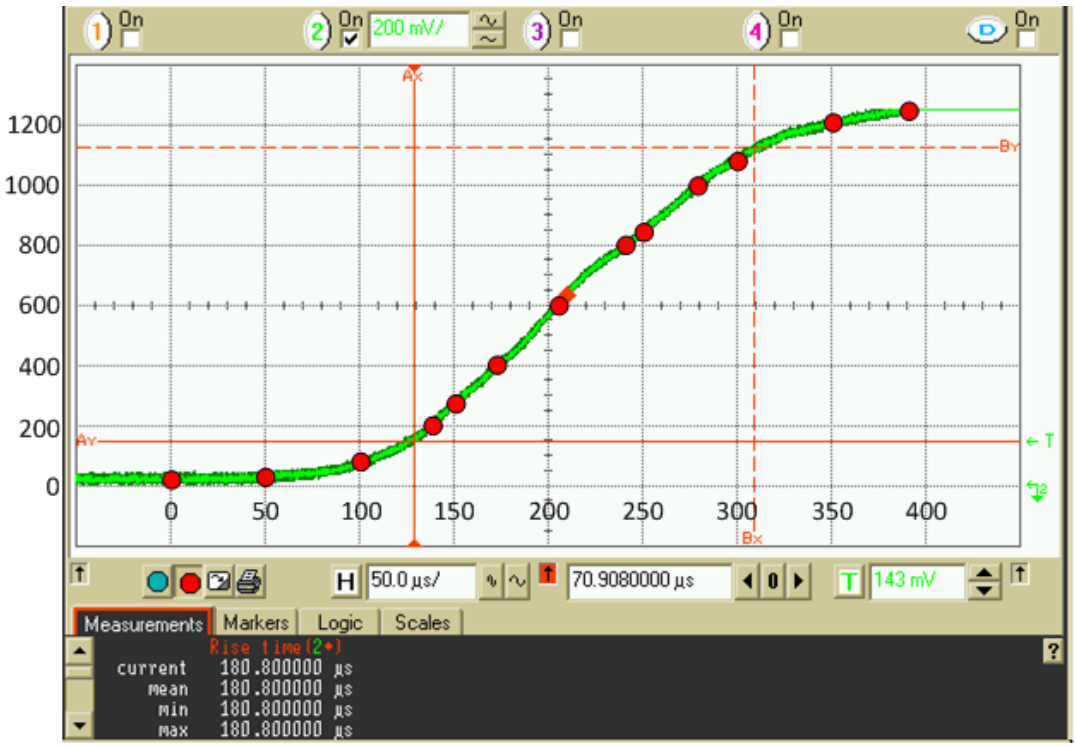

Fig. 6.30. The same signal shown in Fig. 6.29, where data points are collected from the waveform as shown by the red data points.

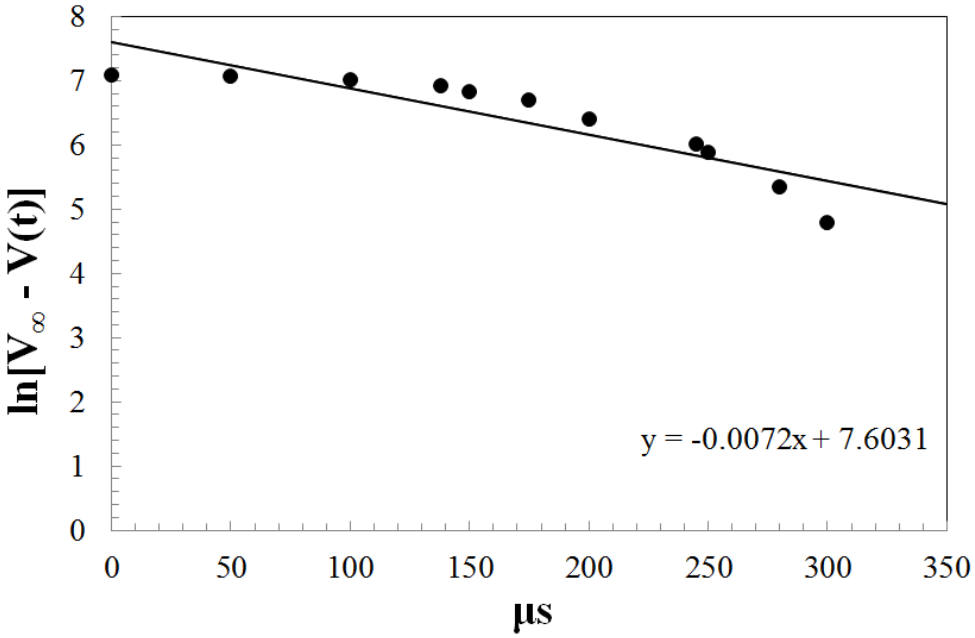

Fig. 6.31. The transit time plot of $\ln[V_\infty - V(t)]$ *vs. time, t. A best fit linear curve was applied to the data. The inverse of the slope yielded the electron transit time through the material.*

The inverse of the slope gave a transit time of 138.9 μs, which matched well to the transit time determined from the 50 rise time measurements (139.9 μs ± 3.4%). The transit time determined from the 50 rise-time measurements was used to find a mobility, μ_e, from Eq. (6.4), of 5.7 $cm^2\ V^{-1}\ s^{-1}$ ± 3.4%. A $\mu_e\tau_e$ product for LiZnP was determined at 8.0 x 10^{-4} $cm^2\ V^{-1}$ ± 4.8%. Common $\mu\tau$ products for spectroscopic grade detectors such as cadmium zinc telluride (CZT) are in the range of 10^{-2} $cm^2\ V^{-1}$ for electrons, and 10^{-4} $cm^2\ V^{-1}$ for holes [76]. However, for neutron detection, where the spectroscopic resolution of the spectral features is not as important, a $\mu\tau$ product in the range of 10^{-4} $cm^2\ V^{-1}$ is adequate for neutron counting performance.

6.4.3 Transient charge technique with LiZnAs

A purified LiZnAs sample was characterized for μ and τ with the same procedure as described for LiZnP. The sample tested is shown in Fig. 6.32, a photograph taken before contacts were applied. Ti/Au contacts were evaporated on the polished surface of the sample in thicknesses of 500 Å / 10,000 Å, respectively.

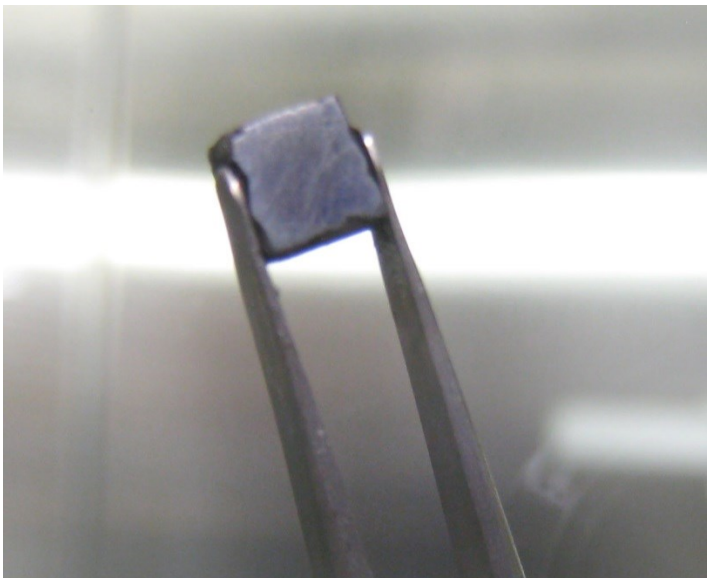

Fig. 6.32. A photo of the LiZnAs sample before contacts were applied. The photo was taken through the view-port of an argon atmosphere glove box.

The sample was placed into a project box, and same alpha particle source, ^{241}Am, as used before was placed at the cathode of the device as shown in Fig. 6.24. Afterwards, the same electronics configuration as used for the LiZnP sample was connected to the project box, as shown in Fig. 6.28. Fifty rise-time measurements were collected, as listed in Table 6.3, where rise-time on the oscilloscope was defined as 10% from initial rise, to 90% of maximum pulse height. Examples of the observed pulse height and rise time measurement are shown in Fig. 6.33 and Fig. 6.34, each collected with 48 volts applied at the detector.

Table 6.3. The results of the 50 rise-time measurements for LiZnAs.

T_R (μs)				
92.0	114.3	198.9	271.9	192.9
240.0	174.6	194.1	208.3	224.2
136.5	135.6	225.0	224.8	173.3
180.0	221.2	229.8	230.6	130.8
157.2	119.2	175.6	265.9	218.0
165.4	162.0	244.3	183.0	251.8
110.4	188.5	186.2	188.3	210.4
137.0	133.5	213.8	230.7	199.8
166.2	229.7	224.7	242.9	188.5
176.7	153.5	185.8	190.2	210.8

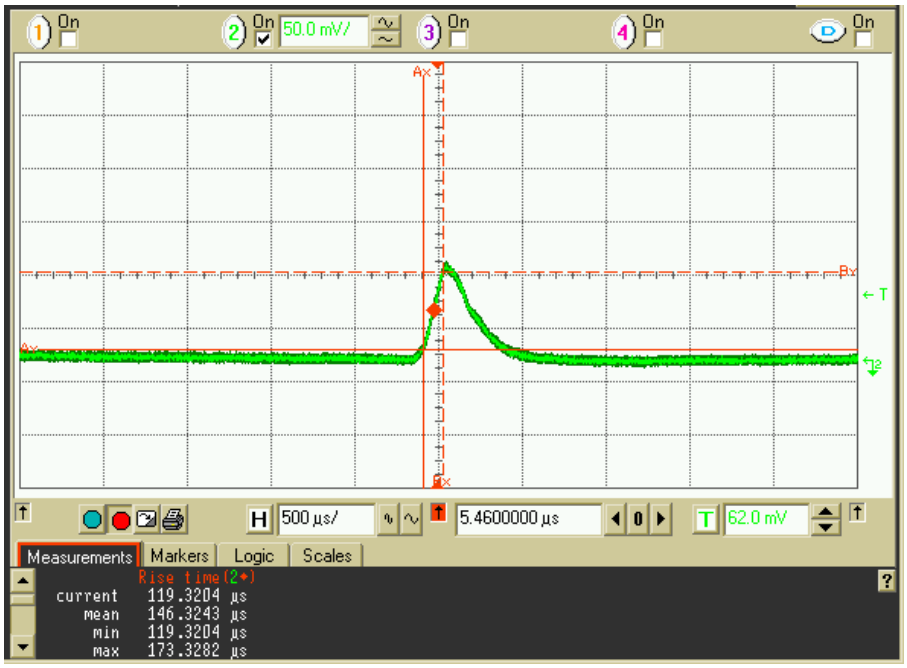

Fig. 6.33. The resulting signal from 5.48MeV alpha partial absorption from cathode irradiation in LiZnAs sample.

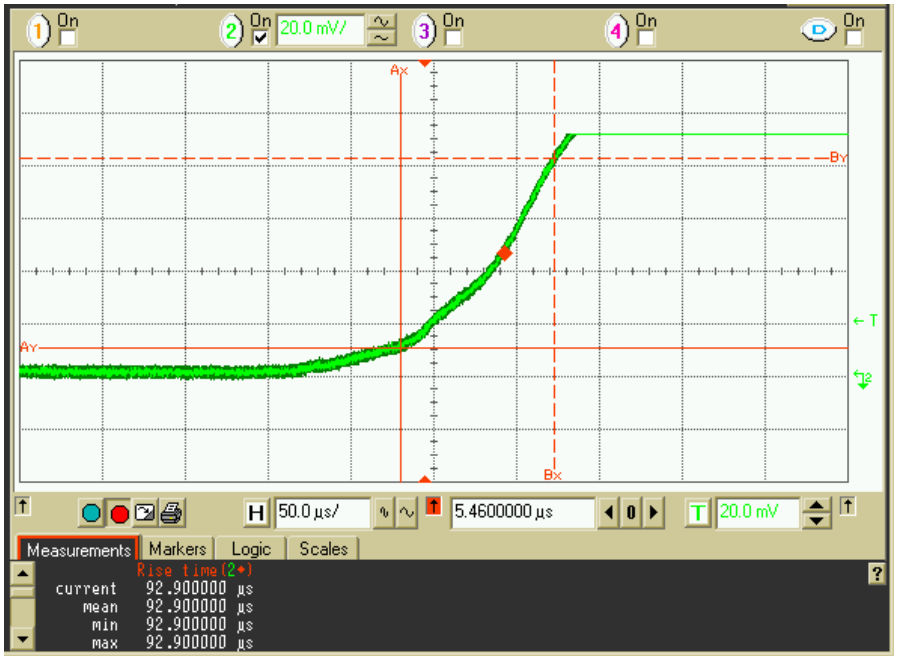

Fig. 6.34. A close-up examination of the resulting signal from 5.48MeV alpha partial absorption from cathode irradiation in LiZnAs.

The 50 rise-time measurements were averaged to find a transit time of 190.2 μs ± 3.1%. The length of the device was 0.21 cm, and 48 volts was measured as applied to the device. Eq. (6.4) was used to determine an electron mobility, μ_e, of 4.8 $cm^2\ V^{-1}\ s^{-1}$ ± 3.1%. No distinguishing signal above the noise was observed for anode irradiation; hence hole carrier $\mu\tau$ was not determined. A determination of the transit time was also performed from a single measurement, as suggested by M. Roth [111], which resulted in a transit time of 106 μsec. The result was the same order of magnitude as the transit time determined by evaluation of the rise-time, indicating some agreement between the two techniques. The transit time determined from the 50 rise-time measurements was used to determine a $\mu\tau$ product for electrons, at 9.1 x 10^{-4} $cm^2\ V^{-1}$ ± 4.4%. This value is on the same order of magnitude as determined for LiZnP, and also indicates a reasonable mobility for neutron counters, without the need of spectral resolution or features in a pulse-height spectrum.

6.5 337 nm Laser Sensitivity Testing

LiZnAs[17] devices were tested for sensitivity to 337 nm laser light. 337 nm light is in the blue – ultra violet range and has an energy of 3.68 eV, high enough energy to excite electron – hole pairs in LiZnAs (reported bandgap of 1.51 eV [58]). The experimental setup included a Laser Photonics LN300 laser with an energy of 250 μJ per pulse at 337 nm. The pulse width was 5 ns with beam dimensions of 9 x 4 mm (hor x ver).

6.5.1 Absorption of 337 nm light in LiZnAs

A LiZnAs sample of dimensions 1.43 x 3.96 x 2.45 mm^3 was mounted in a project box that allowed for light to pass through the back of the box so light could be absorbed in a Si photodetector as shown in Fig. 6.35. The experimental setup included an adjustable iris, silicon

[17] By this time in testing, all LiZnP devices were noisy from neutron testing. Original devices were reprocessed, and the electric field was applied in another crystalline direction, however, neutron sensitivity testing with reprocessed devices also lead to breakdown in device functionality. Reprocessed devices of LiZnAs were only tested up to 10 volts applied bias on the device in order to avoid electrical breakdown.

photo detector and an Agilent Infiniium 54832D MSO oscilloscope as shown in Fig. 6.36. The adjustable iris adjusted to reduce the beam to about a 1.0 mm diameter that was incident on the 3.96 x 2.45mm face of the sample. The intensity, or response, from the Si photodiode was recoded on the oscilloscope without the sample present as shown in Fig. 6.37, and with the sample in the beam as shown in Fig. 6.38. It was observed that an amount of light was transmitted through the 1.43mm of LiZnAs, and a large amount was definitely absorbed in the material.

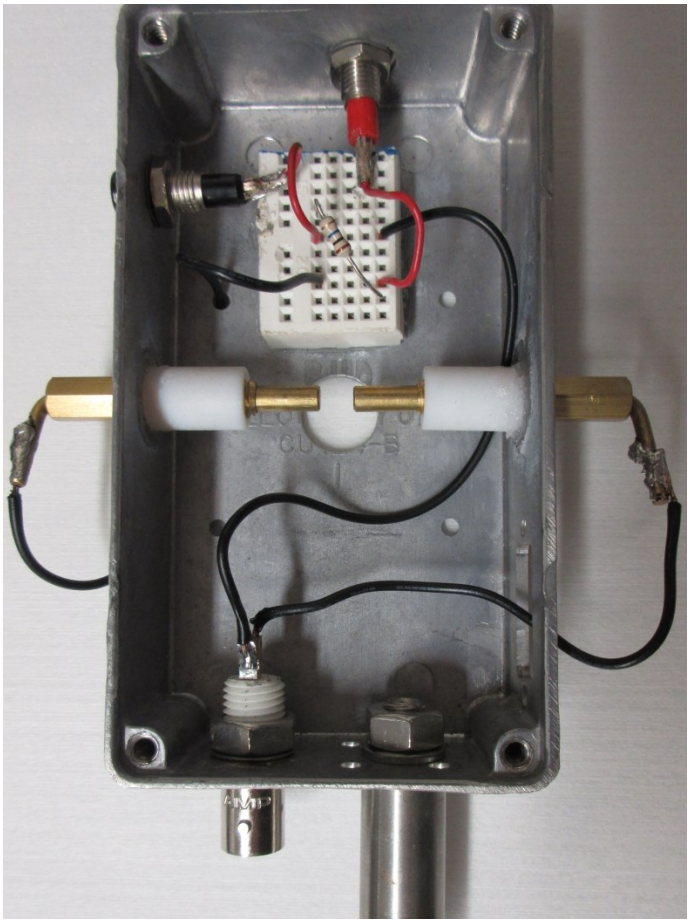

Fig. 6.35. The project box for the 337 nm laser attenuation / absorption studies. The sample was mounted between the brass pressure contacts. The hole behind the sample allowed for the transmitted light to pass into the Si photodetector (The circuit board on the top of the box was intended for measuring the voltage drop across the load resistor to trace the laser pulse).

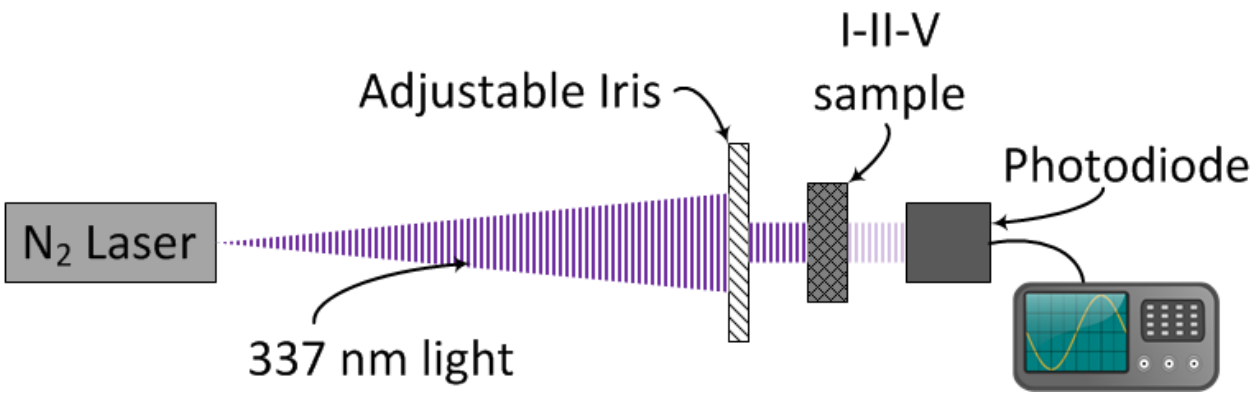

Fig. 6.36. The experimental setup for the 337 nm laser attenuation / absorption studies.

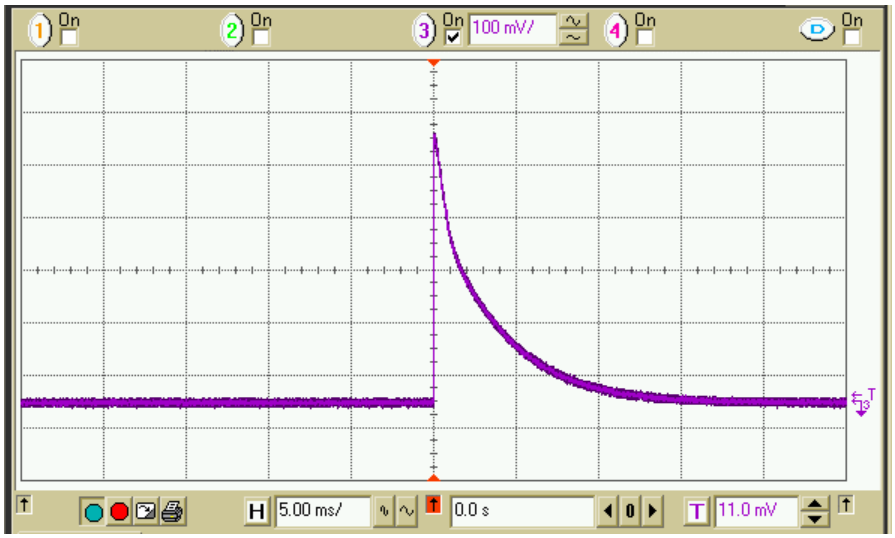

Fig. 6.37. The response from the Si photodiode from a 1.0 mm collimated 337 nm laser pulse.

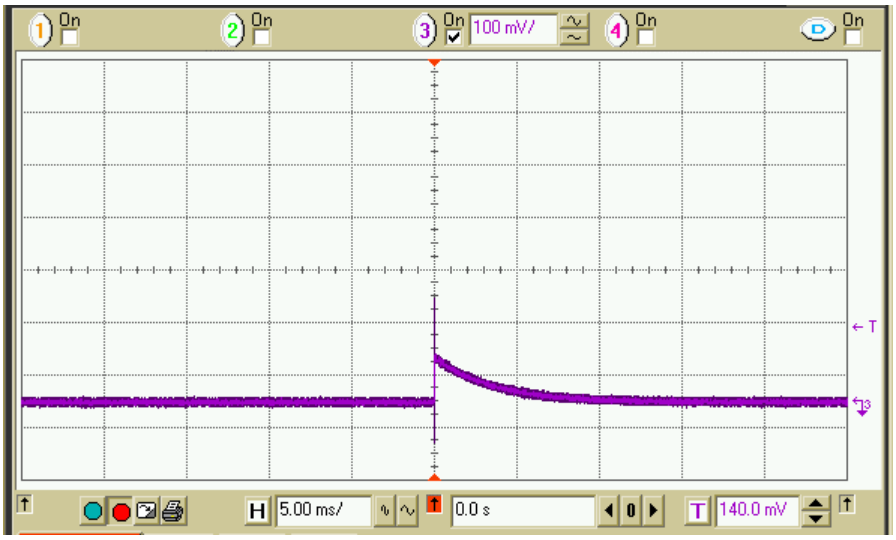

Fig. 6.38. The response from the Si photodiode with the LiZnAs sample in the 337 nm collimated beam.

By comparing the pulse intensities, where the initial unattenuated intensity, I_o, was 500 mV, and the attenuated intensity, *I(1.43 mm),* was 95 mV, it was determined that approximately 81% of the photons were absorbed by 1.43 mm of LiZnAs (assuming negligible absorption in the conformal coating – see section 6.2). Using these parameters an absorption coefficient was determined by

$$I(t) = I_o e^{-xt}, \tag{6.6}$$

where t is thickness of the absorber, x is the absorption coefficient, $I(t)$ is the intensity at thickness t, and I_o is the initial intensity. An absorption coefficient of 0.147 mm^{-1} was determined. The absorption coefficient was used to determine an average thickness of absorption, $\langle t \rangle$, from the expression,

$$\frac{\int_0^t t I_o e^{-xt} dt}{\int_0^t I_o e^{-xt} dt}, \tag{6.7}$$

where t is the sample thickness and x is the absorption coefficient. Eq. (6.7) was integrated from 0 to 1.43 mm, the sample thickness, and an average thickness for absorption was found to be

0.69 mm. The result was a used to confirm that 337 nm laser light was being absorbed in LiZnAs, and also lead to further studies examining the charge transport in LiZnAs.

6.5.2 337 nm laser pulse tracing

LiZnAs samples were tested for sensitivity to 337 nm light using the same collimating iris described in section 6.5.1 open to approximately 1.0 mm, along with an Agilent Infiniium 54832D MSO oscilloscope, and a Melles Griot wide bandwidth amplifier (power supply, preamp and trans-impedance amplifier package) as shown in Fig. 6.39. The wide bandwidth amplifier was a current amplifier, used generally for operating photodiodes in both photovoltaic and photoconductive modes. The particular model was designed with a trans-impedance gain over 5 decades, from 10^3 to 10^7 V/A. This high gain allows for accurate detection of photocurrents from as low as 100pA to 2mA. The maximum frequency response for the 10^3 V/A setting is 5MHz [122]. The maximum frequency responses for other gain settings are listed in Table 6.4

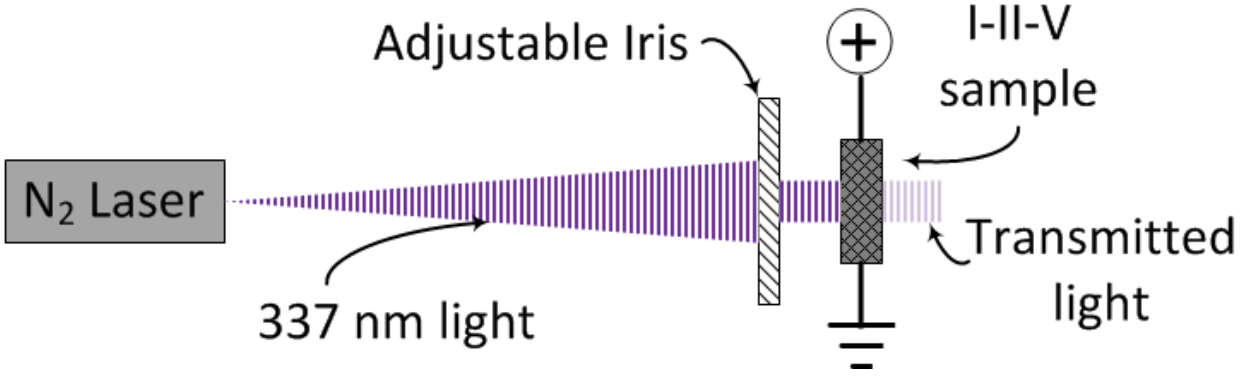

Fig. 6.39. The experimental arrangement for testing the sensitivity of 337 nm photons within LiZnAs.

Table 6.4. The range, or amplifier gain, and corresponding bandwidth maximum for the Melles Griot wide bandwidth amplifier.

Gain (V/A)	Bandwidth
10^3	5MHz
10^4	1.25 MHz
10^5	300kHz
10^6	75kHz
10^7	15kHz

The LiZnAs sample of dimensions 1.59 x 1.39 x 1.42 mm^3 was placed between the contacts of a project box, as shown in Fig. 6.40. A 10.0 volt bias was applied to the sample (at the device) and the laser was set to pulse at approximately 1 Hz. A resulting pulse collected on the oscilloscope is shown in Fig. 6.41.

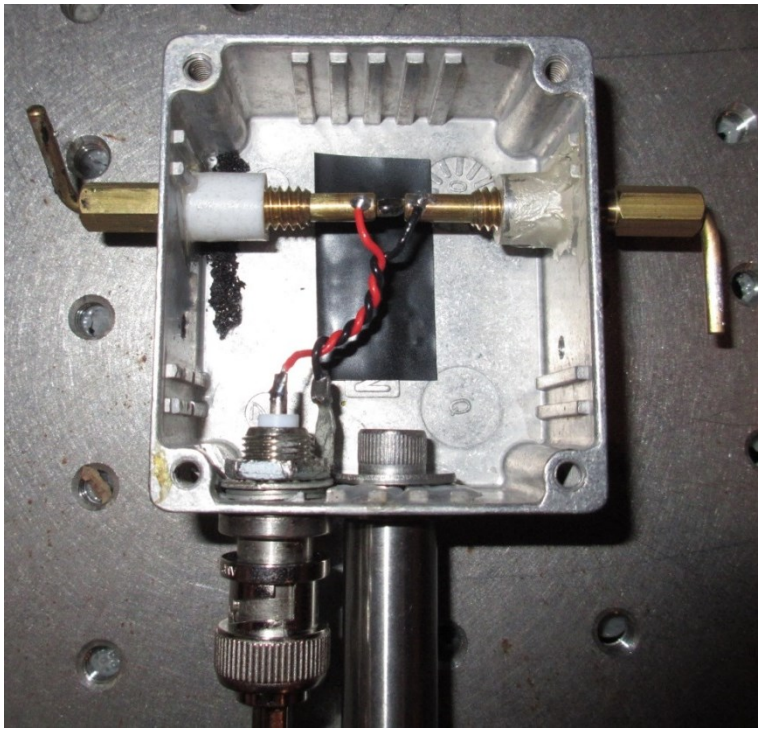

Fig. 6.40. The project box for the sensitivity of LiZnAs samples to neutrons and 337 nm photons. A LiZnAs sample (1.43 x 3.96 x 2.45 mm^3) is mounted between the electrodes.

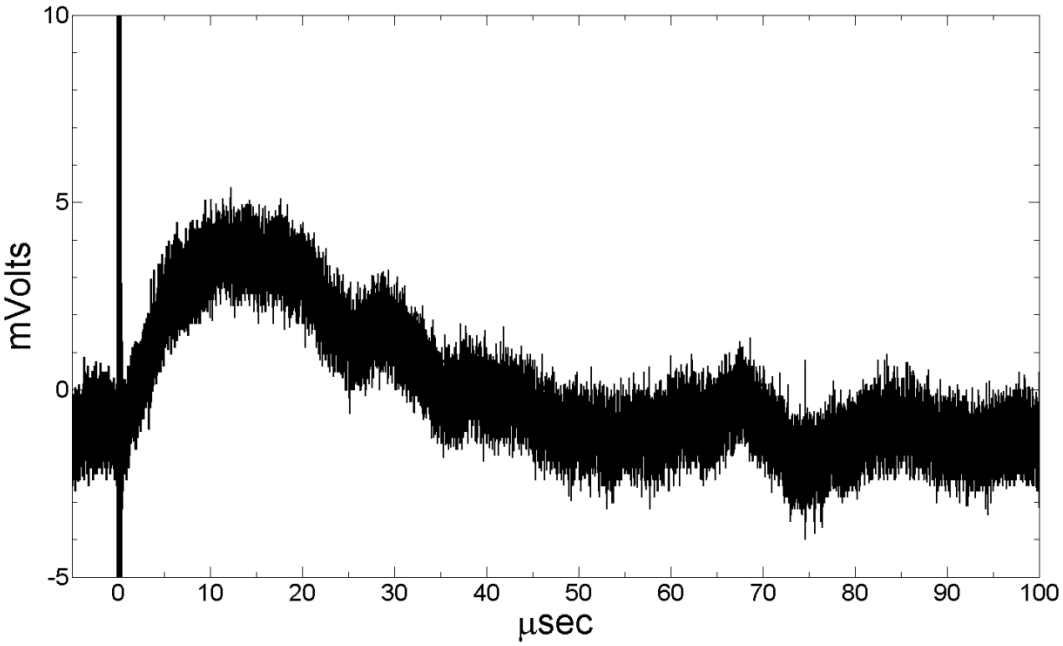

Fig. 6.41. The resulting waveform from a LiZnAs sample (1.59 x 1.39 x 1.42 mm^3) connected to the Melles Griot wide bandwidth amplifier, and irradiated with a 1.0mm collimated 250 μJ pulse of 337 nm laser as recorded on the oscilloscope.

A LiZnAs sample of dimensions 1.43 x 3.96 x 2.45 mm^3 was mounted into the project box, and biased to 10 volts. With the same experimental arrangement shown in Fig. 6.39, the laser was set to pulse at about 1 Hz, and the collimated pulse was traced with the LiZnAs sample, as shown in Fig. 6.42. This particular sample was much more sensitive to the 337 nm photons than the previous sample, and resulted in about a 30 mV pulse, compared to about a 5 mV pulse that was previously observed. Additionally, the electronic noise from the purified samples was much less than what was observed with unpurified samples. Unpurified samples were not tested for 337 nm photon sensitivity due to material degradation over time; however, in alpha and neutron sensitivity testing, noise was found to be a problem, as will be further in further detail in section 6.6. Relatively low noise was observed in the purified samples, as shown in Fig. 6.43, where the full time scale of laser pulse trace is shown.

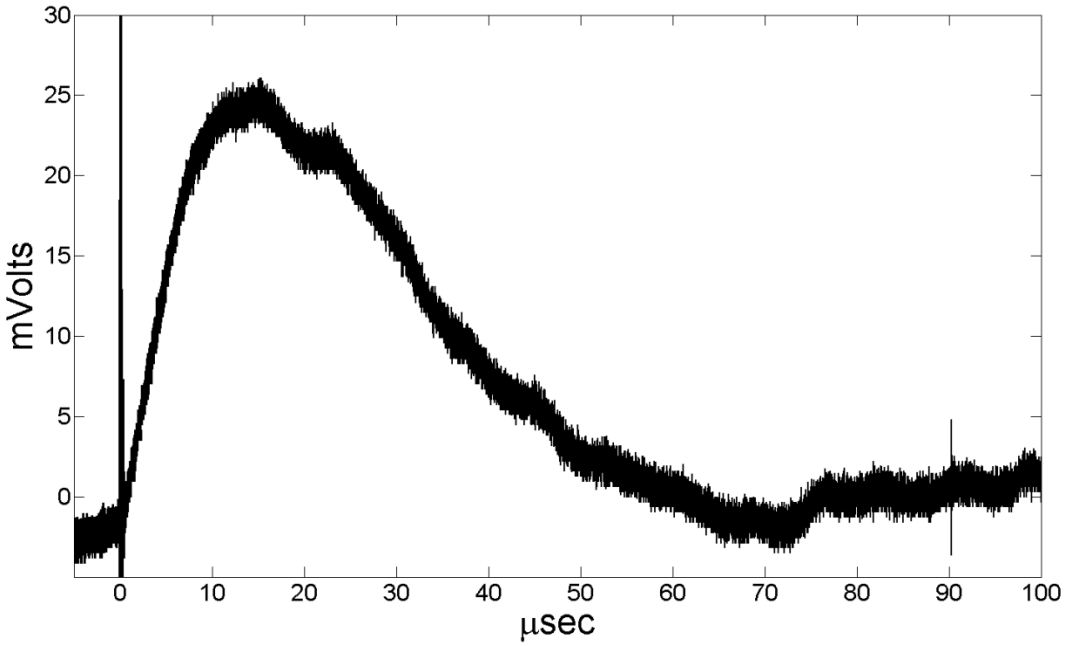

Fig. 6.42. The resulting waveform from a LiZnAs sample (1.43 x 3.96 x 2.45 mm^3) connected to the Melles Griot wide bandwidth amplifier, and irradiated with a 1.0 mm collimated 250μJ pulse of 337 nm laser as recorded on the oscilloscope.

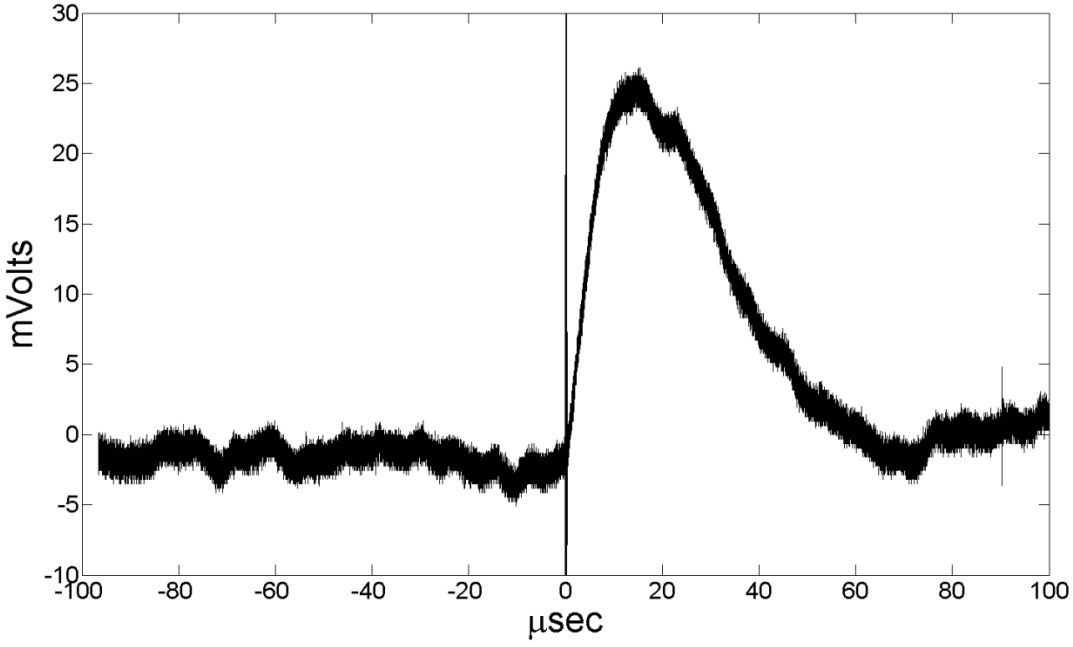

Fig. 6.43. The full-scale resulting waveform as shown in Fig. 6.42 that shows the low baseline noise observed in purified LiZnAs and LiZnP before material breakdown occurs.

It was determined from the 337 nm laser pulse tracing that not all the charge induced was being collected using the Melles Griot wide bandwidth amplifier (transimpedance amplifier). For the particular LiZnAs sample from Fig. 6.42, the transimpedance amplifier gain was set at 10^7 V/A[18]. Therefore, for a 30 mV observed pulse height, approximately 1.5 nA of current, at 10 V applied bias, was induced on the collecting electrodes of the sample. The gain was adjusted from between 10^5, 10^6 and 10^7 V/A where the pulse height increased, and the signal broadened for each adjustment. As gain was increased, the bandwidth maximum allowed by the transimpedance amplifier was reduced with each increment (Table 6.4). However, the pulse height response was not observed to be proportional to the gain increases, which lead to the conclusion that not all the charge was collected. Therefore, it was apparent that additional gain with a higher bandwidth was needed than what the Melles Griot wide bandwidth amplifier could provide. The bandwidth on the Melles Griot wide bandwidth amplifier was limited to a 15 kHz maximum at 10^7 V/A gain as shown in Table 6.4. Therefore, a new electronics package needed to be designed around the material properties to collect all the charge induced in the device.

A trans-impedance amplifier (TIA) was designed to not only collect more of the charge inducted in the device, but also increase the processing speed of the system. The amplifier was designed and fabricated at the Electronics Design Laboratory (EDL) at Kansas State University. The design was based upon a 300 kHz frequency. The TIA was built including a preamp, with a current to voltage gain of 10^6, an amplifier, with a voltage to voltage gain of 10, and output driver amplifier, with a gain of 10^7. The TIA also was designed with 50 Ω output impedance. The TIA, however, resulted in approximately a 150 kHz bandwidth which was limited by the high gain design. The electronics package was built in a single unit with an adjustable voltage from -10 to +10 volts applied at the device as shown in Fig. 6.44 displaying maximum output voltage.

[18] The unit V/A refers to the ratio of voltage out of the circuit : current into the circuit.

Fig. 6.44. Custom electronics package for the high-gain trans-impedance amplifier (TIA) designed and fabricated by the Electronics Design Laboratory (EDL) of Kansas State University.

With the same detector setup as shown in Fig. 6.39, the Melles Griot wide bandwidth amplifier was replaced with the custom trans-impedance amplifier designed and fabricated by the Electronics Design Laboratory (EDL) of Kansas State University. The 1.43 x 3.96 x 2.45mm LiZnAs sample was mounted into the project box the same as previously described. The 337 nm laser as set to pulse at a frequency of approximately 1 Hz. A bias 0.2 volts was applied to the device. The resulting pulse trace, or waveform measured on the oscilloscope, is shown in Fig. 6.45. The voltage was increased to 6.2 volts and the resulting waveform is shown in Fig. 6.46.

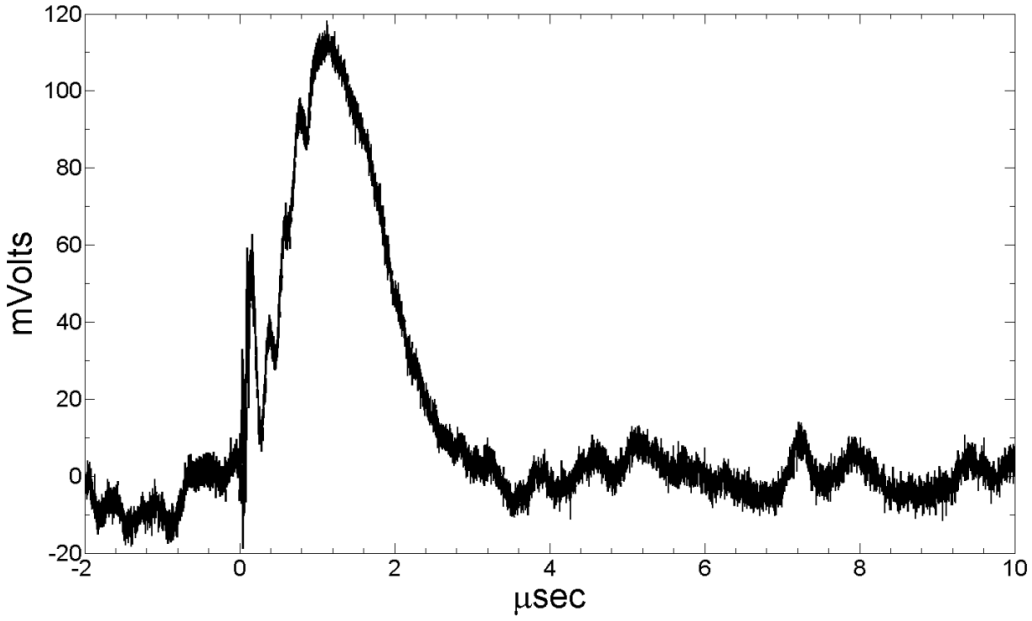

Fig. 6.45. The resulting waveform from a LiZnAs sample (1.43 x 3.96 x 2.45 mm^3) connected to the custom trans-impedance amplifier with 0.2 volts applied at the device. The device was irradiated with a 1.0 mm collimated 250 μJ pulse of 337 nm laser as recorded on the oscilloscope.

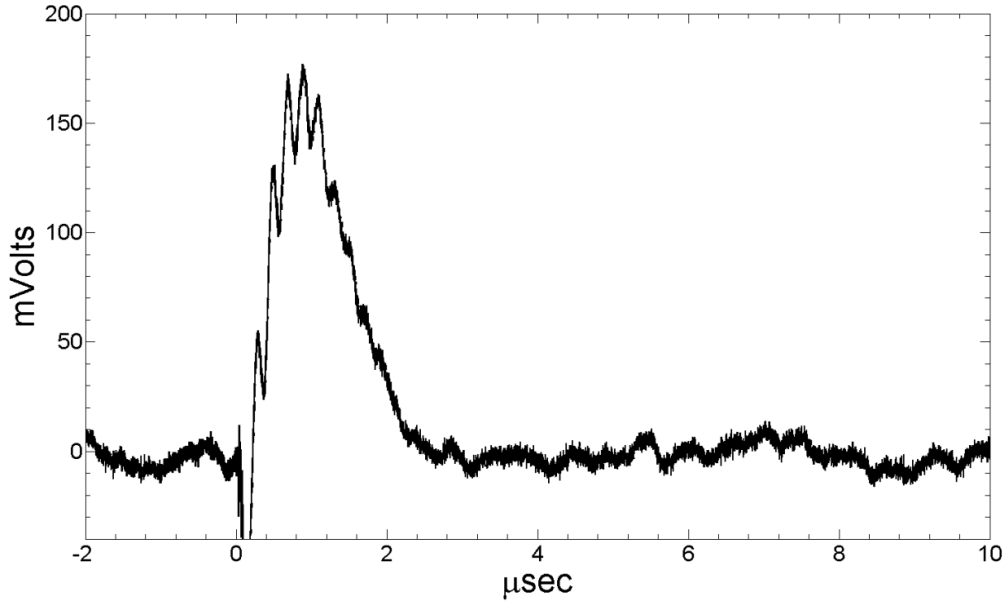

Fig. 6.46. The resulting waveform from a LiZnAs sample (1.43 x 3.96 x 2.45 mm^3) connected to the custom trans-impedance amplifier with 6.2 volts applied at the device. The device was irradiated with a 1.0 mm collimated 250 μJ pulse of 337 nm laser as recorded on the oscilloscope.

It was observed that an increase in the applied bias appeared to also increase the waveform amplitude, as expected if the increase bias worked to also increase the depletion region in the semiconductor. With 0.2 volts applied a ≈115 mV pulse was observed, and with 6.2 volts applied a ≈170 mV pulse was observed. Other applied voltages were explored as well. For instance, with 2.2 volts applied, a ≈120mV pulse was observed, and with 4.4 volts applied a ≈140 mV pulse was observed. Additionally, the new electronics package appeared to collect more of the induced charge compared to what was observed with the Melles Griot amplifier. However, as observed in Fig. 6.45 and Fig. 6.46, there were some oscillations in the signal, likely due to the high bandwidth of the amplifier. The output impedance was designed for a 50 Ω output, and the oscillation could be from impedance mismatch of the BNC cables. However, with impedance matching, the "ringing" in the signal was reduced. Contributions from both the bandwidth, and the high gain design in custom trans-impedance amplifier likely caused the observed oscillations in the signal. Nevertheless, a much larger signal was produced with the same experimental parameters as compared to prior measurements with the Melles Griot amplifier. The custom electronics package was further used for neutron sensitivity testing with LiZnAs samples.

6.6 Neutron Sensitivity Testing

Neutron sensitivity tests were performed at the Kansas State University TRIGA Mark II nuclear reactor. A thermalized neutron beam from a diffractometer beam port was used for majority of the testing. A calibrated beam of 110 ± 10 neutrons cm^{-2} sec^{-1} kW^{-1}, as calibrated with a ^{3}He detector, is present at this beam port. The radial beam from the reactor core is diffracted with a pyrolytic graphite crystal oriented to diffract thermal neutrons (0.0259 eV) from the primary collimated neutron beam into the sample test area. Additional testing was performed at a radial beam port, where the neutron beam is not diffracted and has a Maxwellian distribution of neutron energies along with a distribution of gamma-ray energies. The thermal neutron flux at the radial beam was determined to be approximately 7300 thermal neutrons cm^{-2} sec^{-1} kW^{-1} by a gold foil activation analysis experiment [123]. All detector testing presented here was performed

under vacuum (< 50 mTorr) in a Canberra vacuum chamber, designed for a surface barrier alpha particle detector, to prevent free air ionization from occurring[19]. For purified samples, the Transient Charge Technique (Section 6.4) was performed prior to all neutron sensitivity measurements.

Neutron testing was challenging with not only beam alignment with small samples, but also working with electronic noise issues. *Unpurified* samples would unfortunately suffer from noise "bursts" that would disrupt the measurement. It was originally thought that the noise was caused by surrounding equipment in the reactor bay area, such as cooling pumps, or air conditioning units. However, noise observed from LiZnP and LiZnAs devices was not consistent with the off/on patterns of the reactor bay equipment. Extensive shielding and common grounding added to the experimental setup, which also did not eliminate the noise "bursts". Later it was suspected that a large charge trapping and a long delayed charge de-trapping mechanism was likely occurring in the devices, which required measurements to be collected as "observed" measurements. It was observed on the oscilloscope signal when a noise "burst" would disrupt the signal, and at this point, the measurement was restarted. This continued problem resulted in short measurement collection times, in the range of 3 – 5 min. Additionally, as mentioned in Section 6.5, LiZnP and LiZnAs would notoriously break down from high biases applied over a long period of time. Generally, no more than ±600 volts was applied at the preamplier during testing, and would cause irreparable damage to the device, resulting in a constant noisy device at any voltage applied in subsequent testing. Section 6.3 confirms this phenomenon with I-V curve data before radiation sensitivity testing, and after, where often the devices had become completely conductive after radiation sensitivity testing (where a high voltage was applied to the device for a long period of time). Devices were reprocessed, in this case, where contacts were applied in a different crystalline direction. In some cases, reprocessing devices resurrected an operational device for further testing. In most recent testing, devices were limited to a maximum of ±10 volt applied bias to prevent breakdown of the device and prolong testing capabilities.

[19] Free air ionization is process where reaction products escapes the neutron absorbing bulk (LiZnP or LiZnAs neutron detector), and is ionized in the high electric field around the anode. By placing the detector inside a vacuum chamber, air was removed around the sample, thereby, removing the potential ionizing medium.

6.6.1 Neutron Sensitivity Testing with Synthesized Material (*unpurified*)

Neutron sensitivity was evaluated for the bulk crystalline LiZnP and LiZnAs devices that had silver epoxy anode and cathode contacts, and also for devices with Ti-Au anode and silver epoxy cathode contacts. Examples of these samples are shown in Fig. 6.47 and Fig. 6.48. Tests with *unpurified* samples were performed at the diffracted thermal neutron beam port at the KSU nuclear reactor.

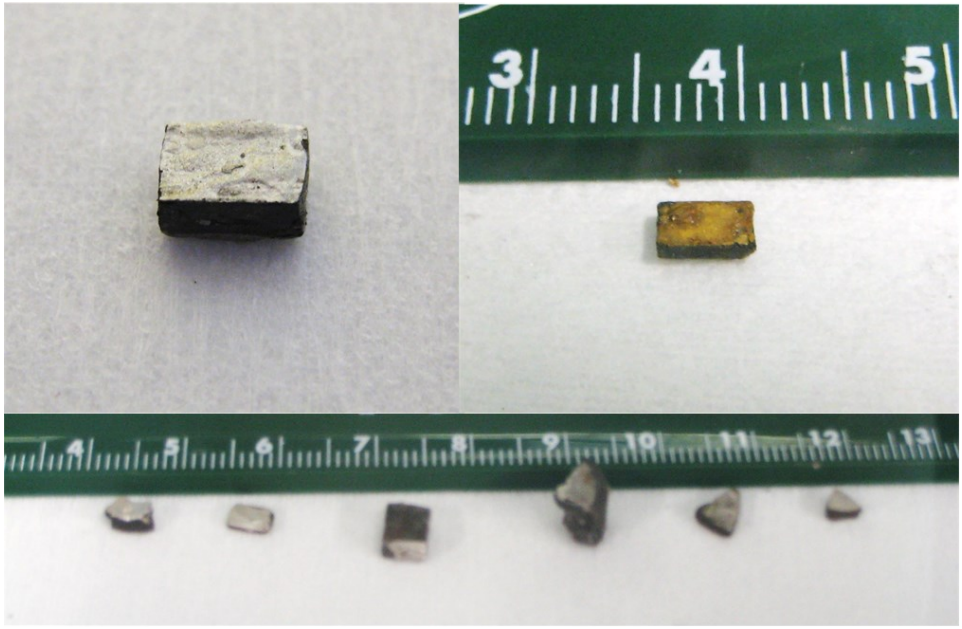

Fig. 6.47. A number of bulk LiZnP and LiZnAs samples that were grown by the high-temperature Bridgman method described in section 5.3. The top left sample is of dimensions 2.01 x 3.48 x 4.91 mm, the sample with the I-V curve response shown in Fig. 6.14. The top right sample is a LiZnP sample with a gold paste contact, however after the contact curing anneal, the sample was extremely conductive and was not tested any further.

Fig. 6.48. A LiZnP sample with a silver epoxy (cathode) contact and a 500 Å / 10,000 Å Ti/Au gold (anode) contact. This is the same sample with the I-V response shown in Fig. 6.15 with approximate dimensions 2.0 x 3.0 x 5.0 mm^3.

All reported testing was performed with the LiZnP sample shown in Fig. 6.48. All testing with other devices were noisy, thereby, leading to inconsistency between measurements. The Ti-Au anode contact appeared to help reduce the noise to a manageable point and allow for testing; however, the aforementioned noise "bursts" were a problem, and appeared more frequently as testing continued. The first spectra collected were for one hour duration measurements where cadmium shutter was either closed (to block neutrons) or open, as shown in Fig. 6.49, for a reactor power of 200 kW. Note that this measurement was not continuously monitored, and a noise "burst" could have affected either measurement. Negative 100 volts was applied through the preamp (Ortec 142A) connected to the device, and the bipolar amplifier (Canberra 2022) output was connected to the MCA (Ortec PCI TRUMP). The bipolar output appeared to help balance the signal back to the baseline in moments of high noise.

With same sample and testing parameters as previously described, continuously monitored measurements were collected assuring that no noise "burst" was measured. Three measurements, each a 100 second duration, were collected for each "shutter open" and "shutter closed" configuration. The three measurements for each were summed and the resulting thermal neutron response spectrum is shown in Fig. 6.50.

Lastly, another set of measurements was collected with the same LiZnP sample at 200 kW reactor power. However, this measurement was collected with an applied bias of -50 volts through the preamplifier, as higher applied biases were already tested with the particular sample.

The bipolar output from the amplifier was connected to the MCA, and the resulting thermal neutron response pulse height spectrum is shown in Fig. 6.51.

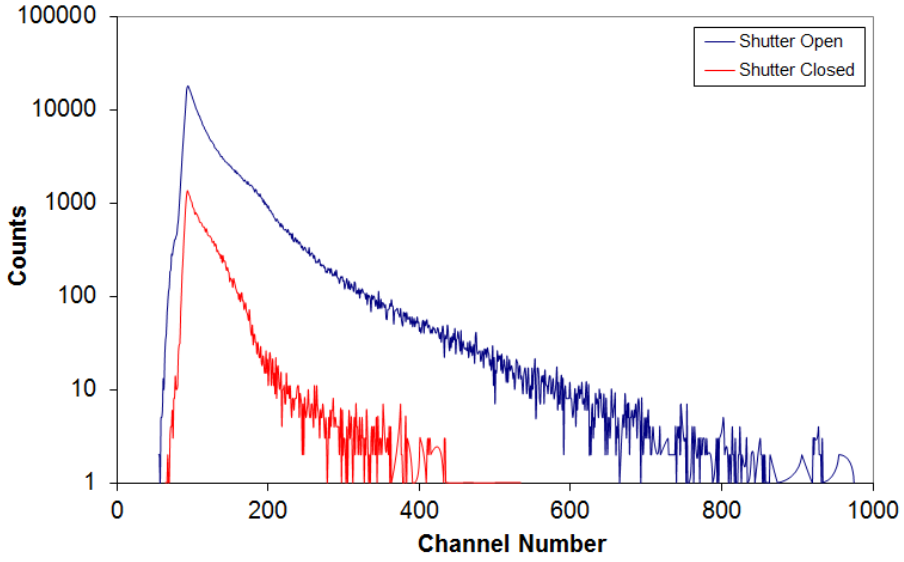

Fig. 6.49. The thermal neutron reaction product pulse height spectrum with the LiZnP sample from Fig. 6.48. Shown are one hour unmonitored measurements, measurements where a noise "burst" may be included in either measurement. Negative 100 volts was applied at the preamplifier, and measurements were collected at reactor power of 200kW.

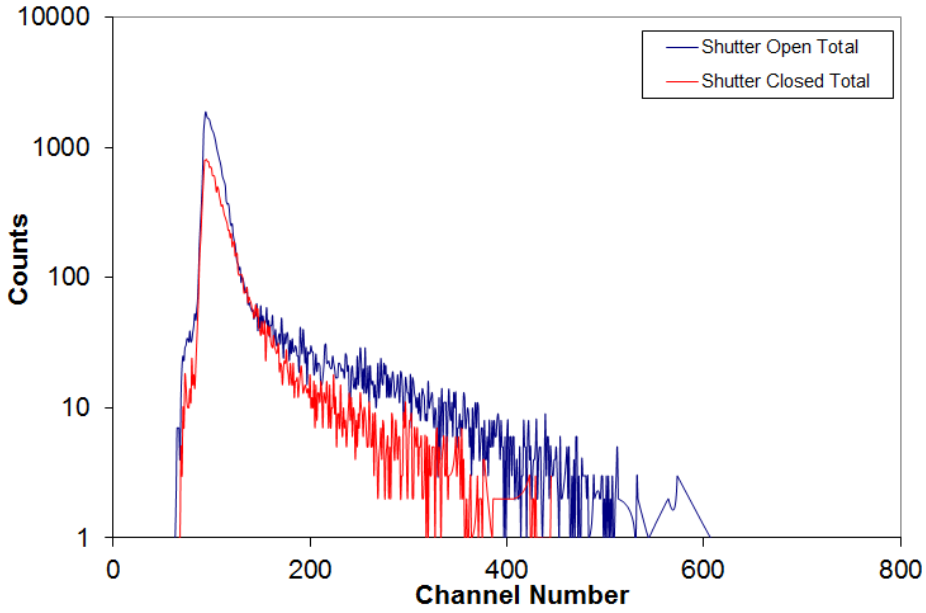

Fig. 6.50. A thermal neutron reaction product pulse height spectrum with the same LiZnP sample as previous. Here, three – 100 second measurements were continuously monitored, and collected for each shutter open and shutter closed condition. The three measurements were summed as shown here. Negative 100 volts was applied at the preamplifier, and measurements were collected a reactor power of 200kW.

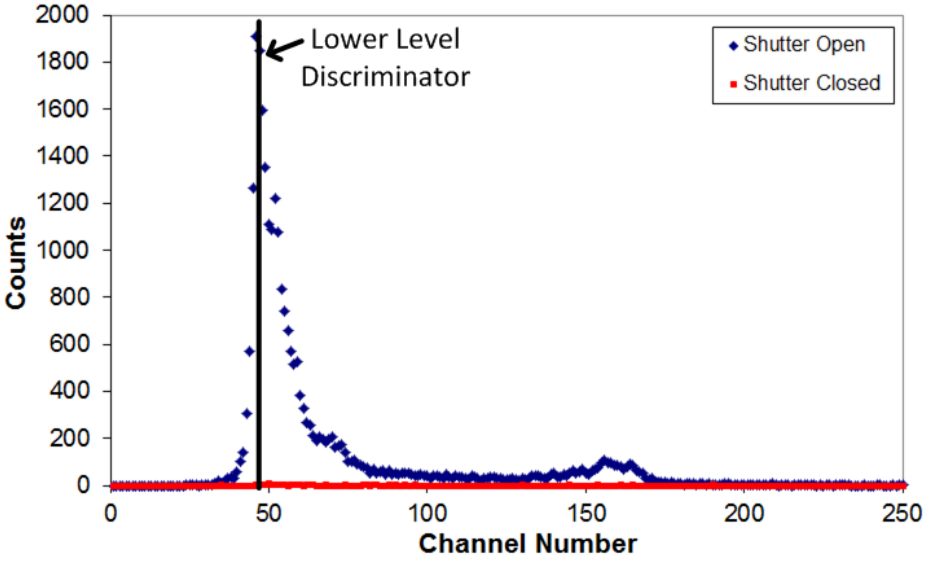

Fig. 6.51. A thermal neutron response measurement with the LiZnP sample. Shown are 300 second measurements collected at a reactor power of 200 kW and -50 volts applied to the preamplifier. The LLD was set to channel number 47.

Neutron sensitivity testing appeared to show LiZnP is sensitive to neutrons; however, noise bursts would randomly disrupt the signal, thereby, making measurement collection difficult. The spectrum shown in Fig. 6.51 was the most convincing spectrum collected. The measurement was continuously monitored for the 300 second duration and the signal on the oscilloscope did not appear to be a typical noise spectrum that could distort a measurement (where noise would be recorded in all channels). Afterwards, measurements indicate that there was an obvious material problem that needed to be addressed, and was likely a result of material impurities. Static sublimation purification was performed of the synthesized material as detailed in section 5.2, and bulk ingots were grown from the purified material as detailed in section 5.3. Devices were fabricated, and tested from the purified material, as will be described in the following section.

6.6.2 Neutron Sensitivity Testing with Purified Material

Thermal neutron sensitivity was also evaluated with *purified* samples grown by a high temperature Bridgman method. Examples of samples evaluated are shown in Fig. 6.52. The noise "bursts" observed with *unpurified* samples was not observed with *purified* devices. However, the breakdown in device performance after prolonged testing continued to be a problem. For example, the thermal neutron response pulse spectrum from a LiZnP sample appeared to be functioning as expected for the duration of the 300 second measurement, as shown in Fig. 6.53. Desirable features were observed here, however, measurements were not always repeatable. After a "shutter closed" measurement was collected, more measurements were desired; however, the measured performance was inconsistent. The applied bias was adjusted to observe the effect on performance. Generally, at this point, the device became noisy and lead to spectral responses as shown in Fig. 6.54, where the bias was also changed to 480 volts. Spectral features were not observed and the noise was at a much higher amplitude, appearing beyond channel 100. The only differentiating feature between the "shutter open" and "shutter closed" measurements was the slightly higher noise spectrum that extended into the higher energy spectrum with the presence of neutrons. Other LiZnP samples were tested, resulting in no response to thermal neutrons, or only an extension of the noise spectrum to higher channel numbers, but not resulting in any distinguishable features. Noise eventually became so prominent in all samples that spectra would become saturated with noise within all channels. Afterwards, I-V curves were collected, as shown in Fig. 6.17, where high conductivity was observed.

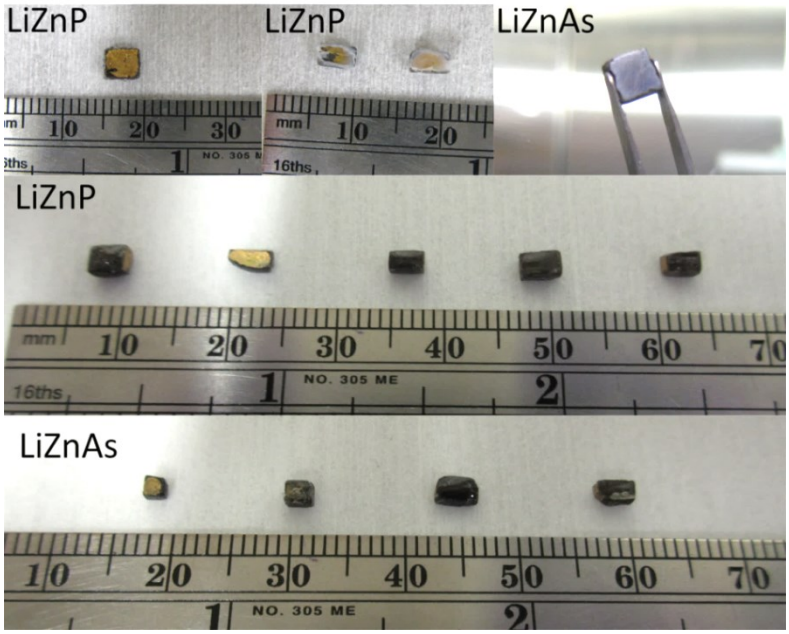

Fig. 6.52. A number of purified bulk LiZnP and LiZnAs samples that were grown by the high-temperature Bridgman method described in section 5.3. The sample on the top left was the sample (2.020 x 3.518 x 4.077 mm^3) with the I-V curve response shown in Fig. 6.16. The sample on the top right is a LiZnAs sample (2.100 x 4.060 x 4.155 mm^3) with the I V curve response shown in Fig. 6.17. The two LiZnP samples across the top are coated in HumiSeal®. After reprocessing, all samples were coated in Epoxy Technology® 301-2, as shown for all of the samples across the middle and bottom pictures.

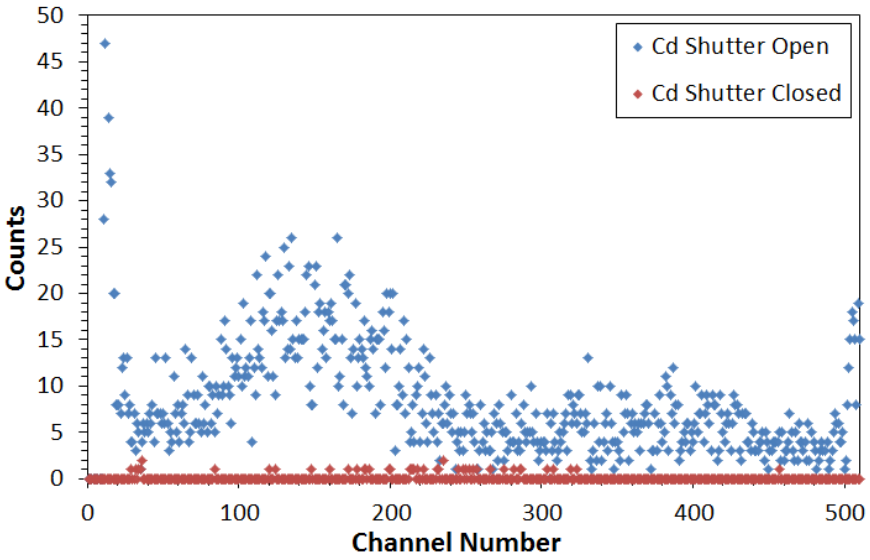

Fig. 6.53. Thermal neutron reaction product pulse height spectrum with a LiZnP sample of dimensions 2.020 x 3.518 x 4.077 mm^3 with 465 volts applied through the preamplifer. Measurements were collected at the thermal neutron beam port at a 200kW reactor power. 300 sec measurements were collected.

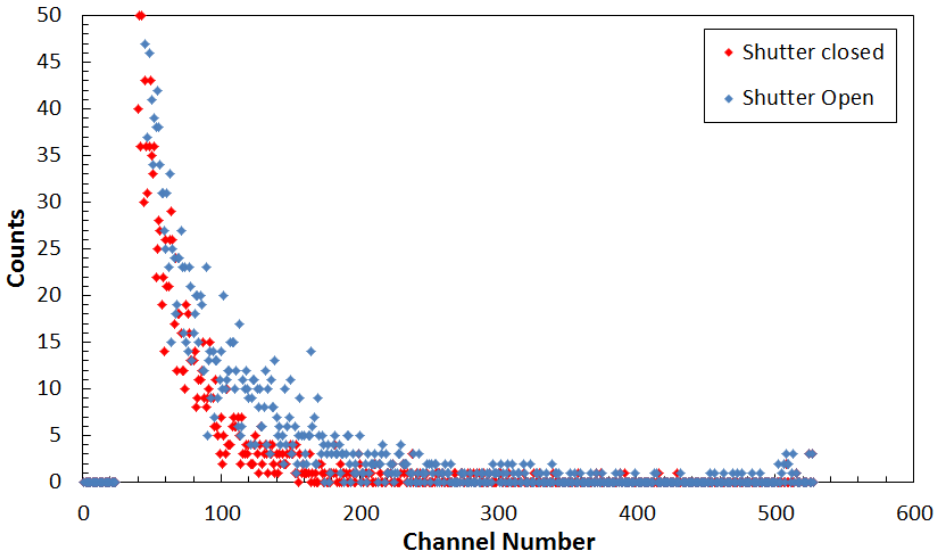

Fig. 6.54. Thermal neutron response pulse height spectrum with the same LiZnP sample as previous (2.020 x 3.518mm x 4.077mm^3). 480 volts was applied at the preamplifier. Measurements were collected for 300 seconds at 200kW reactor power.

Purified LiZnAs samples were also tested for neutron sensitivity at the thermal neutron beam port of the KSU TRIGA Mark II nuclear reactor. Similar to what was observed with LiZnP samples, the measured LiZnAs sensitivity to neutrons was minimal. A pulse height spectrum was collected for 600 seconds, as shown in Fig. 6.55. For each measurement, the reactor power was at 250 kW and the bias 528 volts applied through the preamplifier. The applied bias was adjusted to optimize performance, but did not lead to better spectral features, and instead caused noise problems. At this point, continuous noise, that did not exist prior to the Transient Charge Technique and neutron sensitivity measurements, was being recorded in all channel numbers. Some samples were reprocessed (diced) into different dimensions; however all were reprocessed with contacts in different orientations, so the electric field would be applied to a different crystalline directions. Samples were reprocessed as described in Sections 5.3.3 and 6.1. The samples were coated in Epoxy Technology® 301-2 conformal coating that was characterized as transparent to 337 nm laser light (Section 6.5). I-V curves were collected for all reprocessed samples. Some samples were still noisy, however some samples were highly resistive, and one particular sample exhibited rectifying behavior, as shown in I-V curves in Fig. 6.19 and Fig.

6.20. In order to try to preserve the samples from excessive bias, the bias was limited to ±10 volts for future testing.

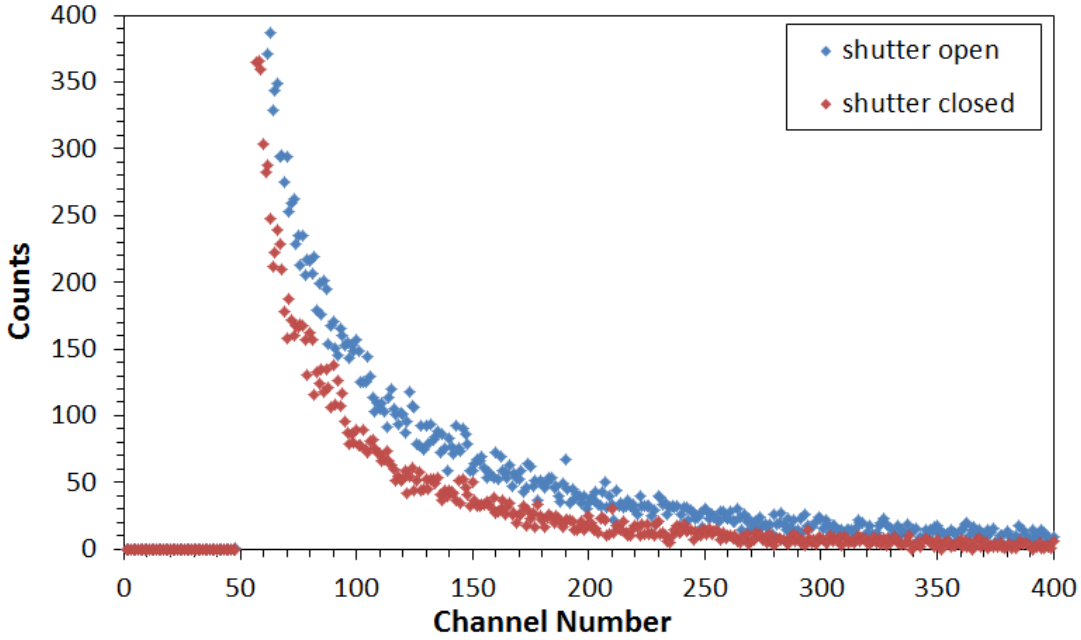

Fig. 6.55. Thermal neutron reaction product pulse height spectrum with a LiZnAs sample of dimensions 2.100 x 4.060 x 4.155 mm^3 with 528 volts applied at the preamplifier. Measurements were collected for 600 seconds at a reactor power of 250 kW.

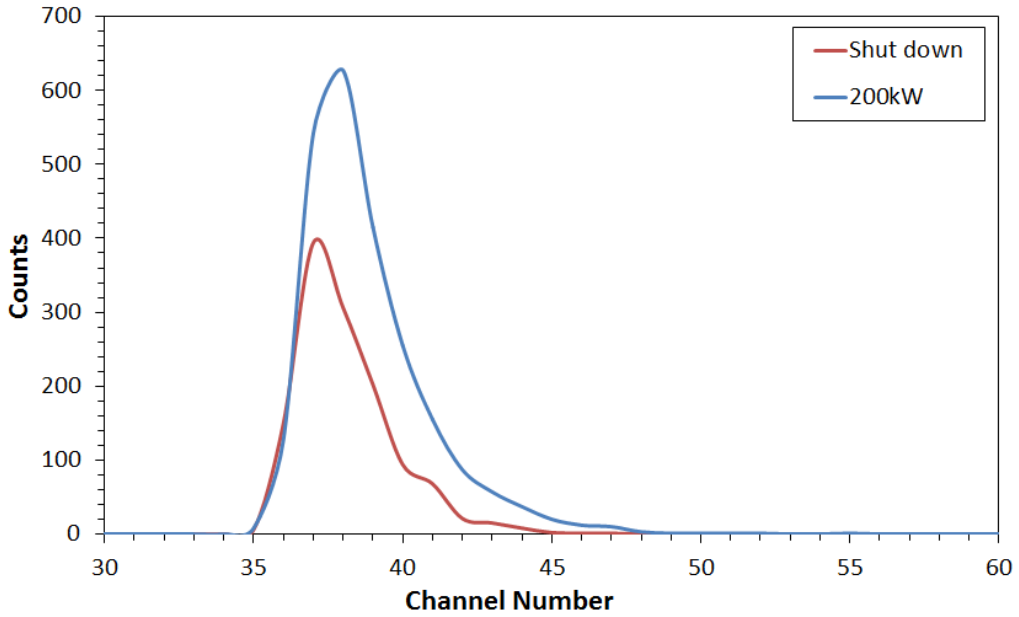

Fig. 6.56. Pulse height spectrum collected at the radial beam of the Triga Mark II nuclear reactor with a LiZnAs sample of dimensions 1.43 x 3.96 x 2.45mm. The custom electronics shown in Fig. 6.44 were used with +10 volts applied at the detector. 300 second measurements were collected at a reactor power of 200 kW. The discriminator was set at channel 37.

Neutron sensitivity testing with the new electronics at the thermal neutron beam did not result in distinguishable reaction product spectra; therefore, a higher flux beam port of the TRIGA Mark II nuclear reactor was used for further testing. The LiZnAs sample was tested at the radial beam port with a thermal neutron flux approximately 7300 cm^{-2} sec^{-1} kW^{-1}. Tests performed here again did not result in distinguishable features, but instead extends the noise continuum to high channel numbers, as shown in Fig. 6.56, for measurements collected with the reactor power of 200kW. Discussed in the following chapter are details of the charge collection, charge transport, and crystallinity of the samples as a likely cause to the observed device performance.

Chapter 7 : CONCLUSIONS AND FUTURE WORK

I think and think for months and years. Ninety-nine times, the conclusion is false. The hundredth time I am right.

- ***Albert Einstein***

Discussed in the following chapter are general conclusions from the presented work. Additionally, reasons for the minimal neutron sensitivity observed in the work are presented. Suggestions and an outline for future work with Nowotny-Juza materials are presented at the end of the chapter.

7.1 Conclusions

The ternary Nowotny-Juza materials, LiZnP and LiZnAs, were synthesized from elemental constituents. Each material exhibited a cubic crystal structure with atom placement in the theoretical locations, and lattice constants consistent with calculations and literature. However, material purity is not ideal, as indicated from the ICP-OES analysis and the XRD phase identification scans. Crystals with in-plane ordering can be found in amongst the synthesized powders and samples. These samples exhibited crystallinity and a reasonable rocking curve FWHM value for initial growths.

Nowotny-Juza compounds, LiZnP and LiZnAs, were synthesized in-house into powder and chunks, and purified by a static sublimation. The ICP-OES data indicate that higher vapor pressure binary and elemental materials can be removed from the synthesized material reducing the impurity level, while retaining the 1:1:1 stoichiometric ratio between constituent elements. The purification material x-ray diffraction studies also indicate that impurities were removed. For LiZnP x-ray diffraction evaluations, phase peaks still exist that cannot be identified. Some

peaks may belong to a binary or elemental material that was included from one or a few of the five total LiZnP synthesis processes that were used in the sublimation process. For LiZnAs x-ray evaluations, all prominent phase peaks were accounted by experimental literature phase locations, or by theoretical phase locations. Because impurity peaks still were identified with LiZnP evaluations, the thermal profile of the purification furnace may have to be explored further to optimize the sublimation process. Ultimately however, a higher quality material was produced, and was used to grow crystalline ingots that were processed into devices.

During this project, the largest known crystalline ingots of LiZnP and LiZnAs were grown for the first time by a modified Bridgman high temperature method. Crystal growth was performed successfully in pyrolytic graphite crucible lined tantalum vessels. The melting temperature observed was experimentally determined to be between 1320 – 1370 ^{o}C for LiZnP crystal growth, and between 1230 – 1250 ^{o}C for LiZnAs crystal growth. LiZnP and LiZnAs bulk samples exhibited a (220) main orientation as characterized by EDXRD and high-resolution XRD. It is clear that these materials prefer to grow in the [110] direction. A reasonable degree of crystallinity and ordering was demonstrated from the out-of-plane and in-plane measurements from LiZnP samples. A reasonable degree of crystallinity and ordering was demonstrated from the out-of-plane and in-plane measurements from LiZnAs samples. From the off-axis phi scans it was clear that three major domains were present in the characterized LiZnAs sample. The bulk crystals exhibited a P-43m space group instead of the F-43m space group. Nevertheless, the desired cubic crystal structure remained, and lithium was still present in the lattice, however, it appears that Li did not fill all interstitial sites, unlike what was observed in the synthesized and purified powders.

Devices were fabricated from the bulk LiZnP and LiZnAs ingots. These devices were characterized for an optimum coating material for protection from humidity in air. HumiSeal®, although fast drying and easy to apply, would often result in flaking and peeling over time. The Epoxy Technology® 301-2 conformal coating was found not only to be transparent to 337 nm light, but a very rugged coating that would not flake and continue to protect the hydroscopic sample to date. I-V curves were collected from the fabricated devices and showed ohmic behavior in some cases, and rectifying behavior in other cases. Resistivities were often high for initial tests (10^{6} – 10^{11} Ω cm), however would often become extremely conductive after prolonged testing. For devices that were high resistivity and performing with low noise, the

Transient Charge Technique was used to characterize the free carrier mobility and mean free drift time. Alpha particle sensitivity was evaluated using an ^{241}Am source (acquired from a smoke detector), where sensitivity was observed above the noise continuum. This not only showed charge can be transported through the material, but also made the transient charge technique possible using short range, high energy radiation. A $\mu_e\tau_e$ product of 8.0 x 10^{-4} cm^2 V^{-1} ± 4.8% and 9.1 x 10^{-4} cm^2 V^{-1} ± 4.4% was determined for LiZnP and LiZnAs respectively. Measurements were performed to characterize the hole mobility and mean free drift time, however, signals were not observed in this case due to hole trapping. Therefore, a $\mu_h\tau_h$ was assumed to be two orders of magnitude less (1.0 x 10^{-6} cm^2 V^{-1}) for charge collection efficiency calculations.

Devices were also tested for sensitivity to 337 nm laser light. It was determined experimentally that for a LiZnAs device of 1.43 mm thickness, 81% of the incident photons from the 250 μJ laser pulse were absorbed in the material. An absorption coefficient was determined to be 0.147 mm^{-1} for 337 nm photons. This proved that photons were being absorbed in the material; therefore, the next step was to verify the induced charge created in the material could be transported through the material. Laser pulses of 337 nm photons were traced on an oscilloscope for two different trans-impedance amplifiers. A pulse height of approximately 30 mV and a pulse width of approximately 70 μs were recorded with a Melles Griot wide bandwidth amplifier for the same 1.43 mm thick LiZnAs device biased at 10 volts. A custom trans-impedance amplifier was designed to collect more of the induced signal[20], and increased the signal processing speed. The signal produced from the 337 nm laser pulse was measured with the custom electronics where approximately a 170 mV pulse height with a 2.5 μs pulse width was recorded with a 6.3 volt bias applied at the device. A faster pulse processing speed was observed, as well as a greater pulse height from the 250 μJ laser pulse.

Neutron sensitivity was evaluated with LiZnP and LiZnAs *unpurified* and *purified* devices. The first neutron induced signals from Nowotny-Juza materials were observed in this study. *Unpurified* samples suffered from noise "bursts" that required that measurements be made with constant observation to ensure that noise would not affect the measurement as it was collected. If a noise "burst" was observed, the measurement was restarted so that a "clean"

[20] It was determined that not all of the induced signal was being collected as the gain was adjusted on the wide bandwidth amplifier, as explained in section 6.5.2.

measurement would be collected. Purification of the synthesized material was performed to help increase the material quality and reduce the noise "bursts" observed with the *unpurified* devices. Devices fabricated from *purified* material did not suffer from the same noise "bursts"; however devices would often breakdown and suffer from continuous noise after prolonged testing with a high applied voltage (> 10 volts) to the device, a problem also observed with *unpurified* devices. Device break down has been observed with other materials with non-injecting blocking contacts (Schottky barrier) applied, and is a common problem [124]. Eventually, a maximum of ±10 volts applied at the device was implemented in order to preserve device performance. Neutron sensitivity was observed with newly prepared devices; however, these measurements did not always produce repeatable results. Devices would either breakdown with excessive electronic noise, or the device would not perform the same as with previous measurements, generally again suffering from noise. These materials suffered from many material problems that all influence the device performance, including the following:

1. Charge trapping – The free charged carriers produced in the device from a radiation interaction are trapped during the drift process, and do not arrive at the collecting electrode.
    a. Material Purity – Ionized impurities in the material can act as charge trapping centers. A purification process helped stabilize the noise observed with LiZnP and LiZnAs samples, but it is clear that impurities still exist. Semiconductor grade materials are generally on the order of 5N purity, and these materials produced in this work are of lower purity.
    b. Multi-faceted, or multi-domained crystals – Grain boundaries that exist between facets, or domains, in a crystalline material are large charge trapping centers. Both LiZnP and LiZnAs samples were characterized with multiple domains, and a particular LiZnAs sample was characterized with three major domains.
2. Electric field effects – Ionized impurities can reduce the electric field strength in affected areas of the device rendering the area inactive, thereby, reducing the sensitivity of the detector.

3. Charge carrier scattering – Ionized impurities can act as scattering centers, thereby, reducing the carrier mobility. A reduction in the charge carrier mobility reduces the charge collection efficiency.
4. Limited charge collection efficiency – From the charge collection efficiency profiles, it is observed that not all of the charge induced from a radiation interaction will be collected at the collecting contacts. Interactions close to the cathode will produce much larger signals than interactions close to the anode.
    a. Poor μτ product – Much of limited charge collection efficiency problem is caused by low $\mu\tau$ products. Experimentally determined $\mu\tau$ products were on the order of 10^{-4} cm^2 V^{-1} largely contributed to mean free drift times for electrons on the order of 100 μsec. A $\mu\tau$ product for holes was not able to be measured indicating extremely poor hole transport properties.
5. Lithium deficiency – It was observed that in LiZnAs bulk samples, the content of lithium was reduced by ¾ where not all of the interstitial sites at (½, ½, ½) were lithium filled. Lithium is still present in the material; however, the content was reduced, thus reducing the neutron sensitivity.

Additionally, it is questionable why the result with the laser induced charge was repeatable when neutron measurements were not as repeatable, or as successful with LiZnP and LiZnAs devices. Recall from section 6.5, the laser used for the experiments was a 337 nm laser at a 250 μJ power within a 5 ns pulse. Assuming complete absorption of the 5 ns pulse of 250 μJ of 337 nm photons, the intensity of the resulting voltage pulse from the preamplifier can be determined based on the incident photon energy and beam intensity. The voltage intensity of 337nm laser inducted pulse can be compared to the voltage pulse intensity from a neutron event.

The 337 nm photons emitted from the laser can be converted to energy (in Joules) with the expression,

$$E = \frac{hc}{\lambda}, \tag{7.1}$$

where h is Planck's constant, c is the speed of light, and λ is the photon wavelength. A photon energy of 5.89 x 10^{-19} J, or 3.68 eV, was determined, and can be converted to total photons using the initial laser power,

$$250\mu J \times \frac{1\ photon}{5.89\times10^{-19} J} = 4.24\times10^{14}\ \ photons / pulse\ . \tag{7.2}$$

Measurements were collected at a distance of 24.625 inches from the laser; therefore, the laser diverges significantly at the location of interaction with the device. The divergence was measured experimentally to be 30.2 mm horizontal x 6.9 mm vertical at 24.625 inches from the laser, and a beam area was calculated to be 208.38 mm^2. Assuming a uniform photon distribution[21] across the incident beam at 24.625 inch distance, the photon flux per pulse was defined in terms of area by,

$$\frac{4.24\times10^{14}\ \ photons / pulse}{208.38\ mm^2} = 2.03\times10^{12}\ \ \frac{photons}{pulse\ mm^2}\ . \tag{7.3}$$

The area of 1 mm diameter collimating iris was determined to be 3.14 mm^2, so the amount of photons incident upon the sample from collimation is,

$$\frac{2.03\times10^{12}\ photons}{pulse\ mm^2}\times 3.14\ mm^2 = 6.37\times10^{12}\ \frac{photons}{pulse}\ . \tag{7.4}$$

The density of electron – hole pairs created from a photon interaction can be determined with the following expression,

$$N = \frac{E}{\varepsilon}, \tag{7.5}$$

[21] Laser beams are emitted with a Gaussian distribution, where the majority of the photon flux is in the middle of the beam. Collimation of the beam was positioned approximately in the center of beam, therefore assuming a uniform photon distribution is a conservative assumption in the calculation.

where E is the absorbed photon energy, and ε is average energy per ion pair (eV / e-h pair). For example, Si, $\varepsilon = 3.6\ eV / e\text{-}h\ pair$, and for Ge, $\varepsilon = 3.0\ eV / e\text{-}h\ pair$ [31]. However, LiZnP and LiZnAs samples were irradiated with a beam of 3.68 eV photons (337nm). These relatively low energy photons have only enough energy to excite one electron – hole pair per photon interaction from the highest energy valence band. Much higher energy photons are required to excite electrons from energy levels of the lower valence bands. Therefore, it is assumed that 1.0 *e-h pair* is excited per 337 nm photon interaction. From section 6.5.1, it was determined that approximately 81% of the incident photons are absorbed in the LiZnAs for a 1.43 mm thickness. For this case, the *e-h pairs per pulse* can be determined assuming 81% absorption, and of the 81%, majority of the interactions are full absorptions, where it is found,

$$81\% \times \left(6.37 \times 10^{12}\ \frac{photons}{pulse} \right) \times 1.0 \frac{e-h\ pairs}{photon} = 5.2 \times 10^{12}\ \frac{e-h\ pairs}{pulse}\ . \tag{7.6}$$

The total charge created in the device in coulombs can be determined using the conversion, *1.602 x 10^{-19} coulombs / e-h pair*,

$$5.2 \times 10^{12}\ \frac{e-h\ pairs}{pulse} \times 1.602 \times 10^{-19}\ \frac{coulombs}{e-h\ pairs} = 8.27 \times 10^{-7}\ \frac{coulombs}{pulse}. \tag{7.7}$$

Assuming all of the charge created in the device was swept out with an applied electric field, and no charge was trapped or recombined in the transit process, a voltage out, V_o, from the preamplifier can be determined from the expression,

$$V_o = \frac{Q_o}{C_f}, \tag{7.8}$$

where Q_o is the initial charge released by the detector (8.27 x 10^{-7} coulombs in this case), and C_f is the feedback capacitance of the preamplifier. An Ortec 142A has a feedback capacitor of 1.0 pF [125], and in the custom electronics package provided by the KSU Electronics Design

Laboratory, a 1.0 pF feedback capacitor was used. Therefore, for the case with either preamplifier used in the measurement, the voltage out of the preamplifer is,

$$V_o = \frac{8.27\times10^{-7}\,C}{1\times10^{-12}\,F} = 827{,}000\ Volts\,. \tag{7.9}$$

Such a high voltage coming from the preamplifier would certainly be clipping the signal processing electronics, however this was not observed. Instead, signals in the mV range were observed, indicating much of the induced charge in the device is being trapped, or recombined, before reaching a collection electrode, which consequently output voltage amplitude.

The voltage out on the preamplifer can be determined for a single neutron interaction in LiZnP or LiZnAs devices and compared to the voltage out from a laser pulse. The Q-value for the ^{6}Li(n,t)^{4}He interaction is 4.78 MeV. Because a much higher energy is induced per thermal neutron event than with the 337nm laser experiments, ε was assumed at *3.5 eV / e-h pair.* Also, assuming a full energy absorption, the *e-h pairs per event* can be determined using Eq. (7.5),

$$N = \frac{4.78\,MeV}{3.5\ eV/e-h\ pair} = 1.37\times10^{6}\,\frac{e-h\ pair}{event}. \tag{7.10}$$

The e-h pairs can be converted to coulombs by,

$$1.37\times10^{6}\,\frac{e-h\ pairs}{event}\times1.602\times10^{-19}\,\frac{coulombs}{e-h\ pairs} = 2.19\times10^{-13}\,\frac{coulombs}{event}. \tag{7.11}$$

Assuming complete charge collection, with no charge trapping, the total charge induced in the device from a neutron interaction in LiZnP or LiZnAs, in coulombs, can be converted to a voltage out from a charge sensitive preamplifier with a 1.0 pF feedback capacitor using Eq. (7.8), where V_o is,

$$V_o = \frac{2.19 \times 10^{-13}\, C}{1 \times 10^{-12}\, F} = 0.219\ Volts\,. \tag{7.12}$$

The difference between the two output voltages is due to large photon flux with the 5 ns laser pulse compared to a single neutron event. LiZnP and LiZnAs devices suffer from poor device performance due to poor material quality and crystal quality. The maximum voltage output voltage of 219 mVolts from a neutron interaction is calculated assuming perfect transport properties, and perfect charge collection. However, a large portion of charge carriers are trapped before being collected, and therefore only a fraction of the initial charge is collected, and contribute to the measured signal. These small signals are often maked in the baseline noise, thereby, being difficult to distinguish from noise. For neutron sensitivity tests, efforts to increase the neutrons incident upon the sample were attempted in order to produce pulses from multiple simultaneous interactions, therefore producing more *e-h pairs* for larger signals. Tests were performed at the radial beam where thermal fluxes up to 7300 thermal neutrons cm^{-2} sec^{-1} kW^{-1} were emitted from the beam port. Also, testing was performed with reactor pulses were reactor powers of approximately 2 GW at 15 milliseconds were achieved. Samples were exposed to approximately 2.1 x 10^7 thermal neutrons from the radial beam over the 15 ms interval with a reactor pulse; however, these signals were still small and indistinguishable above the noise, and could not be traced as demonstrated with laser-induced signals and other neutron sensitivity testing described in sections 6.5 and 6.6 respectively.

7.2 Future Work

LiZnP and LiZnAs devices suffered from charge trapping, largely due to poor material quality and crystal quality. Future work with LiZnP and LiZnAs material needs to focus on material development and bulk crystal growth. Addressing both of these challenges will help reduce the charge transport issues and lead to higher quality neutron detectors.

By using a Differential Scanning Calorimeter (DSC), a complete characterization of the ternary reaction would be explored. The process allows for the heat flow in, or out, of the reaction process to be traced. Melting temperatures of the ternary product can also be

characterized precisely, providing more data points to characterize the melt crystal growth. Once the reaction is characterized using the DSC, the information can be transferred to performing ternary synthesis in a high pressure reactor, or sintering furnace. Removing quartz from the process, thereby, eliminating the probability of fracturing an ampoule during the reaction process, would increase material yields and provide costs savings. Examples of such bench-top style furnaces are provided by venders such as SciDre and MTI corp. These high pressure furnaces can achieve temperatures up to 1100 ^{o}C and pressures up to 150 bar [126, 127]. Over pressure during the synthesis process will help keep the volatiles inside the reaction area, therefore reducing loses at elevated temperatures. Additionally, because there would no longer be a concern of ampoule rupture during the synthesis process, much larger amounts of material could be synthesized at a time.

The ternary product can be analyzed through Inductively-Coupled Plasma Optical-Emission Spectroscopy to provide an indication of the stoichiometry, and impurity content. Depending on the purity, the ternary product may have to be processed further a by static sublimation to remove residual impurity content. The purified ternary material could then be grown into crystalline ingot by a high-temperature modified Bridgman method contained in sealed tantalum vessels as explained previously. However, depending on resources, a vertical Bridgman style high temperature, high pressure crystal growth system would be ideal LiZnP and LiZnAs crystal growth, where precise control of temperature profile would be possible. Commercial systems exist that are capable of achieving temperatures up to 3000 ^{o}C from induction heating, and high pressures, such as the “Bridgman Crystal Growth Station Vertical Type” system provided by Dai-ichi Kiden Co. [128].

Another parameter to consider is lithium purity. At the moment, 99.9% pure natural lithium rod is available from ESPI metals [129]. The trace impurity content as reported by ESPI Metals for lithium at three different purities is listed in Table 7.1. For 95 – 96% enriched ^{6}Li, the lithium purity is in the range of 94 – 95% [40] which is not practical for fabrication of solid-state neutron detectors. The purity desire for semiconductor materials is generally in the range of >5N purity. Because Li is an alkali metal, it is known to be extremely reactive, and consequently, difficult to purify. Therefore, semiconductor grade lithium is not available commercially, and would require in-house purification. Lithium purification was first introduced into the literature in the 1950’s where Li was being explored for nuclear reactor coolants [79, 130, 131]. Vacuum

distillation was the most common method for purifying lithium. Further advances in distillation were introduced by A.G. Ward in a Li still [130]. With a similar distillation system, B.S. Baker was able to increase 97 – 98% purity Li to 99.5% with a distillation yield of 60 – 70% [131]. A higher purity natural Li and enriched ^{6}Li would greatly enhance the performance of LiZnP and LiZnAs neutron detector devices. Researchers using semiconductors that incorporate lithium in the crystal lattice would be able to rule out the degradation in device performance caused by the high levels of impurities in the lithium starting material.

Table 7.1. The trace impurity the results from three different purity Li ingots as provided by ESPI Metals. (3N5 material was not available at the time of purchase for this project)

Material / Purity:	**2N**	**3N**	**3N5**
Ca	100	100	100
K	60	100	100
Cl	50	45	41
Cr	<50	<30	20
Si	<50	<30	20
Al	<50	<30	20
Fe	10	10	10
Na	6000	300	50
Ni	<50	30	20
Co	<50	<30	20
Cu	<50	<30	20

If a higher quality material was produced, undoubtedly device performance would be enhanced. Other Nowotny-Juza materials could be explored, such as LiMgAs, LiMgP, LiMnP and LiMnAs. Some of the Nowotny-Juza materials may include high Z-number elements, such as As, providing more sensitivity to gamma rays, therefore, opening the possibility to a dual neutron and gamma-ray counter. Shown in Fig. 7.1 is a simulated response from a LiZnAs device irradiated by an isotropic Cs-137 source of 662 keV gamma rays, and also irradiated by a 0.5 inch collimated beam of thermal neutrons.

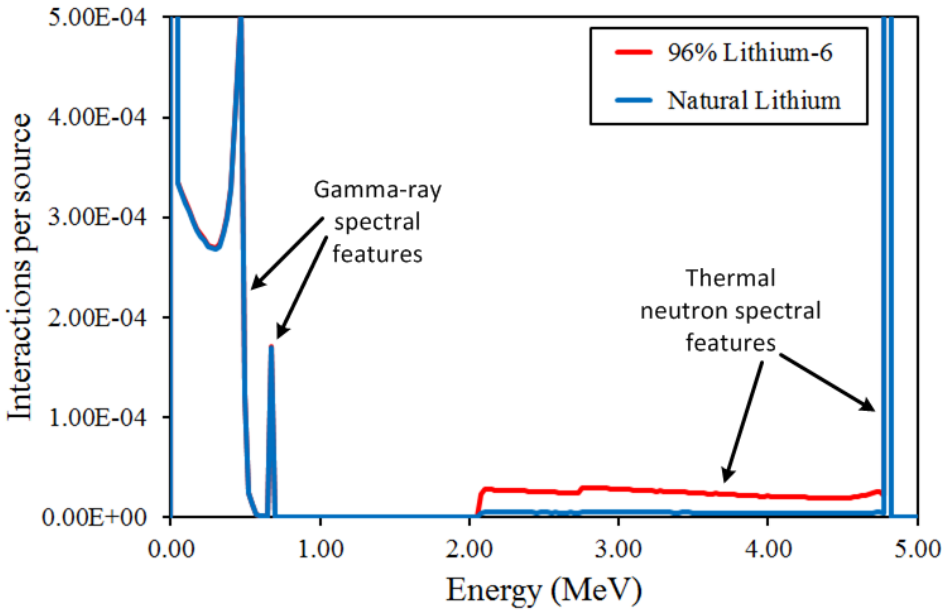

Fig. 7.1. A simulated pulse height spectrum from a LiZnAs device with dimensions 2.100 x 4.060 x 4.155 mm^3. The device simulation included irradiation by an isotropic Cs-137 source and a 0.5 inch incident collimated beam of thermal neutrons.

In the simulation, it was assumed that the sample had perfect transport properties, and no electric field effects; therefore, it is an indication of the possible future for Nowotny-Juza compounds. A common method currently used to distinguish gamma-ray induced signals from thermal neutron induced signals is to use signal processing algorithms. However, in the case of ideal material properties, the pulse height spectrum can be used to distinguish between gamma-ray and neutron interactions.

LIST OF PUBLICATIONS

Refereed:

1. B. W. Montag, M.A. Reichenberger, M. Sunder, K. A. Nelson, P. B. Ugorowski, D.S. McGregor, "Bulk Crystal Growth, and High-Resolution X-Ray Diffraction Results of LiZnAs Semiconductor Material," *J. Crys. Growth*, (2014), *Submitted.*

2. B. W. Montag, M.A. Reichenberger, M. Sunder, K. A. Nelson, P. B. Ugorowski, D.S. McGregor, "Bulk Crystal Growth, and High-Resolution X-Ray Diffraction Results of LiZnP Semiconductor Material," *J. Crys. Growth*, 419 (2015), pp. 143-148.

3. B.W. Montag, M.A. Reichenberger, N. Edwards, M. Sunder, J. Weeks, P. B. Ugorowski, D.S. McGregor, "Static Sublimation Purification Process and Characterization of LiZnP Semiconductor Material," *J. Crys. Growth*, 419 (2015), pp. 133-137.

4. B.W. Montag, M.A. Reichenberger, N. Edwards, M. Sunder, J. Weeks, P. B. Ugorowski, D.S. McGregor, "Static Sublimation Purification Process and Characterization of LiZnAs Semiconductor Material," *J. Crys. Growth*, (2014), *Submitted.*

5. B.W. Montag, M.A. Reichenberger, N. Edwards, P.B. Ugorowski, M. Sunder, J. Weeks, D.S. McGregor, "Synthesis and Characterization of LiZnP and LiZnAs Semiconductor Material," *J. Crys. Growth*, 412 (2015) pp. 103-108.

Conference Proceedings:

1. B.W. Montag, M.A. Reichenberger, N.S. Edwards, M. Sunder, P.B. Ugorowski, J. Weeks, D.S. McGregor, "Purification and Crystallinity Results of LiZnP and LiZnAs Semiconductor Materials," *Conf. Proc. IEEE Nucl. Sci. Symp.*, Seattle, Washington, Nov. 8-15, 2014.

2. Montag, B.W., Reichenburger, M. A., Arpin, K.R., Nelson, K.A., Ugorowski, P.B., McGregor, D.S., Elemental Analysis and Current-Voltage Characteristics of LiZnP and LiZnAs Samples for Solid-State Neutron Detectors, *MRS Conf. Proceedings*, April 1 – 5, 2013, San Francisco, CA.

3. B.W. Montag, K.A. Nelson, M.A. Reichenberger , K.R. Arpin, H.E. McDonald, S.R. Browning, P.B. Ugorowski, D.S. McGregor, "Growth and Preparation of LiZnP and LiZnAs for Solid-State Neutron Detectors," *IEEE Nucl. Sci. Symp.*, Valencia, Spain, Oct. 23-29, 2011, pg 1742-1744.

Other Related Publications: Refereed

1. Kyle A. Nelson, **Benjamin W. Montag**, Niklas J. Hinson, Douglas S. McGregor, "Results of atmospheric exposure to lithium metal foil in mulit-wire proportional counter neutron detectors," *In submission Process*.

2. Nathaniel Edwards, Steven L Bellinger, Ryan G Fronk, Michael A Reichenberger, **Benjamin W Montag**, Kyle A Nelson, BS, Douglas S McGregor, "Synthesis of Enriched Lithium Fluoride Nanoparticles by Low Pressure Vapor Condensation". Nature Nano, *Submitted*.

3. K.A. Nelson, N.S. Edwards, M.R. Kusner, M.R. Mayhugh, **B.W. Montag**, A.J. Schmidt, C.D. Wayant, D.S. McGregor, "A modular large-area Li foil multi-wire proportional counter neutron detector", Radiation Physics and Chemistry (2014), *In Press.*

4. K.A. Nelson, N.J. Hinson, M.R. Kusner, M.R. Mayhugh, **B.W. Montag**, A.J. Schmidt, P.B. Ugorowski, D.S. McGregor, "Characterization of a mid-sized Li foil multi-wire proportional counter neutron detector," Nucl. Inst. and Meth. Vol. 762, (2014) 119-124.

5. K. A. Nelson, S. L. Bellinger, N. S. Edwards, **B. W. Montag**, A. J. Schmidt, C. Wayant, D. S. McGregor, Thermal neutron response and theoretical comparison of LiF coated aluminized Mylar, Nucl. Inst. and Meth. A, Vol. 762, (2014) 130-134.

6. K. A. Nelson, S. L. Bellinger, **B. W. Montag**, A. J. Schmidt, C.D. Wayant, D. S. McGregor, "A LiF coated BoPET multi-wire proportional counter neutron detector," Nucl. Inst. and Meth. A, (2014), *In Press*.

7. K.A. Nelson, S.L. Bellinger, **B.W. Montag**, J.L. Neihart, T.A. Riedel, A.J. Schmidt, D.S. McGregor, "Investigation of a Lithium Foil Multi-wire Proportional Counter for potential ^{3}He Replacement," Nuclear Instruments and Methods, A669 (2012) pg. 79-84.

8. M.J. Harrison, C. Linnick, **B.W. Montag**, S. Brinton, M. McCreary, F.P. Doty, D.S. McGregor, "Scintillation Performance of Aliovalently Doped $CeBr_3$," IEEE Trans. Nucl. Sci., NS-56 (2009) pp. 1661-1665.

Other Related Publications: Conference Proceedings

1. K. A. Nelson, N.J. Hinson, M.R. Kusner, M.R. Mayhugh, **B.W. Montag**, A.J. Schmidt, D.S. McGregor, “Results and Potential Applications of Handheld, Mid-Sized, and Large Area Low Cost Li Foil MPWC Neutron Detectors,” Conf. Proc. IEEE Nucl. Sci. Symp., Seattle, Washington, Nov. 8-15, 2014.

2. Nelson, K.A; **Montag, B.W**.; Schmidt, AJ.; Wayant, C.D.; McGregor, D.S., "A layered ^{6}Li foil multi-wire proportional counter," Nuclear Science Symposium and Medical Imaging Conference (NSS/MIC), 2012 IEEE, pp.597-599, Oct. 27 2012-Nov. 3 2012.

3. Nelson, K.A; Bellinger, S.L.; **Montag, B.W**.; Neihart, J.L.; Riedel, T.A; Schmidt, AJ.; McGregor, D.S., "Investigation of aerogel, saturated foam, and foil for thermal neutron detection," Nuclear Science Symposium and Medical Imaging Conference (NSS/MIC), 2011 IEEE, pp. 1026-1029, 23-29 Oct. 2011.

4. M.J. Harrison, C. Linnick, **B.W. Montag**, S. Brinton, M. McCreary, F.P. Doty, D.S. McGregor, "Radioluminescence and Scintillation Results of Horizontal Gradient Freeze Grown Aliovalently-Doped CeBr3," Conf. Record IEEE Nuclear Science Symp., Dresden, Germany, Oct.19 - Oct. 25, 2008, pg. 2850-2855.

REFERENCES

[1] J. Chadwick, "Possible Existance of a Neutron," *Nature,* vol. 129, pp. 312, 1932.

[2] J. Chadwick, "The Existence of a Neutron," *Proceedings of the Royal Society of London. Series A,* vol. 136, no. 830, pp. 692-708, June 1, 1932.

[3] P. J. Van-Heerden, "The Crystal Counter: A New Instrument in Nuclear Physics," Rijksuniversiteit Utrecht, 1945.

[4] K. A. Yamakawa, "A Suggested Slow Neutron Crystal Counter," *Physical Review,* vol. 75, pp. 1774, 1949.

[5] R. V. Babcock, R. E. Davis, S. L. Ruby *et al.*, "Coated Semiconductor is Tiny Neutron Detector," *Nucleonics (U.S.),* vol. 17, no. 4, pp. 116-122, 1959.

[6] A. N. Laboratory, "Early Exploration - Reactors Designed/Built by Argonne National Laboratory," http://www.ne.anl.gov/About/reactors/early-reactors.shtml, 2014 2014.

[7] Z. W. Bell, K. R. Pohl, and L. Van Den Berg, "Neutron Detection with Mercuric Iodide," *IEEE Trans. Nuc. Sci.,* vol. 51, no. 3, pp. 1163-1165, 2004.

[8] A. G. Vradii, M. I. Krapivin, L. V. Maslova *et al.*, "Possibilities of Recording Thermal Neutrons with Cadmium Telluride Detectors," *Sov.Atom. Energy.,* vol. 42, no. 1, pp. 64-66, 1977.

[9] A. G. Beyerle, and K. L. Hull, "Neutron Detection with Mercuric Iodide Detectors," *Nucl. Inst. and Meth. A,* vol. 256, no. 2, pp. 377-380, 1987.

[10] D. S. McGregor, J. T. Lindsay, and R. W. Olsen, "Thermal Neutron Detection with $Cadmium_{1-x}$ $Zinc_x$ Telluride Semiconductor Detectors," *Nucl. Inst. and Meth. A,* vol. 381, no. 2, pp. 498-501, 1996.

[11] Y. Kumashiro, K. Kudo, K. Matsumoto *et al.*, "Thermal Neutron Irradiation Experiments on ^{10}BP Single-Crystal Wafers," *J. Less Common Met.,* vol. 143, no. 1–2, pp. 71-75, 1988.

[12] W. C. McGinnis, *Film Implementation of a Neutron Detector (FIND): Proof of Concept Device*, SPAWAR Systems Center, Technical Report 1921, 2003.

[13] J. C. Lund, F. Olschner, F. Ahmed *et al.*, "Boron Phosphide on Silicon for Radiation Detectors," *MRS Online P. Libr.,* vol. 162, pp. 601-604, 1989.

[14] F. P. Doty, *Boron Nitride Solid State Neutron Detector*, US-6727504, 2004.

[15] A. N. Caruso, P. A. Dowben, S. Balkir *et al.*, "The All Boron Carbide Diode Neutron Detector: Comparison with Theory," *Mater. Sci. Eng. B,* vol. 135, no. 2, pp. 129-133, 2006.

[16] B. W. Robertson, S. Adenwalla, A. Harken *et al.*, "A Class of Boron-Rich Solid-State Neutron Detectors," *Appl. Phys. Lett.,* vol. 80, no. 19, pp. 3644-3646, 2002.

[17] P. Groot, J. H. F. Grondel, and P. J. Van-Der-Put, "Chemical Vapour Deposition of Boron Phosphides Using Bromide Etchants," *Solid State Ionics,* vol. 16, pp. 95-98, 1985.

[18] A. N. Caruso, R. B. Billa, S. Balaz *et al.*, "The Heteroisomeric Diode," *J. Phys. Condens. Matter,* vol. 16, pp. L139-L146, 2004.

[19] D. S. McGregor, T. C. Unruh, and W. J. McNeil, "Thermal Neutron Detection with Pyrolytic Boron Nitride," *Nucl. Inst. and Meth. A,* vol. 591, no. 3, pp. 530-533, 2008.

[20] D. S. McGregor, M. D. Hammig, Y. H. Yang *et al.*, "Design Considerations for Thin Film Coated Semiconductor Thermal Neutron Detectors—I: Basics Regarding Alpha Particle Emitting Neutron Reactive Films," *Nucl. Inst. and Meth. A,* vol. 500, no. 1–3, pp. 272-308, 2003.

[21] National Institute of Standards and Technology (NIST), "Neutron Scattering Lengths and Cross Sections," *http://www.ncnr.nist.gov/resources/n-lengths/elements/gd.html*, Feb 2014.

[22] W. Nernst, *Theoretical Chemistry*, London, New York: Macmillan and Co., limited, 1904.

[23] A. A. Michelson, and E. W. Morley, "On the Relative Motion of the Earth and the Luminiferous Ether," *American Journal of Science,* vol. 34, pp. 333–345, 1887.

[24] V. Lavrakas, "A History of the Neutron," *Journal of Chemical Education,* vol. 29, no. 6, pp. 281, 1952/06/01, 1952.

[25] K. S. Krane, *Modern Physics*, 2nd ed.: Wiley & Sons, 1996.

[26] W. N. Cottingham, and D. A. Greenwood, *An Introduction to Nuclear Physics*, 2nd ed.: Cambridge University Press, 2001.

[27] Particle Data Group, *Phys. Rev. D,* vol. 66, pp. 01001-113, 2002.

[28] J. K. Shultis, and R. E. Faw, *Fundamentals of Nuclear Science and Engineering*, Boca Raton, USA: CRC Press, 2008.

[29] Oak Ridge National Laboratory (ORNL), "Neutron Sciences | Neutron Science at ORNL," http://neutrons.ornl.gov/, 2014.

[30] D. S. McGregor, and J. K. Shultis, *Radiation Detection and Measurement: Concepts, Methods, and Devices*: CRC Press, Expected 2016.

[31] G. F. Knoll, *Radiation Detection and Measurement*, 3rd ed., Hoboken, NJ: John Wiley & Sons, 2000.

[32] N. Tsoulfanidis, *Measurement and Detection of Radiation*, 2nd ed., Bristol, PA, 1995.

[33] U. Lachish, "CdTe and CdZnTe Crystal Growth and Production of Gamma Radiation Detectors," *guma science*,[1998], http://urila.tripod.com/crystal.htm.

[34] L. Ovechkina, K. Riley, S. Miller *et al.*, "Gadolinium Loaded Plastic Scintillators for High Efficiency Neutron Detection," *Physics Procedia,* vol. 2, no. 2, pp. 161-170, 8//, 2009.

[35] P. Kandlakunta, L. R. Cao, and P. Mulligan, "Measurement of Internal Conversion Electrons from Gd Neutron Capture," *Nucl. Inst. and Meth. A,* vol. 705, pp. 36-41, 2013.

[36] G. Leinweber, D. P. Barry, M. J. Trbovich *et al.*, "Neutron Capture and Total Cross-Section Measurements and Resonance Parameters of Gadolinium," *Nucl. Sci. and Eng.,* vol. 154, pp. 261-279, 2006.

[37] A. Kargar, E. Ariesanti, and D. S. McGregor, "A Comparison Between Spectroscopic Performance of HgI_2 and CdZnTe Frisch Collar Detectors," *Nuclear Technology,* vol. 175, pp. 131-137, 2011.

[38] E. Ariesanti, A. Kargar, and D. S. McGregor, "Mercuric Iodide Crystal growth and Frisch Collar Detector Fabrication," *Nuclear Technology,* vol. 175, pp. 124-130, 2011.

[39] M. A. Lone, R. A. Leavitt, and D. A. Harrison, "Prompt Gamma Rays from Thermal-Neutron Capture," *Atomic Data and Nuclear Data Tables,* vol. 26, no. 6, pp. 511-559, 1981.

[40] Y-12 national security complex, "Li-6 ingot quote," 2014.

[41] A. Syntfeld, M. Moszynski, R. Arlt *et al.*, "^{6}LiI(Eu) in Neutron and Gamma-Ray Spectrometry: A Highly Sensitive Thermal Neutron Detector," *Nuclear Science, IEEE Transactions on,* vol. 52, no. 6, pp. 3151-3156, 2005.

[42] J. Schenck, *Neutron-Sensitive Scintillators*, US Patent 2719127 A, 1955.

[43] S. M. Ignatov, M. G. Mitel'man, V. N. Potapov *et al.*, "Characteristics of CsI(Tl) Scintillating Detector Based on Solid State Photo Multiplier," *Nuclear Science Symposium Conference Record, 2008. NSS '08. IEEE*, pp. 1195-1197, 19-25 Oct. 2008, 2008.

[44] G. F. Knoll, and D. S. McGregor, "Fundamentals of Semiconductor Detectors for Ionizing Radiation," *MRS Sym. Proc.*, pp. 3-17, Pittsburgh, PA, 1993.

[45] S. Sze, *Physics of Semiconductor Devices*, 3rd ed., New York: Wiley, 2007.

[46] D. S. McGregor, and J. Kenneth Shultis, "Spectral Identification of Thin-Film-Coated and Solid-Form Semiconductor Neutron Detectors," *Nucl. Inst. and Meth. A,* vol. 517, no. 1–3, pp. 180-188, 2004.

[47] J. K. Shultis, and D. S. McGregor, "Efficiencies of Coated and Perforated Semiconductor Neutron Detectors," *IEEE Nucl. Sci. Symp.*, pp. 4569-4574, 16-22 Oct., 2004.

[48] S. L. Bellinger, W. J. McNeil, T. C. Unruh *et al.*, "Characteristics of 3D Micro-Structured Semiconductor High Efficiency Neutron Detectors," *IEEE Trans. Nuc. Sci.,* vol. 56, no. 3, pp. 742-746, 2009.

[49] S. L. Bellinger, R. G. Fronk, W. J. McNeil *et al.*, "Improved High Efficiency Stacked Microstructured Neutron Detectors Backfilled With Nanoparticle ^{6}LiF," *IEEE Trans. Nuc. Sci.,* vol. 59, no. 1, pp. 167-173, 2012.

[50] Radiation Detection Technologies (RDT), "MSND Technology Introduction," *http://radectech.com/content/MSND_Gen.pdf*, 2015.

[51] H. Nowotny, and K. Bachmayer, "Die Verbindungen LiMgP, LiZnP und LiZnAs," *Monatsh. Chem. und verwandte Teile anderer Wissenschaften,* vol. 81, no. 4, pp. 488-496, 1950.

[52] H. Nowotny, and K. Bachmayer, *Monatsh. Chem,* vol. 80, pp. 734, 1949.

[53] R. Juza, K. Langer, and K. Von Benda, "Ternary Nitrides, Phosphides, and Arsenides of Lithium," *Angew. Chem. Int. Edit.,* vol. 7, no. 5, pp. 360-370, 1968.

[54] K. Kuriyama, and F. Nakamura, "Electrical Transport Properties and Crystal Structure of Lithium Zinc Arsenide (LiZnAs)," *Phys. Rev. B: Condens. Matter,* vol. 36, no. 8, pp. 4439-41, 1987.

[55] K. Kuriyama, T. Katoh, and N. Mineo, "Crystal Growth and Characterization of the Filled Tetrahedral Semiconductor Lithium Zinc Phosphide (LiZnP)," *J. Cryst. Growth,* vol. 108, no. 1-2, pp. 37-40, 1991.

[56] K. Kuriyama, and T. Katoh, "Optical Band Gap of the Filled Tetrahedral Semiconductor Lithium Zinc Phosphide (LiZnP)," *Phys. Rev. B: Condens. Matter,* vol. 37, no. 12, pp. 7140-2, 1988.

[57] K. Kuriyama, T. Kato, T. Kato *et al.*, "Growth and Photoluminescence Properties of the Filled Tetrahedral Semiconductor LiZnAs," *J. Cryst. Growth,* vol. 166, no. 1-4, pp. 631-635, 1996.

[58] K. Kuriyama, T. Kato, and K. Kawada, "Optical Band Gap of the Filled Tetrahedral Semiconductor LiZnAs," *Phys. Rev. B: Condens. Matter,* vol. 49, no. 16, pp. 11452-5, 1994.

[59] K. Kuriyama, T. Katoh, and S. Tsuji, "Preparation and Characterization of the Filled Tetrahedral Semiconductor Lithium Zinc Phosphide Film on Quartz," *J. Appl. Phys.,* vol. 66, no. 8, pp. 3945-7, 1989.

[60] R. Bacewicz, and T. F. Ciszek, "Preparation and Characterization of Some $A^{I}B^{II}C^{V}$ Type Semiconductors," *Appl. Phys. Lett.,* vol. 52, no. 14, pp. 1150-1, 1988.

[61] R. Bacewicz, and T. F. Ciszek, "Crystal Growth and Characterization of Some Novel $A^{I}B^{II}C^{V}$ Semiconductors," *Acta Phys. Pol. A,* vol. A77, no. 2-3, pp. 379-81, 1990.

[62] A. J. Nelson, M. Engelhard, and H. Hochst, "Synchrotron Radiation Photoemission Study of the Electronic Structure of the Filled Tetrahedral Semiconductors Lithium Zinc Arsenide (LiZnAs) and Lithium Zinc Phosphide (LiZnP)," *J. Electron Spectrosc. Relat. Phenom.,* vol. 51, pp. 623-8, 1990.

[63] D. M. Wood, A. Zunger, and G. R. De, "Electronic Structure of Filled Tetrahedral Semiconductors," *Phys. Rev. B: Condens. Matter,* vol. 31, no. 4, pp. 2570-3, 1985.

[64] F. Kalarasse, and B. Bennecer, "Optical Properties of the Filled Tetrahedral Semiconductors LiZnX (X=N, P, and As)," *J. Phys. Chem. Solids,* vol. 67, no. 8, pp. 1850-1857, 2006.

[65] L. Kalarasse, A. Mellouki, B. Bennecer *et al.*, “Pressure Effect on the Optical Properties of the Filled Tetrahedral Semiconductors LiZnX (X = N, P, and As),” *J. Phys. Chem. Solids,* vol. 68, no. 12, pp. 2286-2292, 2007.

[66] S. H. Wei, and A. Zunger, “Electronic Structure and Phase Stability of LiZnAs: A half Ionic and Half Covalent Tetrahedral Semiconductor,” *Physical Review Letters,* vol. 56, no. 5, pp. 528-531, 1986.

[67] M. P. Bichat, J.-L. Pascal, F. Gillot *et al.*, “Electrochemical Lithium Insertion in Zn_3P_2 Zinc Phosphide,” *J. Phys. Chem. Solids,* vol. 67, no. 5-6, pp. 1233-1237, 2006.

[68] M. P. Bichat, L. Monconduit, J. L. Pascal *et al.*, “Anode Materials for Lithium Ion Batteries in the Li-Zn-P System,” *Ionics,* vol. 11, no. 1 & 2, pp. 66-75, 2005.

[69] D. Kieven, A. Grimm, A. Beleanu *et al.*, “Preparation and Properties of Radio-Frequency-Sputtered Half-Heusler Films for Use in Solar Cells,” *Thin Solid Films,* vol. 519, no. 6, pp. 1866-1871, 2011.

[70] K. S. Shah, "Solid State Neutron Detection with LiZnP," DOE, DE-FG02-98ER82651.

[71] W. Kraus, and G. Nolze, “Powder Cell - A Program for the Representation and Manipulation of Crystal Structures and Calculation of the Resulting X-Ray Powder Patterns,” *J. Appl. Crys.,* vol. 29, no. 3, pp. 301-303, 1996.

[72] L. L. Carter, E. D. Cashwell, and e. al., "Monte Carlo Development in Los Alamos," 1975.

[73] R. F. Pierret, *Advanced Semiconductor Fundamentals*, 2 ed., Upper Saddle River, New Jersey: Pearson Education, Inc., 2003.

[74] University of Pennsylvania Engineering, "Solid State Chemisty," http://www.seas.upenn.edu/. 2013.

[75] W. H. Miller, *Treatise on Crystallography*, Cambridge: Pitt Press, 1839.

[76] A. Kargar, “Characterization and Optimization of CdZnTe Frisch Collar Gamma-Ray Spectrometers and their Development in an Array of Detectors,” Dept. of Mech. and Nuclear Eng., Kansas State University, 2009.

[77] D. C. Stockbarger, “The Production of Large Single Crystals of Lithium Fluoride,” *Rev. of Sci. Instrum.,* vol. 7, no. 3, pp. 133-136, 1936.

[78] M. J. Harrison, A. P. Graebner, W. J. McNeil *et al.*, "Carbon Coating of Fused Silica Ampoules," *Journal of Crystal Growth,* vol. 290, no. 2, pp. 597-601, 2006.

[79] L. F. Epstein, and W. H. Howland, "The Distillation of Lithium Metal," *Science,* vol. 114, no. 2965, pp. 443-444, 1951.

[80] G. Nazri, "Preparation, Characterization and Conductivity of Li3N, Li3P and Li3As," *MRS Online Proceedings Library*, 1988.

[81] M. Winter, "WebElements Periodic Table, Lithium, the essentials," *http://www.webelements.com/lithium/*, 2012.

[82] National Pesticide Information Center (NPIC), "Zinc Phosphide/Phosphine General Fact Sheet," *http://npic.orst.edu/factsheets/znpgen.html*, 2013.

[83] M. Schneider, and M. Krumnacker, "Constitutional Diagram Zinc-Phosphorus," *Neue Huette,* vol. 18, no. 12, pp. 715-18, 1973.

[84] V. M. Glazov, M. Kasymova, and A. P. Regel, *Fiz. Tekh. Poluprovodn,* vol. 13, pp. 2049, 1979.

[85] H. Cole, and H. M. Dunn, *Acta Crystallographica,* vol. 9, pp. 685, 1956.

[86] Y. Maruyama, C. Izawa, and T. Watanabe, "Synthesis of $BiNbO_4$ by the Flux Method," *ISRN Materials Science,* vol. 2012, pp. 5, 2012.

[87] Mersen Inc., "Specialty Graphite Materials - for Continuous Casting," *http://www.mersen.com/uploads/tx_mersen/6-continuous-casting-mersen_06.pdf*, Feb 2014.

[88] A. D. Pelton, "The Li-Zn (Lithium-Zinc) System," *J. Phase Equi.,* vol. 12, no. 1, pp. 42-45, 1991.

[89] R. E. Honig, "Vapor Pressure Data for the More Common Elements," *RCA Rev.,* vol. 18, no. 2, pp. 195-204, 1957.

[90] H. E. Swanson, "Standard X-Ray Diffraction Powder Patterns," Washington, D.C.: U.S Government Printing Office, 1969.

[91] U.S. Environmental Protection Agency, "Method 6010B," *Inductively Coupled Plasma - Atomic Emission Spectrometry*, 1996.

[92] ESPI Metals Inc., "Lithium Rod Typical Analysis," *http://www.espimetals.com/index.php/component/content/article/378-llithium-li/392-llithium-li*, 2009.

[93] Bruker AXS Inc, "brochure_D2_CRYSO.pdf," *http://bruker.poznan.pl/images/stories/AXS/brochure_D2_CRYSO.pdf*, 2009.

[94] S. T. Ali, D. S. Prasad, N. R. Munirathnam *et al.*, "Purification of Tellurium by Single-Run Multiple Vacuum Distillation Technique," *Separation and Purification Technology,* vol. 43, no. 3, pp. 263-267, 2005.

[95] A. M. Hageman, M. J. Harrison, N. Fritz *et al.*, "Purification of Tellurium to 6N Using a Multistage Vacuum Distillation Method," *Proc. SPIE 6707, Penetrating Radiation Systems and Applications VIII*, pp. 67070Z-7, 2007.

[96] G. W. Frances, *Chemical Experiments; The Theory, Practice, and Application...* England: G. Berger, 1842.

[97] M. Schieber, R. C. Carlston, H. A. Lamonds *et al.*, "Purification, Growth, and Characterization of Alpha Mercuric-Iodide Crystals for Gamma-Ray Detection," *J. of Cryst. Growth,* vol. 24–25, pp. 205-211, 1974.

[98] V. M. Zaletin, N. V. Lyakh, and I. N. Nozhkina, "Mass Transport During Growing Mercuric Iodide by Static Sublimation Method," *Crystal Research and Technology,* vol. 20, no. 3, pp. 321-327, 1985.

[99] Galbraith Laboratories Inc., "GLI Method Summary: Inductively Coupled Plasma Atomic Emission Spectrometry,"

[100] M. D. Banus, and M. C. Lavine, "X-Ray Diffraction Studies on Zn_3As_2 and Cd_3As_2 at High Pressure," *High Temperatures - High Pressures,* vol. 1, pp. 269-276, 1969.

[101] H. L. Premarathna, M. J. McLaughlin, J. K. Kirby *et al.*, "Potential Availability of Fertilizer Selenium in Field Capacity and Submerged Soils," *Soil Sci. Soc. Am. J.,* vol. 74, no. 5, pp. 1589-1596, 2010.

[102] A. Le Bail, "Whole Powder Pattern Decomposition Methods and Applications: A Retrospection," *Powder Diffraction,* vol. 20, no. 04, pp. 316-326, 2005.

[103] P. W. Bridgman, "Certain Physical Properties of Single Crystals of Tungsten, Antimony, Bismuth, Tellurium, Cadmium, Zinc, and Tin," *Proceedings of the American Academy of Arts and Sciences,* vol. 60, no. 6, pp. 305-383, 1925.

[104] Los Alamos National Laboratory, "Periodic Table of Elements: Los Alamos National Laboratory," http://periodic.lanl.gov/73.shtml, 2014.

[105] K. Geels, *Metallographic and Materialographic Specimen Preparation, Light Microscopy, Image Analysis and Hardness Testing*, West Conshohocken, PA 19428-2959: ASTM International, 2007.

[106] Pace Technologies Inc., "Abrasive Grinding Paper," http://www.metallographic.com/Brochures/SiCpaper.pdf, 2012.

[107] R. E. Dinnebier, and S. J. L. Billinge, *Powder Diffraction: Theory and Practice*, Cambridge, UK: The Royal Society of Chemistry, 2008.

[108] J. P. Zhao, M. H. Quan, and L. Zhang, "Preparation of Potassium Lithium Niobate Powders with Low Li Content via the Pechini Method," *Ceramics International,* vol. 32, no. 7, pp. 843-846, 2006.

[109] W. Walukiewicz, L. Lagowski, L. Jastrzebski *et al.*, "Electron Mobility and Free-Carrier Absorption in GaAs: Determination of the Compensation Ratio," *Journal of Applied Physics,* vol. 50, no. 2, pp. 899-908, 1979.

[110] M. Martini, J. W. Mayer, and K. R. Zanio, "Drift Velocity and Trapping in Semiconductors - Transient Charge Technique," *Appl. Sol. State. Sci.,* vol. 3, no. 181, 1972.

[111] M. Roth, A. Burger, J. Nissenbaum *et al.*, "Transient Charge Technique Investigation of HgI_2 and CdSe Nuclear Detectors," *IEEE Trans. Nucl. Sci.,* vol. 34, no. 1, pp. 465-469, 1987.

[112] Chase Corp, "HumiSeal® Conformal Coatings," http://www.humiseal.com/conformal-coating/, 2009.

[113] P. L. Rossiter, *The Electrical Resistivity of Metals and Alloys*, Cambridge University Press: Press Syndicate of the University of Cambridge, 1987.

[114] M. H. Du, K. Biswas, and D. J. Singh, "Resistivity, Carrier Trapping, and Polarization Phenomenon in Semiconductor Radiation Detection Materials," pp. 85070M-85070M, 2012.

[115] T. T. Kodas, and M. J. Hampden-Smith, *The Chemistry of Metal CVD*, New York, NY: VCH Publishers Inc., 1994.

[116] G. Lutz, *Semiconductor Radiation Detectors*, New York, NY: Springer Science, 1999.

[117] J. D. Boyd, *A.C. Hall effect measurements on very high resistivity materials exhibiting electrode polarization*, Doctoral Dissertations -Curtis Laws Wilson Library, 1969.

[118] K. Zanio, W. Akutagawa, and J. W. Mayer, "Transport Properties of Semi-Insulating CdTe Using Nuclear Particles," *Applied Physics Letters,* vol. 11, no. 1, pp. 5-7, 1967.

[119] A. Alberigi-Quaranta, C. Canali, and G. Ottaviani, *Rev. Sci. Instr.,* vol. 41, no. 1205, 1970.

[120] Z. H. Cho, M. K. Watt, M. Slapa *et al.*, "Characterization Effort of HgI_2 Radiation Detectors by Pulsed Laser Transient Charge Injection Technique," *IEEE Trans. Nuc. Sci.,* vol. 22, no. 1, pp. 229-240, 1975.

[121] J. F. Ziegler, "SRIM / TRIM: The Stopping and Range of Ions in Matter," 2013.

[122] Artisan Technology Group, "CVI Melles Griot 13AMP005 Wide Bandwidth Amplifier," *http://www.artisantg.com/TestMeasurement/79766-1/CVI_Melles_Griot_13AMP005_Wide_Bandwidth_Amplifier*, 2014.

[123] B. W. Montag, "The Determination of the Fast and Thermal Neutron Fluxes from Radial, Tangential and Diffracted Beam Ports of a TRIGA Mark II Nuclear Reactor ", Kansas State University - Advanced Topics in Nuclear Engineering, Fall 2009.

[124] A. Many, "High-Field Effects in Photoconducting Cadmium Sulphide," *Journal of Physics and Chemistry of Solids,* vol. 26, no. 3, pp. 575-578, 1965.

[125] Ametek Inc., "Ortec 142 A, B, and C," *www.ortec-online.com/download/142A-B-C.pdf*, 2013.

[126] ScIDre GmbH, "High Pressure Multigas Furnace HMO," *http://scidre.de/index.php?id=53*, 2014.

[127] MTI Corp., "100 ml Ni-Based Superalloy High Pressure Hydro-Thermal Reactor 1100°C - RC-Ni200," *http://www.mtixtl.com/rc-ni100.aspx*, 2014.

[128] Dai-ichi Kiden Co., "KDN Dai-ichi Kiden Co.,Ltd./PRODUCTS/Resistive heating crystal growing system," *http://www.d-kdn.co.jp/e_p_resistance_heating.html*, 2014.

[129] ESPI Metals Inc., "Lithium," *http://www.espimetals.com/index.php/online-catalog/392-llithium-li*, 2009.

[130] A. G. Ward, and G. H. Broomfield, "The Purification of Lithium by Vacuum Distillation," *Journal of Applied Chemistry,* vol. 13, no. 8, pp. 329-334, 1963.

[131] P. S. Baker, F. R. Duncan, and H. B. Greene, "Preparation of High-Purity Lithium Metal by Vacuum Distillation," *Science,* vol. 118, no. 3078, pp. 778-780, 1953.

[132] H. L. Larson, *Introduction to Probability Theory and Statistical Interface*, 3rd ed., Canada: John Wiley & Sons, Inc., 1982.

APPENDICES

Appendix A. CRYSTALLOGRAPHY

Appendix A.1. ANGLE BETWEEN TWO PLANES IN A CUBIC LATTICE

In-plane x-ray diffraction measurements are common for evaluation of the crystallinity for orientation within the main orientation. In-plane measurements provide an indication of the crystallinity inside the sample, important for evaluation beyond surface phenomena, and can provide proof of in-plane ordering. In order to perform these measurements, the main orientation must first be evaluated. For example, say the main orientation of a sample is (110) and the in-plane orientation, (211), is an orientation of interest. For a cubic crystal, the angle between the (110) and the (211) can be determined by

$$\cos\theta = \frac{h_1h_2 + k_1k_2 + l_1l_2}{\sqrt{h_1^2 + k_1^2 + l_1^2}\sqrt{h_2^2 + k_2^2 + l_2^2}}, \tag{A.1-1}$$

Where *h,k,l* are the miller indices for the *(hkl)* orientation, and θ is the angle between the $(h_1k_1l_1)$ and $(h_2k_2l_2)$. For the example above, say $(h_1k_1l_1) = (110)$ and $(h_2k_2l_2) = (211)$. Substitute into Eq. (A.1-1),

$$\cos\theta = \frac{1\times2 + 1\times1 + 0\times1}{\sqrt{1^2 + 1^2 + 0^2}\sqrt{2^1 + 1^2 + 1^2}}, \tag{A.1-2}$$

And solve for θ to find,

$$\theta = 30^{\circ}. \tag{A.1-3}$$

Now, the ψ axis on the XRD instrument can be tilted to 30° to explore in-plane (211) ordering in the sample.

Appendix A.2. VECTOR MATH OPERATIONS FOR DETERMINING PROJECTION DIRECTIONS OF OFF-AXIS BRAGG REFLECTIONS ON CRYSTAL SURFACES

In-plane measurements not only help determine in-plane ordering, but also allow for the determination of projection directions onto the main orientation. This allows for the angular geometry with respect to the main orientation of the sample to be determined. For example, say the main orientation of the sample is (110), and an evaluation of the (211) was determined. The projection of the off-axis (211) on the (110) surface can be determined by evaluating the projection of a vector, $\vec{A}$ on a plane, B (whose normal vector is $\vec{b}$) expressed as,

$$\left(\vec{b} \times \left(\vec{A} \times \vec{b}\right)\right). \tag{A.2-1}$$

Therefore, with simple substitution, where $\vec{A}$ = [211] and $\vec{b}$ = [110], the following is determined,

$$\left(\vec{A} \times \vec{b}\right) = [211] \times [110] = \begin{pmatrix} i & j & k \\ 2 & 1 & 1 \\ 1 & 1 & 0 \end{pmatrix} = [\bar{1}11], \tag{A.2-2}$$

$$\left(\vec{B}\times\left(\vec{A}\times\vec{B}\right)\right)_{[110]}\times[\bar{1}11]=\begin{pmatrix} i & j & k \\ 1 & 1 & 0 \\ \bar{1} & 1 & 1 \end{pmatrix}=[1\bar{1}2]\,. \tag{A.2-3}$$

Therefore, it is concluded that the projection of the off-axis (211) on the (110) is along the $[1\bar{1}2]$ direction.

Appendix B. CROSS SECTION DETERMINATION

Appendix B.1. LIZNP

The macroscopic thermal neutron absorption cross section was determined for LiZnP, by

$$\Sigma_{LiZnP} = N_{LiZnP}\sigma_{LiZnP}, \tag{B.1-1}$$

where σ_{LiZnP} is the LiZnP microscopic thermal neutron absorption cross section and N_{LiZnP} is the nuclei density that can be defined as,

$$N_{LiZnP} = \frac{\rho_{LiZnP}}{M_{LiZnP}} A_v, \tag{B.1-2}$$

where ρ_{LiZnP} is the density of LiZnP, M_{LiZnP} is the molecular weight of LiZnP, and A_v is Avogadro's number, 6.022 x 10^{23} atoms/mol. All three constituent elements in the material were considered, Li, Zn and P. The microscopic thermal neutron absorption cross sections, σ, were collected from the National Institute of Standards and Technology (NIST) neutron scattering length and cross sections [21]. Microscopic thermal neutron absorption cross sections for each constituent element can be found in Table B.1.1.

Table B.1.1. Microscopic thermal neutron absorption cross sections for LiZnP and LiZnAs constituent atoms [21].

Constituent atom	Microscopic thermal neutron absorption cross section (barns)
Lithium-6	940
Lithium-7	0.0454
Zinc	1.11
Phosphorus	0.172
Arsenic	4.5

Take for example, the case of natural lithium in LiZnP, the total microscopic cross section can be determined by,

$$\sigma_{LiZnP} = \frac{1}{3}\left(\left(\sigma_{^7Li} \times 0.9241\right) + \left(\sigma_{^6Li} \times 0.0759\right)\right) + \frac{1}{3}\sigma_{Zn} + \frac{1}{3}\sigma_{P} \ , \tag{B.1-3}$$

where 1/3 of each constituent atom is represented since the stoichiometry of LiZnP is 1:1:1. For total lithium, 7.59% was considered ^{6}Li and 92.41% ^{7}Li. By substitution of the microscopic thermal neutron absorption cross sections from Table B.1.1, into Eq. (B.1-3), the total microscopic thermal neutron absorption cross section for LiZnP is,

$$\sigma_{LiZnP} = 2.40 \times 10^{-23} cm^2 \ . \tag{B.1-4}$$

The total molecular weight for LiZnP was determined by,

$$M_{LiZnP} = \frac{1}{3}\left(\left(M_{^7Li} \times 0.9241\right) + \left(M_{^6Li} \times 0.0759\right)\right) + \frac{1}{3}M_{Zn} + \frac{1}{3}M_{P} \ , \tag{B.1-5}$$

where $M_{^7Li}$= 7 g/mol, $M_{^6Li}$= 6 g/mol, M_P= 30.97 g/mol, and M_{Zn}= 65.38 g/mol. By substitution, M_{LiZnP} is,

$$M_{LiZnP} = 34.08 \frac{g}{mol}. \quad \text{(B.1-6)}$$

The density of LiZnP was collected experimentally as described in Section 6.1, where ρ_{LiZnP} = 2.07 ± 0.02 g cm^{-3}. By substitution, into Eq. (B.1-1) and Eq. (B.1-2), the LiZnP macroscopic thermal neutron cross containing natural lithium was determined to be 0.88 cm^{-1}. The same routine was used to determine Σ_{LiZnP} containing enriched ^{6}Li, however the ^{6}Li:^{7}Li ratio was changed to 96% ^{6}Li and 4% ^{7}Li, compared to 7.59% ^{6}Li to 92.41% ^{7}Li for natural lithium containing devices. The Σ_{LiZnP} for devices containing 96% ^{6}Li was determined to be 11.00 cm^{-1}.

Appendix B.2. LiZnAs

The macroscopic thermal neutron absorption cross section was determined for LiZnAs, by

$$\sum_{LiZnAs} = N_{LiZnAs} \sigma_{LiZnAs}, \quad \text{(B.2-1)}$$

where σ_{LiZnAs} is the LiZnAs microscopic thermal neutron absorption cross section and N_{LiZnAs} is the nuclei density that can be defined as,

$$N_{LiZnAs} = \frac{\rho_{LiZnAs}}{M_{LiZnAs}} A_v, \quad \text{(B.2-2)}$$

where ρ_{LiZnAs} is the density of LiZnP, M_{LiZnAs} is the molecular weight of LiZnAs, and A_v is Avogadro's number, 6.022 x 10^{23} atoms/mol. All three constituent elements in the material were considered, Li, Zn and As. The microscopic thermal neutron absorption cross sections, σ, were collected from the National Institute of Standards and Technology (NIST) neutron scattering length and cross sections [21]. Microscopic thermal neutron absorption cross sections for each constituent element can be found in Table B.1.1.

Take for example, the case of enriched ^{6}Li in LiZnAs, the total microscopic cross section can be determined by,

$$\sigma_{LiZnAs} = \frac{1}{3}\left(\left(\sigma_{^{7}Li} \times 0.04\right) + \left(\sigma_{^{6}Li} \times 0.96\right)\right) + \frac{1}{3}\sigma_{Zn} + \frac{1}{3}\sigma_{As} \ , \tag{B.2-3}$$

where 1/3 of each constituent atom is represented since the stoichiometry of LiZnAs is 1:1:1. For total lithium, 96% was considered ^{6}Li and 4% ^{7}Li, as 96% enrichment is commercially available. By substitution of the microscopic thermal neutron absorption cross sections from Table B.1.1, into Eq. (B.2-3), the total microscopic thermal neutron absorption cross section for LiZnP is,

$$\sigma_{LiZnAs} = 3.00 \times 10^{-22} cm^{2} . \tag{B.2-4}$$

The total molecular weight for LiZnAs was determined by,

$$M_{LiZnAs} = \frac{1}{3}\left(\left(M_{^{7}Li} \times 0.04\right) + \left(M_{^{6}Li} \times 0.96\right)\right) + \frac{1}{3}M_{Zn} + \frac{1}{3}M_{As} \ , \tag{B.2-5}$$

where $M_{^{7}Li}$= 7 g/mol, $M_{^{6}Li}$= 6 g/mol, M_{As}= 74.92 g/mol, and M_{Zn}= 65.38 g/mol. By substitution, M_{LiZnAs} is,

$$M_{LiZnAs} = 48.29 \frac{g}{mol} . \tag{B.2-6}$$

The density of LiZnAs was collected experimentally as described in Section 6.1, where ρ_{LiZnAs} = 2.36 ± 0.03 g cm^{-3}. By substitution, into Eq. (B.2-1) and Eq. (B.2-2), the LiZnAs macroscopic thermal neutron cross containing 96% enriched ^{6}Li was determined to be 8.82 cm^{-1}. The same routine was used to determine Σ_{LiZnAs} containing natural lithium, however the ^{6}Li:^{7}Li was changed to 7.59% ^{6}Li to 92.41% ^{7}Li for natural lithium containing devices compared to 96% ^{6}Li and 4% ^{7}Li with enriched devices. The Σ_{LiZnAs} for devices containing natural lithium was determined to be 0.74 cm^{-1}.

Appendix C. STANDARD ERROR

Appendix C.1. ERROR PROPAGATION

When adding and subtracting values that have an associated standard error, for example, $z = x + y$, the total standard error of z, Δz, can be propagated by,

$$\Delta z = \Delta a + \Delta b . \tag{C.1-1}$$

Take for example, if $z = xy$, multiplication or division of values with an associated standard error, Δz, can be propagated by,

$$\frac{\Delta z}{z} = \frac{\Delta a}{a} + \frac{\Delta b}{b}, \tag{C.1-2}$$

where,

$$\Delta z = \left(\frac{\Delta a}{a} + \frac{\Delta b}{b} \right) z , \tag{C.1-3}$$

where Δz is the total standard error in z [132]. Finally, say there is a systematic error associated with a measurement system, Δsys, and an error in the measurement, such as a deviation about a mean, $\Delta meas$, the total error, Δtot, can be propagated in quadrature by,

$$\Delta tot = \sqrt{\left(\Delta sys\right)^2 + \left(\Delta meas\right)^2} . \tag{C.1-1}$$

Appendix C.2. GAUSSIAN STANDARD ERROR

A Gaussian standard deviation from a mean can be defined as,

$$\sigma = \sqrt{\frac{1}{N}\left[\left(x_1 - \bar{x}\right)^2 + \left(x_2 - \bar{x}\right)^2 + ... + \left(x_N - \bar{x}\right)^2\right]}, \tag{C.2-1}$$

Where N is number of measurements, $x_1, x_2, \ldots x_N$ is each value in a data set having the same probability, and $\bar{x}$ is the mean, defined as,

$$\bar{x} = \frac{1}{N}\left(x_1 + x_2 + ... + x_N\right). \tag{C.2-2}$$

The standard error of the mean can be defined as [132],

$$S.E. = \frac{\sigma}{\sqrt{N}}. \tag{C.2-3}$$